Tuning Neutrino Interaction Models to Inclusive Electron Scattering Data

The University Of Sheffield.

Jordan McElwee

Supervisor: Prof. Lee Thompson

Department of Physics and Astronomy
The University of Sheffield

A thesis presented for the degree of
Doctor of Philosophy
in Physics

September 2022

Abstract

As the new generation of neutrino experiments draws ever closer, it is becoming increasingly apparent that the current systematic uncertainties associated with the underlying neutrino-nucleus interactions are not low enough to allow precision measurements of the oscillation parameters. To mitigate this, neutrino experiments are turning toward the electron scattering community to tune interaction models and increase their accuracy. This thesis focuses on the reduction of these systematic uncertainties by tuning interaction models and the calibration of water Cherenkov detectors.

Charged-current quasi-elastic neutrino interactions are T2K's main signal process. This interaction is simulated under the impulse approximation and is later reweighted for use in the oscillation analysis. This approximation does not match other, more sophisticated, models and is an unintuitive depiction of Nature. To move beyond this, a neutral current elastic scattering framework is used to generate electron predictions from the NEUT generator, and is compared to a wide variety of inclusive electron scattering data. A semi-empirical correction is derived to account for discrepancies in the elastic peak position and is applied to the nucleon removal energy in the spectral function ground state model; this correction matches more theoretically rigorous methods, such as relativistic mean field approaches and optical potentials. Its impact on the oscillation analysis and the T2K observables, p_μ and $\cos\theta_\mu$, is also discussed.

The development of an automated monitoring system for the UK light injection system installed in the Super-Kamiokande detector is also described. This is a detailed report on its functioning, which is designed for real-time feedback on the detector's water quality. Attenuation measurements using a diffuser installed in the top of the tank are also implemented, the first analysis completed from the UKLI system, and compared to current, independent methods. This measurement allows for sensitive monitoring of the attenuation length change within the water volume.

"So do all who live to see such times. But that is not for them to decide. All we have to decide is what to do with the time that is given us."

– J. R. R. Tolkien, Lord of the Rings

Acknowledgements

I would like to acknowledge the financial support of the UK Science and Technologies Facilities Council.

It is difficult to make a comprehensive list of all the people who have helped me through the years, with both guidance on my work or a distraction when it was desperately needed.

Firstly, I would like to thank Lee Thompson, who has been much more than a supervisor to me over the years. He has always encouraged me to pursue opportunities that interest me, be it to do with my PhD or around it, and would occasionally put me in my place by thrashing me in a running race. I have to also thank Susan Cartwright, without whom I would likely never have been interested in neutrino physics, and whose door was always open whenever I had a (mostly mundane) question on physics. I owe both of you a great deal.

I have greatly enjoyed being a member of the T2K and SK collaborations over the years, and I'd like to thank all of those who have made the trips memorable. Particular thanks go to Luke Pickering, without whom I'd still be installing NEUT, and Stephen Dolan, with his boundless knowledge on modelling neutrino interactions. Both have shown remarkable fortitude and endless patience putting up with my constant barrage of questions. I must also thank the rest of the NIWG conveners and members over the years, whose input has always helped, along with Kajetan Niewczas, who provided so much detail on simulating lepton interactions and is also a perfect heavy metal singing partner. Additional thanks to Neil McCauley, whose support and guidance regarding SK calibration has been invaluable, along with emotional support when I had my doubts applying for jobs.

Living in Japan will forever be a fond memory, and is due in no small part to the friends there with me. The early mornings sat in the control room were made infinitely more fun by Tristan Doyle, Sam Jenkins, Charlie Ruggles, Joe Walsh and Gabriel Penn. I will miss our regular trips to *Doremi* and *Gyū-Kaku* in the DAQ-mobile, late night Mario Kart tournaments and poker nights. The hunts for melon soda across the 7-Eleven's of Tōkai will be sorely missed.

My years in the department would have been much less interesting if it were not for the people in D36a. Thank you for accepting the inclusion of the beverage bell and our communal jigsaw puzzles. Special thanks to Celeste Pidcott, Henry Israel and (again) Sam Jenkins, for the many laughs during long days in the office. I would also like to particularly thank James Greer and Rob Foster, our weekly karaoke nights and regular pool matches made coming out of lockdown much more enjoyable and whose friendship means a great deal.

Thank you to the friends outside of work and all of whom made lockdown more entertaining than it should have been. Particular thanks to James and Charlotte, who always offered up their home for tea, drinks or board games, and the rest of my D&D group giving

me breaks from reality. Another special thanks goes to my old housemates Rob Worley, Ollie Westbrook and Sam Jenkins (this is the last time...), without you guys I would have gone mad in lockdown, but our playing D&D, (even more) board games and 'front man mode' rock band made the whole thing bearable.

Aleks, thanks for your continued support, and for putting up with my constant stress over the past couple of months. It's likely I would already be a couple of months into my zookeeper training if not for your belief. Finally I'd like to thank my parents and family for all your encouragement through my life, and for always believing in anything I've done. I can't begin to thank you enough for everything you've done for me.

Declaration

The work presented in this thesis is the work of the author, except as noted here or where other work has been cited.

In Chapter 4, the development of the electron scattering was based on the structure for the spectral function implementation, and this benefited from many discussions from the Neutrino Interactions Working Group. The author further developed and adapted this for electron scattering, which had no been previously completed.

In Chapter 5, the derivation of the correction to the removal energy was completed entirely by the author, along with its implementation and the analysis of its effects. Its inclusion into the oscillation analysis, however, was completed by T2K OA group. The discussion on its effect on the OA was still a product of the author.

Chapter 6 is an amalgam of lots of work completed by the SKUK group over the years, however the author worked on all aspects of the monitoring system. The development of the injectors was completed at Warwick, and their beam profiles measured at this institution also. The directionality of the collimators was completed by Pruthvi Mehta, and their inclusion into SKDETSIM was also completed by her. This was based on the formalism made by the author. The tuning of the timing profiles was completed by Dan Martin, though their original implementation and further inclusion (time-of-flight *etc.*) was completed by the author. The bacteria analysis was completed by Pablo Fernando Mendez, but its inclusion into the system was conducted by the author. The process of transforming the raw Super-Kamiokande data to usable ROOT format was completed before this PhD by Adrian Pritchard and Lauren Anthony, however this was implemented into the monitoring by the author.

This thesis was impacted by the coronavirus pandemic, as a significant portion was supposed to be focused on a 3-dimensional calibration system to measure the beam profiles of the UKLI system. This was halted by the pandemic and a new direction had to be taken. Thus much of this thesis was completed under working from home conditions.

Jordan McElwee

Contents

List of Figures

List of Tables

Chapter 1

Introduction to Neutrino Physics

> This was definitely a good idea. There's no chance this wasn't a good idea.
>
> Jez (S1E5 15:48)

Neutrinos are neutral leptons, that only interact via the weak nuclear force and gravity. Meaning "little neutral one" in Italian, the name neutrino is in reference to its small mass, originally thought to be zero. Although it is the smallest particle currently known, the neutrino is also one of the most abundant particles in the universe. This may be reason enough to research this ghostly particle, however they may also pave the way to an explanation of the matter-antimatter asymmetry, one of the great mysteries of modern physics. Therefore, to my mind, the study of these elusive particles could lead to one of the most important discoveries in physics.

1.1 History of Neutrinos

First proposed by Wolfgang Pauli in 1930, the neutrino was the solution to an apparent non-conservation of energy in beta decay [1],

$$n \to p + e^- + \bar{\nu}_e \,; \tag{1.1}$$

a problem originally noticed in 1914, when James Chadwick found the energy spectrum of said decay was continuous [2]. At the time of the neutrino's proposal, only the electron [3] and proton [4] had been discovered, thus the inclusion of an electrically neutral, spin-1/2 fundamental particle was somewhat contentious: increasing the number of fundamental particles by 50%. Nevertheless, Fermi developed a three-body formalism of beta decay [5], suggesting that neutrinos could be detected via inverse beta decay,

$$\bar{\nu}_e + p \to e^+ + n. \tag{1.2}$$

Not everyone was convinced with the proposal, and Niels Bohr suggested that energy need

not be conserved in the decay; this idea was proven unlikely with experiments showing an upper limit on the energy of emitted electron in beta decay [6]. This, along with Chadwick's discovery of the neutron in 1932 [7], made the inclusion of another particle a more enticing option. Due to its extremely low interaction cross-section [8], the observation of such a particle would have to wait until the development of nuclear reactors many years later.

Along with inverse beta decay, Bruno Pontecorvo suggested an alternative technique involving the conversion of chlorine nuclei into argon [9] via the reaction

$$\nu_e + {}^{37}\mathrm{Cl} \rightarrow e^- + {}^{37}\mathrm{Ar}. \tag{1.3}$$

Ray Davis used this idea, and constructed a 3900 litre tank of carbon tetrachloride close to the nuclear reactor at Brookhaven National Lab (BNL, [10]). Though unsuccessful, the experiment confirmed that antineutrinos produced in nuclear reactors were fundamentally different to those required for this method of detection. This lack of success did not dissuade Davis however, and he later used the same method for solar neutrino detection in Homestake (see section 1.2). The discovery of neutrinos did not have to wait too long however: it would only be one year after Davis in 1956 before Fermi's postulate was experimentally verified. After deciding the use of a nuclear bomb would not be the easiest solution[1] [11], Frederick Reines and Clyde Cowan led 'Project Poltergeist', utilising the large neutrino flux expelled from nuclear reactors to overcome the problem of their small cross-section.

Conducting three experiments in the 1950s, Reines and Cowan used a cadmium loaded solvent along with a scintillator solution and employed the delayed-coincidence technique: a positron annihilation followed 5 μsec later by decay photons from neutron capture on the cadmium. Their first experiment at the Hanford reactor in 1953 was critically limited by cosmogenic muons, thus was inconclusive. In 1956, the experiment was moved to exploit the Savannah River reactor and, following drastic improvements to background reduction and detector design, was finally able to confirm the detection of the elusive neutrino [12].

The updated detector, shown in Fig. 1.1, used water loaded with cadmium chloride as a passive target (A and B), while tanks I, II and III are liquid scintillator. A positive signal can only occur in two adjacent scintillator tanks, providing a location for the interaction vertex. This method of determining spatial origin allowed for greater background discrimination and, coupled with a 12 m overburden, reduced backgrounds enough to conclusively prove the neutrino's existence. A final experiment conducted in 1959 [13] yielded a more accurate cross-section for the particle, finding it consistent with theoretical predictions.

Even before the neutrino had been conclusively discovered, results indicated the possibility of two distinct varieties of the particle. Following the muon's discovery in 1937 [14], it was observed the Michel electron (an electron produced from muon decay) had a continuous energy spectrum characteristic of a three-body decay. Here lies the problem: if the muon

[1] This wasn't quite as crazy an idea as it first sounds. Fred Reines worked as project supervisor for several bomb tests for the Manhattan project, so had the expertise to make it safe(ish). Due to the short-lived nature of a nuclear bomb, it would also minimise the number of cosmic backgrounds. Still... using a nuclear reactor was definitely the safer idea.

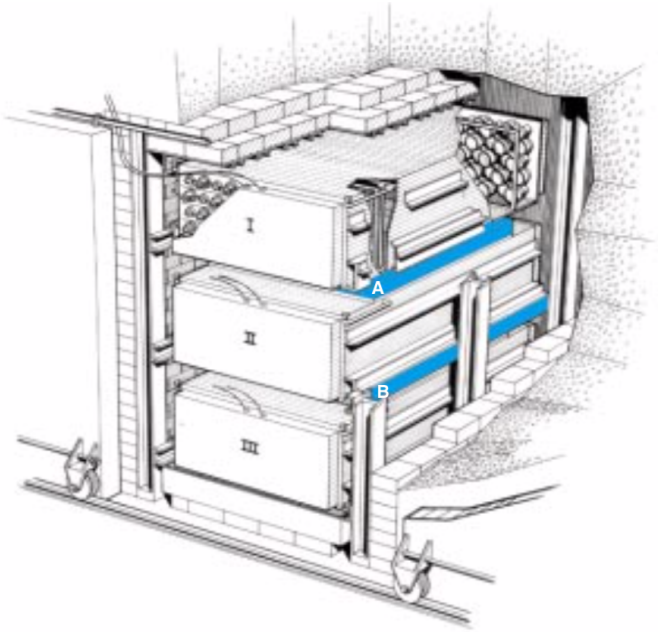

Fig. 1.1: Schematic of the Savannah River detector, shown in its lead shielding. A and B are passive water targets, each loaded with cadmium chloride to increase the neutron capture cross-section. I, II and III are scintillator solutions for electron/positron detection. A signal will only occur in two adjacent scintillators, thus acting as a veto for false signals. Figure taken from [11].

were a only heavier electron, it could be expected to decay via

$$\mu \to e + \gamma;$$

this, in a similar way to the β-decay problem, would produce a single electron energy. After searches for this decay channel found an apparent absence [15], it seemed prudent to introduce lepton number conservation. Muons would then be able to decay into electrons accompanied by two distinct neutrinos,

$$\mu^- \to e^- + \bar{\nu}_e + \nu_\mu. \tag{1.4}$$

In 1962, a team led by Lederman, Schwartz and Steinberger proved this correct [16]. Using the Alternating Gradient Synchrotron (AGS) at BNL, shown in Fig. 1.2, the team produced the first accelerator neutrino beam, pioneering the well-known and widely used pion decay-in-flight method. A charged pion will decay via

$$\pi^{+(-)} \to \mu^{+(-)} + \overset{(-)}{\nu}_\mu \tag{1.5}$$

with a branching ratio of 0.99[2], the charged lepton subsequently decaying via equation 1.4 producing a beam of (anti)neutrinos. If ν_μ and ν_e were identical, one would expect the

[2]This is due to *helicity suppression*. Because of a mismatch between helicity and chirality that arises because of lepton mass, the higher the mass of the lepton the more likely the decay. If the pion were heavy enough, it would decay to a τ instead.

appearance of each charged lepton with equal probability; *i.e.* the same number of electrons and muons produced in the detector. The data, however, showed a statistically greater number of muons than electrons being produced than predictions for no lepton flavour. This indicated neutrino and charged lepton flavour is intrinsically tied, and with it proving the existence of the muon neutrino.

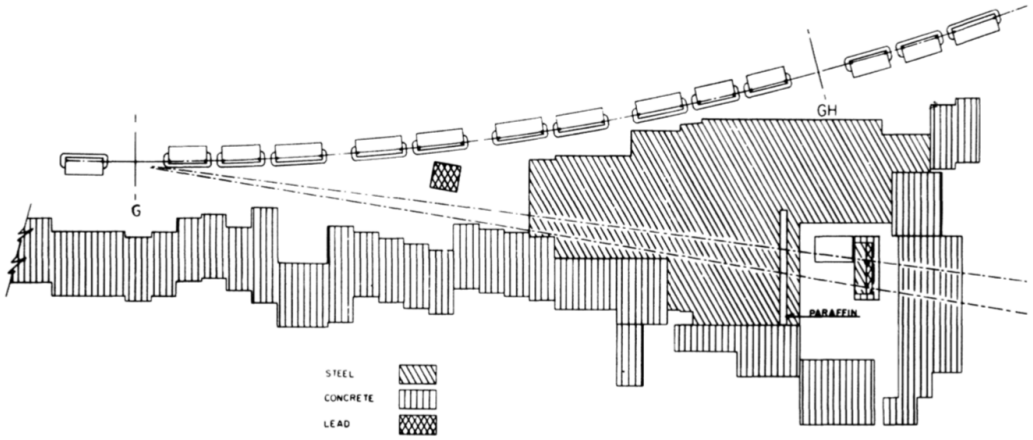

Fig. 1.2: Experimental setup for the AGS at BNL. Protons impinge on a beryllium target producing pions that decay into muons and their corresponding neutrino. The neutrinos pass through the lead shielding into a spark chamber for detection. Figure taken from [16].

The discovery of the τ lepton [17] in 1975 suggested the presence of yet another neutrino flavour; indeed, most physicists were expecting it. Indirect evidence came from the 1989 analyses at Large Electron-Positron Collider (LEP, [18–21]) and the SLAC Large Detector (SLD, [22]), that constrained the number of particles able to couple to the Z^0 boson. Subtracting all observed decays from the Z^0 decay width, the remaining invisible width (Fig. 1.3) is assumed to be due to neutrinos undetected by the experiment. A combined analysis of all LEP data provided a constraint on the number of active light neutrinos with $2m_\nu < m_Z$, finding a value of $N_\nu = 2.984 \pm 0.0082$ [23].

The long wait came to an end in 2000 when the DONUT (Direct Observation of the NU Tau, [24]) collaboration attempted to measure ν_τ interactions directly. Using the 800 GeV proton beam generated by the Tevatron at Fermilab, charmed mesons were produced by interactions in a tungsten beam dump. Neutrinos were subsequently generated by the meson decays,

$$D_S \to \bar{\nu}_\tau + \tau \text{ and}$$
$$\tau \to \nu_\tau + X.$$

The neutrino's charged-current interactions in the nuclear emulsion detector produce a τ which, due to its short lifetime, decayed ~ 2 mm later to a single charged daughter (branching ratio of 0.86). This leads to a 'kink' in the track, identifying the particle as a τ lepton. The number of τ neutrinos found matched Standard Model predictions and was the first observation of the final light species of neutrino. With this, the Standard Model as we know it today was complete (excluding the Higgs Boson).

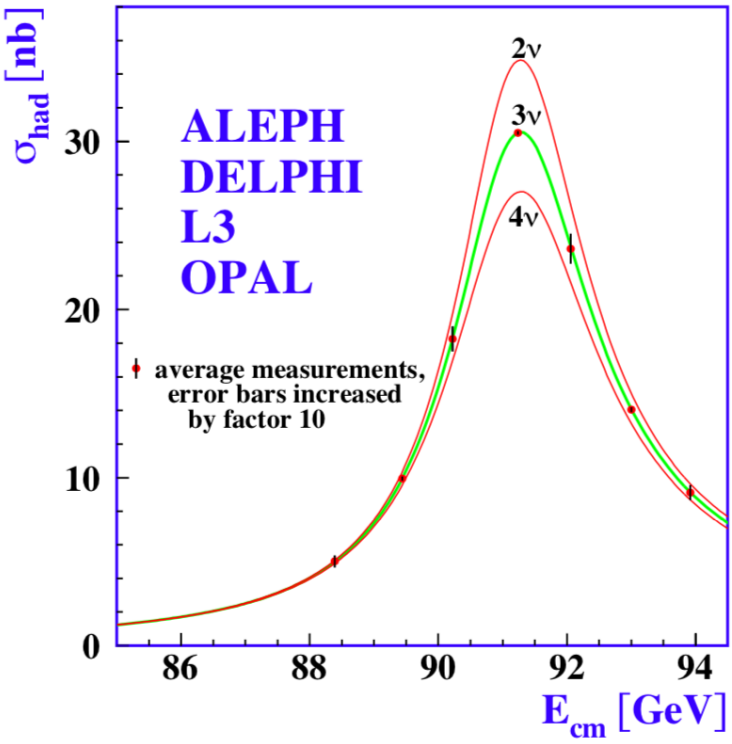

Fig. 1.3: Combined measurements from the ALEPH, DELPHI, L3 and OPAL collaborations of the hadron production cross-section near the Z^0 boson resonance. The curves show Standard Model coupling predictions for two, three and four neutrino species, assuming they account for the invisible decay width. Figure taken from [23].

1.2 Solar and Atmospheric Neutrino Anomalies

Whilst some groups focused on discovering new neutrinos, others attempted to discover their properties and applications to other physics problems. The energy production mechanisms for the Sun had been expressed by Bethe in 1939 [25], discussing both the *pp* chain and CNO cycle[3]; this formed the basis of the energy production in the Standard Solar Model (SSM). John Bahcall built on this to make theoretical predictions of the solar neutrino flux [26, 27], in doing so hoping neutrino measurements would provide constraints to the developing model. Indeed, this was one of the only ways to peer into the interior of a star owing to the high photon opacity of the stellar interior. The total flux comprises of neutrinos from various stages of the complex hydrogen fusion process: the flux predictions for each stage is shown as a function of neutrino energy in Fig. 1.4.

Ray Davis found a null result on his first attempt at detecting solar neutrinos (but placed an upper constraint on the contribution of the CNO cycle) [29], and worked with Bahcall to scale up the experiment. Using the same detection method as his reactor neutrino experiment, a 390,000 litre detector filled with liquid tetrachloroethylene (C_2Cl_4)[4] was built at Homestake mine. The larger size and an overburden of 4,400 metres water equivalent

[3] At the time it was uncertain which dominated in the Sun; it was later discovered that the *pp* chain dominates energy production, accounting for 98.5% of the total [26].

[4] Interestingly, this was just a standard cleaning fluid.

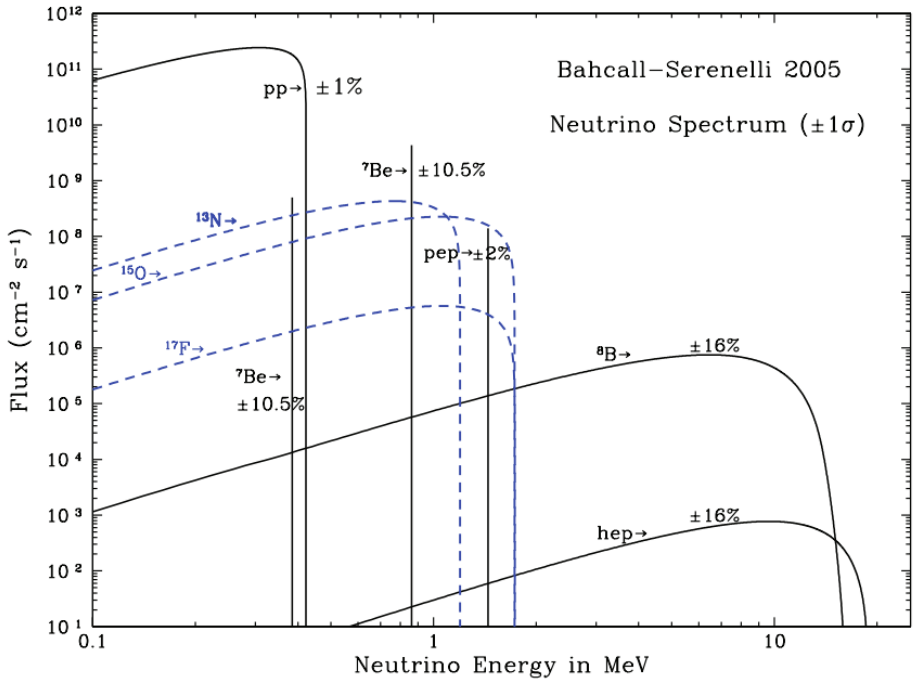

Fig. 1.4: Standard Solar Model predictions for neutrino flux for various steps in the solar fusion chains. Solid lines show the dominant *pp* chain, dashed lines indicate the CNO cycle. Figure adapted from [28].

(m.w.e) significantly reduced backgrounds, though equation 1.3's energy threshold of 814 keV meant the detector was only sensitive to a sample of the solar flux (see Fig. 1.4).

Although the first result again provided an upper limit, regular updates clearly indicated measurements were far below Bahcall's predictions. It was uncertain whether the issue lay with the sensitivity of the experiment, the precision of the theoretical calculations, or both. Upon release of the final Homestake dataset [30], a flux value of $2.56 \pm 0.16(\text{stat}) \pm 0.16(\text{syst})$ SNU (solar neutrino unit; 1 SNU equals 10^{-36} captures per target atom per second) was determined, approximately 1/3 of the theoretical prediction of $9.3^{+1.3}_{-1.4}$ SNU [31]. This became known as the "Solar Neutrino Problem".

Despite the great efforts of the theorists and experimentalists, the tension seemed to only grow stronger between them, with results from the Kamiokande-II experiment [32] agreeing strongly with the Homestake result. Kamiokande (a precursor to Super-Kamiokande (SK), section 3.2) was an imaging water Cherenkov detector, featuring a detector volume of 2140 tons of pure water and 20% photocoverage of photomultiplier tubes. The signal process was neutrino-electron scattering

$$\nu_x + e^- \rightarrow \nu_x + e^-, \tag{1.6}$$

with the outgoing electron direction strongly correlated to the incident neutrino direction. This directionality confirmed that any neutrinos detected emanated from the Sun. Analysis of the Cherenkov ring identified the stellar fusion process a neutrino originated by its reconstructed energy. This technique was drastically different to the one employed at

Homestake, but results remained the same: the data show a deficit in solar neutrinos, with MC/SSM $= 0.46 \pm 0.13(\text{stat}) \pm 0.08(\text{sys})$. It is worth noting that elastic scattering is sensitive to all neutrino flavours, albeit with a reduced cross-section for non-electron neutrinos: electron neutrinos can scatter via both a charged current (exchanging a $W^{\pm}$) and neutral current (exchanging a Z^0), whilst other neutrino flavours can only proceed via the latter. Therefore even attributing all Kamiokande events to a pure ν_e flux, the measured interaction rate is below the prediction. Radiochemical experiments using gallium rather than chlorine were proposed by Bahcall *et al.* in 1978 (based on a method by Kuzmin in 1965) [33, 34], the advantage being

$$^{71}\text{Ga} + \nu_e \rightarrow {}^{71}\text{Ge} + e^- \tag{1.7}$$

has a lower threshold than chlorine at 233 keV. This could detect neutrinos from the *pp* interaction, vital for all further fusion processes, thus a lower than predicted value would dispute some of the criticisms of Homestake.

Two gallium experiments were performed concurrently in the 1990s, GALLEX (Gallium Experiment) and SAGE (Soviet-American Gallium Experiment[5]), conducting the first measurements of low energy solar neutrinos. GALLEX, based in Laboratori Nazionali del Gran Sasso, used a solution of aqueous gallium-trichloride ($GaCl_3$) and chemically extracted the resultant germanium, detecting its decay with a gas proportional counter. SAGE had a target material of liquid gallium metal, but employed the same germanium counting technique as GALLEX. These experiments (including the results of GNO, a follow up to GALLEX), with their increased sampling of the total solar neutrino flux in Fig. 1.4, also found a 50-60% deficit in the number of expected solar neutrinos as compared to theory [35–37]. With these results, an astrophysical explanation for the solar neutrino problem was all but ruled out.

Many ideas were proposed to explain the solar neutrino problem, including the possibility of the Sun's fusion processes being temporarily "turned off"; due to the lengthy time of heat propagation through the Earth, this would take thousands of years to notice using conventional astronomical observations. However, the true reason for the deficit had already been outlined in 1957 (more rigorously in 1967) [38–40]: Pontecorvo had suggested neutrino oscillation as a potential cause for a dearth of solar neutrinos before Homestake obtained any data. Though regularly cited as a plausible explanation for the solar neutrino problem, early measurements from Homestake seemed to be low at 1-1.5 SNU, resulting in a factor of 6 difference between theory and observation. This, coupled with there being only 2 neutrino flavours known at the time, meant neutrino oscillations were not favoured as the cause of the inconsistency. This changed with the strong implication of a third neutrino, following the τ discovery (section 1.1), and updated Homestake measurements settling to within a factor of 3 of theoretical predictions: nicely in line with the number of neutrino types. For this reason, and the discovery of the atmospheric neutrino anomaly, made neutrino oscillations the likely explanation for the neutrino deficit.

[5]This is sometimes known as the Russian-American Gallium Experiment, due to the experiment being conceived before the fall of the Soviet Union. Personally, I think RAGE suits the pursuit of neutrinos better.

Missing neutrinos was not limited to the solar sector, a neutrino shortage was also discovered in the analysis of atmospheric neutrinos, coming to be known as the aforementioned "Atmospheric Neutrino Anomaly". Cosmic ray collisions with nuclei in the upper atmosphere can incite hadronic showers. Amongst the secondary particles generated are pions, whose decays dominate the atmospheric neutrino flux. Due to the nature of charged pion decays, one would expect a ratio of muon to electron neutrinos of $N_\mu/N_e = 2$, as is clear from the decay chain (and the charge conjugates)

$$\pi^+ \to \mu^+ + \nu_\mu,$$
$$\mu^+ \to e^+ + \bar{\nu}_\mu + \nu_e.$$

When both Kamiokande and the Irvine-Michigan-Brookhaven detector (IMB) searched for this ratio, both experiments found an unexplained reduction in the muon neutrino rate [41, 42] (though the electron prediction matched the experimental data), resulting in a ratio significantly smaller than predicted. Kamiokande later extended their search to the multi-GeV region (originally being sub-GeV). Multi-GeV neutrinos have a better angular correlation with their produced charged lepton than the sub-GeV region and are also more likely to penetrate through the Earth, thus observations of an upwards- to downwards-going asymmetry can be achieved. With these effects combined, an investigation of zenith angle dependence on N_μ/N_e can be made. They found that, while the sub-GeV data were isotropic, the multi-GeV data had a large correlation between zenith-angle and excess electron neutrinos [43]. SK later confirmed these results [44], directly demonstrating the oscillatory nature of neutrinos by making high statistics measurements of the upward- to downward-going neutrino asymmetry, the results are shown in Fig. 1.5. Two atmospheric neutrinos of similar energy travelling in opposite directions in the detector (i.e. either up or down), will have travelled significantly different distances, assuming both were produced at the same altitude [44]. Upward-going neutrinos would have a greater propagation distance equal to the diameter of the Earth, thus a greater time to oscillate into other flavours. The zenith angle dependence seen is a clear indication of the disappearance of muon neutrinos (no asymmetry was found in electron neutrinos). SK found a result consistent with an oscillation of ν_μ into ν_τ, with the highest disappearance effect correlated with largest oscillation distance, corroborating Kamiokande's earlier results.

The final nail in the coffin in favour of neutrino oscillations came from the Sudbury Neutrino Observatory (SNO, [46]). SNO employed heavy water (D_2O) as a target in order to test the total solar neutrino flux. Whilst sensitive to a charged current interaction similar to previous experiments,

$$\nu_e + {}^2\mathrm{H} \to p + p + e^-, \tag{1.8}$$

SNO was also sensitive to a neutral current channel

$$\nu_x + {}^2\mathrm{H} \to p + n + \nu_x. \tag{1.9}$$

The neutral current interaction had a much higher threshold at 2.2 MeV, thus sampling

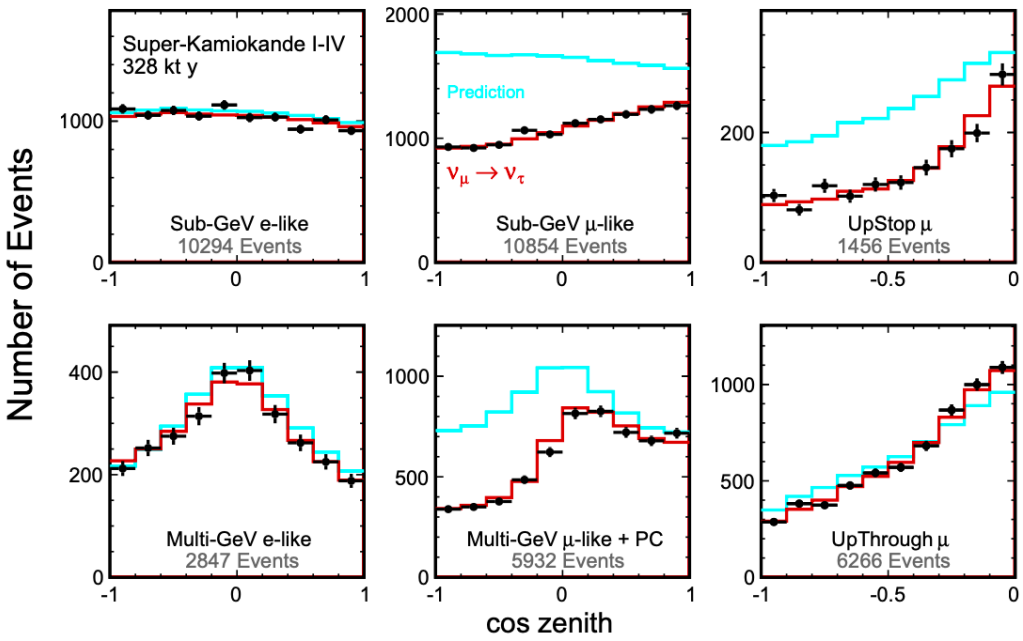

Fig. 1.5: Zenith angle distributions for the Super-Kamiokande detector. The top(bottom) show sub(multi)-GeV data, whilst the left(middle) shows electron(muon) neutrinos. Multi-GeV μ data is a combined histogram with partially-contained events. Upward stopping and upward through-going muons are on the right. Upward-going particles have $\cos\Theta < 0$ and downward-going have $\cos\Theta > 0$. The cyan histogram shows the non-oscillated Monte Carlo predictions, and the red line shows best-fit for $\nu_\mu \leftrightarrow \nu_\tau$, in line with the experimental data. Figure taken from [45].

mostly ^{8}B neutrinos, a much smaller region of Fig. 1.4 than previous data. Crucially however, this interaction is equally sensitive to all neutrino flavours. With a measurement consistent with the Solar Model prediction in this channel, and a deficit in the charged current channel, SNO conclusively proved electron neutrinos from the Sun had oscillated into other flavours [47, 48]. Their final constraints are shown in Fig. 1.6. One final signal channel provided an independent check on oscillation, the same neutrino-electron scattering process used in Kamiokande (equation 1.6). This elastic scattering is also sensitive to all neutrino flavours, but is greatly enhanced for electron neutrinos; if $\phi^{\mathrm{CC}}(\nu_e) < \phi^{\mathrm{ES}}(\nu_x)$, it provides an independent probe for neutrino oscillation. Comparing their charged-current flux to SK's high statistics elastic scattering flux [49] (which matched SNO's measurement), this is exactly what was found.

40 years after Pontecorvo first proposed them, neutrino oscillations had finally been proven as the source of both the solar neutrino problem and atmospheric neutrino anomaly. Due to these measurements, Art MacDonald from the SNO Collaboration and Takaaki Kajita from the SK Collaboration each earned a share of the 2015 Nobel Prize in Physics.

1.3 Oscillation Theory

The neutral leptons are unique in their interactions. A neutrino is a flavour eigenstate produced at the vertex of a weak interaction; the flavour only being determined by the associated charged lepton produced alongside. Whilst the identity of this latter particle can be deduced from its mass (and other properties), the neutrino has two fatal problems: the mass is too small to experimentally determine (at present), and its mass eigenstates are not aligned with its flavour states. Each time a neutrino of flavour α is created, there is some probability mass state i is created alongside it, thus for three-neutrino species a specific neutrino is a coherent superposition of the mass eigenstates such that

$$|\nu_\alpha\rangle = \sum_{i=1}^{3} U^*_{\alpha i} |\nu_i\rangle \qquad \text{and} \qquad |\nu_i\rangle = \sum_{\alpha=e,\mu,\tau} U_{\alpha i} |\nu_\alpha\rangle \,, \tag{1.10}$$

where $U_{\alpha i}$ is the PMNS[6] (Pontecorvo-Maki-Nakagawa-Sakata) mixing matrix [51]. Assuming neutrinos are Dirac fermions, $U_{\alpha i}$ is a 3×3 unitary matrix describing all possible rotations between the flavour and mass neutrino states. It can be described fully by 4 free parameters[7] and decomposed into separate mixing angle matrices given by

$$\begin{aligned}
\mathbf{U} &= \begin{pmatrix} U_{e1} & U_{e2} & U_{e3} \\ U_{\mu 1} & U_{\mu 2} & U_{\mu 3} \\ U_{\tau 1} & U_{\tau 2} & U_{\tau 3} \end{pmatrix} \\
&= \begin{pmatrix} c_{12}c_{13} & s_{12}c_{13} & s_{13}e^{-i\delta_{CP}} \\ -s_{12}c_{23} - c_{12}s_{23}s_{13}e^{i\delta_{CP}} & c_{12}c_{23} - s_{12}s_{23}s_{13}e^{i\delta_{CP}} & s_{23}c_{13} \\ s_{12}s_{23} - c_{12}c_{23}s_{13}e^{i\delta_{CP}} & -c_{12}c_{23} - s_{12}c_{23}s_{13}e^{i\delta_{CP}} & c_{23}c_{13} \end{pmatrix} \\
&= \underbrace{\begin{pmatrix} c_{12} & s_{12} & 0 \\ -s_{12} & c_{12} & 0 \\ 0 & 0 & 1 \end{pmatrix}}_{\text{solar}} \underbrace{\begin{pmatrix} c_{13} & 0 & s_{13}e^{-i\delta_{CP}} \\ 0 & 1 & 0 \\ -s_{13}e^{i\delta_{CP}} & 0 & c_{13} \end{pmatrix}}_{\text{accelerator}} \underbrace{\begin{pmatrix} 1 & 0 & 0 \\ 0 & c_{23} & s_{23} \\ 0 & -s_{23} & c_{23} \end{pmatrix}}_{\text{atmospheric}} ,
\end{aligned} \tag{1.11}$$

where $c_{ij} = \cos\theta_{ij}$ and $s_{ij} = \sin\theta_{ij}$ are the mixing angles between states i and j, and δ_{CP} is the CP violating phase. This latter complex phase introduces differences between neutrino and antineutrino oscillations. Though convention dictates the placement of the CP phase

[6] Also known as the MNS matrix and occasionally, the MNSP matrix. While Pontecorvo proposed the idea, Maki, Nakagawa and Sakata formulated the 3-neutrino mixing matrix.

[7] A 3×3 matrix is conventionally described by 9 free parameters, however 5 of them can be absorbed into lepton fields [52, 53].

onto θ_{13}, each rotation matrix will contribute a complex phase. Unitarity constraints allow the matrix to be rotated to a basis where only one needs to be considered, though it will be some combination of the previous phases ($\delta = \beta\phi_{13} + \gamma\phi_{23} + \xi\phi_{12}$; β, γ, ξ are normalisation constants). If neutrinos are Majorana particles, a final matrix is required including 2 extra complex phases, of the form $\mathrm{diag}(1, e^{i\phi_1}, e^{i(\phi_2+\delta)})$ [54, 55]. It is worth noting that due to charge conjugation, only neutral leptons can be Majorana particles.

Only the mass eigenstates, $|\nu_i\rangle$, are eigenstates of the Hamiltonian, with eigenvalues $E_i = \sqrt{m_i^2 + \mathbf{p}_i^2}$. The mass states evolve according to the time-dependent Schrödinger equation (assuming a vacuum, i.e. no potential)

$$i\frac{\partial}{\partial t}\left|\nu_i(x,t)\right\rangle = \sqrt{m_i^2 + \mathbf{p}_i^2}\left|\nu_i(x,t)\right\rangle = -\frac{1}{2m_i}\frac{\partial^2}{\partial x^2}\left|\nu_i(x,t)\right\rangle; \tag{1.12}$$

the solution of such an equation being a plane wave state, thus

$$\left|\nu_i(x,t)\right\rangle = e^{-i(E_i t - \mathbf{p}_i\mathbf{x})}\left|\nu_i\right\rangle. \tag{1.13}$$

Therefore the time evolution of a flavour state can be simply expressed as

$$\left|\nu_\alpha(x,t)\right\rangle = \sum_{i=1}^{3} U_{\alpha i}^* e^{-i(E_i t - \mathbf{p}_i\mathbf{x})}\left|\nu_i\right\rangle. \tag{1.14}$$

This, combined with equation 1.10, shows after $t = 0$ a neutrino flavour can be expressed as a superposition of all three flavours

$$\left|\nu_\alpha(x,t)\right\rangle = \sum_{\beta=e,\mu,\tau}\sum_{i=1}^{3} U_{\alpha i}^* e^{-i(E_i t - \mathbf{p}_i\mathbf{x})} U_{\beta i}\left|\nu_\beta\right\rangle; \tag{1.15}$$

if $\mathbf{U}$ is not diagonal, flavour state $|\nu_\alpha\rangle$ has a probability of being detected in state $\langle\nu_\beta|$ some time later. This probability is given by the square of the transition amplitude, or

$$P(\nu_\alpha \to \nu_\beta) = \left|\left\langle\nu_\beta|\nu_\alpha(x,t)\right\rangle\right|^2 \tag{1.16}$$

$$= \sum_i \sum_j U_{\alpha i}^* U_{\beta i} U_{\alpha j} U_{\beta j}^* e^{-i((E_i - E_j)t - (\mathbf{p}_i - \mathbf{p}_j)\mathbf{x})}, \tag{1.17}$$

where $\langle\nu_\beta|\nu_\alpha\rangle = \delta_{\beta\alpha}$ due to the orthogonality of the flavour states. Making a reasonable assumption that neutrinos are ultra-relativistic and travel a distance L ($x = t = L$), and assuming all the mass eigenstates are generated with the same energy, E, the plane-wave term can be approximated to[8]

$$E_i t - \mathbf{p}_i\mathbf{x} \approx \frac{m_i^2 L}{2E}. \tag{1.18}$$

[8] $p_i = \sqrt{E_i^2 - m_i^2} \approx E_i(1 - m_i^2/2E_i^2)$: as $m_i \ll E_i$, any terms above second order can be neglected in the binomial expansion.

Due to modelling neutrinos as plane waves, the approximation of mass eigenstates had to be made. If a full derivation were completed with wave-packets instead [56], this would not be required; however, the answer remains the same in each case. This gives the total oscillation probability as

$$P_{\nu_\alpha \to \nu_\beta}(L, E) = \sum_i \sum_j U^*_{\alpha i} U_{\beta i} U_{\alpha j} U^*_{\beta j} \exp\left(-i \frac{\Delta m^2_{ij} L}{2E}\right), \tag{1.19}$$

where $\Delta m^2_{ij} \equiv m^2_j - m^2_i$ is the mass-squared difference. Note, the oscillation probability is only sensitive to the difference in masses, not the masses themselves: one of the difficulties in measuring absolute neutrino mass scales. It is clear to see that neutrino oscillations require at least 2 neutrino masses to be non-zero, a direct departure from the Standard Model.

In the simplified case of 2 neutrino mixing (which is often good enough), there is only one potential unitary mixing matrix,

$$\mathbf{U} = \begin{pmatrix} \cos\theta & \sin\theta \\ -\sin\theta & \cos\theta \end{pmatrix}.$$

When applied in equation 1.19, this single mixing angle θ can describe the oscillation between muon and electron neutrinos in a much simpler form of

$$P_{\nu_\mu \to \nu_e}(L, E) = \sin^2(2\theta) \sin^2\left(\frac{\Delta m^2_{21} L}{4E}\right). \tag{1.20}$$

Due to the sinusoidal nature of this equation, this is the cause of "oscillation", the maximal effect lying at $\Delta m^2_{21} L/4E = \pi/2$. Accelerator neutrino experiments can tune L/E such that their far detector sits at the oscillation maximum and has the greatest sensitivity to oscillation effects. This 2 neutrino mixing parameterisation is only possible due to the small value of θ_{13} and the similarity of 2 of the masses, therefore it is only valid in the atmospheric ($\nu_\mu \leftrightarrow \nu_\tau$) and solar ($\nu_e \leftrightarrow \nu_x$) mixing regimes.

The formalism presented above is for plane-waves in a vacuum, however neutrinos travelling through matter will experience different effects depending on their type. As used by SNO, all neutrinos participate in neutral current forward scattering $\nu_l + X \to \nu_l + X$; in some cases of neutrino-electron scattering however, a further channel is available. Electron neutrinos can exchange both a Z and W boson, therefore undergoing charged current coherent forward scattering. This adds an effective potential to the Hamiltonian, thus effecting the time evolution of the states as described by equation 1.12 and consequently altering the mass eigenstates and mixing angles from the non-perturbed system. Known as the Mikheyev-Smirnov-Wolfenstein (MSW) effect [57, 58], it depends on the electron density of the medium the neutrinos are passing through. Whilst the effect is negligible for an experiment such as T2K, the MSW effect plays a large part in solar neutrino measurements, causing neutrinos to exit the Sun in mostly the $|\nu_2\rangle$ eigenstate, and producing the signal for which SNO received the Nobel prize.

1.4 Experimental Status

Since their discovery, there has been a wealth of data from numerous experiments working toward the measurement of neutrino oscillation parameters. However, neutrino physics still has some outstanding questions: normal or inverted mass hierarchy, the octant of θ_{23}, and the possible existence of CP violation in the neutrino sector. A large number of currently running experiments are attempting to answer these questions, each with their own sensitivity to different parameters; the experimental regime where a parameter is dominant is shown underneath equation 1.11. In a three-flavour framework, all experiments depend on a non-trivial combination of the oscillation parameters. However most experiments analyse their data in terms of 2-neutrino mixing, and thus can make high precision measurements of a couple of leading order neutrino parameters. A summary of the current experimentally determined values is given in Table 1.1.

It is worth a note on the mass hierarchy before continuing. Until now neutrino masses have been given in terms of the difference in their squares. The sign and size of the difference between eigenstates 1 and 2 has been known for some time (see the following section), however the sign of the final mass remains illusive. This leads to two prospective mass orderings: the normal hierarchy (NH, $m_1 < m_2 < m_3$) and the inverted hierarchy (IH $m_3 < m_1 < m_2$). The determination of this is important, not only for the sake of understanding the fundamental properties of the neutrino, but also due to the degeneracies it can cause. In accelerator neutrino experiments, the CP violating phase and the mass hierarchy are intrinsically linked, thus a precision measurement of the former is difficult with the latter unknown. It is also used as an input in cosmological models and is vital in understanding the results from neutrinoless double β decay experiments. The determination of this neutrino property could therefore be the next stepping stone in producing more sensitive neutrino experiments; further details related to this will be explored in sections 1.4.1 and 1.4.2. From now on, the terms 'hierarchy' and 'ordering' will be used interchangeably[9]. Full details of the impact of the mass hierarchy are given in [59] and [60].

The tightest constraints on θ_{12} and Δm^2_{21} are given by variety of solar experiments, along with the KamLAND [64] reactor experiment. The Kamioka Liquid Scintillator Antineutrino Detector (KamLAND) sits in the excavated cavern previous filled by Kamiokande. Located approximately 180 km from 56 nuclear reactors, this long baseline allows KamLAND to be more sensitive to the mass splitting Δm^2_{21} than the solar neutrino experiments themselves. A recent global analysis [65] showed tension between their results [66] ($\Delta m^2_{21} = 7.5^{+0.19}_{-0.20} \times 10^{-5}$ eV^2) and the solar results from the radiochemical experiments [30, 67, 68], Borexino [69], Super-Kamiokande [70–72] and SNO [73]($\Delta m^2_{21} = 4.8 \times 10^{-5}$ eV^2); this tension is reduced upon the inclusion of the recent Super-Kamiokande [74] solar data, however the global fits are still dominated by KamLAND. The MSW effect is sensitive to the sign of the mass splitting, thus whilst KamLAND dominates Δm^2_{21} global fits, the solar data establishes $m_2 > m_1$ and breaks the degeneracy in θ_{12} seen in the KamLAND data [75], with $\sin^2\theta_{12} = 0.318 \pm 0.016$.

[9] There is one final mass hierarchy: the so-called degenerative case where $m_1 \approx m_2 \approx m_3$. This occurs when the absolute mass of the lightest neutrino is large in comparison to the mass differences.

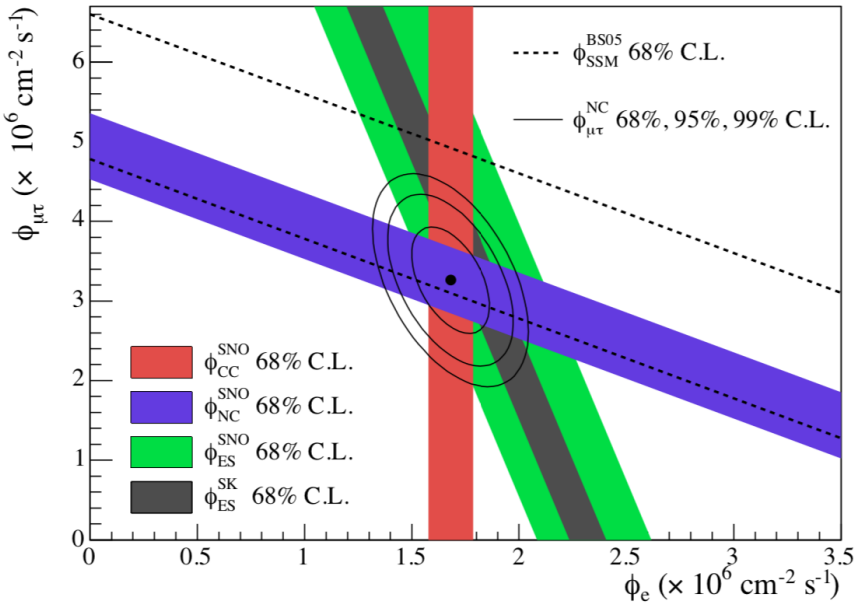

Fig. 1.6: Constraints on the e, μ and τ neutrino fluxes of solar origin from SNO. The point represents the best fit, with 68%, 95% and 99% Confidence Level contours surrounding. Each band represents data obtained from different interaction channels, with high statistics Super-Kamiokande elastic scattering data included. The dotted lines show the SSM prediction, consistent with the experimental data. Figure taken from [50].

Parameter	Normal Ordering	Inverted Hierarchy
$\sin^2\theta_{12}$	$0.304^{+0.013}_{-0.012}$	$0.304^{+0.012}_{-0.012}$
θ_{12} (°)	$33.45^{+0.78}_{-0.75}$	$33.45^{+0.77}_{-0.75}$
$\sin^2\theta_{23}$	$0.450^{+0.019}_{-0.016}$	$0.570^{+0.016}_{-0.022}$
θ_{23} (°)	$42.1^{+1.1}_{-0.9}$	$49.0^{+0.9}_{-1.3}$
$\sin^2\theta_{13}$	$0.02246^{+0.00062}_{-0.00062}$	$0.02241^{+0.00074}_{-0.00062}$
θ_{13} (°)	$8.62^{+0.12}_{-0.12}$	$8.61^{+0.14}_{-0.12}$
δ_{CP} (°)	230^{+36}_{-25}	278^{+22}_{-30}
$\frac{\Delta m^2_{21}}{10^{-5}\text{eV}^2}$	$7.42^{+0.21}_{-0.20}$	$7.42^{+0.21}_{-0.20}$
$\frac{\Delta m^2_{3l}}{10^{-3}\text{eV}^2}$	$+2.510^{+0.027}_{-0.027}$	$-2.490^{+0.026}_{-0.028}$

Table 1.1: Summary of the best fit ($\pm 1\sigma$) three flavour oscillation parameters from a global fit. These results include the Super-Kamiokande atmospheric data [61] and χ^2 mapping for the relevant neutrino parameters [62] with updated ν_e and $\bar{\nu}_e$ classification and subsampling. Data taken from NuFIT 5.1 [63].

Along with KamLAND, there are a few other reactor experiments dedicated to measuring θ_{13}, sometimes known as the electron neutrino disappearance parameter. These are the short-baseline reactor experiments. Each reactor experiment works in a similar way, searching for electron antineutrino disappearance from nearby reactors using Inverse Beta Decay (IBD, equation 1.2) as a signal process. Global fits to the short baseline reactor data from RENO [76] and Daya Bay [77] have a best fit of $\sin^2\theta_{13} = 0.02200^{+0.00069}_{-0.00062}$, with their independent results being extremely consistent with one another. θ_{13} is the smallest mixing angle, and was the last to be determined. In the tribimaximal mixing model [78], it was assumed this mixing angle (and the associated CP phase) was zero, however after indications from Double Chooz [79] and firm evidence from Daya Bay [80], this model was excluded to 5.2σ. This non-zero measurement is important as θ_{13} is coupled to δ_{CP}, thus CP violation in the neutrino sector requires this mixing angle to be non-zero. While the reactor experiments are sensitive to Δm^2_{31}, the main constraints come from long baseline accelerator experiments, as reactors are actually sensitive to an effective mass, $\Delta m^{2\,eff}_e = \cos^2\theta_{12}\Delta m^2_{31} + \sin^2\theta_{12}\Delta m^2_{32}$ [81].

The early experiments to detect atmospheric neutrinos were investigating them as a background in the search for nucleon decays, examples being Kamiokande [42] and IMB [41][10]. In current atmospheric neutrino experiments, the main observation channel is $\nu_\mu \to \nu_\mu$ disappearance, as such they are most sensitive to θ_{23} and Δm^2_{32}. Some experiments built primarily for neutrino astronomy, such as IceCube DeepCore [84] in Antarctica and ANTARES [85] in the Mediterranean sea, can also measure atmospheric neutrinos. ANTARES recently made a measurement of ν_μ disappearance, finding $\Delta m^2_{32} = (2.0^{+0.4}_{-0.3}) \times 10^{-3}$ eV^2 and $\theta_{23} = (45^{+12}_{-11})^\circ$ [86], these results are comparable to both DeepCore ($\Delta m^2_{32} = (2.31^{+0.11}_{-0.13}) \times 10^{-3}$ eV^2 and $\sin^2\theta_{23} = (0.51^{+0.07}_{-0.09})$) [87] and Super-Kamiokande ($\Delta m^2_{32} = (2.5^{+0.13}_{-0.31}) \times 10^{-3}$ eV^2 and $\sin^2\theta_{23} = (0.587^{+0.036}_{-0.069})$) [61]. There is some slight tension between the Super-Kamiokande results, whose data show a weak preference for the upper octant for θ_{23}, whereas DeepCore prefers maximal mixing. As mentioned, ν_μ disappearance is dominated by $\nu_\mu \to \nu_\tau$ oscillations, thus the observation of ν_τ appearance would be an experimental proof of the oscillations. Due to the high threshold, this is a difficult reaction to detect, however Super-Kamiokande and IceCube have observed their appearance in atmospherics [88, 89], whilst the OPERA experiment has observed ν_τ appearance [90] in the CNGS beam [91].

Long baseline experiments use accelerators to produce a neutrino beam using the meson decay-in-flight method established in 1962, briefly described in section 1.1. By studying ν_μ disappearance, the atmospheric parameters θ_{23} and Δm^2_{32} can be determined, the former can be measured by the position of the oscillation minimum of the neutrino energy spectrum, whilst the latter determines its depth. The observation of ν_e appearance gives the long baseline experiments sensitivity to θ_{13} with the height of the electron neutrino spectrum (albeit in a combined measurement with θ_{23} and Δm^2_{32}) and to a subleading order to the CP violating phase δ_{CP}. Current best constraints for these parameters come from the

[10] Others were Frejus [82] and NUSEX [83], both iron tracking calorimeter experiments. At the time when Kamiokande and IMB were finding a deficit of atmospheric neutrinos, both of these seemed to be finding results consistent with solar model predictions. This contributed to the atmospheric neutrino anomaly.

ongoing T2K [92] and NOνA [93] experiments. Old long baseline experimental data, such as those from K2K [94] and MINOS [95] is still used in global fits, however is overshadowed by the current experiments' sensitivity. They were of course, important in their own right, as K2K was the first accelerator neutrino experiment to measure oscillation parameters, whilst MINOS provided the first direct precision measurements that the atmospheric oscillation parameters are the same regardless of neutrino or antineutrino. Along with high precision measurements of the atmospheric oscillation parameters, in 2020 T2K became the first experiment to find evidence for a non-zero measurement of δ_{CP} to a 3σ significance [96]. When originally presented, these data showed considerable tension in the normal ordering with NOνA results, though a reanalysis of the data concluded results are consistent to a 1.7σ level even under the normal hierarchy [63], this is presented visually in Fig. 1.7.

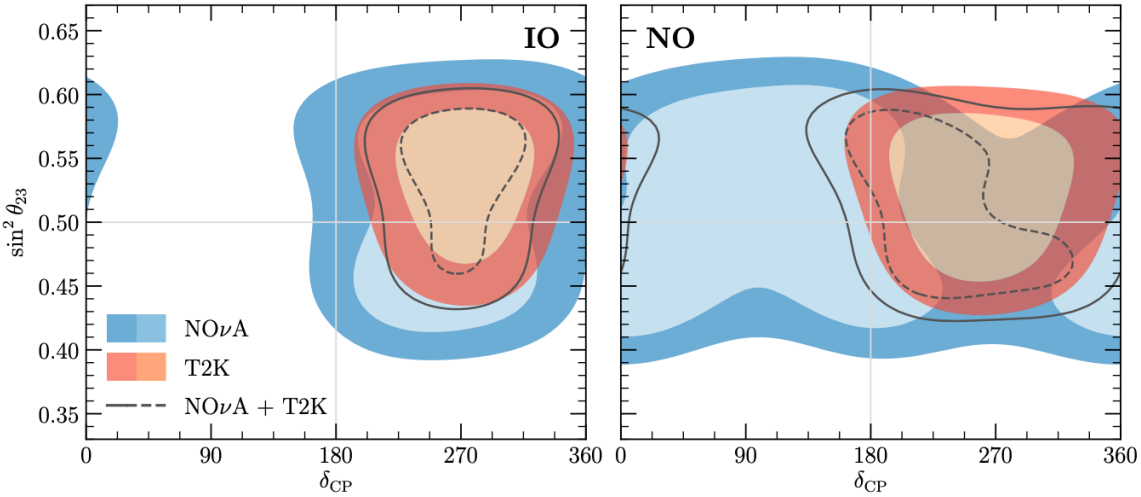

Fig. 1.7: T2K (red) vs NOνA (blue) 1σ and 2σ allowed regions for the CP violating phase, with inverted(normal) mass ordering shown on the left(right). Results are minimized for $\Delta m_{3\ell}$, with the figure taken from [63].

1.4.1 Absolute Mass Scale

Oscillation experiments are only sensitive to the mass difference and mixing angles, thus to probe the absolute mass scale of the mass eigenstates a different approach is required.

In principle, the end point of a β-decay spectrum can access the neutrino mass. The best constraints on the effective electron antineutrino[11] mass come from KATRIN [97], determining the upper limit to be 1.1 eV to a 90% confidence limit. Achieved by studying the tritium (^{3}H) β-decay spectrum, the KATRIN experiment aims to make a measurement of the absolute neutrino mass down to a sensitivity of 0.2 eV at a 90% CL. This is not the first experiment to attempt this measurement, with the Mainz [98] and Troitsk [99] experiments constraining $m_\beta < 2.2$ eV to a 95% CL, however KATRIN achieved a higher sensitivity

[11] Though the β decay spectrum can access individual masses, current sensitivities are too small to make these measurements. Thus experiments are only sensitive to the effective electron neutrino mass $m_\beta^2 = \sum_{i=1}^{3} |U_{ei}|^2 m_i^2$.

during its early data-taking. Crucially, although this method has a lower sensitivity than the following procedures, it is completely model-independent, and thus will always be an appropriate method for probing neutrino masses. The limits on other neutrinos come from π^- and τ^- decay for $m^{eff}_{\nu_\mu}$ and $m^{eff}_{\nu_\tau}$ respectively, the Particle Data Group (PDG) set the limits as $m^{eff}_{\nu_\mu} < 190$ keV at 90% CL and $m^{eff}_{\nu_\tau} < 18.2$ MeV at 95% CL [45].

Neutrinoless double β decay ($0\nu\beta\beta$) is another method of determining neutrino mass, however this is contingent on neutrinos being Majorana fermions. Double β decay ($2\nu\beta\beta$) usually occurs in isotopes where a single β decay is forbidden by energy conservation, as if another nucleus changing decay is possible, the rate of $2\nu\beta\beta$ is often too low to be observed[12]. Using the lifetime of double β decaying isotopes such as ^{76}Ge or ^{130}Te and assuming neutrino exchange is the dominant mechanism behind $0\nu\beta\beta$, one can constrain the effective Majorana neutrino mass [101]. Lower bounds for the half life of various isotopes have been set by a range of experiments, such as GERDA for ^{76}Ge [102], CUORE for ^{130}Te [103] and KamLAND-Zen and EXO for ^{136}Xe [104, 105]. Current limits on these experiments provides a conservative upper limit on the effective Majorana mass to be $m_{\beta\beta} < 350$ meV. Interestingly, a measurement by KATRIN of effective mass of this value or higher would likely point to neutrinos being Dirac particles, or an incomplete understanding of $0\nu\beta\beta$. Due to the lepton-number violating nature of this decay, it could be a direct way of generating matter in the universe and contribute to the matter-antimatter asymmetry observed.

The strongest constraints come from cosmological considerations, however these are very model dependent. Whilst the direct measurement of relic neutrinos is difficult and as yet unobserved (though future experiments such as PTOLEMY [106] aim to do so), they directly affect cosmological evolution; cosmological observations can therefore directly constrain the neutrino mass [107, 108]. Small fluctuations in the temperature and polarization of the Cosmic Microwave Background (CMB) radiation can give insight into both the sum of neutrino masses and also the number of neutrino species experiencing a gravitational force, providing an independent measurement on the existence of more neutrinos from the joint LEP results. Fits to these data often include information from large scale structure formation like baryon acoustic oscillations (BAO), as these break degeneracies in the CMB data [109, 110]. The tightest constraint comes from the most recent results from Planck [109] which, when combined with other observations have placed incredibly tight limits of $\sum m_\nu < 0.12$ eV and $N_{eff} = 2.99 \pm 0.17$. The model used in these observations is ΛCDM which, although matches our current data extremely well, might require improvement. Including neutrino masses is a 'natural' extension to the model, as from oscillation experiments it is clear neutrinos must have mass, thus will clearly affect the observables.

These are brief summaries of a large area of research into the measurement of the absolute mass scale of neutrinos. Though interesting, it does not affect the results of oscillation experiments and therefore no further discussion will take place about these topics.

The Standard Model (SM) includes neutrinos as massless particles, whereas the parti-

[12] This is not always the case, as ^{238}U has been observed to undergo $2\nu\beta\beta$ while also being an α emitter [100]. It's also worth noting that in isotopes where single β decay isn't possible, this is due to spin-coupling. An even number of protons and neutrons causes a lower energy state than would be achieved through β decay.

cles' oscillation show this cannot be the case. The experiments above, which are attempting to measure their mass, do not go so far as explaining why the neutrino has a mass that is extremely small when compared to the other SM particles. The Type-I See-Saw mechanism [111] explains this, by coupling the observed left-handed neutrinos to right-handed Majorana neutrinos. The mass matrix describing these is

$$\begin{pmatrix} 0 & M_D \\ M_D & M_M \end{pmatrix}, \tag{1.21}$$

where M_D and M_M are the Dirac mass and Majorana mass respectively. The eigenvalues of this will derive the absolute neutrino mass, with values

$$m_{1,2} = \frac{M_M \pm \sqrt{M_M^2 + 4M_D^2}}{2}. \tag{1.22}$$

If we assume the Majorana mass is on the scale of Grand Unified Theories (GUT, $\sim 10^{16}$ GeV) and the Dirac mass is on the electroweak scale ($\sim$ 100 GeV), the masses reduce to $m_1 \approx M_D^2/M_M$ and $m_2 \approx M_M$. This naturally generates a very small neutrino mass, but again requires the neutrinos be their own antiparticle. It also raises the question of how a non-weakly interacting neutrino would affect oscillations. If this particle were to participate in neutrino mixing, it would require equation 1.11 be non-unitary in its standard (3×3) form. The inclusion of these 'sterile' neutrinos could go some way to explaining [112] the current background excess seen by the short-baseline experiments LSND [113] and MiniBooNE [114][13]. Again, although an interesting area, this is irrelevant to this thesis and will not be discussed further.

1.4.2 Future Prospects

The measurement of neutrino parameters has progressed rapidly in the past few decades, with the most sensitive experiments yet to come. This section will summarise some of the future prospects for neutrino physics in the coming years. Due to the exciting and varied future of the field, there will inevitably be experiments that have been missed. The different regimes will be separated in the following discussion, however many of these experiments will measure various aspects of neutrino properties; indeed, the future of neutrino measurements likely falls to 'synergistic' measurements between experiments with different degeneracies.

Atmospheric neutrinos will continue to be a source of information in the next generation of neutrino experiments. All experiments plan to make new, competitive measurements of the 'known' neutrino parameters, such as θ_{23} and $|\Delta m^2_{23}|$, however with increased sensitivities capable of measuring of measuring the mass ordering and octant of θ_{23}. Atmospheric measurements are largely insensitive to the CP violating phase, and the large resonant matter effect (MSW) from neutrinos travelling through the Earth allows these new generation

[13] Interestingly, KARMEN did not see this excess [115], and restricted the LSND parameter space.

of experiments to break the octant degeneracy and determine its value. The Precision IceCube Next Generation Upgrade (PINGU, [116]) is an extension of the IceCube experiment in the Antarctic, which will achieve a 3σ measurement of the mass hierarchy within 5 years - though this estimate is conservative based on NH or IH. The Cubic Kilometre Neutrino Telescope (KM3NeT, [117]) continues the work of the ANTARES experiment and will complement PINGU. ORCA (Oscillation Research with Cosmics in the Abyss) is one of several large subdetectors, and will be optimised to measure atmospheric neutrino oscillations. This should make a $4.4\sigma(2.3\sigma)$ measurement of the normal(inverted) mass hierarchy in 3 years. Both PINGU and ORCA are water Cherenkov detectors and have similar operating principles, however they are in opposite hemispheres and thus offer global coverage of atmospheric neutrinos. Another detector at the India-based Neutrino Observatory (INO), the magnetized iron calorimeter (ICAL, [118]) using a very different technique will measure the mass hierarchy to 3σ within 10 years of operation, if the energy of the outgoing hadron is also reconstructed. Of course, a global fit to all these data will increase the sensitivity and also provide a comparison between the two experimental techniques.

Exciting new prospects are occurring in the accelerator neutrino sector, with the building of Hyper-Kamiokande (HK, [119]) and DUNE [120]. HK is the successor to SK, with a fiducial mass of 190 kton. Sitting at the same baseline of 295km, HK will use the upgraded accelerator and beamline at J-PARC for a greater sensitivity to oscillation measurements (along with a rich physics programme of its own) for the T2K experiment. As the matter effects over this short baseline is small, the experiment will have limited access to the mass ordering, however CP violation can be measured for 76%(57%) of possible δ_{CP} values to $3\sigma(5\sigma)$. A joint analysis with their atmospheric sample is complementary and can reject the wrong mass hierarchy to 3σ, along with establishing the octant of θ_{23}, showing the power of combining the analyses. The mass hierarchy enters the ν_e appearance equation at sub-leading order, as such to increase the scale of the perturbation the energy must be increased, and in turn so must the baseline in order to stay at the oscillation maximum [59, 121]. The effect of increasing the baseline can be seen in Fig. 1.8, which shows DUNE can provide an unambiguous measurement of the mass hierarchy regardless of the δ_{CP} value. The collaboration anticipates to determine the hierarchy to 5σ within 6 years (this is incredibly conservative, for $\delta_{CP} = -\pi/2$ predictions are within a year). DUNE also has great prospects to discover CP violation, determining 50% of δ_{CP} values to 5σ in 9 years, or in its absence they can set stringent limits. There is also a good chance of determining the octant of θ_{23}, even for values close to maximal mixing. The JSNS^2 [122] is a short-baseline neutrino experiment, planned also at J-PARC, sensitive to eV scale sterile neutrinos in order to solve the LSND anomaly, however there is currently no planned measurements of the unknown oscillation parameters.

While DUNE and HK will have a rich accelerator programme, they can also complete solar neutrino measurements. The JinPing Neutrino Experiment [123] aims to improve measurements of neutrinos from solar fusion processes. The JinPing Laboratory is unique in having the lowest background radioactivity, the highest overburden and the lowest reactor background. These traits, along with the longest free solar neutrino path through the Earth,

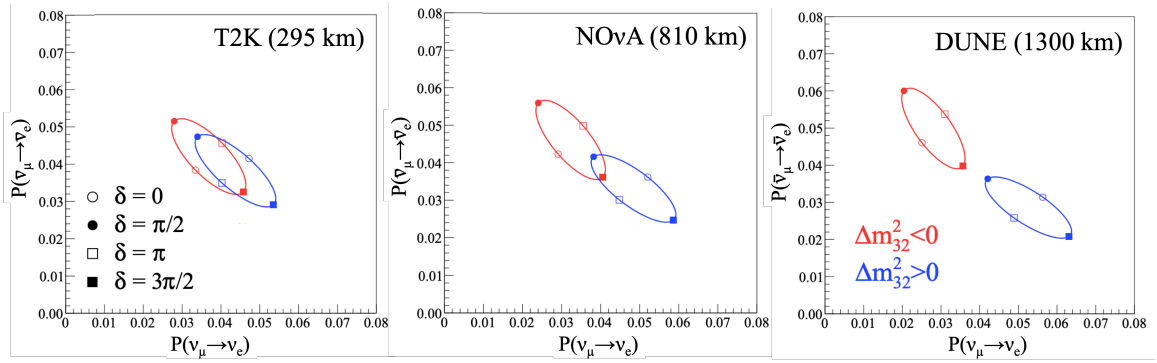

Fig. 1.8: ν_μ vs $\bar{\nu}_\mu$ disappearance probability for a full δ_{CP} phase space. There is little mass hierarchy discimination for the T2K baselines. As the baseline and energy increases, the mass hierarchy discrimination improves steadily, with DUNE offering unambiguous determination of the mass hierarchy independent of the size of CP violation. This is illustrative, with oscillation parameters fixed at $|\Delta m^2_{32}| = 2.4{\times}10^{-3}$ eV^2, $\sin^2(2\theta_{23}) = 1$ and $\sin^2(2\theta_{13}) = 0.09$, and $L/E = 0.4$ km/MeV. Figures adapted from [121].

identify it as a competitive low energy neutrino site. With this low background, it is proposed to make high precision measurements of the products of the *pp* chain and potentially the discovery of CNO cycle neutrinos. It could also provide a tighter constraint on the vacuum-matter transition to the MSW effect. Though, like JSNS^2, JNE will not make measurements of the oscillation parameters, it will make important measurements for solar models, geo-neutrinos, and dark matter.

Upcoming reactor experiments are also unique in their ability to determine the mass ordering, with some having almost no dependence on δ_{CP} or θ_{23}. The Jiangmen Underground Neutrino Observatory (JUNO) [124, 125], primarily a liquid scintillator detector, can reach the required confidence level of 3σ within 6 years, independent of the degeneracies caused by the inclusion of other unknown parameters. Their technique relies on the first simultaneous measurement of oscillations driven by atmospheric and solar neutrino mass differences, and with this are able to make precision measurements of many oscillation parameters, namely $\sin^2\theta_{12}$, Δm^2_{21} and Δm^2_{ee}. Measuring these in a model-independent way is not just an exercise in curiosity, but an important discriminator in testing neutrino extensions to the Standard Model. These measurements will be supplemented by an extension to RENO, RENO-50 [126], that will reach a similar precision on the oscillation parameters. JUNO and RENO-50 are not the only upcoming reactor experiments, however they are the only ones whose main purpose is the study of oscillations. Further reading about reactors searching for sterile neutrinos can be found in references [127–132].

As stated, though each experiment has its own sphere of influence, combined measurements between different experiments will provide much more sensitive measurements to the unknown properties of neutrinos. These will break degeneracies seen in the long baseline and atmospheric experiments, improving measuremnents of the mass hierarchy and δ_{CP}. This will in turn propagate into measurements of neutrinoless double beta decay [133], thus the Majorana nature of the neutrino, and into the measurement of the see-saw measurement and leptogenesis in the early universe [134]. In the next few years it seems there will be a

slew of new data providing highly sensitive insights into the world of neutrinos.

For more reading into new experiments on the absolute mass scale and the Cosmic Neutrino Background, see references [106, 135–138].

1.5 Thesis Structure

This chapter has summarised the history of neutrino physics and its near future. The focus has shifted from discovery of new neutrino phenomena, as was the case up until the early 2000s, to precision measurements of neutrino properties. To achieve this, the uncertainties on oscillation experiments must be reduced. This thesis focuses on the improvement of the removal energy systematic for the charged-current quasi-elastic interaction, T2K's main interaction channel. The structure of this thesis is as follows:

- Chapter 2 presents an overview of neutrino interactions with nuclei, covering the mathematical description of interactions (with a specific focus on quasi-elastic and elastic scattering) and the underlying nuclear models.
- Chapter 3 provides an overview of the T2K and Super-Kamiokande experiments of which this thesis is associated with. This includes a description of the functioning of electron scattering experiments, whose data is extensively used.
- Chapter 4 introduces the electron extension to NEUT, T2K's event generator. This describes the implementation and validation of the model for quasi-elastic scattering.
- Chapter 5 describes an updated treatment for the nuclear removal energy, moving beyond the standard impulse approximation approach.
- Chapter 6 moves on to Super-Kamiokande detector monitoring, using the newly installed light injection system. It also touches on the first analyses completed with this system.
- Chapter 7 contains concluding remarks on the thesis as a whole.

Chapter 2

Neutrino Interactions

how
Bash: Command not found.

Jim Gresta

Measurements of neutrino parameters are currently one of the key priorities in particle physics. Undescribed by the standard model of particle physics, the non-zero neutrino mass has required the careful design of new, high statistics oscillation experiments. Neutrino detectors can only measure the rate of interactions, given by

$$R(\vec{x}) = \Phi(E_\nu) \times \sigma(E_\nu, \vec{x}) \times \epsilon(\vec{x}) \times P(\nu_\alpha \to \nu_\beta) \tag{2.1}$$

where $\Phi(E_\nu)$ is the neutrino flux as a function of neutrino energy E_ν, $\epsilon(\vec{x})$ is the detector efficiency as a function of the (reconstructed) kinematics $\vec{x}$, $\sigma(E_\nu, \vec{x})$ is the interaction cross-section for ν_β and $P(\nu_\alpha \to \nu_\beta)$ is the oscillation probability. It is clear that to fully exploit oscillation programs and extract oscillation parameters, the unoscillated flux, cross-section and detector efficiency must be well understood. These crucially depend on a precise knowledge of the neutrino energy, which must be reconstructed from the kinematics of the detected final state particles. This can only be achieved through knowledge and modelling of neutrino-nucleus interactions, thus a careful knowledge of these is required. These models enter the picture through Monte Carlo simulations, or "event generators", which give the detail required given neither the initial state neutrino energy or interaction kinematics are known, or can be measured. It is then obvious that any problems that feature within an interaction model can be propagated through the measurement, leading to an inaccurate final analysis of oscillation parameters. As such, experiments often apply large systematic errors to these results in order to minimize their effect on analyses. Most experiments are now sensitive enough, and with a long enough running time, that we are now becoming dominated by systematic errors in the models, rather than our statistics. This has led to a drive in the development of better nuclear theories and their implementation into event generators.

At a glance, neutrino interactions are entirely covered by electroweak theory; this simple

theory is hampered by nuclear effects such as final state interactions, and the uncertain conditions of the initial state. Previous experiments, such as neutrino-deuterium scattering, could skirt these issues by using a simple target nucleus and remaining in a relatively low energy regime. The current state of the field exists in the 'intermediate energy' (0.1 - 20 GeV) where there is yet to exist an overarching theory which describes all data. Therefore we split our model per interaction type, mainly: quasi-elastic (QE), resonant excitation (RES) and deep inelastic scattering (DIS), the Feynman diagrams for these (and 2-particle-2-hole, 2p2h) is shown in Fig. 2.1. The turn on of each of these interactions is dictated by the energy transfer, though obviously the distinctions are blurry. One quickly finds that a theoretical description for one energy, will break down completely for higher energies.

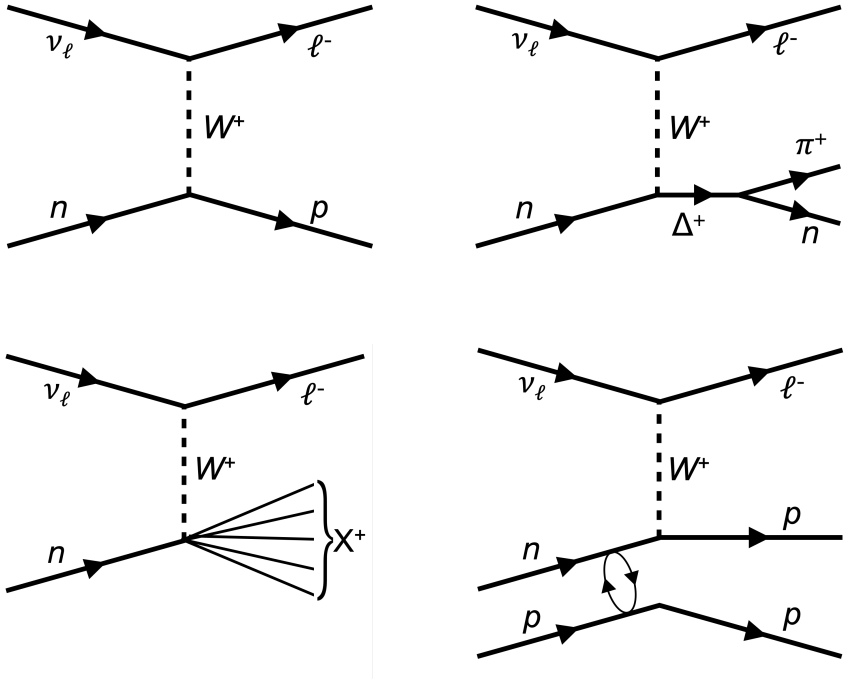

Fig. 2.1: Feynman diagrams for the main charged-current neutrino-nucleon interaction channels. The diagrams show (from left to right) charged-current quasi-elastic (CCQE), RES, DIS and 2p2h. For DIS, X represents a hadron shower coming from the interaction. Similar diagrams can be drawn for neutral current interactions, mediated by the Z boson.

A full description of a neutrino-nucleus interactions involves a variety of different things: a nuclear ground state model, describing the distribution of nucleons within the nucleus; a cross-section model, predicting a specific interaction channel between a nucleon and a neutrino; and a final state model which modifies the products of the initial interaction, known as final state interactions (FSI). This chapter will describe the theoretical ingredients necessary in order to build a cross-section model, followed by a description of the available nuclear ground state models. This thesis focuses on the modification and development of T2K's neutrino event generator, NEUT[1] [140]; thus more consideration is given to models available in this generator and other models to which it has been compared.

[1]Named after NEUTrino.

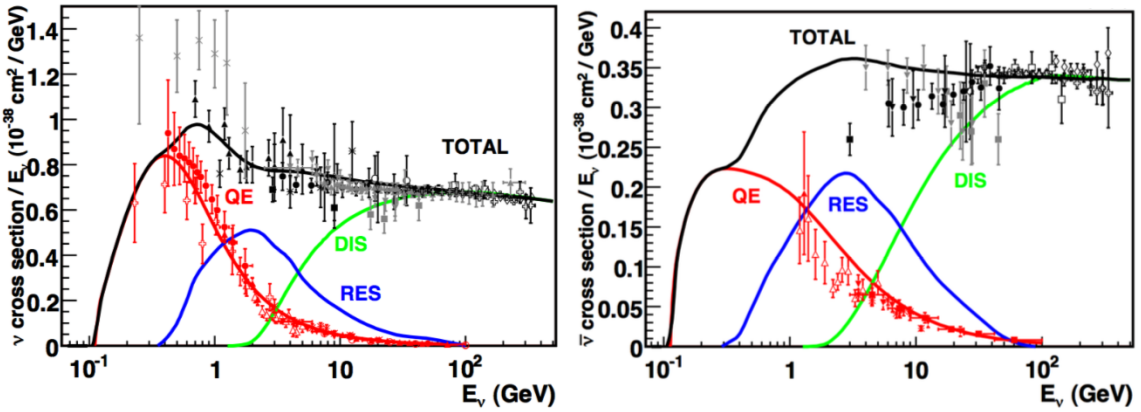

Fig. 2.2: NUANCE cross-section predictions compared to experimental data. (Anti)Neutrino data is shown on the (right)left. The available energy dictates the turn on of different interactions, showing how deeply the probe can penetrate the nucleus. Figure taken from [139].

2.1 Interaction Models

In the following sections a theoretical description of various neutrino interactions will be described. This will start at the relatively low energy transfer (q_0) regime, working up toward higher energy transfers. The notation used in the subsequent calculations is

$$\nu_\ell(k) + A(p) \rightarrow \ell(k') + A'(p') \tag{2.2}$$

where $k = (k_0, \vec{k})$ is the incident neutrino four-vector, $p = (p_0, \vec{p})$ is the initial nucleon four-vector, $k' = (k'_0, \vec{k'})$ is the outgoing lepton four-vector and $p' = (p'_0, \vec{p'})$. The four-momentum transfer is calculated as $q = (q_0, \vec{q_3}) = k - k'$ and the square is $Q^2 = -q^2$. Another commonly used (and measured) variable is the *leptonic* energy transfer $\omega = k_0 - k'_0 = {q_0}^2$.

2.1.1 Charged-Current Quasi-Elastic

Charged-current quasi-elastic scattering (CCQE) is the simplest interaction channel and, with a peak beam energy of 0.6 GeV, the dominant channel for the T2K experiment (see Fig. 2.2). This proceeds via the exchange of a $W^\pm$ (hence *charged*-current), where the target neutron is converted to its isospin partner[3], *i.e.*

$$\nu_\ell + n \rightarrow \ell^- + p \ , \tag{2.3}$$

$$\bar{\nu}_\ell + p \rightarrow \ell^+ + n \ , \tag{2.4}$$

shown in Fig. 2.1. The Llewellyn-Smith (LS) model has been used extensively since the 1970s (a full review can be found in [141]), with the free nucleon differential cross-section

[2] In the electron scattering community this is usually denoted as ν.
[3] Hence the *quasi*-elastic name - the outgoing states are not the same as the initial states.

expressed as

$$\frac{d\sigma^{\nu,\bar{\nu}}}{dQ^2} = \frac{M^2 G^2 \cos^2\theta_C}{8\pi E_\nu^2}\left[A(Q^2) \pm B(Q^2)\frac{(s-u)}{M^2} + C(Q^2)\frac{(s-u)^2}{M^4}\right] \tag{2.5}$$

where G_F is the Fermi coupling constant, M and m are the nucleon and lepton masses respectively, E_ν is the incident neutrino energy, θ_C is the Cabbibo mixing angle, s and u are Mandelstam variables with $s - u = 4ME_\nu - Q^2 - m^2$ and the sign change corresponds to neutrino or antineutrino cross-sections respectively.

The functions $A(Q^2)$, $B(Q^2)$ and $C(Q^2)$ are defined as

$$\begin{aligned} A(Q^2) = \frac{(m^2+Q^2)}{M^2}\Bigg[&(1+\tau)\,F_A^2 - (1-\tau)\,(F_V^1)^2 \\ &+ \tau\,(1-\tau)\,(\xi F_V^2)^2 + 4\tau F_V^1 \xi F_V^2 \\ &- \frac{m^2}{4M^2}\left((F_V^1 + \xi F_V^2)^2 + (F_A + 2F_P)^2 - 4\,(1+\tau)\,F_P^2\right)\Bigg] \end{aligned} \tag{2.6}$$

$$B(Q^2) = \frac{Q^2}{M^2} F_A (F_V^1 + \xi F_V^2) \tag{2.7}$$

$$C(Q^2) = \frac{1}{4}\left[F_A^2 + (F_V^1)^2 + \tau\left(\xi F_V^2\right)^2\right] \tag{2.8}$$

where $\tau = Q^2/4M^2$, $\xi = \mu_p - \mu_n$ and μ_p and μ_n are the proton and neutron anomalous magnetic moments. F_V^1, F_V^2, F_A and F_P are form factors representing the spatial distribution of the nucleon charge, which depend upon the Q^2 transferred to the target by the incoming particle.

F_V^1 and F_V^2, known as the Dirac and Pauli electromagnetic isovector form factors respectively, can be measured in electron scattering experiments if the Conserved Vector Current hypothesis (CVC, [142]) is employed; the BBBA05 model [143] is widely used for these parameters. $F_V^{1,2}$ can be expressed in terms of their Sachs form factors,

$$F_V^1(Q^2) = \frac{G_E^V(Q^2) + \tau G_M^V(Q^2)}{1+\tau}, \tag{2.9}$$

$$\xi F_V^2(Q^2) = \frac{G_M^V(Q^2) - G_E^V(Q^2)}{1+\tau}, \tag{2.10}$$

where, again by the CVC, the vector currents can be written as

$$G_E^V(Q^2) = G_E^p(Q^2) - G_E^n(Q^2), \tag{2.11}$$

$$G_M^V(Q^2) = G_M^p(Q^2) - G_M^n(Q^2), \tag{2.12}$$

where $G_{E,M}^{p,n}$ are the electric and magnetic form factors of the proton and neutron. The functional form of these in the BBBA05 model is achieved by fitting the equation

$$G_{E,M}^{p,n} = \frac{\sum_{k=0}^{2} a_k \tau^k}{1 + \sum_{k=1}^{4} b_k \tau^k} \tag{2.13}$$

to available electron scattering data [143, 144]. A fit to higher order polynomial form factors was also produced, BBBA07 [145], though is less commonly used.

This BBBA05 formalism superseded the previous dipole approximation, which assumed the proton had an exponential spatial charge distribution $\rho = \rho_0 e^{-r/r_0}$, where r_0 is the nucleon radius scale. The form factors are related to the Fourier transform of this distribution, leading to the dipole form

$$G^{p,n}_{E,M}(Q^2) = C^{p,n}_{E,M} G_D(Q^2) = \frac{C^{p,n}_{E,M}}{1 + \frac{Q^2}{M_V^2}} \tag{2.14}$$

where $G_D(Q^2)$ is a dipole function, $C^{p,n}_{E,M}$ is a constant depending on the form factor, and $M_V \simeq 0.71$ MeV [146, 147] is an empirical value extracted from data. This approximation works well at low-Q^2, though a number of groups discovered discrepancies at Q^2 grows [143, 148], leading to the current formalism.

Moving onto the axial components of the form factor, it is common to again assume a dipole form for the axial form factor, albeit with a different coupling and mass term

$$F_A(Q^2) = \frac{F_A(0)}{\left(1 + \frac{Q^2}{M_A^2}\right)^2}, \tag{2.15}$$

where $F_A(0) = 1.269 \pm 0.003$ [149] and M_A is the axial mass. The coupling, or axial charge, $F_A(0) = g_A$ is determined from neutron β decay [150]. The axial mass is essentially a free parameter and is determined either from fits to the Q^2 shape of (anti)neutrino-deuterium scattering, or from similar fits to pion electroproduction data [151]. There was an original disagreement between the weak and electromagnetic probes, however this was solved with the inclusion of hadronic effects, leading to a world average of $M_A = 1.026 \pm 0.021$ GeV [152]. The MiniBooNE experiment found an axial mass inconsistent with the average by 20-30%, with $M_A = 1.35 \pm 0.17$. It was assumed this was an "effective" axial mass, encompassing all of the missing nuclear effects; theoretical predictions however, expect the axial mass in heavier nuclei to be smaller than for deuterium [153]. However, at high probe energies, the observed value of M_A are consistent with expectations [141, 154]. This disagreement between high and low energy neutrinos (i.e. high and low values of Q^2) was known as the axial mass anomaly, and led to the development of new forms for the axial form factor, such as the z-expansion parameterisation [155]. This anomaly will be further explored in section 2.3.1.

In neutrino scattering experiments, it is theoretically possible to measure the pseudoscalar form factor, the final piece of the puzzle, however as it only enters equation 2.6 scaled by m^2/M^2, it is difficult to measure. Using the Partially Conserved Axial Current (PCAC) hypothesis [142], the pseudoscalar form factor can be expressed as a function of the axial component by means of the Goldberger-Treiman relation [156]:

$$F_P(Q^2) = \frac{2M^2}{Q^2 + m_\pi^2} F_A(Q^2), \tag{2.16}$$

where m_π is the mass of the pion.

2.1.2 Neutral Current Elastic

The previous section described the charged current interaction, neutral current elastic scattering (NCEL) can be modelled in a similar fashion, where equations 2.5-2.8 are still valid. In NCEL, the interaction is mediated by the Z^0 instead of the W. The NCEL reactions

$$\nu + n \to \nu + n\,, \qquad \bar{\nu} + n \to \bar{\nu} + n\,,$$
$$\nu + p \to \nu + p\,, \qquad \bar{\nu} + p \to \bar{\nu} + p\,,$$

do not have an energy threshold for free nucleons, different from CCQE as the final states have a higher invariant mass. If the nucleons are bound, *i.e.* in a nucleus, there is always an energy threshold arising from the Pauli blocking.

In the case of NCEL, the form factors have to be altered to include additional coupling constants and strange quark contributions. Some of these can come in via the Sachs form factors,

$$G_E^V = \frac{1}{2}(G_E^{p,n} - G_E^{n,p}) - 2\sin^2\theta_W G_E^{p,n}, \tag{2.17}$$
$$G_M^V = \frac{1}{2}(G_M^{n,p} - G_M^{p,n}) - 2\sin^2\theta_W G_M^{n,p}, \tag{2.18}$$

where θ_W is the weak mixing angle, and can be included in equations 2.9 and 2.10.

The additional strange couplings alter the form factors in a less trivial way, but can still be included with,

$$F_{V,NC}^1(Q^2) = F_V^1(Q^2) - \frac{F_1^s(Q^2)}{2}\,, \tag{2.19}$$
$$F_{V,NC}^2(Q^2) = F_V^2(Q^2) - \frac{F_2^s(Q^2)}{2}\,, \tag{2.20}$$
$$F_{A,NC} = \frac{g_A\epsilon}{2(1+\tau)^2} - \frac{F_A^s(Q^2)}{2}\,, \tag{2.21}$$

where F_α^s are the strange form factors, and $\epsilon = +1(-1)$ for an interaction on a proton(neutron) [157]. These are often assumed to be a dipole, and the strange axial form factor including the contribution from the strange quark to the nucleon spin Δs [139],

$$F_A^s(Q^2) = \frac{\Delta s}{(1+\frac{Q^2}{M_A^2})^2}\,. \tag{2.22}$$

It is worth noting here the form factors presented in equations 2.19-2.21 are derived assuming dipole forms of the electric and magnetic form factors, which depend upon $\mu_{p,n}$. These strange form factors are absorbed into the fit when taking an empirically driven approach to the form factors.

Both CCQE and NCEL are the dominant interactions for energies up to a few GeV and

thus are of vital importance to this thesis.

2.1.3 Resonant Pion Production

As the energy of the incoming neutrino increases, the available Q^2 phase space increases and it becomes possible for the struck nucleon to be excited into a resonant state. As the invariant mass of the incoming lepton and the struck nucleon is close to the mass peak of one of the baryon resonances, there is an increased probability of exciting the nucleon into one of these resonances. This resonance decays back to the ground state, producing a slew of other particles such as pions, other mesons and photons. The lowest lying state is the $\Delta(1232)$[4] resonance, which produces final states of a nucleon and a pion. The possible single pion production resonances on a free nucleon for a neutrino are:

$$\begin{aligned}
&\overset{(-)}{\nu}_\mu + p(n) \rightarrow \mu^{-(+)} + p(n) + \pi^{+(-)}\,, && \overset{(-)}{\nu}_\mu + p \rightarrow \overset{(-)}{\nu}_\mu + p + \pi^0\,,\\
&\overset{(-)}{\nu}_\mu + n(p) \rightarrow \mu^{-(+)} + p(n) + \pi^0\,, && \overset{(-)}{\nu}_\mu + p \rightarrow \overset{(-)}{\nu}_\mu + n + \pi^+\,,\\
&\overset{(-)}{\nu}_\mu + n(p) \rightarrow \mu^{-(+)} + n(p) + \pi^{+(-)}\,, && \overset{(-)}{\nu}_\mu + n \rightarrow \overset{(-)}{\nu}_\mu + n + \pi^0\,,\\
& && \overset{(-)}{\nu}_\mu + n \rightarrow \overset{(-)}{\nu}_\mu + p + \pi^-\,.
\end{aligned}$$

The Rein-Sehgal model [158] is most often used by simulators, which describes the production of single pions up to $W = 2$ GeV in the resonance region. This considers the 18 resonances up to this energy limit, and includes multi-pion events and interference terms. As this model assumes leptons are massless, NEUT also includes the Berger-Sehgal model [159], which does not make this assumption.

The structure set up in the Rein-Sehgal model is also used to simulate the production of single kaon, eta and photons [160]. The main difference between these and the previous productions is the branching fraction. The secondary hadrons are subject to final state interactions, which will be discussed in section 2.3.3.

Tuning and validation of pion production models is often a difficult process, as the final states can be contaminated with a contribution from DIS pion channels [161]. These non-resonant pion production channels must be considered, as a fraction of DIS sample appears below $W < 2$ GeV, the phase space of the Rein-Sehgal model. DIS events will be discussed in the following section (section 2.1.5).

An recent updated method is the MK model [162–164] that, similar to the Berger-Sehgal model, includes lepton mass effects and also includes non-resonant single pion production backgrounds and the associated interference. Fits to bubble chamber data show the MK model provides a better description than does the often default Rein-Sehgal model. The MK model is still under development, with the most recent update coming earlier this year [164].

[4]The impinging neutrino causes one of the quarks to flip its spin and become an isospin quartet. The extra energy of all quark spins being aligned causes the large increase in mass.

2.1.4 Coherent Pion Production

Rather than interacting with an individual nucleon, it is possible for the probe to scatter coherently off the nucleus as a whole. These are typically low energy (Q^2) events, with negligible nuclear response and forward scattered pions. This process can be mediated by both W and Z bosons and leaves the nucleus (A) in its ground state,

$$\nu_\mu + A \to \mu^- + A + \pi^+ , \qquad \nu_\mu + A \to \nu_\mu + A + \pi^0 ,$$
$$\bar{\nu}_\mu + A \to \mu^+ + A + \pi^- , \qquad \bar{\nu}_\mu + A \to \bar{\nu}_\mu + A + \pi^0 .$$

In NEUT the base model is again the Berger-Sehgal model [165], an improvement over the Rein-Sehgal model [166], which works well at high neutrino energies. The correct modelling of coherent pion production is important for oscillation analyses, as it produces almost collinear pions which are a dominant background at low energies (a few hundred MeV). This background will be discussed slightly more in section 3.1.2.2.

2.1.5 Deep Inelastic Scattering

As the probe energy increases still further, it can begin to resolve the nucleon constituents. The neutrino can scatter off an individual quark and liberate it from a nucleon in a process known as deep inelastic scattering. Due to colour confinement, the individual quark cannot be detected, and the final state is a hadronic shower[5]:

$$\nu_\ell + N \to \ell^- + X^+ , \qquad \nu_\ell + N \to \nu_\ell + X ,$$
$$\bar{\nu}_\ell + N \to \ell^+ + X^- , \qquad \bar{\nu}_\ell + N \to \bar{\nu}_\ell + X .$$

As shown, these processes can take place via CC or NC interactions. DIS events have been reasonably well studied at high energies, with most measurements placing a kinematic cut to isolate this process from the lower energy QE or RES events. However, in the transition region between resonant pion production and DIS, it is difficult to separate the two processes.

The differential cross-section is written in terms of three Lorentz invariant variables[6] and, similarly to CCQE and NCEL, three structure functions representing the structure of the nucleus[7]. These in turn are described by Parton Distribution Functions (PDFs), giving the probability of finding a quark with a given momentum. In NEUT, these follow the formalism described by the Bodek-Yang model [168].

[5] It's interesting to note that above the Hagedorn temperature [167], also called the "boiling point" of matter, the energy in the system is so high it becomes energetically favourable to spontaneously produce new quark-antiquark pairs. This system is also called quark matter, and can be viewed as unbound quarks and gluons.

[6] The four-momentum transfer (Q^2), the inelasticity (y) and the Bjorken scaling variable (x).

[7] 2 are relevant for electron scattering, whilst the third is the vector-axial interference term.

2.1.6 Meson Exchange Currents

All of the interactions described above occur on a single nucleon, however there are mechanisms for multi-nucleon knockout. The highest contributor to these are meson exchange current (MEC) events, also called (2p2h) events. They occur when two nucleons within a nucleus exchange a weak meson (usually a pion) from the leptonic current, leading to 2 hadrons produced at the primary vertex. The importance of correct MEC modelling comes from electron scattering, where models failed to correctly predict the inclusive cross-section in the "dip region", the gap between the tail of QE events and the turn on of resonant interactions [169]. This was shown to be essential in the description of neutrino cross-section measurements, which were only able to match experimental data with their inclusion [170]. These events are not to be confused with short-range correlations, which also have a 2 hadron final state, and are discussed in section 2.2.3.

2.2 Nuclear Models

The preceding sections have assumed (except for section 2.1.4 and 2.1.5) the interaction has taken place on a single nucleon. Generators generally employ the impulse approximation (IA, [171]) which states that a) at high momentum transfers, the probe can resolve an individual nucleon which is quasi-free (*i.e.* not interacting with the nuclear potential) and b) the outgoing nucleon wavefunction exits without any distortion (the effects of Pauli blocking and final state interactions (FSI) are neglected), and the (A-1) nucleus is a spectator. Whilst this considerably simplifies the calculation, this breaks down at low energy transfers where the probe cannot resolve individual nucleons (resolution power goes as $1/|q|$).

Nucleons in a nucleus are not at rest. The Pauli exclusion principle states no two fermions can be in identical momentum (energy) and spin states, thus nucleons must be in motion in order for the nucleus to contain more than two nucleons. A model must then describe the probability of finding a nucleon with some momentum (often called the Fermi momentum) and the energy required to liberate it from a nucleus, also called the removal energy. Although any model describing the momentum distribution is in general called a "spectral function", this is usually reserved for more sophisticated models. Fig. 2.3 shows a selection momentum distributions from different nuclear models and these will be described further in the proceeding sections.

2.2.1 Relativistic Fermi Gas

The simplest spectral function and one of the first to be widely used in generators is the Relativistic Fermi Gas (RFG) model, developed by Smith and Moniz [173]. The nucleons are treated as plane waves in a nuclear potential, where they are independent of each other (*i.e.* non-interacting). Each nucleon fills successive momentum states up to a Fermi surface

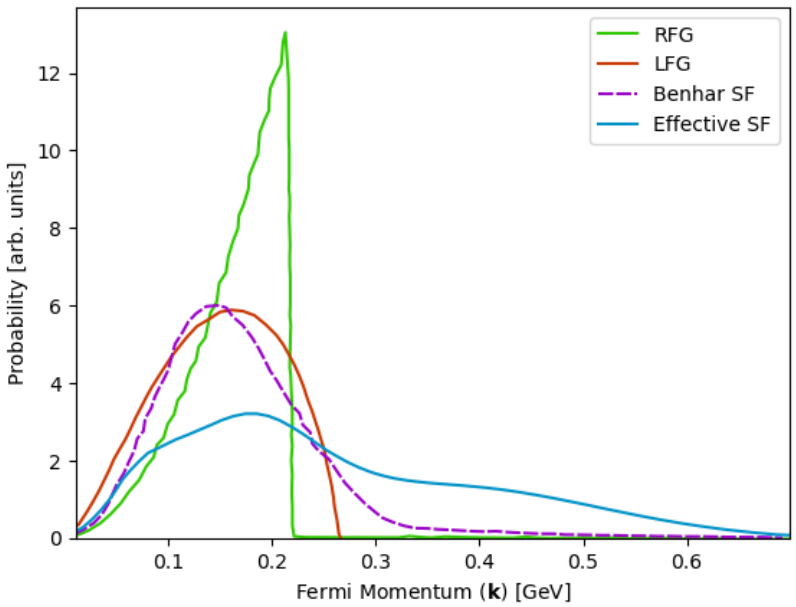

Fig. 2.3: One-dimensional nucleon momentum distributions in a ^{12}C nucleus. The green and red curves are the relativistic and local Fermi gas respectively, dashed magenta is the Benhar-Fantoni spectral function and blue is the effective spectral function. The Benhar implementation is T2K's ground state model. Figure reproduced from [172].

p_F^{RFG}, and everything above is no longer bound. The distribution is given by

$$P_{RFG}(|\vec{p}|, E_B) = \frac{6\pi A}{(p_F^{RFG})^2}\Theta(p_F^{RFG} - |\vec{p}|), \tag{2.23}$$

where A is the nucleus atomic number, and Θ is the Heaviside step function. For particles to be liberated from the nucleus they must exceed the Fermi surface or, due to all momentum states being filled, be Pauli blocked. In this model, the removal (or binding) energy is constant, and the effects of Pauli blocking are usually over-exaggerated. The removal energy, E_B, and Fermi momentum, p_F, are obtained through fits to electron scattering data [174], where E_B is determined through the quasi-elastic peak position, and p_F determines its width[8].

2.2.2 Local Fermi Gas

The Local Fermi Gas (LFG) is an extension to the RFG model, where the local nucleon density $\rho(r)$ incites a change in the Fermi momentum. This makes the Fermi momentum radially dependent,

$$p_F^{LFG}(r) = \left[3\pi^2\rho(r)\right]^{1/3}; \tag{2.24}$$

the probability of finding a nucleon with a specific momentum is still extracted from equation 2.23, albeit with the modification of the Fermi surface [175]. It also leads to a more realistic approach to Pauli blocking, which is calculated using the local nucleon density.

[8] This is not absolutely perfect of course, but is true to a first approximation.

2.2.3 Benhar-Fantoni Spectral Function

The Benhar-Fantoni spectral function [176] is a 2 dimensional spectral function (SF) describing the probability of finding any particular nucleon with a specified momentum and removal energy. It is composed of two parts: a mean field term which can be built from exclusive electron scattering data, or directly from mean field calculations; a theoretical component accounting for initial state correlations between nucleons. This latter term accounts for $\sim 20\%$ of the total probability distribution, and includes a high momentum tail to the SF missing from Fermi gas based models. These short-range correlated pairs (SRCs) are brief fluctuations of high momentum nucleons. Their wave-functions overlap and, while their individual momenta exceed the Fermi surface, their combined momentum lies below it, and thus are still bound within the nucleus [177]. This is only possible if their momenta are mostly equal and opposite. It should be noted that while the SF includes these two particle interactions, the IA is still at play, and the interaction only occurs on a single nucleon; in NEUT, the correlated nucleon is still ejected, and assumed to have a momentum equal and opposite to that of the struck nucleon[9].

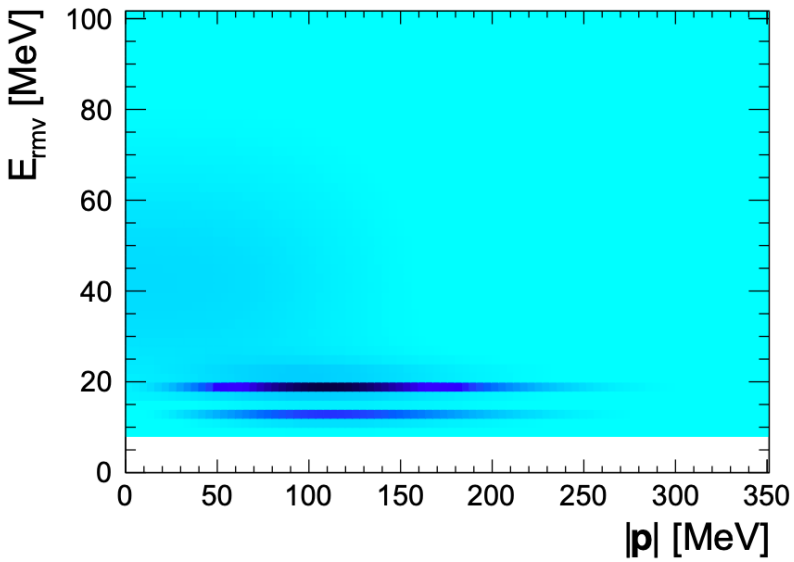

Fig. 2.4: The Benhar-Fantoni 2-dimensional spectral function for oxygen as implemented in NEUT. The darkness of colour represents a higher probability of finding a nucleon with that particular Fermi momentum and removal energy. Figure taken from [178].

The viability of the SF is greatly supported by fits to electron scattering data [179] and exclusive neutrino cross-section measurements [180, 181] over the RFG - a comparison of the 1-dimensional momentum projection is shown in Fig. 2.5. Due to the high energy tail shown, the model has a greater ability to predict the dip region mentioned in section 2.1.6. However, this model is only designed to generate quasi-elastic interactions, as such any other interaction must use a different formalism. It is also limited in that it can only be used on nuclei where electron-scattering data are available, thus restricting the choice of target in generators.

[9] These do not account for MEC events, discussed in section 2.1.6.

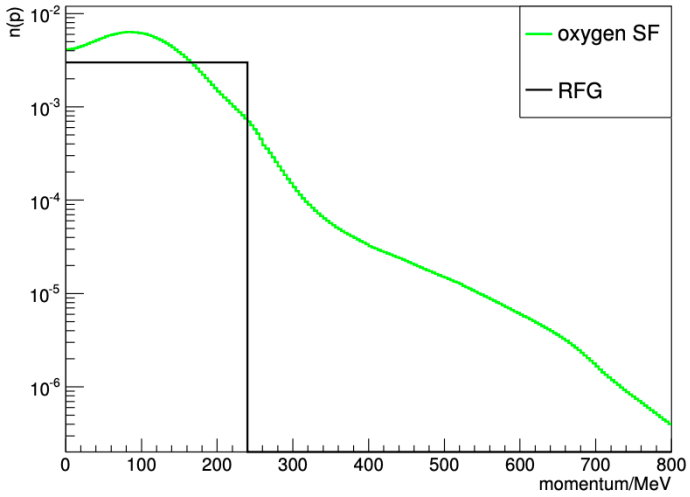

Fig. 2.5: Comparison between the Spectral Function and Relativistic Fermi Gas momentum distribution for oxygen. The green line shows the spectral function and the black shows RFG with a Fermi momentum of 220 MeV. The log scale shows the tail of the correlation term extending to high momenta. Figure taken from [182].

The SF does not have a natural definition for Pauli blocking, and a thorough approach would be similar to that of the LFG, as the SF is in part based on calculations of nuclear density. However, NEUT implements an RFG-like approach, where an average nuclear density is used to give a hard cutoff at the Fermi surface[10]. It should also be noted that the data used to build the SF are from electron-proton final states, thus the model is only suitable for protons; it is approximated to be the same for neutrons, but there will be some small differences between the two.

As this is the model that most of the analysis has built off, and is the current nuclear ground state model for T2K, any further mention, unless otherwise specified, of the spectral function will refer to this model.

2.2.4 Super-Scaling Approach

Scaling phenomena have been discovered in the scattering of a single impinging particle off a many-body system. The description of the response of the complex system can often be written in terms of two variables, however in some circumstances these can be constructed into a single variable, upon which the response depends. This is known as the scaling variable[11].

In the simplest case, the RFG model has been found to follow scaling phenomena, and is part of the motivation behind a more phenomenological model [184, 185]. In the RFG, one must simply divide the quasi-elastic (e,e′) cross-section by an averaged single-nucleon cross-section derived from Fermi gas assumptions[12]. The RFG scaling variable takes the

[10]It should be noted in the 2021 oscillation analysis, a new dial was added which gave some freedom to the Fermi surface.

[11]In fact, the Bjorken scaling variable mentioned in section 2.1.5 is an example of this [183].

[12]This assumes that the inclusive (e,e′) cross-section is constructed mainly of exclusive (e,e′N) scattering,

form

$$\psi \equiv \frac{1}{\sqrt{\epsilon_F}} \frac{\lambda - \tau}{\sqrt{(1+\lambda)\tau + \kappa\sqrt{\tau(1+\tau)}}}, \tag{2.25}$$

where $\lambda = \omega/2m_N$, $\kappa = q/2m_N$, $\epsilon_F = \sqrt{1+(k_F/m_N)^2} - 1$ and $\tau = Q^2/4m_N^2 = \kappa^2 - \lambda^2$. These are dimensionless variables of the momentum transfer, energy transfer, four-momentum transfer and Fermi kinetic energy. The basis for the superscaling approach (SuSA) is to replace the scaling function of the RFG model,

$$f_{RFG}(\psi) = \frac{3}{4}(1-\psi^2)\theta(1-\psi^2), \tag{2.26}$$

with one derived from more robust methods, $f_{SuSA}(\psi)$. Here, superscaling is defined when both scaling of the first (no dependence on energy transfer) and second (no dependence on nuclear species) kind are satisfied. Originally, SuSA used a function derived from experimental inclusive longitudinal (e,e′) scattering data, which automatically encompassed nucleon correlations and final state interactions. Whilst this was sufficiently successful, it was relatively simple, treating the transverse and longitudinal nuclear response as identical. Here, longitudinal and transverse data refer to the polarisation of the virtual photon, the former being Coulomb scattering (electric charge), whilst the latter is magnetisation [186]. SuSA also encountered problems at higher energy transfers, where contributions from multi-nucleon final states and inelastic scatterings cause violations of first kind scaling [187, 188].

An updated version of SuSA, SuSAv2, used the fact that the scaling function derived from electron scattering data can be reproduced from microscopic models such as the relativistic mean field (RMF) model [189, 190]. The asymmetric scaling function found in electron scattering data is automatically built into the model via final state interactions and the treatment of the initial and final state nucleons as solutions to the same Dirac equation in the same potential. RMF models model nucleons as solutions to the Dirac equation using both scalar (attractive) and vector (repulsive) potentials. This works well at low energies, however at high momentum transfers it breaks down as FSI is expected to be weaker. This is due to the energy-independent choice of potentials, causing the QE peak to shift to too high energies and cause disagreements to data. In order to remedy this, SuSAv2 blends between RMF calculations and relativistic plane-wave impulse approximation scaling (RPWIA) functions at high energies, which describes the outgoing nucleon as a pure relativistic plane wave with no distortion. Another key improvement is that RMF predicts different scaling functions for the longitudinal and transverse responses. The transverse response is seen to be enhanced over the longitudinal, *i.e.* $f_T(\psi) > f_L(\psi)$.

The RMF model also predicts the peak of the QE response evolves as a function of $|q|$. Thus the SuSAv2 model builds this dependence into its scaling function by including an energy shift, E_{shift}, in order to force the maximum of the scaling functions to sit at $\psi = 0$. One finds both the transverse and longitudinal response E_{shift} is linearly dependent on q_3, a feature of the model that will be discussed further in section 5.1.

thus explicitly requiring the impulse approximation.

SuSAv2 has also been extended to include the inelastic regime and contributions from MEC. The 2p2h contributions are however, taken from a Fermi gas model rather than calculations based on an RMF spectral function.

2.2.5 Effective Spectral Function

As described above, it has long been observed that longitudinal electron data can be described by a "superscaling" function [191]. The Effective Spectral Function (ESF, [192]) can attribute its conceptual basis to the Benhar-Fantoni SF (section 2.2.5). While the BFSF is a sophisticated description of the initial state nucleon momenta and removal energy, it fails to reproduce the outgoing lepton kinematics; the ESF modifies this initial state nucleon distribution in order reproduce the superscaling data. Specifically, the model is tuned to reproduce the ψ' superscaling model, which includes E_{shift} mentioned previously: this is simply as $\lambda' = \lambda - E_{shift}/2M_n$. In order to reproduce the transverse response, the ESF employs the Transverse Enhancement Model (TEM, discussed more in section 2.3.1) which is tuned to transverse electron scattering data. The ESF reproduces electron scattering (both longitudinal and transverse) data extremely well by construction, and essentially wraps up all final state effects in the initial state nucleon distribution. However due to being a spectral function model, it is simple to include in event generators whilst reproducing the more sophisticated superscaling models.

2.3 Nuclear Effects

As the resolution power of the impinging particle reduces, it becomes possible the probe can experience more than one nucleon at the interaction vertex. It has been suggested that the axial mass anomaly introduced in section 2.2 is a consequence of these nucleon correlations, whose effects had been absorbed by unnaturally inflating the axial mass, contrary to the theoretical expectations. A number of models have succeeded in explaining this apparent axial mass discrepancy seen in both the MiniBooNE and MINERνA by increasing the CC0π cross-section whilst keeping the axial mass constant [193, 194]. These switched from measuring a specific interaction (such as CCQE), to measuring a final state topology (*i.e.* CC0π) as it became clear the final state included properties of other interactions types due to FSI (discussed in section 2.3.3).

2.3.1 Transverse Enhancement Model

The Transverse Enhancement Model (TEM, [195]) was motivated by the suggestion that bound nucleon correlations could cause the axial mass anomaly, and measurements in the electron scattering community showing the transverse response does not superscale, and is enhanced with respect to predictions as a function of Q^2.

The TEM modifies the transverse response in a process driven purely by empirical fits

to the data. This takes the form

$$\mathcal{R}_T = 1 + AQ^2 e^{-Q^2/B}\,, \tag{2.27}$$

where A and B are free parameters. These are tuned to electron scattering data, with the best fit to carbon giving values of $A = 6.0 \pm 0.7$ GeV^{-2} and $B = 0.34 \pm 0.01$ GeV^2, this fit is shown in Fig. 2.6.

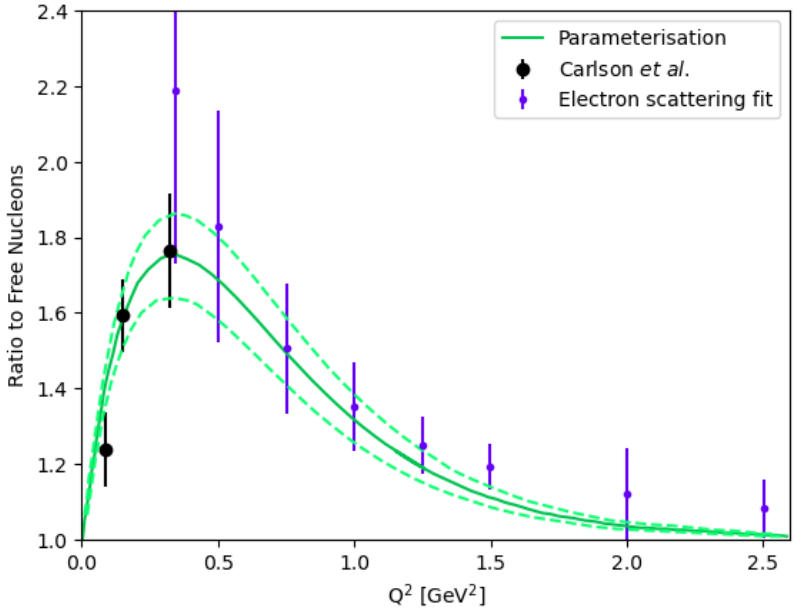

Fig. 2.6: The ratio of transverse to longitudinal response from electron data on ^{12}C as a function of Q^2. The black points are from Carlson *et al.* [196] and the purple error bars are from the JUPITER Collaboration [192]. The green solid line is the TEM parameterisation, while the green dashed lines are the error bands. Figure reproduced from [195].

This enhancement enters the cross-section via a modification to the nucleon magnetic form factors introduced in equation 2.12 (as the transverse component is the magnetic response), given by

$$G_M^{p(n)}(Q^2) = G_M^{p(n)}(Q^2) \times \sqrt{1 + AQ^2 e^{-Q^2/B}}\,. \tag{2.28}$$

It should be noted this enhancement is attributed to MEC, and not a measurement of the enhancement of the magnetic form factors. Using this approach, MINERνA discovered their best fit to the CCQE-like cross-section was in fact using $M_A = 0.99$ *including* the TEM, rather than the M_A found previously [194]. In order to categorise events, TEM uses the number of pions in the final state. Events are assumed to a CCQE transverse enhancement if there are no pions, but otherwise the event will be categorised as an inelastic contribution.

2.3.2 Random Phase Approximation

In contrast, the random phase approximation (RPA) is another way of introducing nucleon-nucleon correlations in a more theoretical way. This considers 1p1h excitations of correlated nucleons and introduces an effective nucleon-nucleon field (denoted V in Fig. 2.7) which

can change the bare propagator to include particle loops. This is a modification in the propagators self-energy and changes the electroweak coupling in the nuclear medium due to strongly interacting nucleons [175, 197]. RPA is illustrated in Fig. 2.7, and the summation enters the 1p1h response in Fig. 2.8a and modifies the CCQE cross-section. Whilst the total cross-section is not greatly affected by the RPA, the differential cross-section is significantly suppressed at low Q^2 where the resolving power of the probe is low [198].

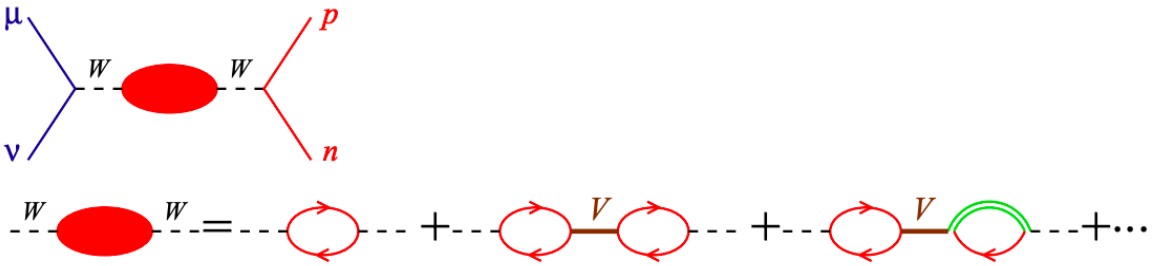

Fig. 2.7: Random Phase Approximation correction to the CCQE scattering. Arrows pointing to the right (left) denote particles (holes), the double line represents the Δ. The V is an effective interaction between nucleons to account for long range correlations. Figure taken from [175].

Both the Nieves [199] and Martini [200] models are microscopic calculations of np-nh interactions assuming an LFG nuclear ground state. They consider a large number of propagator self-energy diagrams which can contribute to a CCQE-like final state and building in higher order corrections from multiple nucleon corrections. Fig. 2.8 shows the possible processes considered in these models, employing Cutkosky rules [201] which take all intersected particles and place them on-shell in the calculation and allowing many possible vertex diagrams to be included in the nuclear response. Possible vertices contributing to the 1p1h1π (Figs. 2.8c and 2.8d) final state are shown in Fig. 2.9, with the final cross-section involving a summation over all possible diagrams.

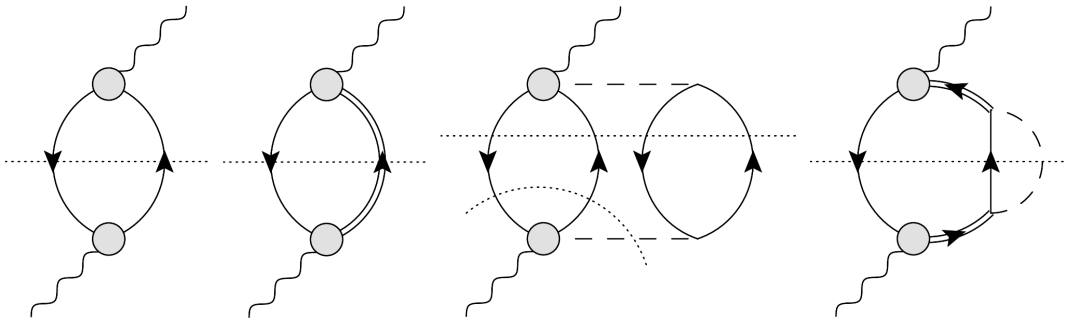

(a) 1p1h **(b)** Δ Resonance **(c)** 2p2h **(d)** 1p1h1π

Fig. 2.8: W-boson self-energy diagrams used in the Nieves and Martini models for different interactions. Solid lines represent particles and holes, the double lines represent the Δ resonance and dashed lines represent mesons (pions). Dotted lines are Cutkosky lines, where the lines intersect the particles are put on-shell and represent a possible final state: (a) 1p1h, (b) 1Δ1h, (c) 2p2h or 1p1h1π and (d) 1p1h1π. Grey circles represent any possible vertex that contributes to the correct initial and final state particles. Figure taken from [202].

It is therefore clear of the importance of including higher order terms, such as the 2p2h

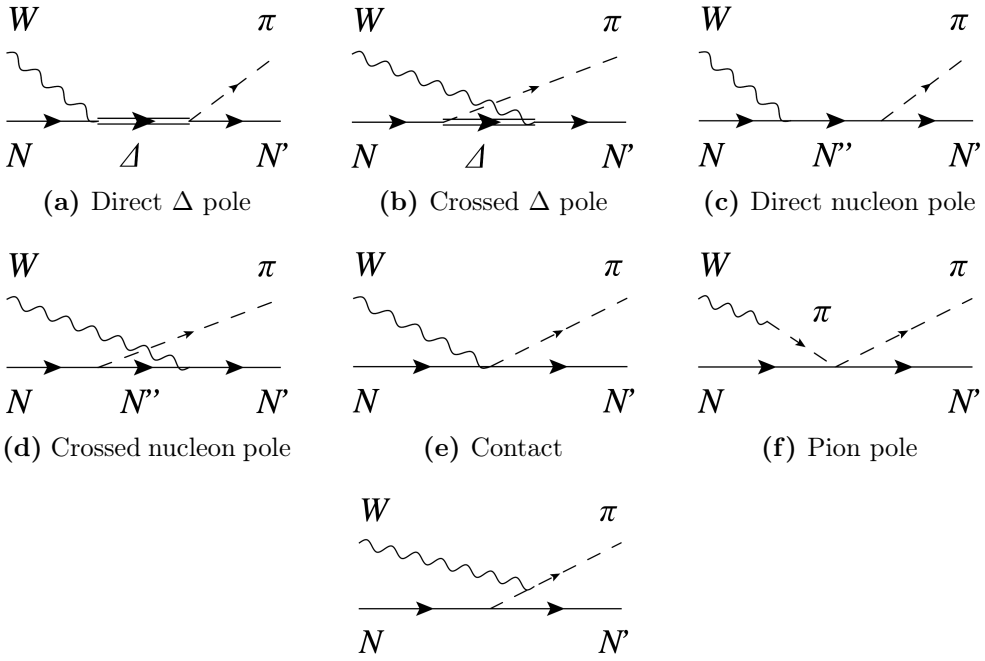

(a) Direct Δ pole **(b)** Crossed Δ pole **(c)** Direct nucleon pole

(d) Crossed nucleon pole **(e)** Contact **(f)** Pion pole

(g) Pion in flight

Fig. 2.9: Possible pion production vertices considered in the W self-energy diagrams in Figs. 2.8c and 2.8d. Figure reproduced from [202].

contributions, into the calculations for the experimental CC0π topology. By including both the CCQE (or 1p1h as it is known in the Nieves and Martini models) and 2p2h it is possible to reproduce the MiniBooNE neutrino and antineutrino cross-section data without having to inflate the axial mass [203–206]. It should be noted that both the Nieves and Martini models are different instances of the same underlying model - under the umbrella of an RPA framework. Their only differences lie in the choice of self-energy diagrams considered.

2.3.3 Final State Interactions

Once the hadrons have left the primary interaction vertex, they have to propagate through the nuclear medium before they are detected and have a non-zero chance of re-interacting with the spectator nucleus' nucleons. Illustrated in Fig. 2.10, produced pions can undergo charge exchange, can elastically or inelastically scatter, and can be absorbed by a nucleon. These secondary interactions, known collectively as Final State Interactions (FSI), can significantly alter the energies and multiplicities of the final state hadronic system. This makes it impossible to determine the interaction type based on the final state particles.

Most generators (excluding GiBUU [208]) use a semi-classical intranuclear cascade (INC) model to simulate hadron reinteractions [209]. Any hadron produced in the nucleus is stepped through the nuclear medium from its production point to its escape. The interaction probability at each step is calculated from the total cross-section for each particle in the cascade. The particular re-interaction they undergo depends on the relative cross-section for each process. If any particles are produced in the interaction, they are added to the cascade; this process is repeated until there are no particles left - either they have been absorbed,

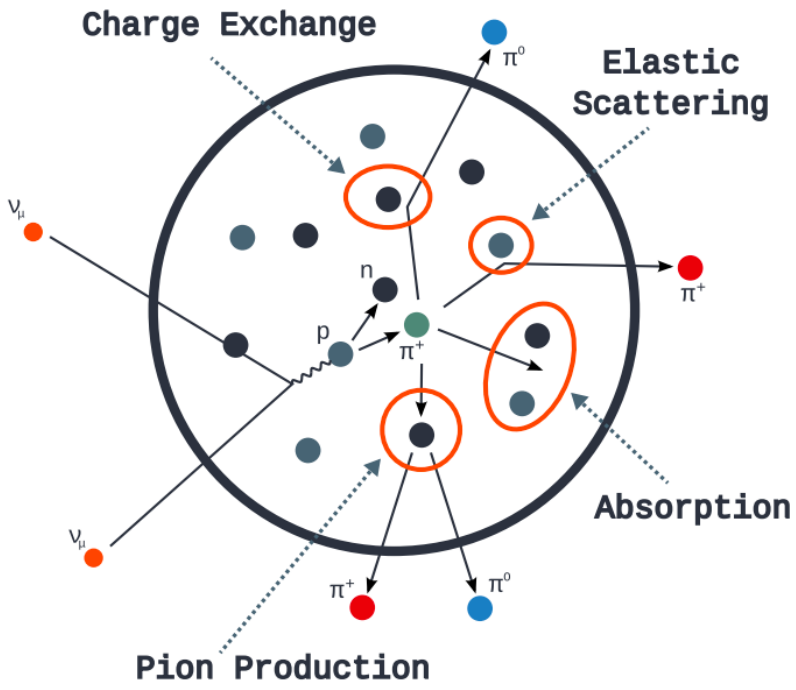

Fig. 2.10: Possible re-interactions of a simple CCQE interaction and exhibiting the effects FSI can have on the final state topology. Figure taken from [207].

or have left the nucleus[13]. The nucleus is modelled here with a local Fermi gas and using a Woods-Saxon nucleon density function [211] in order to calculate the interaction position and kinematics and the size of the nucleus [160].

Generators also include a so-called formation zone/time (FZ/T), the concept of which was originally discovered in the context of multiple electrons passing through a material [212]. At high four-momentum transfers, a produced quark system can be created with a small transverse size, and during hadronisation any interaction can take place coherently over the whole hadronic shower. This suppresses the cross-section for individual particles, and is particularly important for pion re-interactions [210]. Generators include a FZ or FT within which the particles are unable to interact with the nuclear medium, in order to build this suppression on top of the model.

In the investigation of nuclear effects and FSI, an important step forward came with the examination of transverse kinematic variables [213]. By projecting the scattered lepton and struck nucleon kinematics onto the transverse plane (Fig. 2.11), one can start to investigate the properties of the underlying nuclear effects; there is a transverse kinematic imbalance (TKI), which is the sum of the Fermi motion and intranuclear momentum transfer (which includes FSI and multi-nucleon interactions). In the absence of any nuclear effects, the nucleon and lepton momenta will be equal and opposite in this plane. This imbalance can

[13]The hadron is defined as "outside" the nucleus if the potential is 10^{-4} of the maximum [210].

be inferred from single transverse variables defined as

$$\delta\vec{p}_T \equiv \vec{p}_T^{\,\ell'} + \vec{p}_T^{\,N'} \,, \tag{2.29}$$

$$\delta\alpha_T \equiv \arccos \frac{-\vec{p}_T^{\,\ell'} \cdot \vec{p}_T}{\vec{p}_T^{\,\ell'} \vec{p}_T} \,, \tag{2.30}$$

where $\vec{p}_T^{\,\ell'}$ and $\vec{p}_T^{\,N'}$ are the projections of the final-state lepton and nucleon transverse to the neutrino direction and $\delta\alpha_T$ is the transverse boosting angle. In the case of no FSI, $\delta\vec{p}_T$ would be the projection of $\vec{p}_T^{\,N'}$ and $\delta\alpha_T$ the angle between $\vec{p}_T^{\,N'}$ and $\vec{q}$, the momentum transfer (if the scattering occurred on a stationary free nucleon, $\delta\vec{p}_T$ would be zero). To a first approximation, this means $\delta\vec{p}_T$ is independent of neutrino energy and the transverse angle would be constant as the Fermi motion is isotropic. Therefore transverse variables are an important probe for FSI effects and have model separation power, with both T2K [214] and MINERνA [215] recently releasing analyses containing these variables.

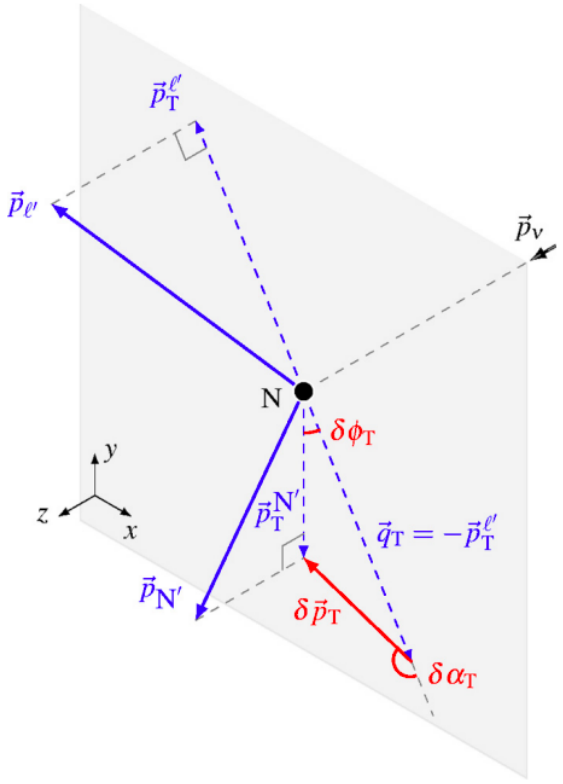

Fig. 2.11: Illustration of the single transverse kinematic imbalance, with the plane defined transverse to the neutrino direction. Figure taken from [213].

2.3.4 Optical Potential

Under the impulse approximation, the bound nucleon and the remnant nucleus evolve independently after the hard scatter. This also assumes the lepton is a plane-wave before and after the scattering event, implying the lepton and nuclear ground state are unaffected by each other's presence. This is a simple case, one which is not physically accurate, however in the case of complex nuclei the exact solution of a quantum many-body problem of a probe

from said nuclei is intractable. These calculations can be made much simpler by reducing the many-body problem to a few-body one, replacing the individual probe-nucleon interactions with a complex mean-field potential (in a similar fashion to the microscopic RMF models).

The nuclear optical potential is a phenomenological representation of the effective interaction between the probe and the struck nucleus [216, 217]. It is akin to the behaviour of a light wave (hence the name) that can be refracted or absorbed by a medium: a particle wave can be scattered or absorbed by a complex potential. Here the imaginary part of the refractive index accounts for the absorption of light, in the nuclear case this describes contributions from non-elastic reactions.

A full mathematical description of different optical potential models is beyond the scope of this thesis, however most follow the general form of

$$V = \sum_n U^n f(r)^n + i \sum_m W^m g(r)^m \,, \tag{2.31}$$

where U ($f(r)$) and W ($g(r)$) are the real and imaginary potential depths (form factors) respectively [218–220]. The summation relates to the terms considered in the model (such as surface- and volume-peaked terms, or the inclusion of isospin). The forms for each of the terms vary widely, with some using more theoretically driven forms of the potentials, while others use a generic polynomial form. In either case, the free parameters are tuned to elastic scattering data in order to provide a potential which can modify the outgoing lepton kinematics. This moves beyond the impulse approximation described in earlier sections, and accounts for differences in a scattering event taking place on the 'surface' of the nucleus (*i.e.* at low momentum transfers) or deeper in the 'volume'.

2.4 Summary

This section has summarised the key parts of neutrino interactions and their application to generators. However, it must be noted that all of these approaches come with limitations. Obviously, it would be desirable to have a consistent model which incorporates all of the interactions discussed above: at least, it would be useful to model each interaction with the same definition of the ground state nucleus. This is unfortunately not the case; the Benhar-Fantoni Spectral Function (along with superscaling approaches) is only designed to model quasi-elastic interactions, whereas most other interactions occur on a RFG model, or even LFG in the case of hadron re-scattering.

It is also common for models to provide a decent description of the outgoing lepton kinematics, but provide little information on the kinematics of the outgoing hadrons. In NEUT and NuWro, this is implemented by enforcing energy and momentum conservation and Pauli blocking on the outgoing hadrons [221], though currently no model describes how momentum is shared between multi-nucleon systems.

Franken-models such as these are not a fully consistent description of Nature, and confronting these inconsistencies will be key for future oscillation experiments.

Chapter 3

Lepton Interaction Experiments

> Just look at me. I'm 18 years old and I look like I'm well over 40.
>
> Kark (S2E4 23:20)

This chapter will describe the T2K experiment in section 3.1, as most of the work completed has been under the T2K banner. Due to a large body of work also being completed on Super-Kamiokande monitoring, this experiment will also be described (section 3.2). Much of this thesis hinges on the examination of electron scattering data, therefore these types of experiments will be described in section 3.3.

3.1 The T2K Experiment

T2K (Tokai-to-Kamioka) is a long-baseline accelerator neutrino oscillation experiment based in Japan. It is designed to make precision measurements of neutrino oscillation parameters, most notably the measurement of θ_{13}, originally the last unknown mixing angle, by observing electron neutrino appearance in a muon neutrino beam.

T2K uses a neutrino beam produced in Tokai, which is directed toward a near detector complex 280 m away from beam production, and a far detector 295 km away in Kamioka. Each of these sits at an angle of 2.5° from the beam centre, as T2K employs an off-axis method to generate a narrow-band energy spectrum peaking at ∼0.6 GeV which maximises neutrino oscillation effects.

As seen in equation 1.20, T2K has optimized the L/E parameter to maximise the oscillation probability. Electron neutrino appearance vs muon neutrino disappearance measurements give sensitivity to different parameters: the former measures θ_{13}, whilst the latter gives Δm_{23} and θ_{23}. This is a consequence of measuring ν_μ disappearance (including oscillations into ν_τ) where the latter parameters can be measured by the position of the oscillation minimum and its depth respectively. Unfortunately, ν_τs cannot be observed in the far detector as the beam energy is too low to produce the associated charged lepton.

Whilst measuring the height of the ν_e energy peak is important for the determination of θ_{13}, at next-to-leading order it also depends on the CP-Violating phase δ_{CP}. This gives T2K some sensitivity to the size of the CP-violating effect in the lepton sector, thus making headway on the issue of matter-antimatter asymmetry. As mentioned in section 1.4, a recent measurement has been made of this effect [96].

3.1.1 The Neutrino Beam

The T2K neutrino beam is produced at the Japan Proton Accelerator Research Complex (J-PARC, [223]) in Tokai, and comprises of 3 accelerators: a linear accelerator (LINAC), a rapid-cycle synchrotron (RCS) and the main ring (MR). H- ions are accelerated up to 400 MeV by the LINAC, before being removed of their electrons by charge-stripping foils as they pass into the RCS which accelerates them to 3 GeV. $\sim$ 5% of the proton bunches are supplied to the MR, where they are accelerated up to 30 GeV for the neutrino beamline.

Beam spills extracted from the MR are focused and steered using a series of magnets in the primary beamline. Magnets prepare and tune the beam to be accepted by the arc section, which redirects the bunches toward the far detector in Kamioka. These are refocused and directed toward the target. This proton beam is monitored pre-collision to ensure it is well-tuned for neutrino production.

The protons impinge on a graphite target producing a variety of secondary hadrons, most notably pions and kaons. These hadrons are focused by three magnetic horns, that mostly select pions, and direct them toward a 96 m long decay pipe. These pions decay in flight to produce muons and muon (anti)neutrinos. The leptons pass through a beam dump at the end of the decay volume, removing particles other than neutrinos and purifying the beam. A muon monitor (MUMON), characterises the neutrino beam by sampling the remaining muons. Beam production can be executed in neutrino or antineutrino mode by reversing the direction of the magnetic horn current.

The kinematics of a two-body decay results in a large neutrino beam energy spread if viewed on-axis. As the off-axis angle increases, the neutrino energy spectrum becomes more defined and the peak position reduces as shown in Fig. 3.2. By tuning the off-axis angle one can achieve a narrow-band neutrino energy spectrum and select a peak located at the maximum oscillation probability. At T2K, the off-axis angle is 2.5°.

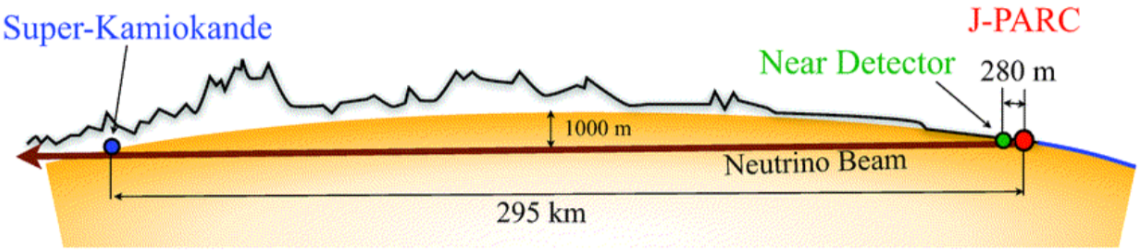

Fig. 3.1: Diagram of the neutrino's journey from production at the beamline, through the near detector at 280 m and toward the far detector 295 km away. Figure taken from [222].

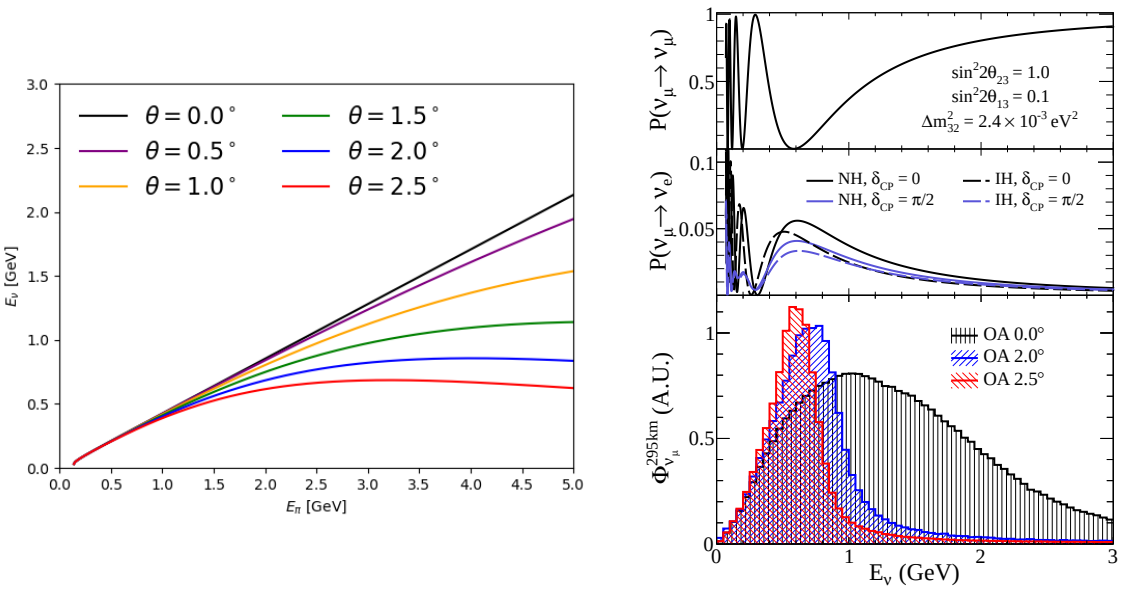

(a) **(b)**

Fig. 3.2: **(a)** Predicted neutrino energy as a function of pion energy. As the off-axis angle increases it predicts a maximum neutrino energy. **(b)** Normalised neutrino energy spectrum for a beam sampled at various on- and off-axis angles (*bottom*). As the angle increases, the beam produces a tighter distribution of energies. This energy is tuned to correspond to the minimum survival probability for ν_μ (*top*), and maximum appearance probability for ν_e (*middle*). Figure taken from [224].

The neutrino energy can be expressed as

$$E_\nu = \frac{m_\pi^2 - m_\mu^2}{2(E_\pi - p_\pi \cos\theta_{OA})} \tag{3.1}$$

where m_π, E_π and p_π are the mass, energy and momentum of the pion, m_μ is the mass of the muon and θ_{OA} is the off-axis angle [225]. This is a simple derivation from the kinematics of a 2-body decay. As the off-angle increases, the difference between the initial pion energy and the outgoing momentum projected along the neutrino axis increases, thus the neutrino energy decreases. This also explains why the neutrino energy becomes more narrow banded: in an off-axis direction there is a maximum in neutrino energy, and a wide range of pion energies map onto a (almost) single neutrino energy (Fig. 3.2a).

3.1.2 Near Detector Complex

Situated 280 m from the beam, the near detector complex consists of multiple detectors. INGRID measures the beam profile and direction to a precise degree. ND280 constrains neutrino interaction parameters to reduce systematic errors in the T2K oscillation analysis. A final detector, WAGASCI-BabyMIND, has recently been included in the near detector suite to further reduce the systematic errors.

3.1.2.1 INGRID

INGRID (Interactive Neutrino GRID) is located directly on-axis, and is used to precisely measure the beam direction and intensity. It consists of 16 modules: 14 in a cross with vertical and horizontal components, 2 located at off-axis directions from the cross. A diagram of the setup is shown in Fig. 3.3a.

Each module is a sandwich of 9 iron plates and 11 scintillator planes, the former serving as the target material and the latter used for tracking. Each scintillator plane is composed of 24 scintillator bars glued perpendicularly to a further 24.

These modules form a transverse plane of 10 m × 10 m, with the centre of the cross defined as 0° with respect to the proton beamline. This allows INGRID to measure the beam centre to a precision of 0.4 mrad.

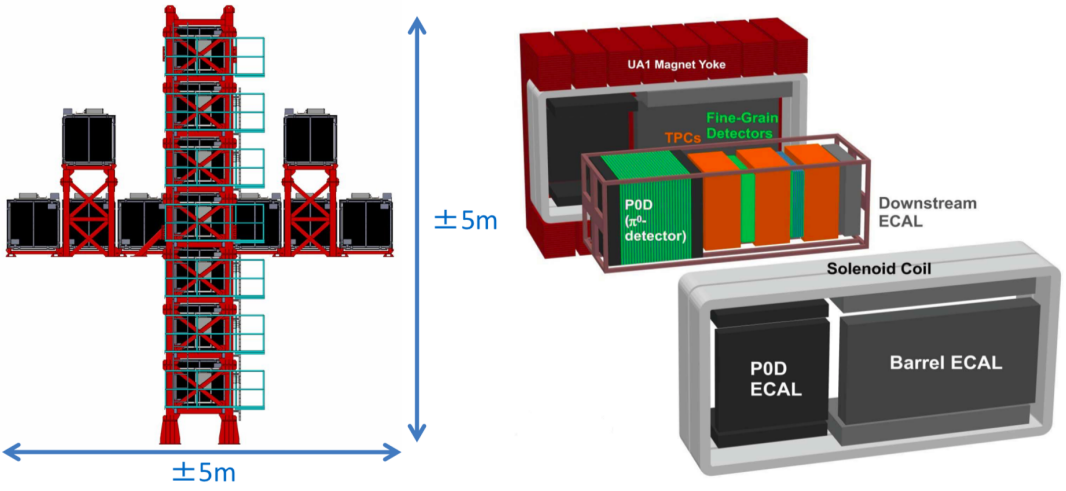

(a) (b)

Fig. 3.3: *Left.* INGRID on-axis detector. The 16 transverse modules sample a 10 m × 10 m section of the neutrino beam - figure taken from [226]. *Right.* Exploded view of the ND280 off-axis detector, showing the individual subdetectors that form it. The neutrino beam enters on the left. Figure taken from [227].

3.1.2.2 ND280

ND280 is a magnetised, segmented detector used to measure ν_μ and ν_e quasi-elastic and resonant interactions on both carbon and oxygen, and sits at the same off-axis angle as the far detector. ND280's main function is to characterise the signal and background for Super-Kamiokande (importantly single π^0 production) by measuring the neutrino beam energy, flux and electron neutrino contamination. Due to the proximity to the beam production, ND280 samples a pre-oscillated beam and can also be used independently for measurements of neutrino-nucleus cross-sections.

Shown in Fig. 3.3b, the refurbished UA1 magnet encloses the detector, providing a 0.2 T magnetic field perpendicular to the neutrino direction for particle identification. The most upstream subdetector is the PØD [228], whose primary objective is to observe neutral cur-

rent π^0 production, a significant background at Super-Kamiokande. Scintillator bars are interleaved with water bags: data is taken with these filled or empty and a subtraction method used to calculate the π^0 production cross-section.

Downstream of the PØD is the tracker region, composed of two Fine Grained Detectors (FGDs, [229]) and three Time Projection Chambers (TPCs, [230]). The FGDs act as the main target mass for neutrino interactions, also serving as active tracking from the interaction vertex. The upstream FGD(1) is built from 9.6 × 9.6 × 1864.3 mm polysterene scintillator bars, alternating horizontal and vertical layering in the x-y plane perpendicular to the beam. This arrangement gives a full 3-dimensional reconstruction of the interaction vertex. FGD2 is similar to the first, however alternate layers of plastic scintillator are replaced with a passive water target. Comparing event rates in FGD1 and FGD2 can determine the neutrino cross-sections on water and carbon individually, thus reducing uncertainties on extrapolating cross-sections from different targets between the near and far detectors.

The TPCs are filled with an argon gas mix. A charged particle passing through will cause ionisation and the resulting electrons drift in the magnetic field to generate an event signal. A 3-dimensional track can be produced by examining both the position and timing of each particular readout. As the TPCs sit in a magnetic field, they can be used to determine the momentum of each particle and, when combined with ionisation energy loss, are a powerful tool for identifying particles produced elsewhere in the detector. An example of this identification procedure is shown in Fig. 3.4.

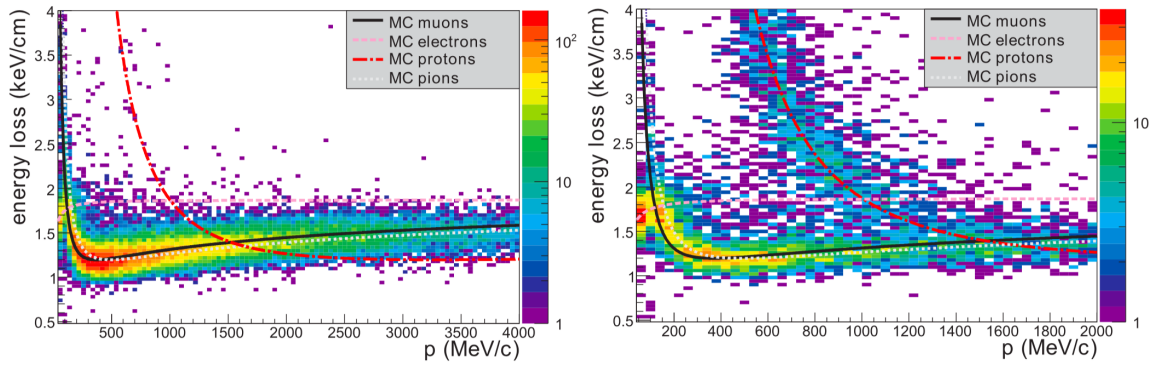

Fig. 3.4: *Left (right).* Distribution of energy loss as a function of momentum for negatively (positively) charged particles compared to their expected value for different particles, from Monte Carlo simulation. Figure taken from [230].

Electromagnetic calorimeters (ECal, [231]) surround the PØD and the tracker region, though sit inside the magnet yoke, and are separated into three sections: the PØD-ECal, barrel-ECal (around the tracker) and the downstream-ECal adjacent to the final TPC. These are sampling calorimeters, using layers of active plastic scintillator bars sandwiched between lead absorber, and are essential for the correct identification and energy reconstruction of neutral and charged particles through electron/positron showers. Shower clustering algorithms are used in order to match calorimeter showers with particle trajectories in the tracker region.

The final piece of the detector puzzle is the Side Muon Range Detector (SMRD, [232]), which are scintillator modules inserted between the steel plates in the magnet. Its main function is to act as a veto-trigger for cosmic ray muons that penetrate the detector and for interactions occurring inside the magnet. The SMRD also records hard scattered muons detected at high angles to the beam direction.

3.2 Super-Kamiokande

Super-Kamiokande (SK) is the world's largest man-made water Cherenkov detector and, whilst having a broad range of physics goals itself, serves as the far detector for T2K [233], whose goals are discussed in section 3.1. Over the years SK has released many high profile scientific publications, some of which were discussed in chapter 1.

Originally, the Kamiokande family's primary aim was to conduct a search for proton decay[1], with mentions of studies of neutrino oscillation in the atmospheric sector [234]. However, it was not until the proposal of SK[2] where the search for neutrino oscillation in the solar and atmospheric sectors really became a focus; this led to the Nobel prize in 2015. SK's scientific goals include proton decay and the study of neutrinos from various sources: supernovae; the Sun; the atmosphere; gamma-ray bursts; and, of course, accelerator neutrinos.

Inside SK, neutrino events are detected from their charged partners produced in charged-current interactions with nuclei in the detector volume. If the partner is moving fast enough, it produces Cherenkov light which can be detected by photomultiplier tubes (PMTs) mounted on the walls. These convert the photons to electrons, which are amplified and collected for readout. The following sections explain this process in more detail; further details of the calibration of the SK detector will be given in chapter 6.

3.2.1 Super-Kamiokande Tank

SK sits 295 km west of the T2K beam production, at the first oscillation minimum for the T2K experiment. It has a nominal water capacity of 50 kton with a 2,700 metres-water-equivalent (m.w.e) overburden acting as a cosmic ray muon shield. This is an otherwise irreducible background, as no muon with an energy less than 1.3 TeV can penetrate to this 2700 m.w.e. depth.

The detector itself is a 39 m diameter and 42 m tall stainless-steel cylindrical tank separated into two distinct volumes: the inner and outer detectors (ID and OD respectively) [233]. These are optically isolated by Tyvek® sheets. The ID contains 11,146 PMTs[3] facing

[1] Indeed, the name KamiokaNDE originally meant Kamioka Nucleon Decay Experiment, before efforts were refocused and it became the Kamioka Neutrino Detection Experiment.

[2] Also proposed as JACK - the Japan America Collaboration at Kamioka. This was a turbulent time in the proposals, where everyone was uncertain whether to focus on neutrino detection due to the rapidly evolving situations in the solar and atmospheric sectors.

[3] Half of these PMTs were destroyed in a cascading implosion after one PMT imploded during refilling. This resulted in a reduced photocoverage of 47% before until the beginning of the second phase of the

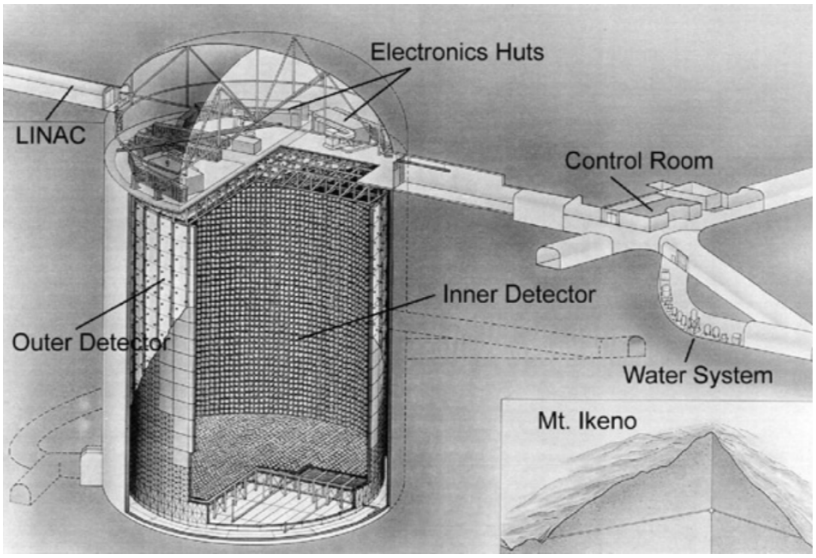

Fig. 3.5: Sketch of the Super-Kamiokande detector, located under Ikenoyama. The cutaway shows the inner and outer detector covered with photomultiplier tubes. Figure taken from [233].

inwards for a total photocathode coverage of 40%. These PMTs were developed by Hamamatsu and are 20 inches (50 cm) diameter hemispheres, which detect the main signal in the SK fiducial volume (FV). The FV is defined 2 m from the ID wall, serving as passive shielding and reducing bias in reconstructing events close to the PMTs. The OD contains 1,885 photomultiplier tubes (PMTs) facing outward, each one 8 inch (20 cm) diameter hemispheres, also from Hamamatsu, but mostly recycled from the IMB experiment. The OD PMTs are primarily used as an anti-coincidence counter against incoming particles, while the OD volume serves to passively reduce neutron and γ ray backgrounds from the surrounding rocks, these events are often induced by cosmic rays. It can also be used to constrain whether an event is fully-contained (FC) or partially-contained (PC), dependent on the OD light patterns showing consistency with exiting particles; this only gives a lower limit on the neutrino energy.

The operation of the PMTs is standard, though the ID PMTs were specifically designed to be sensitive to Cherenkov light and have a high photoelectron collection efficiency. A Cherenkov photon passes into the vacuum of the PMT and impinges on the photocathode (a Sb-K-Cs bialkali), releasing an electron via the photoelectric effect. This electron is focused and accelerated onto a dynode, where secondary emissive electrons are released. These secondaries are accelerated towards another dynode, and the process continues until the electrons reach the anode, causing a sharp current pulse detectable by the electronics. The dynodes are set in a venetian-blind structure (Fig. 3.6b) often employed in large diameter PMTs, with each successive dynode set at a higher potential in order to accelerate the secondary electrons.

The ID PMTs had their photocathodes chosen in order for the peak PMT response to lie between 300 and 500 nm, Fig. 3.6a, in the same region as the 420 nm peak exhibited by

experiment in 2002.

Cherenkov radiation (section 3.2.2, [235]). The timing and energy response was improved from their previous design, which is vital for vertex reconstruction inside the detector volume. As the OD PMTs were reused, their peak response is not tuned for Cherenkov radiation; instead acrylic wavelength-shifting (WLS) plates are installed around each PMT. This reradiates the UV Cherenkov light as blue-green, matching the peak response of the PMTs, and increasing the light collection by 1.5.

The geomagnetic field also causes issues with the highly sensitive PMTs, exerting an average field of 450 mG at an angle of 45° with respect to the horizon. The strength of this field can cause a systematic bias in the secondary electron trajectories and timing of each of the PMTs, with a 100 mG field causing a 10% reduction in the collection efficiency [233]. 26 coils are employed (14 horizontal and 12 vertical) around the tank, which leaves a residual field of around 32 mG, and only reducing the collection efficiency by $\sim 1 - 2\%$.

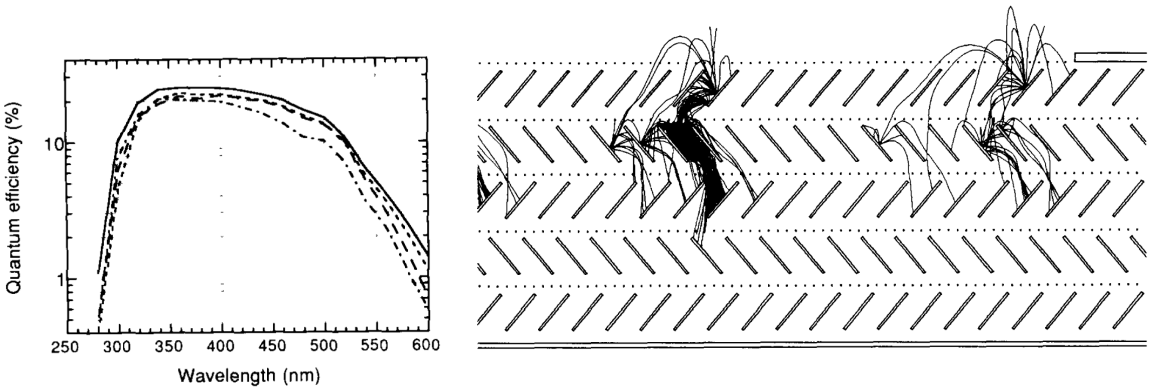

Fig. 3.6: **(a)** The peak wavelength response of an ID PMT. **(b)** Venetian-blind layout inside the PMTs, showing the secondary emission of electrons. Figures taken from [235].

3.2.2 Particle Identification

As mentioned, SK is a water Cherenkov detector. A charged particle travelling through a dielectric can emit Cherenkov radiation if its velocity is greater than the phase velocity of light in that medium, *i.e.*

$$\frac{c}{n} < v_p, \tag{3.2}$$

where c is the speed of light, n is the refractive index of the medium and v_p is the velocity of the particle. A neutrino interacting via a charged current process can produce a particle (lepton flavour corresponding to the initial neutrino flavour) whose energy exceeds this threshold and emits light in ring patterns detected by the PMTs. It is not the particle itself which produces the radiation, but the molecules of the medium surrounding it. These are excited and asymmetrically polarised along the direction of the particle, and upon de-excitation the photons constructively interfere with one another causing a ring to form: this being the Cherenkov radiation. This only occurs if the condition in equation 3.2 is satisfied, otherwise

the polarisation is symmetric and the de-excitation is random. The opening angle, θ_C of the Cherenkov cone with respect to the incident particle is

$$\cos\theta_C = \frac{1}{n\beta}\,, \tag{3.3}$$

where $\beta = v_P/c$. As the refractive index of water is 1.34, this corresponds to a Cherenkov opening angle of $\sim 42^\circ$ ($\beta \approx 1$ as the particles are ultrarelativistic).

To distinguish between muons and electrons, as is required by the experiments rich physics program, SK employs a likelihood function which exploits systematic differences in shape and opening angle between these particles [236, 237]. Due to their larger mass, muons are unlikely to undergo multiple scatterings, leading to a sharp Cherenkov ring. In contrast, electrons can incite electromagnetic showers, of which many particles can undergo multiple scatterings, leading to a less defined, or 'fuzzy', ring. Fig. 3.7 shows the difference between two event displays for electrons and muons, and Fig. 3.8 shows the particle identification distribution for data as compared to Monte Carlo predictions. Although the latter figure is an ideal case, there is clear separation between e-like and μ-like ring samples. The energy threshold for inciting a Cherenkov cone is different for each particle, this is summarised in Table 3.1.

Particle	Energy Threshold [MeV]
$e^\pm$	0.767
$\mu^\pm$	157.4
$\tau^\pm$	209.7

Table 3.1: The Cherenkov energy thresholds for the charged leptons detected in the Super-Kamiokande tank. These values are the same for any water detector.

3.2.3 Water Filtration and Purification

As water is the main detection medium inside SK, it needs to optimised just like the detectors themselves. The water is sourced from within the mine itself, as there is a stream near to the detector. The water is purified[4] and constantly recirculated inside the SK tank during operation to ensure a high water transparency, and remove radioactive substances (such as radon) from the water to reduce backgrounds.

The water first passes through a 1 μm mesh filter which removes dust and other small particles. A heat exchanger removes heat introduced to the system from the circulation pump: a higher water temperature causes PMT dark noise levels to rise and promotes bacterial growth which also reduces water transparency. Thus the water temperature is kept mostly stable around 14°C. Remaining bacteria are killed with an ultra-violet sterilizer. A

[4]Indeed, it's so pure there have been many stories about its lethality. Someone left a wrench in the bottom of the tank when it was filled in 1995, by the time the tank was drained in 2005, only its outline remained.

cartridge polisher removes heavy ions (removing radioactive species), increasing the resistivity of the water to 18.24 MΩcm which approaches the theoretical limit. A reverse osmosis membrane removes additional particulates. An air-melting system dissolves radon-free air into the system, that then assists the vacuum degasifier in removing radon (a large background in solar neutrino analyses) and oxygen, which again stimulates bacterial growth. A membrane degasifier is used to support the previous stage. As a final stage, an ultra-filter is employed to remove any molecules of a size greater than 10 nm. Radon-free air is pumped into the gap between the surface of the water and the tank, in order to stop radon-heavy air from entering and leeching radon into the detector [233].

This filtration process is continuously in use during normal operation (and during the filling of the detector) and is monitored on a daily basis. 8 thermometers sit around the ID and OD, while water absorption and scattering coefficients are monitored using a laser analysis, which will be described in more detail in chapter 6.

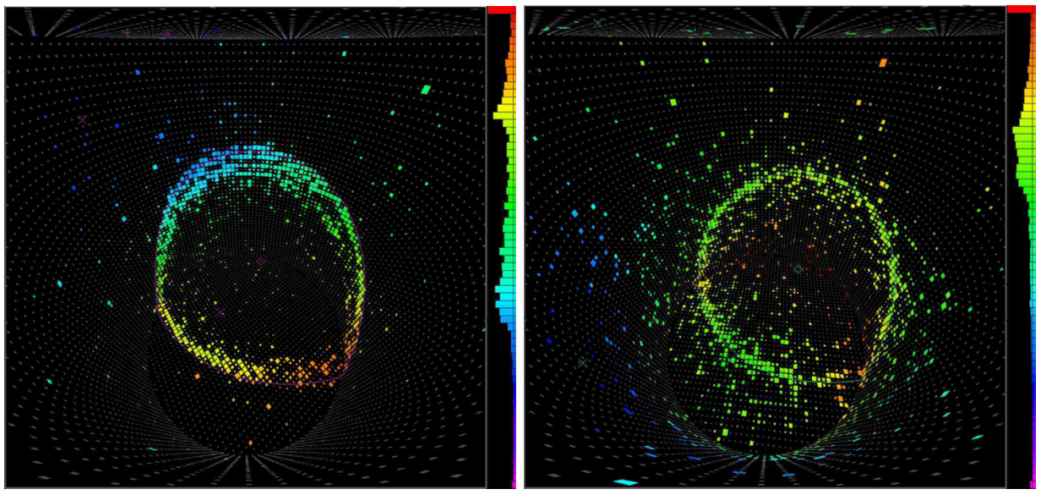

Fig. 3.7: Two images of event displays in the Super-Kamiokande detector showing a muon (*left*) and electron (*right*) Cherenkov ring. Notice the difference in 'fuzziness' due to electromagnetic showers and multiple scatterings. Figure taken from [238].

3.3 Electron Scattering Experiments

The analysis presented in this thesis will make extensive use of available electron scattering data, thus it seems appropriate to briefly describe the experiments that provided it.

3.3.1 Experimental Setup

Electron scattering experiments work in a similar way to neutrino scattering experiments. Electrons are accelerated to high energies before impinging on a target, where the particles are scattered and measured by a detector. Without exception, the detector in these scattering experiments has been a magnetic spectrometer[5] which sits on a moving arm to

[5]Perhaps the most famous magnetic spectrometer is the Alpha Magnetic Spectrometer, installed on the International Space Station and designed to detect antimatter in cosmic rays.

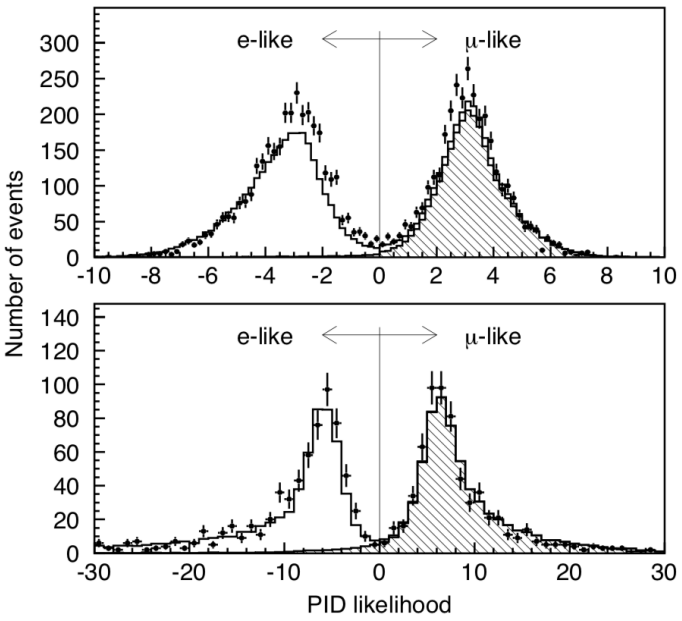

Fig. 3.8: Distribution of particle likelihood for sub-GeV (*top*) and multi-GeV (*bottom*) fully contained single-ring events. Data is given by the points, whilst Monte Carlo predictions are shown as histograms. Although an ideal case, there is clear separation between e-like and μ-like events. Figure taken from [236].

measure different scattering angles. An example of the detector arm is shown in Fig. 3.9. In most cases, the electron tracks are reconstructed with a multiwire chamber and the primary trigger is a fast scintillator plane (hodoscope). Often a Cherenkov counter is used for particle identification and pion rejection, and occasionally a calorimeter to assist in particle identification.

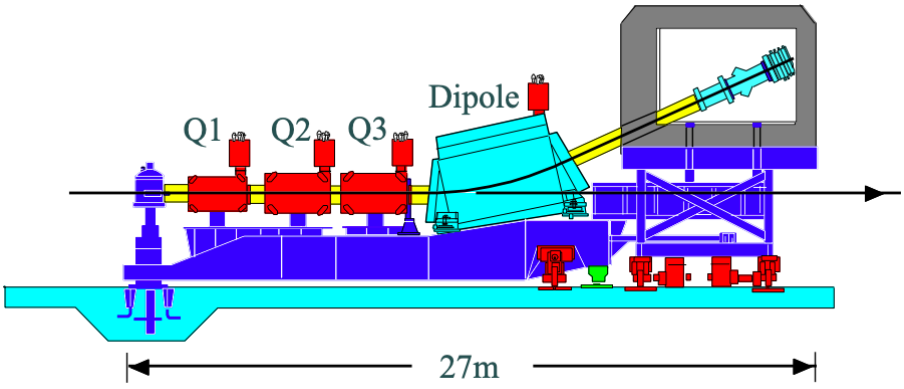

Fig. 3.9: Side view of the High Momentum Spectrometer at Jefferson Lab Hall C. The Qs are the focusing quadrupole magnets. The black line shows the scattered beam, whilst the continuing arrow is the unbent beam heading to the beam dump. The detector itself is in the heavily shielded grey hut. Figure taken from [239].

3.3.1.1 Linear Accelerators

Whilst J-PARC uses a cyclical synchrotron accelerator in order to accelerate protons, it becomes inefficient to do so for electrons. The power radiated via synchrotron radiation is proportional to $1/m^4$, thus the energy loss for electrons would be $\sim 10^{13}$ times the amount of a proton for the same energy. Due to this, electron scattering experiments often use linear accelerators (LINACs) in order to accelerate electrons to high energies[6]. The basic principle of a LINAC is simple, relying on the acceleration of charged particles placed in an electric field.

In the simplest case, particles pass through drift tubes *in vacuo* which are connected to alternate terminals of a radio-frequency (RF) oscillator. Correctly charged particles are accelerated along the electric field to the first tube and, as they travel through it, the polarity of the tubes are switched. This causes the particles to be accelerated toward the second tube, and the process continues. Timing is key to the usefulness of these, as the accelerated particles must remain in phase with the alternating electric field in order to be continuously accelerated. LINACs of this type are often used for the first stages of acceleration, called injectors, where the particles they accelerate are passed off to more powerful accelerators (this is the case with LINAC in J-PARC) [240]. If the applied voltage is the same across all tubes, the acceleration gaps must be further apart as the particle gains speed. An example setup is shown in Fig. 3.10.

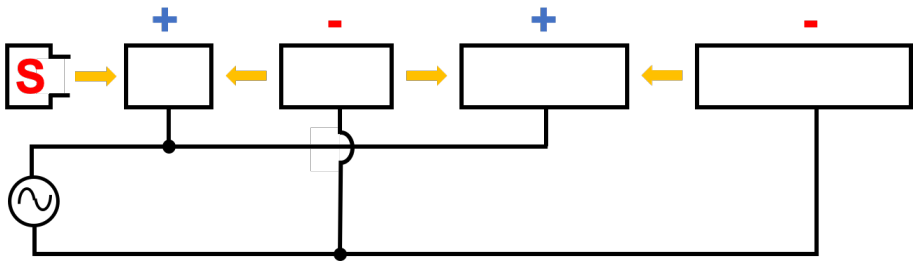

Fig. 3.10: An example setup of a linear accelerator. An alternator (circle with a wave) provides alternating polarities to the drift tubes (black rectangles), to which the particles from the source (red 'S', negative in this example) are accelerated. The orange arrows between tubes is the direction of the acceleration (in this case, opposite to the electric field).

At high particle speeds, the magnetic force is stronger than the electric force, thus quadrupole magnets are used to focus the beam in the transverse plane. As each quadrupole can only focus in one transverse direction, a series must be used in order to focus in the full plane. In the longitudinal direction, particles can also be focused. Particles entering the tube on the rising face of the RF oscillation (those at the front) will undergo less acceleration due to the lower voltage. Those particles that arrive later are accelerated slightly more, and overtake those at the front. This is known as phase stability and makes it necessary to accelerate particles in bunches, rather than as a continuous beam.

Above a few MeV, electrons reach velocities close to the speed of light and do not appre-

[6]The Large Electron-Positron Collider (LEP) is an obvious exception to this, being the most powerful lepton accelerator to date.

ciably gain in speed for any increase in energy. It then becomes appropriate to use a slight variation on the above method, by supplying a series of cylindrical metal cavities with an oscillating electric field along the direction of the tube. By adjusting the frequency of the waves inside the cavity, you can cause the electrons to 'ride the crest' of the wave and gain an energy kick from the electric field [241].

The largest LINAC created was the Stanford Linear Accelerator (SLAC, [242]), 3.2 km long understood to be the world's straightest object[7]. Whilst powerful, the SLAC had a high cost due to the need for many RF drives. Recirculated Linear Accelerators (RLA) can solve this in a similar way to ring colliders, by reusing RF cavities. However, they do not suffer many of the potential drawbacks of ring colliders as the particles are only recirculated a few times, and also have a high beam quality [243, 244]. The best example of this is the Continuous Electron Beam Accelerator Facility (CEBAF, [245]) at the Thomas Jefferson National Accelerator Laboratory. Much of the data used in later chapters was obtained using these two accelerators.

3.3.1.2 Target

Before impinging on the target, magnets are often used in order to focus the beam. These are placed very close to the target to force the vertical beam dimension to be as small as possible: this is essential for a high energy resolution.

To gain cross-sections on a variety of targets (such as those of interest to neutrino scattering), a variety of liquid and solid targets are used. Solid targets, such as ^{12}C, Cu and Fe, are relatively simple to use and can be cut into any shape required. These are placed into some form of target wheel so the target can be changed automatically. Cryogenic targets are also used in order to perform measurements on elements such as H, ^{2}H and ^{4}He. These have to be kept in containers (like aluminium 'tuna cans') where a scattering event could take place on either the target itself or in the container. Measurements of the contribution from the container have to be taken into account with a dummy container. The contents of these cells are constantly recirculated with a heat exchanger to keep the target material at the correct temperature and density.

3.3.1.3 Magnetic Spectrometers

A number of experiments have been undertaken to measure the inclusive electron cross-sections and spectra of many nuclei. In order to do this, without fail experiments have used magnetic spectrometers. Here the High Momentum Spectrometer (HMS) is used as an example detector [246], however most spectrometers work in a similar way. Other detectors will be summarised in Table 3.2.

Magnetic spectrometers use momentum in order to analyse the electrons. In HMS, scattered electrons are focused using an array of quadrupole magnets (the same way as a LINAC), with a dipole magnet bending the beam and selecting the central momentum.

[7] Until the European Free-Electron Laser Facility opened in 2017.

This is all mounted on an "arm" which can rotate about a fixed central axis in order to measure electron scattering at a variety of angles, shown in Fig. 3.9. Before being focused, the particles have to pass through a collimator to set the angular acceptance of the detector. A schematic of the layout of the detectors in HMS is in Fig. 3.11.

Similarly to the TPCs in section 3.1.2.2, the drift chambers are used for particle tracking. A form of multiwire proportional chamber, any charged particle passing through the gas-filled chamber will ionize the gas, and the subsequent electrons drift toward the nearest wire. These wires are typically laid out orthogonal to one another, and using their position and the drift time of the detected electron, the particle's track can be determined to a high precision. In order to do this, the time the particle travelled through the drift chamber is required, which is information acquired through the scintillator paddles.

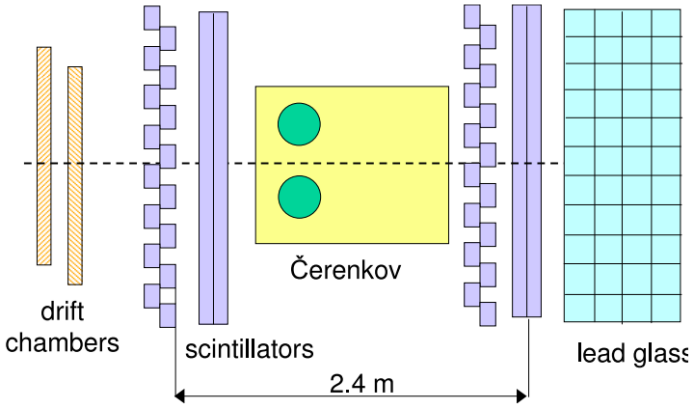

Fig. 3.11: The High Momentum Spectrometer detector stack in JLab Hall C. Figure taken from [246].

The HMS has two scintillar planes in an alternating XY orientation. As with the previous scintillators, charged particles passing through excite the molecules in the scintillator bars and cause them to emit light along the panel. Light lower than the angle of internal reflection gets collected by PMTs located at the ends of the paddles along light guides. As these were used as the fast trigger for the drift chamber, the timing of each signal had to be corrected for the pulse height offset and distance travelled through the paddle.

Electron scattering experiments often use a gas Cherenkov detector as a pion veto (as opposed to the signal detection as in SK). Gases have a lower index of refraction than water, thus the energy of a particle needs to be greater in order to produce Cherenkov radiation. For HMS, the gas used has a refractive index of 1.0005, after being depressurized to 0.35 Atm. The resulting Cherenkov thresholds are 16 MeV and 4.4 GeV for electrons and pions respectively, therefore any erroneous pion events can be categorised as such by the Cherenkov detector. These are constructed with 2 PMTs (the green circles in Fig. 3.11), with spherical mirrors on the downstream wall which reflect and focus the light onto these PMTs.

Calorimeters are then used in conjunction with the Cherenkov veto for particle identification. Electrons radiating photons via Bremsstrahlung can incite pair production, the products of which subsequently radiate photons, thus inciting a "cascade shower" in the de-

tector. As long as the energies are greater than ~ 300 MeV, pions act like minimum ionising particles (MIPs) and deposit a near constant energy, whereas electrons and positrons deposit all of their energy in the detector. Some complications can occur when pions undergo nuclear interactions in the calorimeter, leading to a shower-like signal. Thus the calorimeter has to be used in conjunction with the Cherenkov counter. In HMS, the calorimeter is built of 4 layers of lead glass blocks with PMTs attached to the ends, with the electronics having an energy threshold to discriminate the MIP-like pions.

Practically, a fully inclusive quasi-elastic scattering spectrum has to be collected with stepped values of the central spectrometer momentum; this is due to a full spectrum being greater than the momentum acceptance of the dipole magnet. If data can be taken with a sufficient overlap in momentum values, one can determine the dependence of $\Delta p/p_{central}$ on detector angular acceptance [247].

3.3.2 CLAS12

Though none of the data will be used in this thesis, it would not be complete without talking about the CLAS12 detector. The e4ν collaboration have proposed to extend the phase-space to a wide range of exclusive and semi-exclusive scattering measurements to test neutrino energy reconstruction techniques as a direct input to improve neutrino interaction generators. This will include data from the CEBAF Large Acceptance Spectrometer (CLAS) and new data taken with the new CLAS12 detector. Although CLAS12 uses similar detection techniques to the previous 'swinging arm' method, it is unique in its large acceptance. This allows detection of secondary hadrons that can isolate channels that contribute to specific interactions at the vertex. It is also able to detect events with secondary neutrons, which are typically not detected in neutrino experiments and are important in measurements of CP violation. The effort by the collaboration originally focused on QE events measured in the CLAS detector, but will now include a more systematic study using the more advanced CLAS12. The features of this detector will be briefly described, as its data will be invaluable in the development of event generators and future oscillation measurements: this will be explored further in future chapters. A schematic of the detector is shown in Fig. 3.12.

3.3.2.1 Experimental Setup

The CLAS12 detector is separated into two volumes, the forward detector (FD) and the central detector (CD). The FD operates at polar (laboratory scattering) angles up to 35°, with full 360° coverage in the azimuth. It is magnetised by a toroidal magnet, and is mainly used for low Q^2 events. Six drift chamber (DC, [271]) sectors of 36 layers make up the tracker region and are angled in order to have high resolution in the polar angle, at the detriment of a lower resolution in the azimuthal angle. The multiple DC layers build in redundancy in the tracking, with an average spatial resolution of 500 μm. Two threshold Cherenkov counters, high (HTCC, [272]) and low (LTCC, [273]) are part of the particle identification. The HTCC separates electrons from heavy charged hadrons and acts to rejects these events, along with being a fast trigger for events. It is filled with

Year	Laboratory	Accelerator	Energy	Angle	Tracker	Particle Identification	Ref.
1971	HEPL	Stanford Mark III Accelerator	0.5	60	-	FC-75 fluorochemical liquid Cherenkov (1.278)	[248–252]
1974	DESY	German Electron Synchrotron	$2 - 2.7$	15.0	Spark Chamber	Freon-13 gas Cherenkov (1.0137) & Sampling lead scintillator calorimeter	[253–256]
1983	Saclay	Saclay Linear Accelerator (ALS)	$0.120 - 0.600$	36.0, 60.0, 90.0, 145.0	MWPC	Plexiglass Cherenkov (1.5)	[257, 258]
1987	Bates	Bates Linear Accelerator	0.537, 0.730	37.1	MWPC	Freon gas Cherenkov (1.0014)	[259, 260]
1987	SLAC	Stanford Linear Accelerator*	$0 - 4$	$15 - 39$	MWPC*	Nitrogen gas Cherenkov (1.0020) and Lead-glass calorimeter*	[261, 262]
1988	Yerevan⋆	YerPHI Electron Synchrotron	$1.9 - 2.1$	16.0, 18.0	-	Sampling lead scintillator calorimeter	[263, 264]
1988	SLAC	$*$	$1 - 1.5$	37.5	$*$	$*$	[265]
1989	SLAC	Stanford Linear Accelerator†	$1 - 1.5$	37.5	MWDC†	Isobutane gas Cherenkov (1.3518) & lead-glass calorimeter†	[266, 267]
1995	SLAC	†	$2.0 - 5.0$	$15 - 57$	†	†	[268]
1998	JLAB	CEBAF‡	4.045	$15 - 55$	MWDC‡	Perflubutane gas Cherenkov (1.0005) & lead-glass calorimeter‡	[239, 245, 269]
2011	JLAB	‡	5.766	$18.0 - 55.0$	‡	‡	[239, 245, 246]

Table 3.2: Summary of electron scattering experiments utilised in later analyses. MWPC and MWDC stand for Multi-Wire Proportional Chamber and Multi-Wire Drift Chamber respectively. The number in brackets beside the Cherenkov counters are the mediums refractive index: if no value could be found the general value at STP was given. Without exception the hodoscope used was always a plastic scintillator. If the same equipment was used in multiple measurements, one of the symbols $*$, † or ‡ is used to indicate the detector used.
⋆ Information translated from Russian to the best of the author's ability.

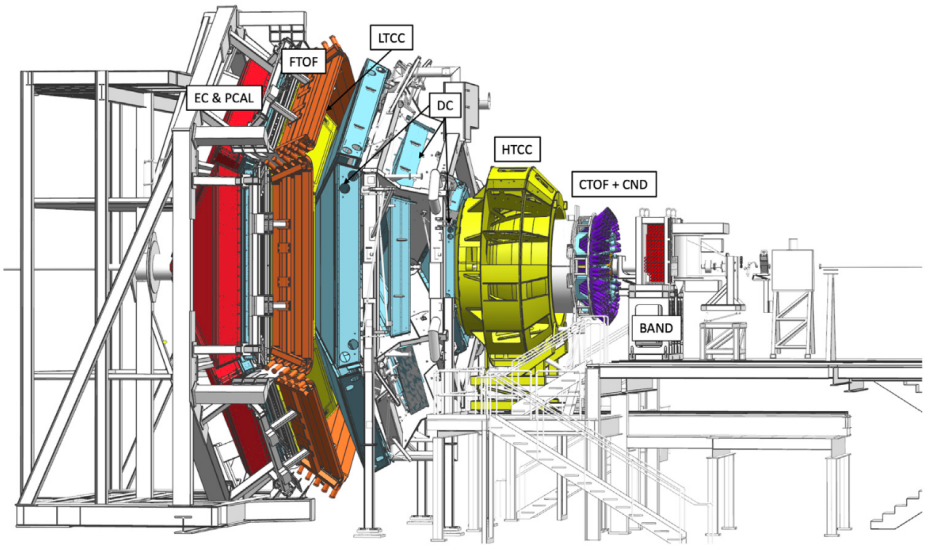

Fig. 3.12: Schematic of the CLAS12 detector located in JLab Hall B. The beam enters from the right and impinges on the target located just before BAND. The entire CLAS12 detector extends for 13 m. Each detector labelled is described in the text. Figure taken from [270].

dry carbon dioxide gas. The LTCC system detects charged pions at greater than 3.5 GeV and is made up of 4 boxes filled with perflubutane (C_4F_{10}) that were previously used in CLAS. These were refurbished, with the PMTs coated with a wavelength shifter to better match the detector's quantum efficiency. A Ring Imaging Cherenkov (RICH, [274]) detector supports the identification of kaons from pions between 3-8 GeV, using aerogel as a medium. A segmented plastic scintillator system measures the time-of-flight (TOF, [275]) from the target, again supporting particle identification, with a minimum timing resolution of 155 ps. A lead-scintillator sampling calorimeter [276] is placed at the back with a spatial resolution of 2 cm, performing final energy measurements of the FD.

A forward tagger (FT, [277]) works in the very small polar angle ($2.5° \leq \theta \leq 4.5°$) region to detect very forward scattered electrons and can be used for electroproduction measurements. It is composed of a crystal calorimeter, a micro-strip gas tracker and a scintillator hodoscope. This system can be turned on or off depending on the measurements being made. If turned off, extra shielding can be added to reduce background in the FD DCs.

Particles scattered between $35° \leq \theta \leq 125°$ are detected in the CD, which is magnetised by a solenoid electromagnet, still having a 360° acceptance in the azimuth. The central vertex tracker (CVT) contains a silicon vertex tracker [278], a form of semiconductor detector, and a barrel micromegas tracker [279], a development on the wire chamber, that provides very high momentum resolution. A TOF system [280], once again using plastic scintillator, provides particle identification with a 80 ps timing resolution. A central neutron detector (CND, [281]) is positioned behind the TOF detector to measure the energy deposited by neutrons. A final neutron detector is positioned 3 m downstream of the target to measure backward neutrons. The back angle neutron detector (BAND, [282]) uses scintillator TOF and also a

charged particle veto to measure neutrons in a 155° to 175° polar angle.

3.4 Summary

The data collected from the electron experiments described in this chapter have been extensively used in order to better constrain the removal energy systematic for T2K oscillation analyses. Obviously these experiments are making useful measurements in their own right, however the use of electron scattering data will be vital for future neutrino measurements.

While SK was also summarised, more information regarding the calibration of the detector (which is prudent to this thesis) will be given at the beginning of chapter 6.

Chapter 4

Electron Extension to NEUT

Ph'nglui mglw'nafh Cthulhu R'lyeh wgah'nagl fhtagn.

H. P. Lovecraft (The Call of Cthulu)

This chapter describes the implementation of an electron scattering extension to the Benhar-Fantoni spectral function in NEUT, and makes the first comparisons to electron scattering data and output from other event generators, GENIE [283] and EWRO [284] (the electron generation within the NUWRO [285] generator). Whilst NEUT was developed for atmospheric measurements in the Kamiokande family and grew organically from there, the others come from other motives. NUWRO is a theory-driven generator, developed to understand the impact of various theory implementations of neutrino interactions. As such, new models are often first included into this generator. GENIE on the other hand, is an international collaboration whose leading mission statement is to supply the experimental neutrino community with a Monte Carlo generator. Both of these latter generators are open source and are therefore used more widely in neutrino experiments.

This will cover the conversion of neutrinos to electrons, and the different ways of including them into generators. This extension will later be used in chapter 5.

4.1 Electron Scattering for Neutrino Physics

Uncertainties in the modelling of neutrino-nucleus interactions continue to be one of the biggest systematic uncertainties in neutrino physics. Until fairly recently this has been low priority due to being overshadowed by statistical uncertainty, however current and future experiments will no longer be limited by this lack of events. The total systematic uncertainty on the electron neutrino sample has to be improved to (maximum) the 3% level, with a DUNE study showing that an uncertainty increase in this sample from 1% to 3% doubles the exposure time required to make a CP violation measurement [286]. This is shown in Fig. 4.1.

Oscillation spectra are a function of the true neutrino energy, however experimentally

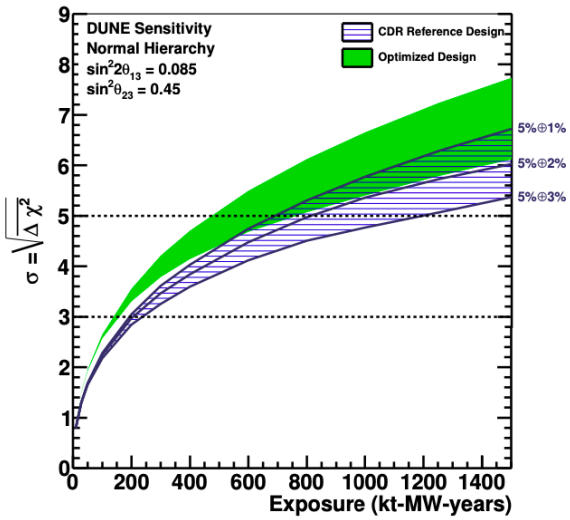

Fig. 4.1: DUNE sensitivity to a CP violation discovery as a function of the total exposure time. This is the sensitivity for 50% of $\delta_C P$ values. $5\% \oplus 3\%$ refers to the total uncertainty on ν_μ and ν_e sample respectively. The bands represent beam designs: the blue hash is the design as in the conceptual design report, the green is an optimised design. Figure taken from [286].

this can only be reconstructed from the kinematics of the outgoing particles: these depend on the interaction mechanism. Neutrino experiments, such as T2K, have energies that range from a few 100 MeV to a few GeV; in this region many different interactions can contribute to the cross-section. In order to make a measurement, one has to constrain a nuclear model, the nuclear response to the probe, the interaction mechanism and final state interactions (FSI) that alter the final state topology. The nuclear model and FSI should be identical in electron scattering experiments, whilst the fact that both e- and ν-scattering are electroweak interactions means that important information about neutrino processes can be obtained using electrons. This has previously been seen in section 2.1.1, where the high interaction cross-section and more refined kinematic reconstruction provided strong constraints on the vector part of the lepton-nucleus cross-section.

Many groups have indicated that if neutrino-nucleus interactions are not modelled correctly, it can lead to large biases in the measurement of neutrino oscillation parameters [287–289]. Of particular interest for this thesis is the impact of the removal energy, with T2K predicting that a 20 MeV shift in the removal energy imparts a 20% and 40% bias on $\sin^2\theta_{23}$ and Δm^2_{32} [290] respectively. Experiments can constrain this with the use of a near detector, however these cannot account for unseen energy in the final state nucleus. The near detectors also suffer from limitations in detector acceptances and thus still rely on a prediction of particle kinematics; this is compounded with the difficulty of detecting certain particles, such as neutrons. These are important in CP-violation (CPV) studies as charged-current neutrino interactions proceed via

$$\nu + n \to \ell^- + p\,,$$

whereas charged-current *anti*neutrino interactions are typically

$$\bar{\nu} + p \rightarrow \ell^{+} + n\,;$$

these final state neutrons need to be characterised in order for a precise CPV measurement, though are notoriously difficult to detect and have not been extensively studied[1].

Water Cherenkov detectors are only sensitive to the outgoing charged lepton and pions. In order to measure oscillation spectra, one must find a proxy for the true energy which, in the case of the two-body charged current quasi-elastic interaction, can be estimated with the reconstructed energy using

$$E_{\mathrm{QE}}^{rec} = \frac{2m_N E_B + 2m_N E_\ell - m_\ell^2}{2(m_N - E_\ell + k_\ell \cos\theta_\ell)}\,, \tag{4.1}$$

where E_{QE}^{rec} is the reconstructed neutrino energy, m_N is the mass of the struck nucleon and E_B is the single-nucleon separation energy. Here, E_ℓ and k_ℓ are the energy and momentum of the outgoing lepton, m_ℓ is its mass, and θ_ℓ is the angle between the outgoing lepton and the neutrino beam. In a perfect charged-current quasi-elastic (CCQE) case this method works well, however as has been stated experiments can only measure the final state topology. Multiple processes can contribute to the CC0π (charged current with no pions) final state, which in the case of no final state interactions (FSI, section 2.3.3) would be a purely CCQE sample. Non-CCQE, such as resonant events or two-nucleon knockout, can contribute if the pion is reabsorbed or the second nucleon is not detected: this causes the proxy to be far from the correct value [291, 292]. It also assumes a constant removal energy, however as is seen in the spectral function (SF, section 2.2.3) the nucleon removal energy is drawn from a shell-like model with a range of E_B. The effect of different nuclear properties and other interactions on the reconstructed energy is shown in Fig. 4.2. The need to test these reconstruction methods becomes clear with a recent study by the CLAS and e4ν collaborations, who show that for carbon only 30-40% of events correctly reconstruct to within 5% of the beam energy [293]. This percentage reduces with energy and atomic number, as only 20-25% of iron interactions correctly reconstruct. This latter study highlights the importance of electron scattering acting as a vital testbed for validating both energy reconstruction techniques (using beams of known energy) and nuclear models.

It is worth a quick aside on the reconstruction techniques observed by calorimetric detectors, such as the liquid argon and magnetised iron detectors. These can in principle reconstruct the entire energy of an event (taking into account the removal energy) with

$$E_{cal} = E_\ell + T_N + E_B\,, \tag{4.2}$$

where T_N is the kinetic energy of the struck nucleon. Note, this is again for an event with no pions, but this process could be applied to non-CCQE events. Although the full final state could be detected, difficulties in the reconstruction of neutrons and neutral mesons can lead

[1]Though the ANNIE experiment will make the first measurement of neutron yields from neutrino interactions.

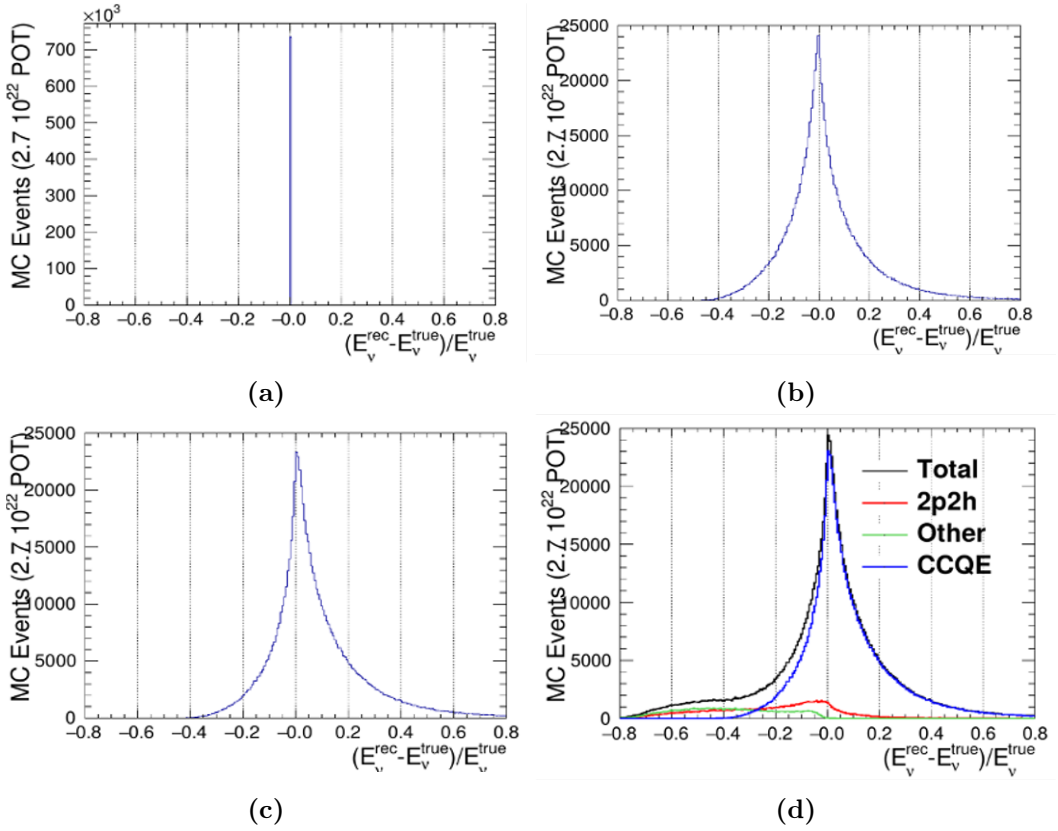

Fig. 4.2: Effect of nuclear structure on E^{rec}_{QE}. **(a)** shows the perfect case for CCQE only on a stationary nucleon. The Fermi motion of the nucleons causes a smearing of the perfect case in **(b)**. The removal energy introduces a bias seen in **(c)**. **(d)** shows the proxy for different interaction mechanisms, clearly the proxy of E^{rec}_{QE} is not good for non-CCQE processes. Figures taken from [294].

to an underestimation of the neutrino probe energy [295].

4.1.1 Introducing Electrons

Electrons and neutrinos differ only in their interaction at the primary vertex: electrons exchange a photon whilst neutrinos interact via W and Z bosons. The electromagnetic interaction is purely vector, whereas the weak interaction proceeds via vector and axial currents. However, as they are both part of the same electroweak processes, many of the difficulties in making measurements with neutrino interactions can be inferred from electron interactions. Considering this, there are some broad benefits to electron scattering:

1. **Mono-energetic beam.** The mono-energetic beam allows a precise knowledge of the incoming beam, thus the kinematics of the interaction. These beams can be used in order to test energy reconstruction algorithms, thereby testing the proxies often used for initial neutrino energies (such as the reconstructed neutrino energy). Importantly for chapter 5, this also means the three-momentum transfer, $\mathbf{q_3}$, can be calculated accurately.

2. **Identifying interactions.** The interaction type responsible for features in the data are easy to identify, such as the quasi-elastic peak; this peaks at $Q^2/2m_N$, where Q^2 is the four-momentum transfer squared and m_N is the mass of the struck nucleon. This is difficult to calculate with neutrino scattering, as it relies on the precise reconstruction of the initial energy. Due to the point above, this is much easier to achieve in electron scattering.

3. **Data availability.** There is lots of electron scattering data available, much of which are described in section 3.3.1. The much higher interaction cross-section ($\mathcal{O}(10^7)$ larger) also means the data have much lower statistical uncertainties, leading to much tighter constraints on the underlying models.

4. **Nuclear models.** In neutrino scattering the nucleus is used as a 'detector' for a beam of unknown properties, whereas in electron scattering the nucleus is the object of study. This is again a product of the known beam energy, and this subtle difference in philosophy makes electrons a useful tool.

Due to the reasons outlined above, electrons have been crucial in the development of scattering theory. The importance of electrons in describing the vector part of the neutrino interaction has been well described in section 2.1.1 through the conserved vector current (CVC) hypothesis, however they could also participate in measuring the axial component. In leptonic (or semi-leptonic) processes, there is always a component of weak interactions. In the case of electron scattering this contribution is masked by the much stronger electromagnetic interaction, however the electron can still exchange a Z^0 in place of photon. In parity violating electron scattering the axial characteristics of the weak interaction can be explored, thus could provide constraints with a probe with more defined kinematics [296, 297].

Of course, electrons are not perfect substitutes for neutrino scattering. As has been discussed, neutrinos have an axial component, whereas electrons are purely a vector process. The former interaction is mediated by W and Z bosons whose masses give rise to a constant propagator term, electron interactions on the other hand exchange the massless photon. This masslessness of the photon leads to a Q^{-4} in the cross-section, causing the electron scattering distributions to be extremely forward peaked (whereas neutrino interactions are more transverse). Another sticking point is that a charged current process is purely isovector, whereas electron scattering has both isovector and isoscalar contributions. Neutrinos can also excite different nuclear states than electrons, so these must be taken into account: although the decay of any resonances is necessarily the same.

These differences must be carefully considered, however the use of electrons is still considered highly important to constrain neutrino interactions (the hadronic response, Pauli blocking and short-range correlated pairs are all very similar). It is therefore important for event generators to include some form of electron scattering simulation.

4.1.2 Event Generators

Without event generators, the measurement of oscillation parameters would not be possible. Due to the unknown nature of the neutrino energy before its interaction, we rely on generators to make full predictions of the outgoing particles over a variety of interaction mechanisms, and provide the kinematics to the detector simulation. Ideally, one would have a fully consistent input theory which covers the whole energy range for each interaction, predicting all outgoing particles for every scattering target. Of course, such a model does not currently exist: this is where event generators come into play.

Generators treat models for each interaction independently and combine them to make a full cross-section prediction. These models tend to take the most up-to-date theory understanding[2] and tune them to scattering data, and therefore are a combination of theory and empirical extrapolation. Assumptions have to be made when employing the models in order to make computations tractable, with interaction parameters supplied to oscillation fitters as nuisance parameters. This can lead to the significant biases described in the previous sections. One example of such an assumption is the impulse approximation (IA, section 2.2), which separates the ground state from the interaction vertex and sums them incoherently. Some help can be provided with measurements of the final hadronic state, but this can provide no separation between the fundamental interaction and final state interactions.

Historically the focus has been on modelling the $\sim$ 1 GeV region [298], where QE is dominant and the simple 2-body reconstruction techniques outlined above can be applied. However, with experiments such as DUNE using a broader beam energy (1-6 GeV), and Hyper-Kamiokande and JUNO planning atmospheric neutrino measurements with energies reaching $\sim$ 20 GeV, it is becoming vital for better models at these higher energies: though this is beyond the scope of this thesis.

[2]Though typically it takes quite some time for a new theoretical model to make an appearance in generators, but this is a very different discussion.

As the bulk of the signal from T2K is from QE, this thesis focuses on constraining our model of this interaction with electron scattering data. Due to the simplicity of the interactions and the similarities between them, neutrino event generators should be able to predict QE electron scattering measurements and use these to constrain their neutrino models: reducing the uncertainty to purely the axial contribution. The rest of this chapter will focus on the implementation of a QE only electron scattering mode in the NEUT generator.

4.2 Turning Neutrinos into Electrons

In order to provide useful constraints to neutrino interactions, it is important for the electron implementation to follow as much of the prescription of the neutrino case as is possible. The model originally followed the implementation of the Benhar-Fantoni SF in NEUT, as the description of the ground state and the final state interactions should be identical in both cases. However, as the ground state is independent of the interaction, any ground state model can used as a nucleus for electron scattering.

Before continuing, it is worth describing the individual electron- and neutrino-nucleon cross-sections. The inclusive electron-nucleon scattering cross-section can be completely described with two structure functions ($F^e_{1,2}$)

$$\frac{d^2\sigma^e}{dxdQ^2} = \frac{4\pi\alpha^2}{Q^4}\left[\frac{1-y}{x}F_2^e(x,Q^2) + y^2F_1^e(x,Q^2)\right], \tag{4.3}$$

where α is the fine structure constant, $Q^2 = \mathbf{q}^2 - \omega^2$ is the four-momentum transfer squared ($\mathbf{q}$ and ω are the three-momentum and energy transfers respectively), $y = \omega/E_e$ is the fraction of energy lost by the electron, and finally $x = Q^2/(2m\omega)$ is the Bjorken scaling variable[3].

Neutrino interactions occur in a very similar way. This has been described in much more detail in section 2.1.1, but reproduced in a similar form to equation 4.3:

$$\frac{d^2\sigma^\nu}{dxdQ^2} = \frac{G_F^2}{2\pi}\left[\frac{1-y}{x}F_2^\nu(x,Q^2) + y^2F_1^\nu(x,Q^2) - y(1-y/2)F_3^\nu(x,Q^2)\right] \tag{4.4}$$

where G_F is the Fermi coupling constant, $F^\nu_{1,2}$ are very similar to the electron ones and are parity conserving, whilst F^ν_3 is a new parity-violating structure function. If we take the elastic scattering limit (*i.e.* where $x = 1$), the parity conserving functions reduce to the Dirac and Pauli form factors described in section 2.1.1. This formula can be used for both CCQE and neutral current elastic (NCEL, section 2.1.2) interactions, this will be explored further in the following section.

[3]This formula is only valid when $Q^2 \gg m$, otherwise the structure functions interact in a much more complicated way.

4.2.1 Neutral Current

The connection between electrons and neutrinos has been extensively stated, therefore it is possible to use the framework already established for neutrino interactions for electron scattering. This is also preferred, as will be discussed more in section 4.2.4. However, one must be careful with the choice of model used for this framework; as T2K's main signal process is CCQE, it would make sense to use this as a base. Charged-current interactions are purely isovector, as the exchange of a charged boson is associated with an isospin $T = 1$. It is important to remember the proton and neutron form part of an isospin (nucleon) doublet of

$$\psi = \begin{pmatrix} p \\ n \end{pmatrix} , \tag{4.5}$$

i.e. the proton can be considered a nucleon with $T_z = +\frac{1}{2}$ and the neutron a nucleon with $T_z = -\frac{1}{2}$. Thus the charged-current process implies an isospin change of $|\Delta T_z| = 1$ where the neutron (proton) turns into a proton (neutron), hence the isovector nature.

The weak exchange bosons form a triplet state under the SU(2) group of isospin, with charged W bosons and the neutral exchange boson (Z^0). In the neutral case the z-component is 0, thus in order to construct the interactions one must consider both isovector and *isoscalar* contributions to the interaction vertex. Electromagnetic interactions are the same, where the struck nucleon does not change. The effect of having different isoscalar and isovector components has not been studied and could have a large impact, thus to be cautious neutral current interactions must be used as a framework for electron scattering.

This connection between neutral current weak interactions and electromagnetic interactions should not come as a surprise. These interactions are unified under SU(2)×U(1) describing electroweak theory. The fields in electroweak theory are the weak isospin fields W_1, W_2 and W_3 (weak isospin labelled T) and the weak hypercharge field B (labelled Y_W). In spontaneous symmetry breaking the W_3 and B combine to make the physical Z^0 and γ via

$$\begin{pmatrix} \gamma \\ Z^0 \end{pmatrix} = \begin{pmatrix} \cos\theta_W & \sin\theta_W \\ -\sin\theta_W & \cos\theta_W \end{pmatrix} \begin{pmatrix} B \\ W_3 \end{pmatrix} , \tag{4.6}$$

where θ_W is the weak mixing angle[4]. For completeness, the W_1 and W_2 combine to make the massive $W^{\pm}$ via

$$W^{\pm} = \frac{1}{\sqrt{2}}(W_1 \mp iW_2) . \tag{4.7}$$

[4]Under this, the electric charge arises with the combination of $Q = T_3 + \frac{1}{2}Y_W$.

4.2.2 Coupling Constant

The weak interactions are mediated by the massive $W^{\pm}$ and Z^0 bosons[5], whilst EM interactions are mediated by the massless photon. Due to the masslessness, there is a $1/Q^2$ in the propagator term (one on each vertex) giving rise to the Mott cross-section, whereas the massive weak bosons have constant propagators. In the $e4\nu$ collaboration, they reweight their electron events by $1/\sigma_{Mott}$ in order to compare to neutrino scattering. In our case, to turn neutrinos into electrons we must multiply the cross-section by

$$\frac{\sigma_{Mott}}{\sigma_0} = N\frac{\alpha^2}{G_F^2 Q^4}\,, \tag{4.8}$$

where σ_0 is the neutrino cross-section, N is a normalisation factor (in this case it is $8\pi^2$)[6] and the other terms have been described above. This is easily calculated by comparing equations 4.3 and 4.4. This dependence on Q^4 causes the electron scattering distributions to be very forward peaked, as is clear in Fig. 4.3, and for any given energy the electron events are concentrated at a low momentum transfer. The cause of this forward peak is obvious by examining a slightly different form of the Q^2 equation from section 2.1

$$Q^2 = -2EE'(1-\cos\theta)\,, \tag{4.9}$$

where θ is the scattering angle, and E and E' are the incident and scattered electrons respectively: this is clearly different to the more transverse reactions of neutrinos.

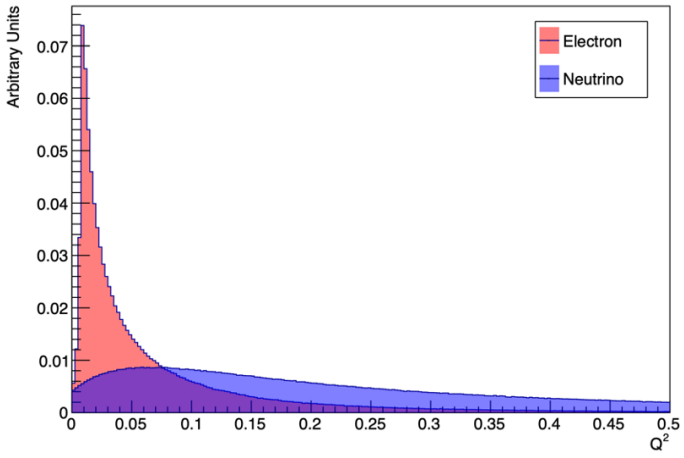

Fig. 4.3: Comparison of the Q^2 distributions for neutrinos and electrons, each normalised to the area. The electron distribution is very forward peaked due to the Mott cross-section arising from the massless propagator.

[5]The Z has a mass slightly different than the W's due to the spontaneous symmetry breaking. This is given by $m_Z = \frac{m_W}{\cos\theta_W}$.

[6]The size of this depends on which terms are absorbed into the lepton and hadron tensors.

4.2.3 Coulomb Correction

For an atom with atomic number Z greater than one, one must take into account the effect of the electrostatic field on the incoming and outgoing leptons: these are known as Coulomb corrections. The size of this correction depends on the size and nucleon composition of the target nucleus. The full treatment is complex [299] and the effective momentum change should be a local quantity, but for our case it is sufficient to treat the energy change of incident/scattered leptons relating to the average Coulomb potential. This can be applied simply during event generation using

$$E_{eff} = E_0 + |V_{eff}| \quad \text{and} \quad E'_{eff} = E' - |V_{eff}|\,, \tag{4.10}$$

for the incident and scattered electron energy respectively, where $E_0^{(\prime)}$ is applied to the incident (scattered) particle, and $|V_{eff}|$ is the effective Coulomb potential.

Ideally experimental values will be used for $|V_{eff}|$, which are determined through quasi-elastic electron and positron scattering; the nuclei that experimental data are available for are summarised in Table 4.1. If experimental values are not available, the effective momentum approximation (EMA) can be used in order to extract the value for other nuclei. The electrostatic potential ($V(r)$) for a particular nuclei with mass number A can be written as

$$V(r) = \frac{3\alpha Z}{2r_c} + \frac{r\alpha Z}{2r_c^2} \tag{4.11}$$

where r_c is assumed to be the radius of a uniform charge distribution. This can be calculated with the equation

$$r_c = [1.1A^{1/3} + 0.775A^{-1/3}] \tag{4.12}$$

which gives a value in femtometres (fm). The effective potential (V_{eff}) felt by an incident or outgoing electron can be described using a slightly modified version of the above potential,

$$V_{eff} = -0.8V(r=0) = -0.8\frac{3\alpha Z}{2r_c}\,. \tag{4.13}$$

The values of $|V_{eff}|$ agree with the experimental values within errors [300]. Here the EMA is only applied to electrons, however this is also relevant for the outgoing lepton in charged-current neutrino scattering (and can be neglected for neutral current). For T2K, this is applied during the oscillation analysis as a global shift in the lepton distribution, but is not present in the event generation.

This scattering process is a 1p1h (1-particle 1-hole) interaction, and as a result the effective potential can be altered upon the ejection of the struck nucleon. With neutrons this is not an issue, as only the protons contribute to the electrostatic potential. If the probe interacts with a proton, the outgoing effective potential is reduced by

$$|V_{eff}^P| = \frac{Z-1}{Z}|V_{eff}|\,. \tag{4.14}$$

	Experimental [MeV]	EMA [MeV]	r_c [fm]
$^{12}_{6}$C	3.1 ± 0.25	3.6	2.86
$^{16}_{8}$O	3.4	4.5	3.08
$^{27}_{13}$Al	5.1	6.3	3.56
$^{28}_{14}$Si	5.5	6.7	3.60
$^{40}_{18}$Ar	6.3	7.8	3.99
$^{40}_{20}$Ca	7.4 ± 0.6	8.7	3.99
$^{48}_{20}$Ca	7.4 ± 0.6	8.2	4.21
$^{50}_{23}$V	8.1	9.3	4.26
$^{56}_{26}$Fe	8.9 ± 0.7	10.2	4.41
$^{58}_{28}$Ni	9.8	10.9	4.46
$^{90}_{40}$Zr	11.9 ± 0.9	13.5	5.07
$^{154}_{64}$Gd	15.9 ± 1.2	18.2	6.09
$^{197}_{79}$Au	18.5	20.9	6.53
$^{208}_{82}$Pb	18.9 ± 1.5	21.3	6.65

Table 4.1: Size of the Coulomb corrections, $|V_{eff}|$, used in the generation of 'pseudo-electrons', comparing both the experimental and effective momentum approximation values. r_c is the calculated charge radius. Experimental values with errors taken from [299], without errors are from [300].

The above is a first-order effect, but there are higher order effects for heavier nuclei, which is known as focusing. Due to the attractive potential of the nucleus, the incoming electron's wave function will be focused toward the nucleus. This enhancement of the cross-section can be described by

$$F_{foc} = 1 + \frac{|V(0)|}{E_0}\,, \tag{4.15}$$

where F_{foc} is the focusing factor. Any EMA corrected cross-section should be multiplied by F_{foc}^2, as the focusing enters the equation quadratically. This effect is reversed for a positron beam.

The implementation followed here is slightly different to the original form of the EMA. Equation 4.15 works well as an *average* focusing factor, taking into account different focusing strengths of different areas of the nuclear potential. This strength also does not fall off in the transverse plane. Equation 4.11 on the other hand, caused the EMA to under-predict the cross-section. This is due to the nucleons forming an extended distribution rather than concentrated at the centre, so the potential 'felt' is lowered. The strength of this also depends on how far off axis the beam strikes the nucleus. Therefore, a factor of 0.8 is included in the calculation (equation 4.13), bringing the EMA more in line with experimental data.

4.2.4 Form Factors

The final step to be taken into account is the nucleon form factors. Form factors encapsulate properties of an interaction without understanding all of the underlying physical processes. In our case, an electron scattering off a nucleon is a very complicated calculation involving interactions between a sea of quarks and gluons: this cannot be completed from first principles. This information is 'hidden' in the form factors by providing a suitable matrix element for the calculation.

The vector form factors for electron and neutrino scattering are intrinsically linked by vector current conservation (CVC), thus codes for both of these electrons should be generated in the same way. This means that updates from electron scattering can be supplied to directly update the neutrino form factors.

It is a fairly simple process to convert the form factors from a weak process to an electromagnetic one. As the form factors in section 2.1.1 have been written in Sach's form, one must only change the electric and magnetic form factors of the proton and neutron. In the weak case, the probe 'feels' a mixing between the different nucleons. In contrast, the electromagnetic probe only encounters the distribution of the electric and magnetic fields, and the form factors can be simply written as

$$G_E^V = G_E^{p,n} \qquad \text{and} \qquad G_M^V = G_M^{p,n}\,. \tag{4.16}$$

The electromagnetic interaction is purely vector, as opposed to have a contributing axial component. Therefore these can simply be set to 0 in order to remove their impact,

$$F_{A,P} = 0\,. \tag{4.17}$$

The strange contribution to the form factors also needs to be removed, as there is no mixing between the generations in the electromagnetic interaction. However, as the strange component often appears only in the form factors, these should already be accounted for in the above prescription. For completeness, the strange axial form factor should be set to 0, *i.e.*

$$F_A^s(Q^2) = \frac{\Delta s}{(1 + \frac{Q^2}{M_A^2})^2} = 0\,. \tag{4.18}$$

4.3 NEUT Implementation

The implementation of electron scattering in NEUT originally followed the prescription set out by the existing Benhar-Fantoni SF, described in section 2.2.3, and much of the framework was reused. The electron model can be expanded to other models, which will be discussed in section 4.5.1. For simplicity, only the SF implementation is described here, however all other models follow the same basic principle.

4.3.1 NEUT Fundamentals

NEUT, like most other event generators, works via rejection sampling. This is a Monte Carlo technique which is able to sample data from a sophisticated function (*i.e.* one from which a probability distribution function cannot be made) - a full mathematical description is given in Appendix A.1.

The basic event generation algorithm is as follows:

1. Select a neutrino energy based on the pre-calculated $\sigma(E_\nu)$ tables.
2. Randomly select an initial state nucleon momentum and removal energy from the spectral function $S(E_B, \vec{p_i})$, using rejection sampling.
3. Calculate the centre-of-mass energy, E_{COM}. This must satisfy the condition: $E_{COM} > m_N + M_\ell$, where N is the struck nucleon and ℓ is the outgoing charged lepton. If not, go back to step 2. If fulfilled, boost into the COM frame.
4. Generate a random direction for the outgoing nucleon and lepton (constrained by energy and momentum conservation).
5. Boost back to the lab frame.
6. Apply Pauli blocking: if p_f is lower than the Fermi surface, reject the event and go to step 2.
7. Calculate q and $\tilde{q} = (\tilde{\omega}, \vec{q})$, where $\tilde{\omega} = E_{\mathrm{p}'} - E_{\mathrm{p}}$.

8. Calculate the event weight from the cross-section formula in equation 4.19 - the leptonic-hadronic tensor contraction, $L_{\mu\nu}H^{\mu\nu}$, is calculated using $\tilde{\omega}$.

9. Draw against the maximum cross-section at E_ν using this weight to decide whether to accept this event using rejection sampling. If not accepted, go to step 2.

10. Check whether the interaction is in the correlated tail of the Benhar SF. If so, add a second nucleon with equal and opposite momentum[7].

To reiterate once again, this process is only for the Benhar SF, and will be slightly different for other models (such as step 10, which will not be the case for RFG models).

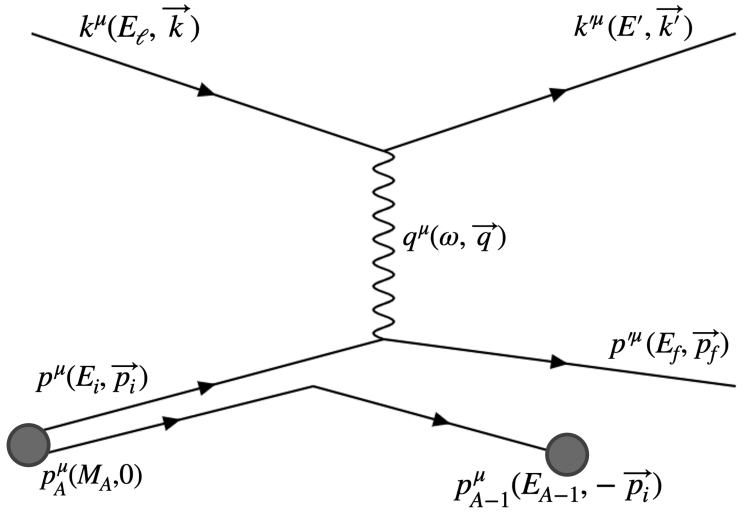

Fig. 4.4: Feynman diagram for the 1p1h interaction. The four-vectors are named as follows: the incident lepton is k^μ; the outgoing lepton, k'^μ; initial state nucleon, p^μ; final state nucleon, p'^μ; and the four-momentum transfer, $q^\mu = k^\mu - k'^\mu$. The nucleus and its recoiling daughter are p_A^μ and p_{A-1}^μ. Here, the E_i is the energy an initial nucleon would have with momentum $\vec{p_i}$. ℓ can be a charged or neutral lepton.

All the nuclear models available in NEUT can be described by spectral functions, describing the initial state nucleon distribution of the nucleus in terms of the nucleon momentum (Fermi momentum), $\vec{p_i}$, and the removal energy, E_B, required to liberate the nucleon. The total cross-section for a *neutrino* interaction is given by

$$\sigma_\nu = \int d^3p_i \int dE_B \int d^3k' \delta(\omega - M_A - E_B - E_{p'}) L_{\mu\nu}H^{\mu\nu} \frac{G_F^2 \cos^2\theta_C}{8\pi^2 E_\ell E' E_{\mathrm{p}'} E_{\mathrm{p}}} S(E_B, \vec{p_i}) \,, \quad (4.19)$$

where G_F is the Fermi coupling constant, θ_C is the Cabibbo mixing angle, $L_{\mu\nu}H^{\mu\nu}$ is the contraction of the leptonic and hadronic tensors, $S(E_B, \vec{p_i})$ is the spectral function and the Dirac delta function imposes energy conservation. The removal energy is defined within the spectral function as

$$E_B = M_A + \omega - E_{\mathrm{p}'} \,. \quad (4.20)$$

[7]This is a first approximation of the secondary nucleon kinematics; the FSI effects are expected to be more important than getting exact kinematics.

The cross-section is slightly altered as the calculation is completed in the neutrino-nucleus centre-of-mass frame, thus a Jacobian, J_{CM}, is included. This Jacobian facilitates the difference in the cross-section due to a change in rest frame between the centre-of-mass and lab frames.

4.3.2 Beyond the Impulse Approximation

The preceding outlines briefly the inner workings of the NEUT generator for the SF, and this all remains in place for the electron mode. However, as stated in section 4.2, the neutrinos must be altered to run as electrons.

Within NEUT, the process described previously is used to convert neutrinos to electrons. As a summary, this is:

1. Use neutral current interactions as a framework.
2. Edit the coupling constant, accounting for the Mott cross-section and the massless propagator.
3. Apply a Coulomb correction accounting for the charge of the impinging particle.
4. Edit the form factors for electron scattering.

This is all automatically available upon choosing an electron as the incident particle at the generation stage. As this was built from the neutral current interaction from neutrino scattering, this implementation does not include the mass of the electron in the calculation of the kinematics. Due to the electron's small mass however, for a first pass this was not included as it would have a negligible impact on the electron predictions[8].

If only the corrections above were implemented, the electron predictions generated would not predict available electron scattering data with any reasonable success. This is a limitation of the IA of which NEUT is built upon. This approximation separates the lepton kinematics and the nuclear ground state, leading to the incident lepton sampling the same ground state regardless of its energy. This is not physical, and can be accounted for by applying an approximately linear correction to the ground state removal energy, ΔE_B, defined by

$$\Delta E_B = m\mathbf{q_3} + c\,, \tag{4.21}$$

where m and c are derived from fits to the data. The derivation of these constants will be explored in chapter 5.

4.3.2.1 Effects of the Massless Propagator

An important difference practically in simulating electrons versus neutrinos is the difference of the propagator, a photon against the Z^0 boson, leading to the inclusion of the four-momentum transfer into the cross-section. This leads to a very forward peaked distribution,

[8] For T2K kinematics, a 600 MeV electron beam including the electron mass would alter the electron momentum by $\sim 0.00004\%$.

but causes practical issues during simulation as Q approaches 0. There are 2 ways to deal with this during the simulation:

1. Simulate events at a particular scattering angle (or window) which cannot tend to 0. This is the approach taken in NuWro.
2. Simulate events over the full solid angle, placing a threshold Q^2 under which events are not simulated. This is the approach taken by GENIE.

Due to the limited framework of NEUT, either situation would result in a large reduction in efficiency. NEUT throws events isotropically around the interaction vertex, and the events are selected dependent on the cross-section once the full event has been generated. Though the former option (generating in a small $\mathbf{q_3}$ or θ window) is technically possible, the generation would be incredibly inefficient and be completely dependent on the width of the window selected around the angle.

It was therefore decided to place a low Q^2 threshold on the event. Of course, if analysing a particular scattering angle, generating enough events will take the same length of time as the above method, but rather than throwing events away these are saved and multiple scattering angles can be examined. The value of the Q^2 cut will change based on the incident electron energy, as a too high choice of threshold could cut a significant number of events for lower energy electron beams. This will be discussed later.

4.4 Implementation Validation

This section will be split into two parts, one dealing with 'ad-hoc' electrons and one presenting a full electron prediction. Of course, these should produce similar results, and will be compared at the end of the section.

4.4.1 Counterfeit Electrons

As mentioned, NEUT has a rather restricted framework within which to work. The easiest way to implement an electron generator is to take the opposite method to the e4ν collaboration, and reweight neutrino data to give electrons. In this case, events are generated with neutrino kinematics (although the form factors have been altered to electromagnetic ones), with the outgoing lepton kinematics reweighted with the Mott cross-section (*i.e.* with a factor of $1/Q^4$) and the Coulomb effect felt by the outgoing lepton is included at the analysis stage. The initial Coulomb effect is included as an increase in energy to the incident beam. The effect of the Q^2 reweight on the lepton energy transfer is shown in Fig. 4.5.

Fig. 4.6 shows the NEUT electron predictions compared to electron scattering data, and also electron predictions from two other generators, NuWro and GENIE. Here the predictions have been artificially scaled in comparison to the electron data to show the position of the elastic peak. The NEUT and NuWro predictions give similar results of the peak position, as is expected with both using a SF based model (GENIE has been generated with

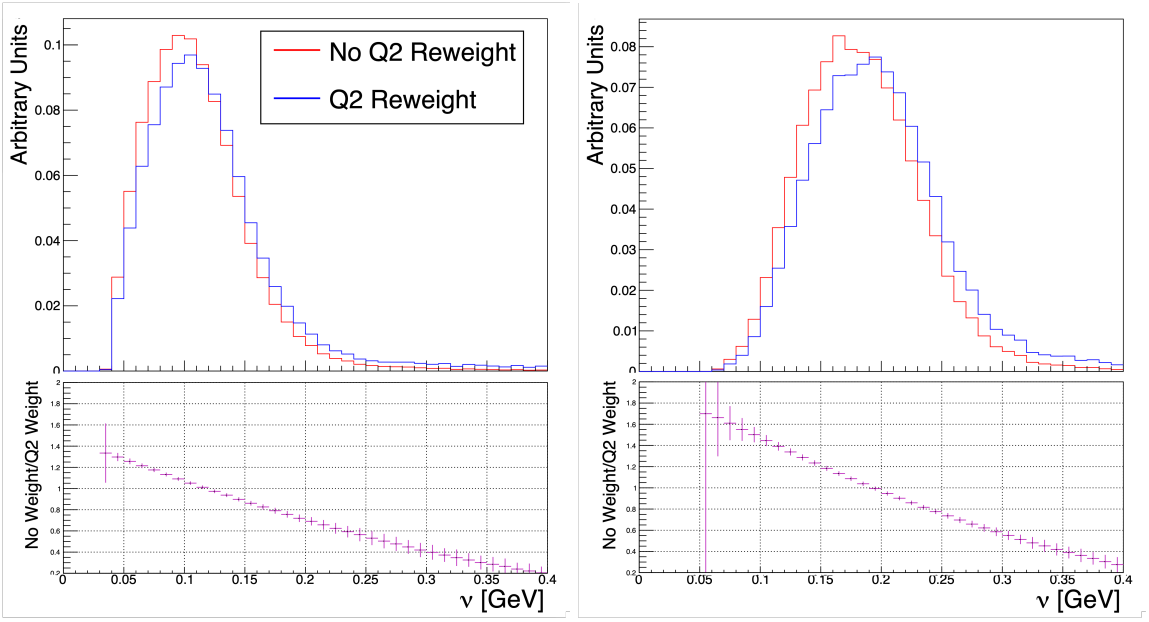

(a) **(b)**

Fig. 4.5: Effect of the Q^2 reweight on the lepton energy transfer, ν. Each of these is with a 620 MeV incident beam, over 2 scattering angles: **(a)** 36° and **(b)** 60°. The effect of the reweight is larger on higher scattering angles as the energy transferred between the lepton and the nucleus is larger.

SuSAv2, a relativistic mean field model). However, this does include two different beyond IA effects that one would expect might change the position of the peak between the two predictions, however these match to a high degree. This will be explored in chapter 5.

Fig. 4.7 shows the cross-section predictions for NEUT, NuWro and GENIE electron scattering. Whilst all predictions seem to be somewhat consistent with one another, with NEUT and GENIE producing the most similar results, NuWro seems to be slightly different. However, it should also be noted these predictions have been scaled down by a factor of 6 in order to match with the (e,e′) data. This discrepancy is likely due to using NUISANCE [302] to flatten the data from each generator. This software was built primarily to make neutrino comparisons and the updated methods in each generator for electron scattering has not yet been considered, and it is unlikely to produce realistic cross-section predictions. This could be why the NuWro predictions are so different, as this generates electron scattering events in a small angular region, whereas neutrino data tends to be generated over an entire solid angle.

As the important factor is the position of the elastic peak, no hard analysis on the overall cross-section prediction was completed for this method. However, as the overall normalisation matches well to the GENIE (and to some extent, NuWro) data, it adds some credibility to the elastic peak predictions, and their use in the following chapter. There does also seem to be some angular dependence on the cross-section, where lower angles under predict the data and higher angles over predict. This is not observed in the other generators, and could be due to NuWro and GENIE 'correctly' generating electrons, *i.e.* with the correct Q^2 distribution, rather than reweighting the neutrino four-momentum transfer distribution.

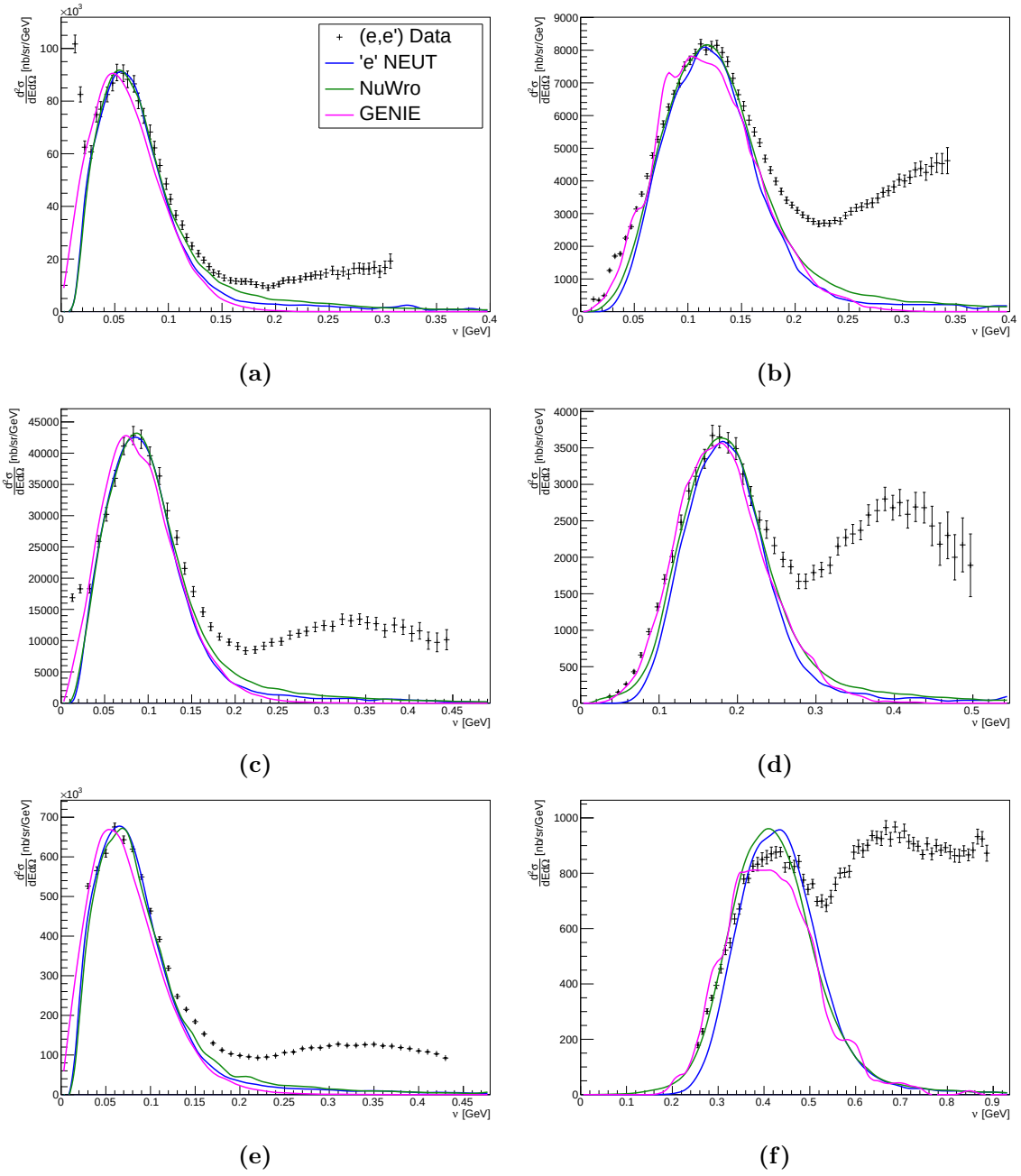

Fig. 4.6: NEUT electron scattering predictions against inclusive electron scattering data. NUWRO and GENIE predictions are also shown. The predictions have been scaled to match the normalisation of the data elastic peak, in order to show how each generator predicts said peak. Clearly, NUWRO and NEUT match each other closely, along with the data. The incident energy and scattering angle of each is: **(a)** 480 MeV and 36°; **(a)** 480 MeV and 60°; **(a)** 620 MeV and 36°; **(a)** 620 MeV and 60°; **(a)** 1500 MeV and 11.95°; **(a)** 1501 MeV and 37.5°. Data taken from [301].

This angular dependence is shown in Fig. 4.8.

As is clear, this method of producing electron scattering simulations is perfect for producing a prediction of the elastic peak, but is not so good at producing a full cross-section prediction. This is not a problem for the main analysis in this thesis, but is something that needs to be looked into in the future. This could be due to NUISANCE's ability to flatten electron predictions, though this does not explain the angular dependence of the NEUT electron predictions.

The benefit to this method is, however, the generation efficiency. As shown in Fig. 4.3, electrons are very forward peaked and to achieve a large enough sample at greater scattering angles is difficult. The pre-existing NUWRO and GENIE electron predictions take a substantial time to generate (particularly at higher scattering angles). Due to the more transverse nature of neutrino interactions, it is much easier (and quicker) to generate a large sample of events at higher scattering angles. This, in combination with its ability to predict the position of the elastic peak, is the reason this method was used for the analysis in chapter 5.

4.4.2 Authentic Electrons

The method in the previous section is the 'quick and dirty' generation, allowing us to have pseudo-electrons for a small amount of work and no great computational cost, whilst being able to predict the elastic peak. This is also an easy way for new generators to implement an 'electron scattering' model (if they have not done so already) in order to test their underlying ground state implementations.

However, it is apparent that having a fully implemented electron scattering mode built directly into the generator is an important milestone. This takes into account everything mentioned beforehand, with the Coulomb 'kick' applied during generation and also the events are weighted accordingly. As the SF uses cross-section tables for its accept/reject condition[9], there are two ways of dealing with this: generate events using the neutrino cross-section tables, or generate new tables for electron interactions.

4.4.2.1 Neutrino Cross-Section Tables

Ideally, one would have electron cross-section tables available to be sampled from, but the generation of such tables is not always an easy process - this is explored slightly more later. To begin with, the former possibility will be studied. As mentioned above, a lower Q^2 limit must be placed on the predictions in order to cut out those events whose cross-sections tend to infinity at lower energy transfers. Events of this style are generated by modifying the cross-section calculation to take into account the Mott cross-section, and using the set Q^2 threshold as the ceiling for the rejection condition. With these in place, this produces the Q^2 distribution expected for the massive leptons, *i.e.* very forward peaked. This is shown in Fig. 4.9, where the full distribution (over all angles) is compared to GENIE, and also at a particular angle compared to NUWRO.

[9]To reiterate, this is the premise behind rejection sampling.

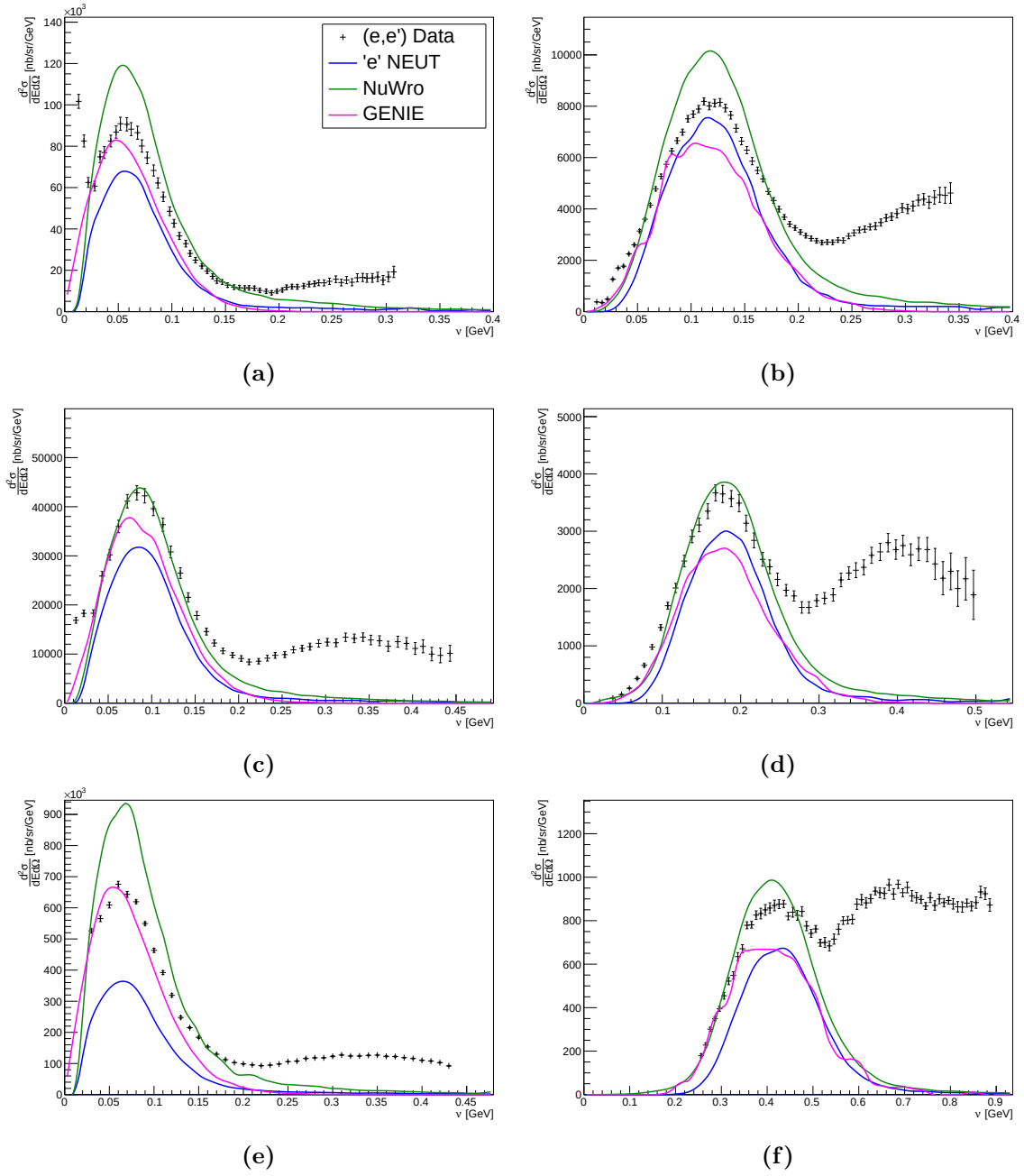

Fig. 4.7: NEUT electron scattering predictions against inclusive electron scattering data. NUWRO and GENIE predictions are also shown. These have been scaled to a cross-section from NUISANCE output. The overall normalisation between generators matches well, however these have been artificially reduced by a factor of 8 in order to match the data. The incident energy and scattering angle of each is: **(a)** 480 MeV and 36°; **(a)** 480 MeV and 60°; **(a)** 620 MeV and 36°; **(a)** 620 MeV and 60°; **(a)** 1500 MeV and 11.95°; **(a)** 1501 MeV and 37.5°. Data taken from [301].

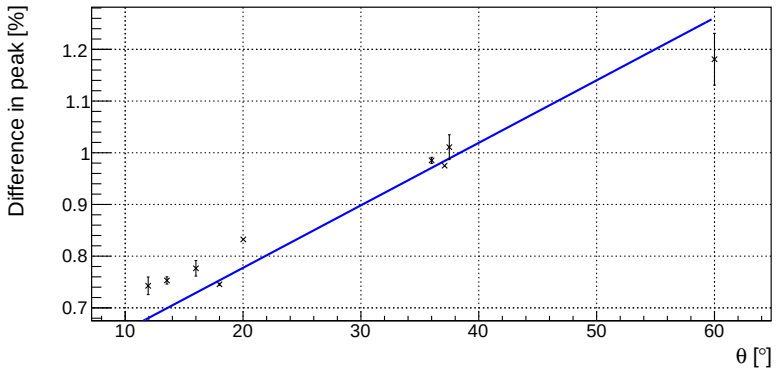

Fig. 4.8: Angular dependence of the overall cross-section scaling. Each data point is averaged over data with the same scattering angle. Those without errors contain a single data point.

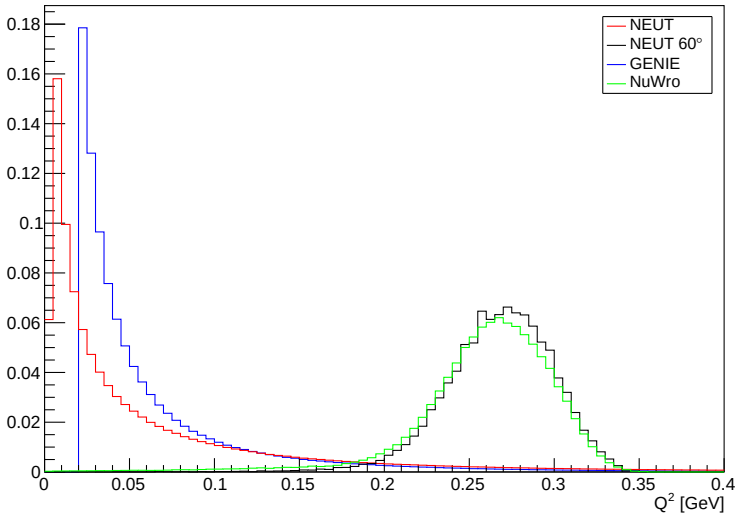

Fig. 4.9: Q^2 distribution of the NEUT and GENIE generators when generating with an electron cross-section. These have been normalised to an area of unity. The different lower bounds come from the different Q^2 thresholds. The GENIE and red NEUT lines are over all scattering angles, whilst NuWro and the black NEUT line are a 60° scattering.

However, this technique tends to produce energy transfer distributions that do not contain the width expected from the NuWro predictions, and those which the previous NEUT method produced. This is seen in the blue lines of Fig. 4.10, where the rise of the elastic peak matches well, but the tails do not. This shifts the position of the elastic peak to lower energy transfers, and once the beyond IA methods have been applied (Fig. 4.10 does not include this correction), it leads to a clear discrepancy in the elastic peak. Fig. 4.11 represents this clearly, where the blue NEUT predictions show a large offset from the other predictions. Of course, the method for moving beyond factorisation has used the previously stated NEUT predictions, and so it would be possible to derive an independent method which would fit these predictions. However, as the peak widths did not match the other models, this was not completed.

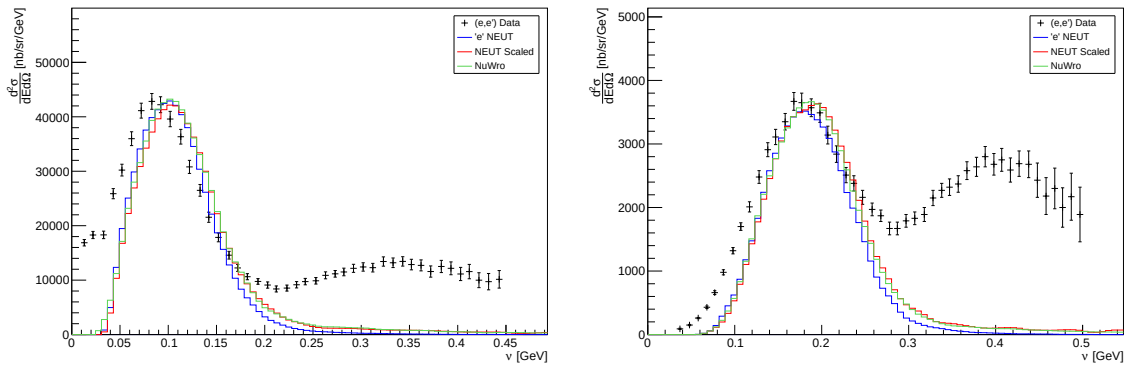

(a) **(b)**

Fig. 4.10: NEUT predictions using neutrino spectral function tables modified to return an electron cross-section. These are under the impulse approximation. These return predictions whose width does not match with other predictions. Data taken from [301].

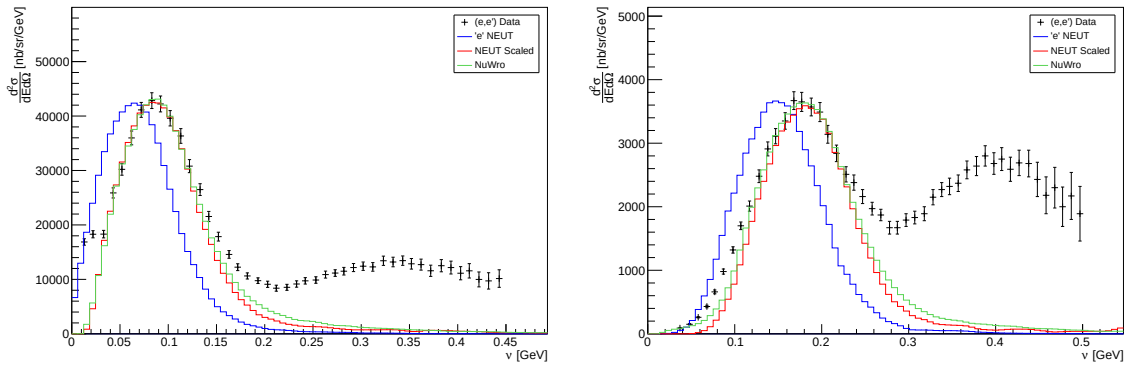

(a) **(b)**

Fig. 4.11: As in Fig. 4.10, however using beyond impulse approximation methods. Due to the problem with the peak width, this returns a large difference between predictions and the elastic peak. Data taken from [301].

It would also be expected that the choice of Q^2 cut would have an effect on the distributions obtained. However, as Fig. 4.12 shows, as long as the cuts are well below the kinematics of the event there is not a large effect. In this case, the cuts were placed at 0.01

and 0.02 GeV^2 with an incident electron energy of 620 MeV. Clearly, the different thresholds have very little effect on the overall kinematics of the event.

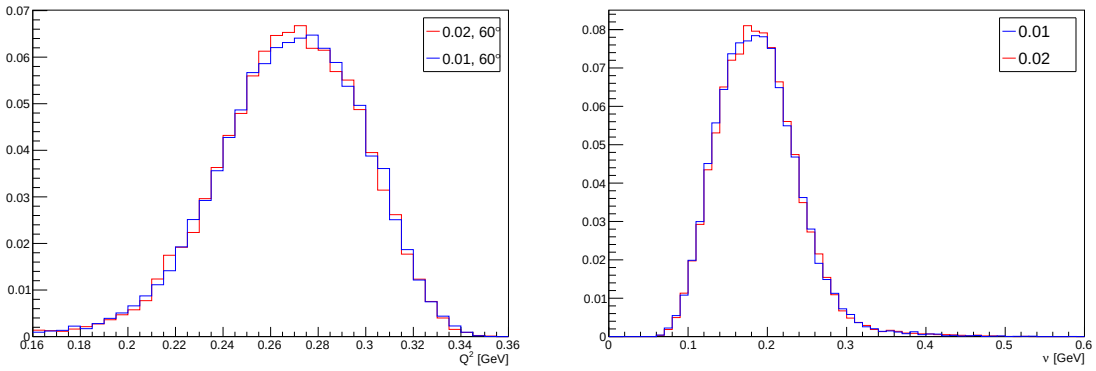

(a) **(b)**

Fig. 4.12: Effect of the Q^2 threshold on energy transfers, Q^2 and ν. These are for a 620 MeV incident electron, scattered at 60°. Even though the cut has been doubled, there is not a large effect on the energy transfers.

This method had the potential to be useful as it produces the correct Q^2 distributions, but produces an elastic peak too narrow that does not match other predictions. Although not shown here, it has no ability to predict the overall cross-section. Compounding this is the extremely inefficient event generation: as electron events are very forward scattered and events are sampled in a random scattering angle, many events are rejected before generation is completed. It should be noted the generation speed is not only a problem seen in NEUT, but also in other generators, where typically the electron generation takes longer than the corresponding neutrino one. This inefficiency can be somewhat mitigated with an appropriate choice of the Q^2 threshold, however this does not solve the narrow elastic peak seen here. The cause of this is unclear, and is likely hidden within the confines of the NEUT generator. It is possible this narrower peak is a correct prediction, however as this is identical to the model used in NuWro, it is expected they produce similar results. This is the case when using the 'pseudo-electrons'.

4.4.2.2 Cross-section Calculation

As stated above, the cross-section tables from the neutrino SF were used to generate the electron events. This potentially could be the cause of the narrow elastic peak, and also produced large problems with the cross-section scaling. Therefore it was decided that new cross-section tables would be produced, in the hope this would mitigate the problems seen above (and the exact factors contained in the leptonic and hadronic tensors would be known). The $\sigma(E_\nu)$ and maximum differential cross-section tables ($\frac{d\sigma}{dE_\nu}$) are produced with the same algorithm and formulae as presented in section 4.3.1, with the modification for the electromagnetic interaction:

$$\sigma_e = \frac{1}{\cos^2\theta_C}\frac{N\alpha^2}{G_F^2 Q^4}\sigma_\nu \,, \tag{4.22}$$

where $1/\cos^2\theta_C$ is a factor of moving from CCQE to NCE. 1 million events are generated for E_ν values in 50 MeV increments between 0 and 10000 MeV, with the maximum differential cross-section saved for each energy. The differential cross-sections of all throws are averaged to obtain a total cross-section. These tables have been generated for the spectral functions available, *i.e.* ^{12}C, ^{16}O and ^{56}Fe. The total cross-section prediction is shown in Fig. 4.13, with the neutral current electron neutrino total cross-section for comparison. Using the neutral current prediction as a reference and multiplying by the change in coupling, the total cross-section gives reasonable results, but the true test is still an estimate of the differential cross-section as compared to data.

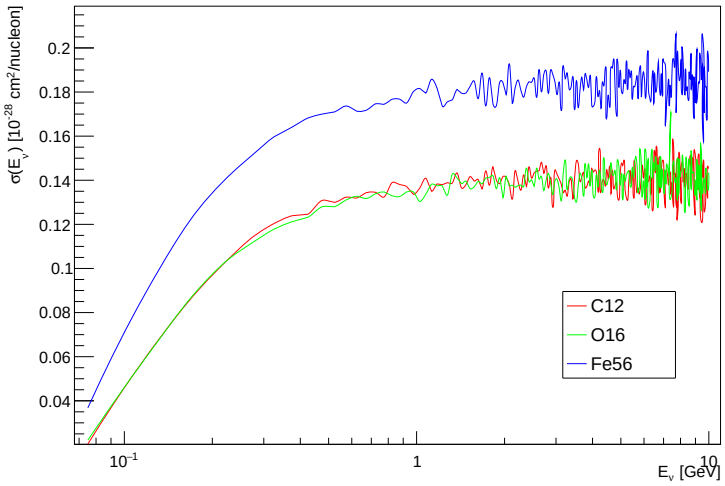

(a)

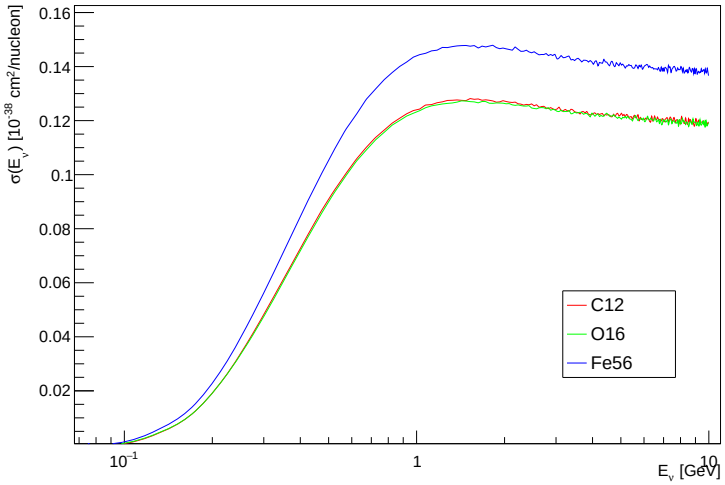

(b)

Fig. 4.13: **(a)** Electron total cross-section as a function of the electron energy. This is for the 3 different nuclei available for the spectral function. **(b)** As for (a), but for neutral current electron neutrino scattering.

A slight complication is the inclusion of the low Q^2 threshold. As $Q \to 0$, $\sigma_e \to \infty$. However, as events are generated using the maximum differential cross-section, this upper limit will change dependent on the value chosen for the threshold. A comparison of 3 different Q^2 cuts is shown in Fig. 4.14. As expected, the total cross-section changes dependent on

the threshold, where the smallest threshold gives the highest value for the cross-section. It is this difference that makes the total cross-section difficult to compare to other generators.

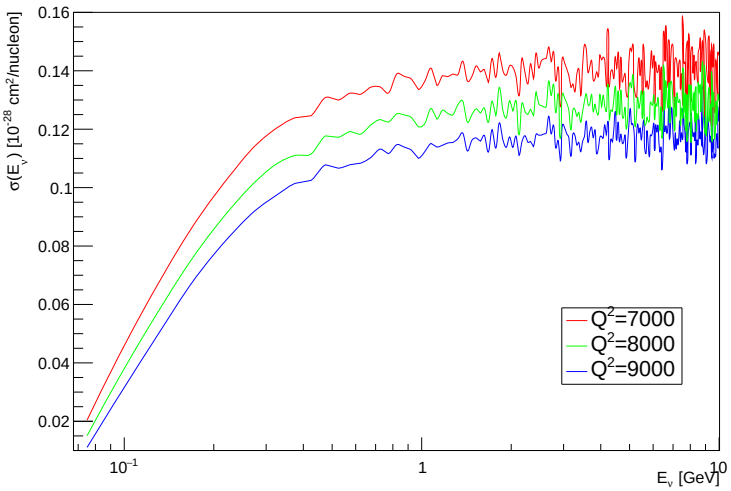

Fig. 4.14: Effect of the Q^2 cut on the total electron scattering cross-section. The cut values are given in MeV. As expected, the smallest cut produces the largest cross-section.

The change in the cross-section with the cut causes the use of pre-generated cross-section tables to be difficult, as using a table with a different Q^2 threshold will not yield correct results for the differential cross-section[10]. From a purely practical perspective, it is not possible to pre-generate every table that may be needed. Thus, only one table is generated for the inclusion into 'base' NEUT, and the ability to generate independent cross-section tables for different threshold values has been made readily available.

This limitation with the cross-section tables is interesting, as it begs the question as to whether it would be easier to generate tables 'on-the-fly'. This would speed up a one-off electron simulation, but would be more detrimental if many similar electron scattering events were being simulated. This will not be discussed further, but is an important thing to remember moving forward.

4.4.2.3 Electron Cross-Section Tables

Using these generated tables, the same predictions as above can be made. It quickly became clear these were not working completely as intended, as shown in Fig. 4.9. This shows the four momentum-transfer for the events generated with the electron tables at a fixed angle, and also over all angles. As before the scattering angle distributions are very similar (though there is a small shift between them), however the full angle distribution is completely unexpected. While this is mostly forward peaked, it contains a long tail of events to high momentum transfers, unlike the forward peaked distribution expected. The reason for this is uncertain, as this closely follows the implementation used for the neutrino-to-electron case, which does produce the correct outgoing distribution. It is possible there is some problem

[10]Though as can be seen in Fig. 4.14, it would likely not be too far off.

in the generation of the differential cross-section, however this is not confirmed[11]. It seems likely if this long tail is removed, the distributions of a particular scattering would match more closely, due to a lot of the high momentum transfer events being shifted toward lower transfers and effectively shifting the peak in the same direction.

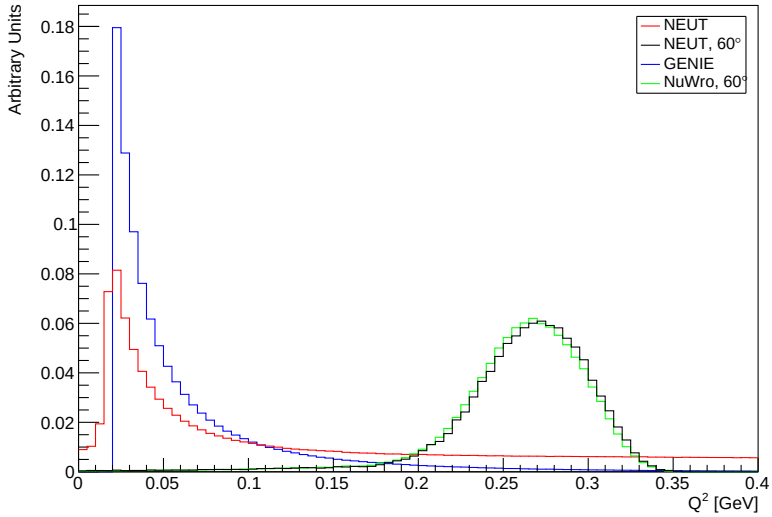

Fig. 4.15: Q^2 distribution of the NEUT and GENIE generators when generating with electron cross-section tabls. These have been normalised to an area of unity. The different lower bounds come from the different Q^2 thresholds. The GENIE and red NEUT lines are over all scattering angles, whilst NuWro and the black NEUT line are a 60° scattering.

Whilst this does not produce the expected Q^2 distributions, the predictions of the lepton energy transfer are much closer to the NuWro predictions. The width of the elastic peak matches well, but it seems they are shifted by a few MeV towards lower energy transfers, shown in Fig. 4.16. If the Q^2 distribution were somehow corrected, it is possible this would resolve this issue. However, it is equally likely this would produce distributions similar to the predictions generated when using the neutrino cross-section tables. There also still lies a problem with the cross-section scaling when using these tables (although they are closer than when using the neutrino tables). This is most likely due to the Q^2 distribution, which has a direct impact on the electron scattering cross-section, producing too few events in the low Q^2 region. This reasoning comes from the fact an opposite angular dependence in the scaling is seen here, indicating there are too few events in the lower scattering angles (*i.e.* under-predicting the cross-section) and the inverse at higher scattering angles. The cross-section predictions are shown in Fig. 4.17, where the previous comments about overall cross-section scaling still apply.

[11] As NEUT has been continuously developed by multiple developers over the years, the true cause of this could be buried deep in an old piece of the software. Unfortunately, some problems with NEUT can be intractable.

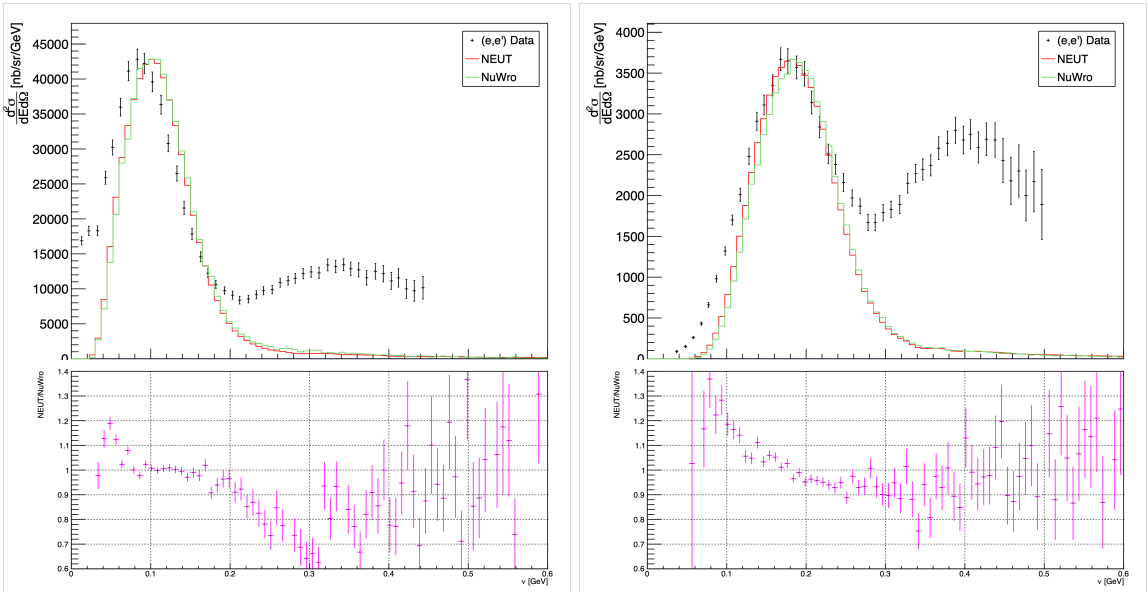

(a) **(b)**

Fig. 4.16: NEUT electron scattering predictions using generated electron cross-section tables. These prediction are under the impulse approximation. The top panels show the lepton energy transfer predictions (scaled to the elastic peak of data), whilst the lower panels show the ratio between the NEUT and NUWRO predictions (when the area is scaled to unity). The NEUT prediction are different from the NUWRO peak by a few MeV. This is for an incident electron energy of 620 MeV, scattered at **(a)** 36° and **(b)** 60°. Data taken from [301].

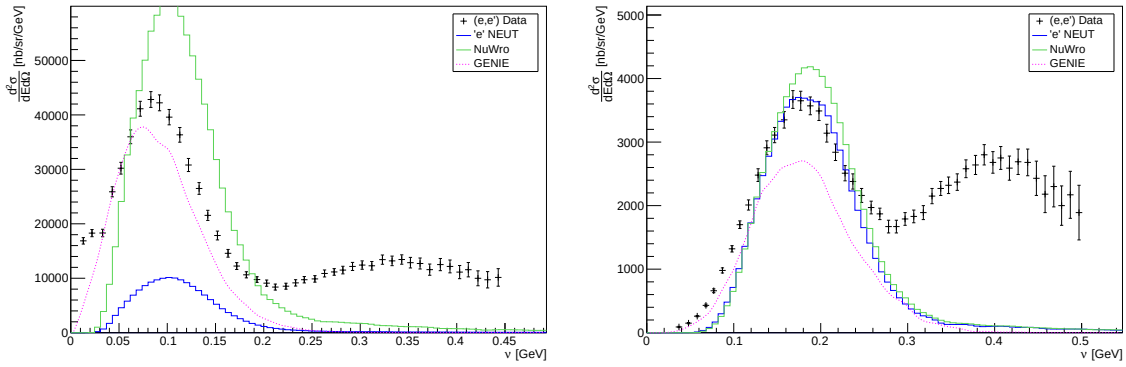

(a) **(b)**

Fig. 4.17: NEUT cross-section predictions using the generated electron scattering tables. The NEUT scalings appear to have the opposite problem than with the spectral function tables, and have been artificially scaled as before. This is for an incident electron energy of 620 MeV, scattered at **(a)** 36° and **(b)** 60°. Data taken from [301].

4.5 Final Comments

4.5.1 Expansion to other models

The rest of this section has described the implementation of an electron scattering generator with the SF as the nuclear ground state model. However, it is still useful for other nuclear models to be available for electron scattering in order to make comparisons between them. The simplest way to achieve this is using the 'pseudo-electron' technique described in section 4.4.1, which can easily be applied to different models by reweighting the events after the generation is complete. It is this method that is used for the relativistic Fermi gas predictions in chapter 5. This method is also easy for other generators to apply to their models, that may not be available in NEUT.

It would also be possible to build a fully contained electron scattering mode for an RFG nuclear state in NEUT, however this was not completed. This is potentially simpler than the SF implementation, as the RFG throws its events by sampling the Q^2 distribution as opposed to sampling the total cross-section. Therefore the correct distribution could simply be applied during generation.

An electron scattering model was also built based on the effective spectral function (ESF). However, due to problems with the ESF implementation itself, comparisons with electron scattering data could not be made[12]. However, as the ESF implementation was designed on the existing Benhar SF code, this was tested using the (correctly installed) Benhar cross-section tables.

4.5.2 Moving Forward

This section has described the process behind implementing an electron scattering model into generators, specifically focusing on NEUT. This has covered converting neutrinos into electrons, and also multiple methods of creating an electron prediction within NEUT.

It has been decided that in the subsequent analyses, the 'pseudo-electron' approach will be taken. This is due to the electron kinematics matching well with the NuWro predictions, which use the same ground state model and thus should be the same. This also has the benefit of being much quicker to generate a large range of incident electron energies for a relatively inexpensive computing cost.

Unfortunately, there still remains issues relating to the Q^2 distributions for the fully integrated electron generation inside NEUT. It is unclear the cause of these issues, and it likely due to some quirk of the NEUT generator. The effect seen is typical of what would be expected if the accept/reject condition is not being obeyed (*i.e.* some events with a cross-section larger than the reject ceiling are being accepted), though this does not appear to be the case. Further development of the full electron scattering model is required to produce the correct outgoing kinematics of the very forward scattered electrons.

[12] This was a problem with the ESF's cross-section tables, which were not being sampled from correctly. This was broken at some stage before this work began.

Chapter 5

Momentum Transfer Dependent Removal Energy

> The best I can give you is a fake smile and dead eyes.
>
> Robin (S01E16)

The previous chapter has described an extension to the NEUT event generator to produce an electron scattering simulation based on a neutrino neutral current framework. By comparing this to electron scattering data, new insights about the dominant interaction channel for T2K, charged-current quasi-elastic (CCQE) scattering, can be gleaned, allowing for a more accurate description of interaction event. This chapter will describe the comparison between the new electron scattering simulation and inclusive electron scattering data in order to derive a semi-empirical correction to the interaction.

5.1 The Factorisation Approach

First introduced in chapter 2, NEUT is built under the plane-wave impulse approximation (PWIA), stating that a scattering event occurs on a single, non-relativistic nucleon and the lepton exits without any final state interactions (FSI). Under this assumption, the nuclear ground state and the lepton-nucleon interaction factorises, and the exclusive neutrino-nucleus cross-section can be written as

$$\frac{d^6\sigma}{dE_\ell d\Omega_\ell d^3p'} = K\sigma_{\ell n}S(E,\mathbf{k})\,, \tag{5.1}$$

where K is a kinematic factor, $\sigma_{\ell n}$ is the single neutrino-nucleon cross-section and $S(E,\mathbf{k})$ is the spectral function (SF) describing the nuclear ground state. Due to the kinematics of the incoming lepton being abstracted from the calculation of the cross-section, and the separation of the ground state, it is expected the SF will be identical for both neutrinos and electrons.

Therefore, by definition, under the IA the nuclear ground state does not depend on the observable kinematics of the incoming or outgoing lepton. However, models based on more sophisticated calculations, such as the microscopic relativistic mean field (RMF) calculations that SuSAv2 is based on, predict a strong momentum dependence on the removal energy. Analysing the peak of the transverse and longitudinal scaling functions, one finds the peak position evolves as a function of q. This implies that scaling of the first kind (the scaling function should have no dependence on the energy/momentum transfer) is broken. Thus, in order for the scaling approach to apply, an energy shift, E_{shift}, needs to be applied to place the peak of the scaling functions at $\psi' = 0$, where ψ' is the scaling variable. This is shown in Fig. 5.1. It is clear that the RMF longitudinal and transverse responses are approximately the same, exhibiting a linear dependence on the momentum transfer. This breaking of first kind scaling was also noticed in semi-relativistic models, with similar results [303].

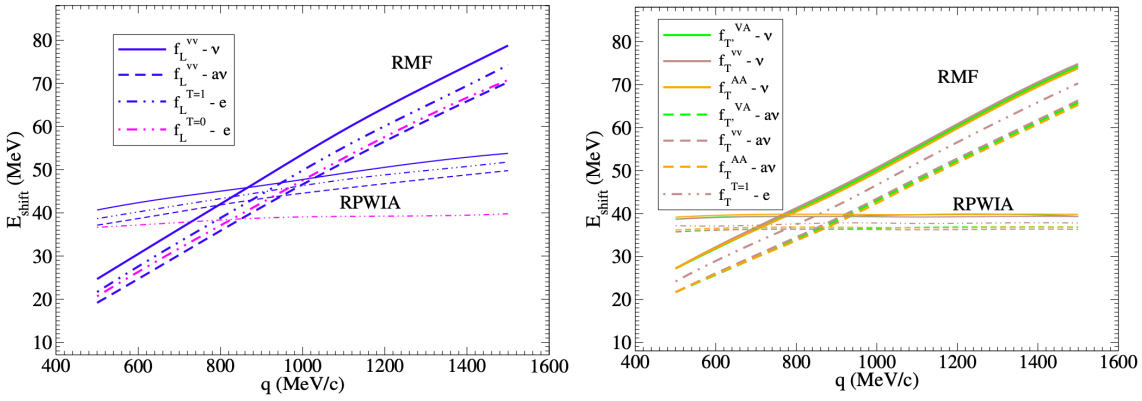

Fig. 5.1: The E_{shift} required in order to place the peak of the scaling function at $\psi' = 0$ as a function of the momentum transfer q. **(a)** The longitudinal scaling functions, both RMF and RPWIA are linearly dependent on q. **(b)** The transverse scaling functions. Only the RMF is dependent on q, the RPWIA model obeys first kind scaling. Figure taken from [187].

Interestingly, the relativistic plane wave impulse approximation model (RPWIA) shows no dependence on the lepton kinematics in the transverse response, and only a weak dependence in the longitudinal contribution. As the two models are both based on the relativisitic IA, it is likely due to the difference in their treatments of the final state: the RPWIA treats the outgoing nucleon as a relativistic plane wave whilst the RMF includes FSI on the outgoing nucleon by applying the same mean field as used when bound in the nucleus.

If this momentum transfer dependent effect can be included into the models used by T2K, such as the currently used Benhar-Fantoni SF, the limitations of the factorisation approach can begin to be mitigated. This should be able to reproduce the results of the more complicated models, without the computational expense of performing the full calculations.

5.2 Determining a Kinematic Correction

In this section, data from the inclusive electron scattering cross-section archive [301] is compared to NEUT predictions in order to derive a function that can move beyond the IA. This data is available as a function of the incident beam energy and the outgoing scattering angle and hence as a function of the measured energy transfer, denoted here with ν[1]. Fig. 5.2 shows example electron scattering measurements for two scattering angles as a function of incident energy. Contrary to the predictions of the IA based Fermi gas and SF models, there is a clear evolution of the elastic scattering peak (the first observed peak) as a function of the beam kinematics.

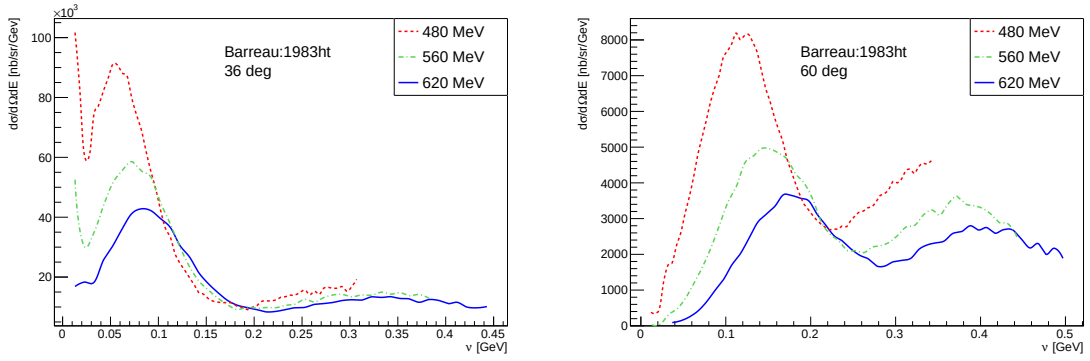

(a) **(b)**

Fig. 5.2: Inclusive electron cross-section measurements for an outgoing scattered electron angle of 36° (left) and 60° (right) for varying incident beam energies as a function of the energy transfer (ν). There is a clear evolution of the elastic scattering peak in ν for a changing beam energy (and therefore changing $\mathbf{q_3}$). Data taken from [301].

As mentioned in section 4.1.1, the elastic peak position for electron scattering off a free nucleon of mass m_N is expected to occur at

$$\nu = \frac{Q^2}{2m_N}\,, \tag{5.2}$$

where Q^2 is the four-momentum transfer squared. If this nucleon is bound, the removal energy acts to translate the position of this peak, in such a way that a shift in the peak almost directly maps to a change in the removal energy. An example of this shift can be seen in Fig. 5.3a. In a similar way, the width of the elastic peak can be a direct measurement of the Fermi momentum within the nucleus, shown in Fig. 5.3b. It is, in fact, utilising these features of the elastic peak that SF models are built from (in particular the Benhar-Fantoni SF [176]).

This same behaviour of the quasi-elastic peak can be used to move beyond the IA. An analysis of NEUT predictions for the peak position can facilitate the derivation of a correction to the nucleon removal energy.

[1]Our field is horrendously inconsistent with labelling energy transfer. It is frequently written as ν, q_0 or ω: in this section I endeavour to use mostly ν. I apologise for any inconvenience.

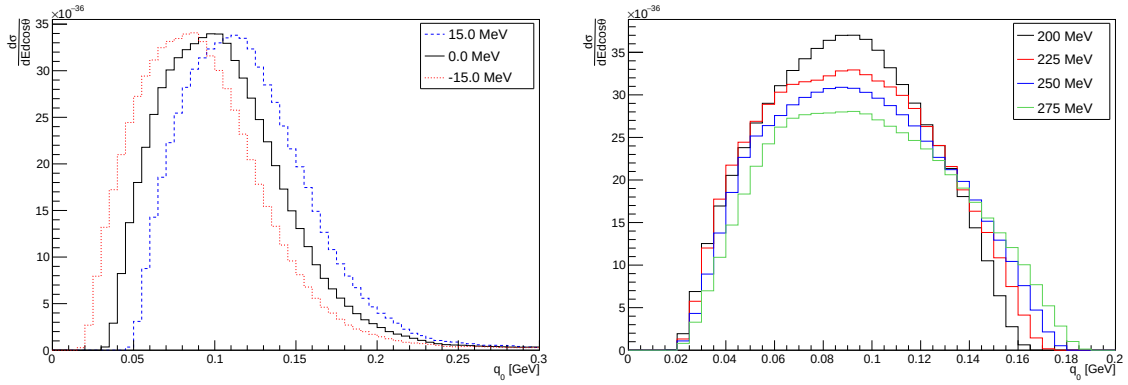

(a) **(b)**

Fig. 5.3: **(a)** Effect of varying the removal energy on the energy transfer. This is a 620 MeV mono-energetic neutrino beam scattered at 36°. A shift in removal energy is a translation in the quasi-elastic peak. **(b)** Effect of changing the Fermi surface, as the surface increases it broadens the quasi-elastic peak. The beam is as before, except using a relativistic Fermi gas model.

Fig. 5.4 shows NEUT electron scattering predictions, held purely under the IA, against inclusive electron scattering data. The elastic peak clearly does not describe the data well, with the peaks offset by varying amounts. In order to improve this, the central value of each peak (data and simulation) must be calculated. These can be used to find the peak offset and therefore improve both the electron and CCQE predictions.

Ideally, the elastic peaks would be fit using a physically motivated function designed to describe the data to a high degree. Such a function is not easily available, and it was decided that a 5^{th} degree polynomial would be used. This parameterisation successfully reproduces the shape of the peak (both the peak width and position). Higher degree polynomials were rejected as certain data sets have a limited number of data points populating the elastic peak, and such polynomials provide more free parameters than the number of fitting points. This polynomial also acts as a smoothing function, and with this choice does not tend to over fit the data.

The difference in elastic peaks is calculated using the maxima of the two polynomial fits, with the difference being entirely attributed to the removal energy. This is correct to a first approximation, as shown in Fig. 5.3a, however there will be some slight differences related to FSI: these have been assumed to be negligible for this analysis. The elastic scattering data peak is used to calculate the kinematics of the event to test whether the shift observed is dependent on said kinematics. The three-momentum transfer, $\mathbf{q_3}$, is given by

$$\mathbf{q_3} = \sqrt{Q^2 + \nu^2}\,, \tag{5.3}$$

where all symbols are defined as above, and

$$Q^2 = 2E_\ell(E_\ell - \nu)(1 - \cos\theta)\,, \tag{5.4}$$

where E_ℓ is the incident electron energy and θ is the electron scattering angle relative to

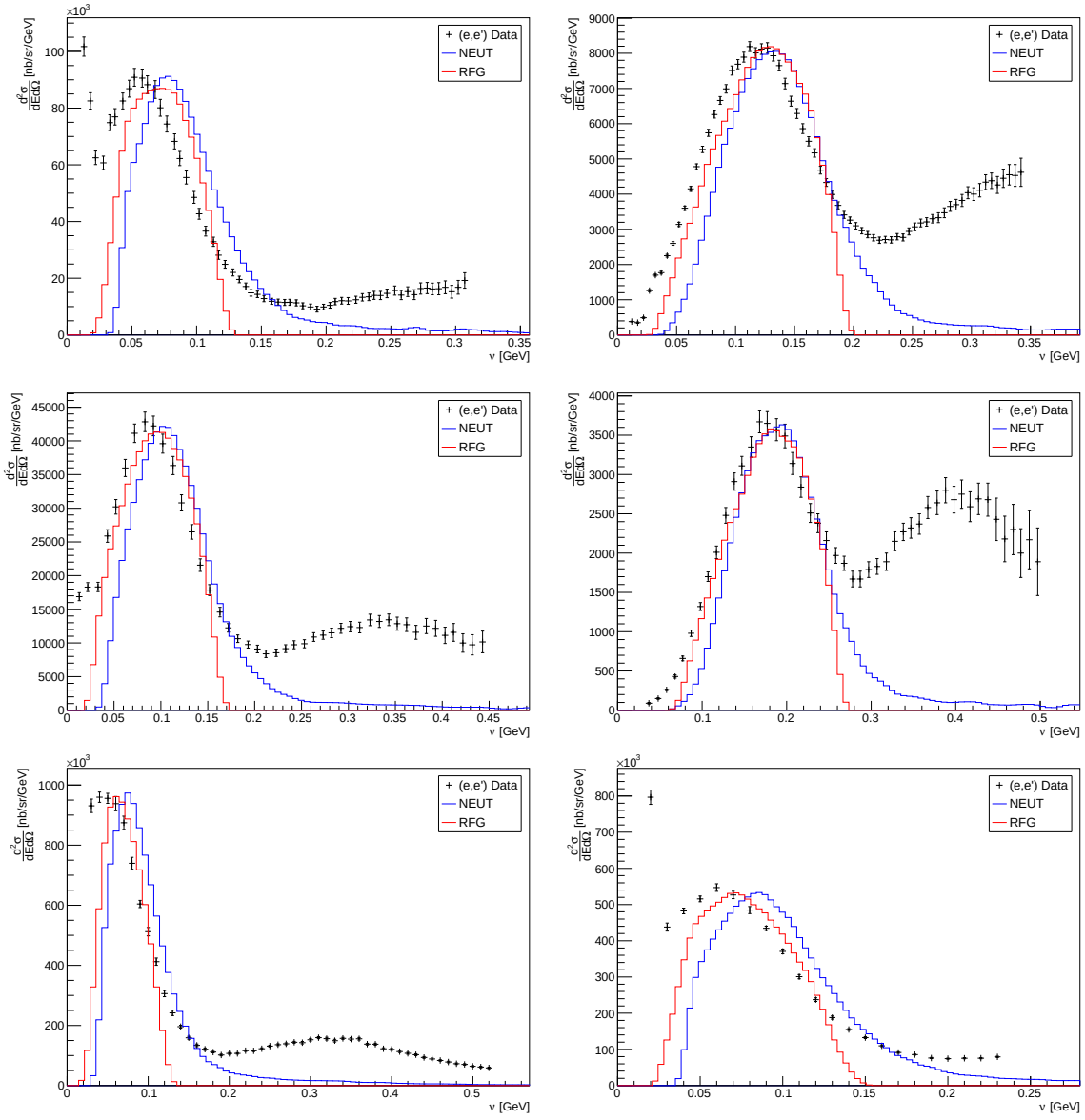

Fig. 5.4: Inclusive electron cross-section measurements (black points) compared to elastic electron scattering predictions in NEUT (blue histogram) for the spectral function. The relativistic Fermi gas is also plotted in red. The comparison is made for a variety of scattering angles and beam energies. The beam energy and scattering angle are as follows: **Top:** 480 MeV. *Left*, 36°; *right*, 60°. **Middle:** 620 MeV. *Left*, 36°; *right*, 60°. **Bottom:** 1300 MeV. *Left*, 11.95°; *right*,, 13.54°. Data taken from [301].

the incoming beam direction. It is worth noting here that the overall normalisation of the electron predictions does not matter, only the peak position, thus any problems in scaling to a cross-section can effectively be ignored when deriving any correction. Examples of the peak fitting is shown in Fig. 5.5. The removal energy shift, ΔE_B, is defined by the difference between the data, d_{peak}, and simulation, s_{peak}, peaks, *i.e.*

$$\Delta E_B = d_{\text{peak}} - s_{\text{peak}} \,. \tag{5.5}$$

The results of all the fits for the SF are summarised in Table 5.1 as an example: this is the last time these are given in tabular format.

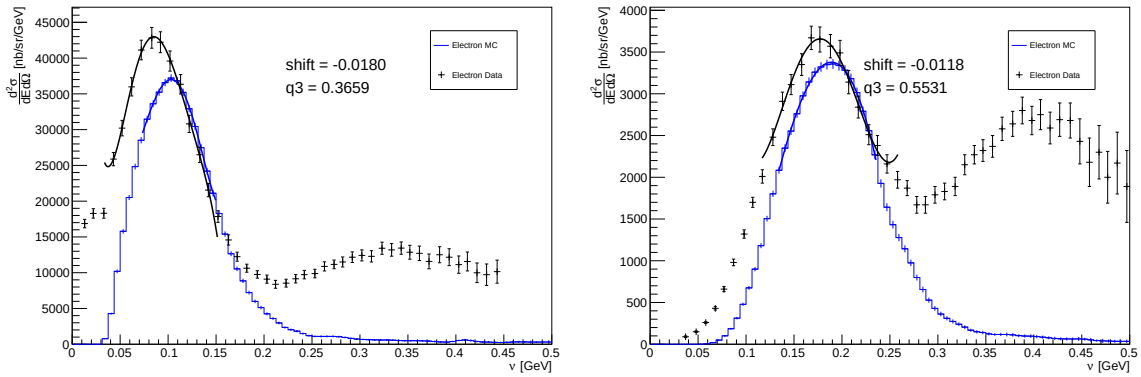

Fig. 5.5: Polynomial fits to the elastic peak of both electron scattering measurements (black points) and NEUT predictions (blue histgram). The fits act to smooth the data and find the peak position. The difference in the peaks is shown, with $\mathbf{q_3}$ calculated at the data elastic peak. **(a)** 620 MeV beam, 36° outgoing lepton scattering angle. **(b)** As before, but a 60° scattering. Data taken from [301].

As discussed in section 5.1, more sophisticated exclusive model calculations suggest a linear relationship between the removal energy and the three-momentum transfer. To evaluate this, the derived correction is plotted against $\mathbf{q_3}$, as shown in Fig 5.6 for the SF. As with the other models, a linear fit is well suited to describe the evolution of the elastic peak as a function of the interaction kinematics, showing the IA is limited by not including the interaction kinematics in its calculations of the scattering event.

It is important to note this effect is not limited to the spectral function but is a by-product of the IA, and similar results can be obtained for other models. The red histograms in Fig 5.4 show the relativistic Fermi gas (RFG) model, which also do not describe the elastic peak well. Fig 5.4 also presents a nice representation of the more sophisticated nature of the SF over the RFG, with the latter not describing the elastic tail (and therefore the dip region). After the same analysis is performed on the RFG data, the derived linear function is shown in Fig 5.7. This gives a substantially different fit than the SF, and will be discussed in more detail later in this chapter.

The derived $\mathbf{q_3}$-E_B fit can now be applied during event generation in order to apply effects moving beyond the factorisation approach on top of the 'simple' IA. This is only the case if the shifts are interpreted as a removal energy effect. Due to the somewhat rigid

Energy	Angle	$\mathbf{q_3}$	Data (d_{peak})	NEUT (s_{peak})	Shift (ΔE_B)
320	36	190.8	28.8	58.7	-29.9
320	60	294.5	60.3	81.9	-21.6
361	60	330.0	74.9	91.5	-16.5
400	36	238.0	39.2	69.4	-30.1
401	60	365.2	87.4	105.0	-17.6
440	60	398.5	103.4	116.8	-13.4
480	36	284.3	56.4	77.7	-21.3
480	60	432.9	119.2	133.1	-13.9
500	60	449.5	129.3	138.2	-9.0
519	60	467.1	132.5	147.3	-14.7
560	36	330.9	73.0	91.3	-18.3
560	60	502.8	147.4	164.1	-16.7
560	145	757.4	332.8	329.0	3.8
620	36	365.9	85.1	103.4	-18.3
620	60	553.0	177.8	187.7	-9.9
680	36	400.8	99.8	118.8	-19.0
680	60	603.6	207.8	213.8	-6.0
730	37.1	441.6	115.1	131.9	-16.9
961	37.5	585.0	192.9	202.8	-9.9
1108	37.5	674.8	248.6	252.7	-4.1
1300	11.95	269.9	48.3	74.9	-26.6
1300	13.54	305.3	60.7	84.2	-23.6
1500	11.95	312.2	64.1	84.6	-20.4
1500	13.54	353.4	80.9	97.8	-16.9
1501	37.5	920.7	423.2	412.5	10.6
1650	11.95	344.4	78.9	94.1	-15.1
1650	13.54	389.2	93.4	109.3	-15.9
1930	16	540.5	170.5	175.7	-5.2
1930	18	606.3	203.6	209.4	-5.8
2000	15	524.5	153.0	167.9	-14.9
2020	15.02	530.5	154.5	169.9	-15.4
2020	20.02	704.1	255.1	262.0	-6.9
2130	16	598.6	199.2	203.0	-3.8
2130	18	675.4	255.9	245.9	10.0
2500	15	663.6	232.3	237.6	-5.3
2700	15	724.0	281.5	271.6	9.9

Table 5.1: Summary of the removal energy shifts as determined from polynomial fits to the elastic peak. Energy is the incident energy of the electron beam, and the angle is the scattering angle in degrees. All energies and energy/momentum transfers given in MeV. The shift is the difference in the elastic peak position between data and simulation. All data are taken from [301].

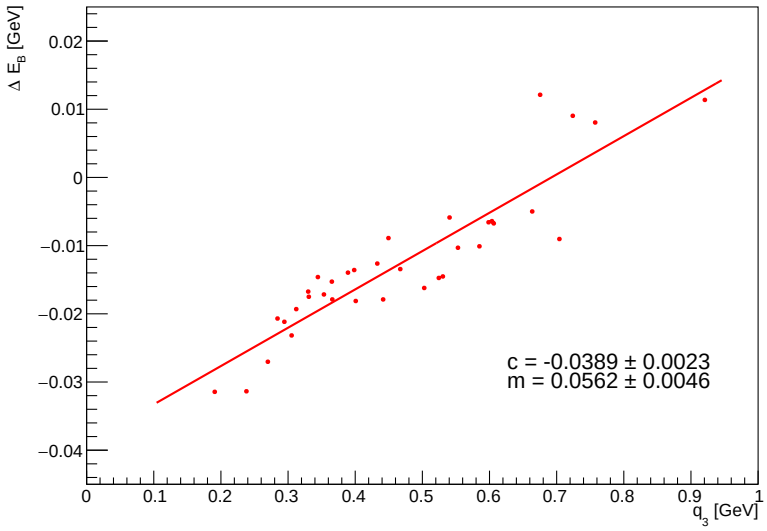

Fig. 5.6: Relationship between ΔE_B and q_3 for the Benhar-Fantoni spectral function. This reveals an approximately linear relationship between the kinematics and the removal energy, as expected from more sophisticated model calculations. Fit parameters are shown on the plot.

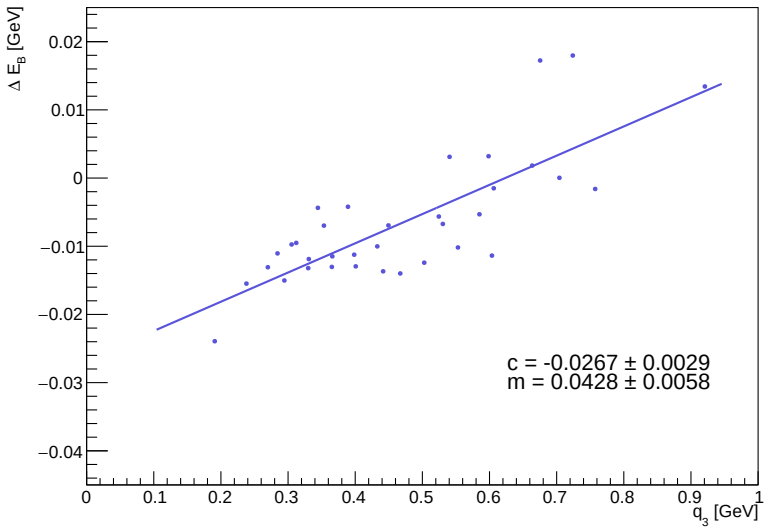

Fig. 5.7: Relationship between ΔE_B and q_3 for the relativistic Fermi gas. As for the spectral function, there is an approximately linear relationship between the kinematics and the removal energy. Fit parameters are shown on the plot.

structure of NEUT's event generation, described in section 4.3, the application of this shift is rather cyclical:

1. Randomly select nucleon momentum and removal energy from the SF.
2. Calculate centre-of-mass (COM) energy and boost into this frame.
3. Generate a random direction for the outgoing nucleon and lepton.
4. Boost back to lab frame.
5. Calculate removal energy shift using

$$\Delta E_B = m\mathbf{q_3} + c \tag{5.6}$$

6. Re-calculate COM energy with ΔE_B and boost into that frame.
7. Set outgoing lepton and nucleon momentum using previously calculated direction.
8. Boost back into lab frame.

After applying this fit, the NEUT electron scattering predictions as compared to (e,e′) data is shown in Fig. 5.8. It is clear the kinematic dependent removal energy more accurately predicts the elastic peak (of course, this is by design). Performing the same analysis as before, *i.e.* finding the difference between the fitted peaks, one can see if the effect has been accounted for, and is shown in Fig. 5.9. Although there is still some some residual effect, this is well within the fitting errors, and there is no longer any dependence of the removal energy on the kinematics of the event. This is important, as a precise measurement of the neutrino oscillation parameters is possible if the average reconstructed energy value is unbiased [300]. Including this fit will allow this to be the case.

5.2.1 Impact of the Kinematic Removal Energy

Due to the nature of this fit changing the missing energy, it will necessarily change the outgoing lepton kinematics (as it was designed to do) and will thus have an effect on the cross-section measurements. Its impact on CCQE interactions for the T2K ν_μ flux as a function of the outgoing lepton kinematics (*i.e.* the observables in a near detector fit) are shown in Fig. 5.10. The most notable effect is in the low-$\mathbf{q_3}$ region, which is expected from Fig. 5.6 where the correction to the removal energy is largest. This region, with $\cos\theta > 0.75$ (or $\theta > 42°$), are the very forward scattered events, which corresponds to $\sim 50\%$ of the T2K events, as is shown in Fig. 5.11.

As this is an empirical correction to the model, it can often be difficult to describe a physical motivation for its inclusion. In this case, one possible interpretation is that very forward scattered muons tend to only graze the nucleus, scattering off loosely bound nucleons rather than penetrating deep into the nucleus. These would sample a different region of the SF, however this is a feature not captured under the factorisation scheme allowed by

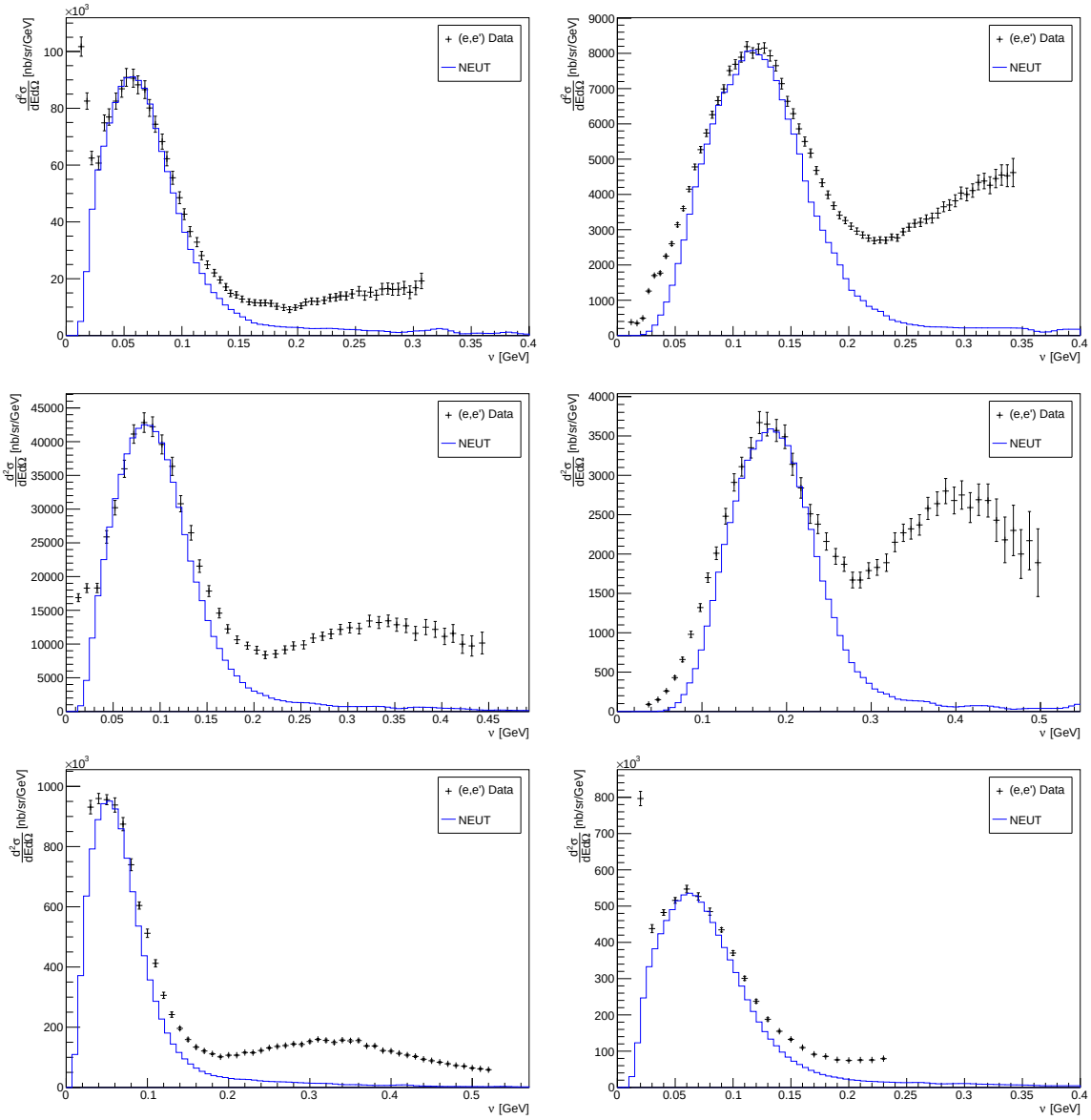

Fig. 5.8: Inclusive electron cross-section measurements (black points) compared to elastic electron scattering predictions in NEUT (blue histogram) for the spectral function, including the kinematic dependent removal energy. These clearly, and by definition, describe the data more accurately. The angles and beam energies are as before: **Top:** 480 MeV. *Left*, 36°; *right*, 60°. **Middle:** 620 MeV. *Left*, 36°; *right*, 60°. **Bottom:** 1300 MeV. *Left*, 11.95°; *right*,, 13.54°. Data taken from [301].

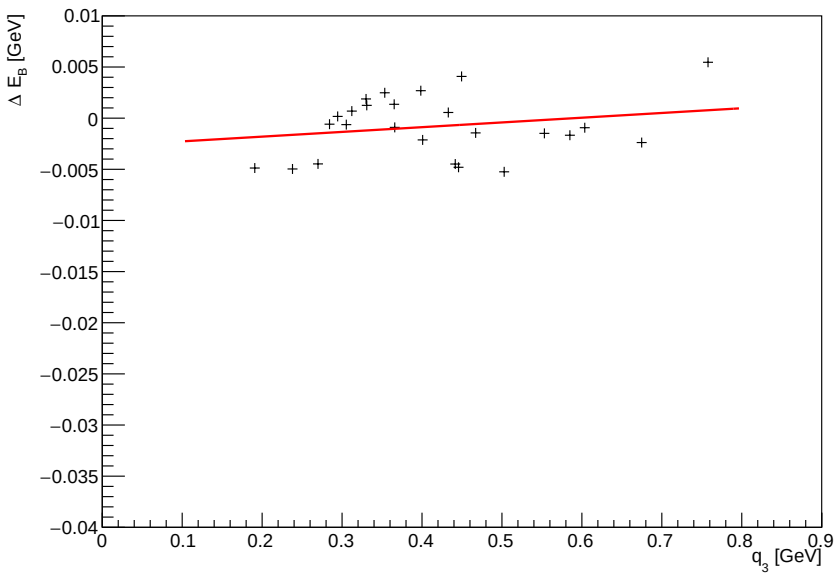

Fig. 5.9: Residual $\mathbf{q_3}$-E_B after applying the kinematic dependent shift to the removal energy during event generation. There is still some slope to the fit, but this is within the fitting errors. The fitting parameters are $m = 0.004 \pm 0.004$ and $c = 0.002 \pm 0.002$.

the IA. Therefore including this on top of our model, we can begin to move away from the factorisation approach, and capture features that appear once lepton kinematics are included into the nuclear ground state.

The empirical nature of the correction also leads to an interesting effect on the missing energy distribution, which is shown pre-correction in Fig. 5.12a. Once the fit is applied, a non-negligible proportion of events shift into having a negative removal energy: the missing energy distribution of this is shown in Fig. 5.12b. This effect occurs for 9.7% of total events. This is not the first time this has been noticed, with events in NuWro showing a similar effect [305].

These events are clearly unphysical, however there are no prescribed methods of dealing with them. These could be taken into account in the following ways if $E_B < 0$:

1. Keep negative removal energy events.

2. Cut at $E_B = 0$, throwing away events below this.

3. Redraw event from the SF distribution. The resulting removal energy distribution is shown in Fig. 5.13a.

4. Truncate the distribution to 0, in such a way that satisfies

$$E_B = \begin{cases} 0 & \text{if } E_B < 0 \\ E_B & \text{otherwise} \end{cases} . \tag{5.7}$$

The resultant removal energy distribution is shown in Fig. 5.13c.

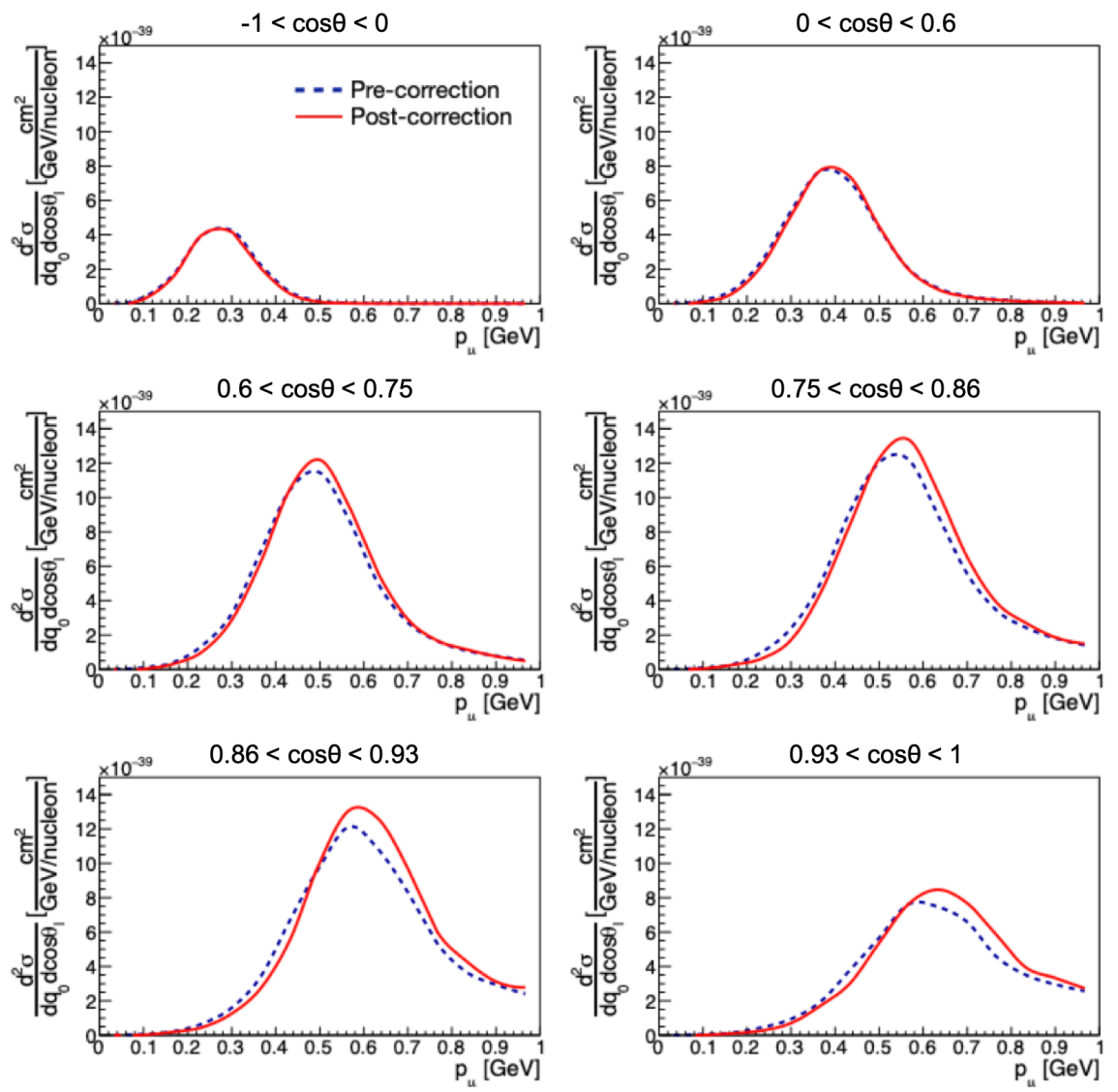

Fig. 5.10: Difference between the SF predictions for CCQE interactions applying (red, solid) and not applying (blue, dashed) the derived $\mathbf{q_3}$-dependent removal energy correction. These are generated with the T2K flux on a ^{12}C target. These are binned using typical T2K binning. The greatest effect is seen in the low $\mathbf{q_3}$ region (final 3 panels); these contain ∼50% of the cross section.

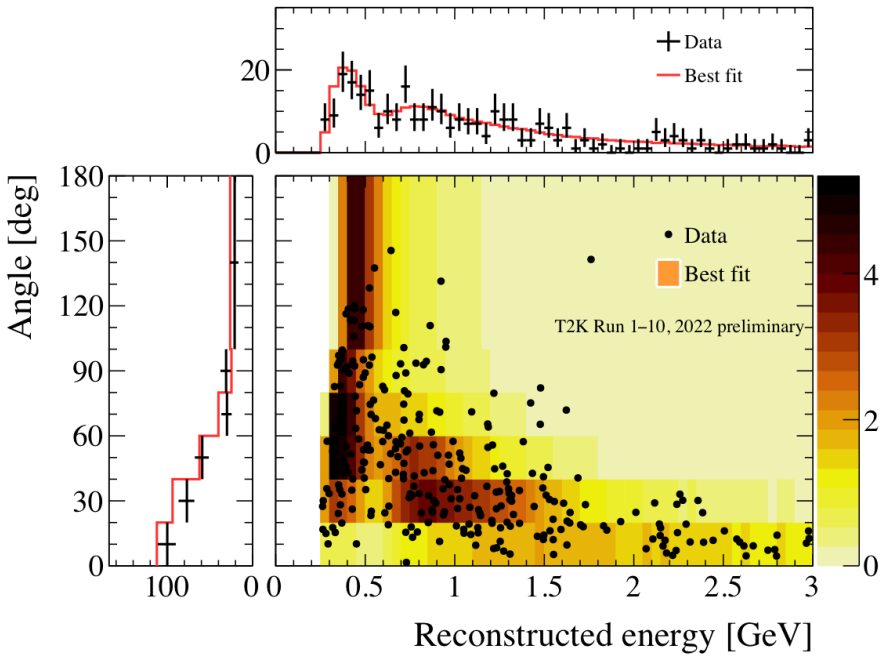

Fig. 5.11: Predicted spectra against data as a function of reconstructed energy (E_{rec}) and angle (θ_μ) with respect to the beam direction for the forward horn current 1 ring μ sample. The data contain events from runs 1-10. Error bars represent a 68% confidence interval on the mean. Figure taken from [304].

	Gradient (m)	Intercept (c) [MeV]
Negative E_B events	0.001 ± 0.005	-1 ± 3
Cut $E_B < 0$	0.033 ± 0.007	-19 ± 3
Redraw events	0.032 ± 0.006	-19 ± 3
Truncate to 0	0.005 ± 0.005	-4 ± 2

Table 5.2: Summary of the effect of different negative removal energy treatments on the resultant $\mathbf{q_3}$-E_B fit. Truncating the events to zero keeps everything physical, whilst successfully mitigating the residual kinematic dependent fit within the error. Removing any events below zero, *i.e.* redrawing and cutting, significantly worsens the effect of the correction and thus should not be used.

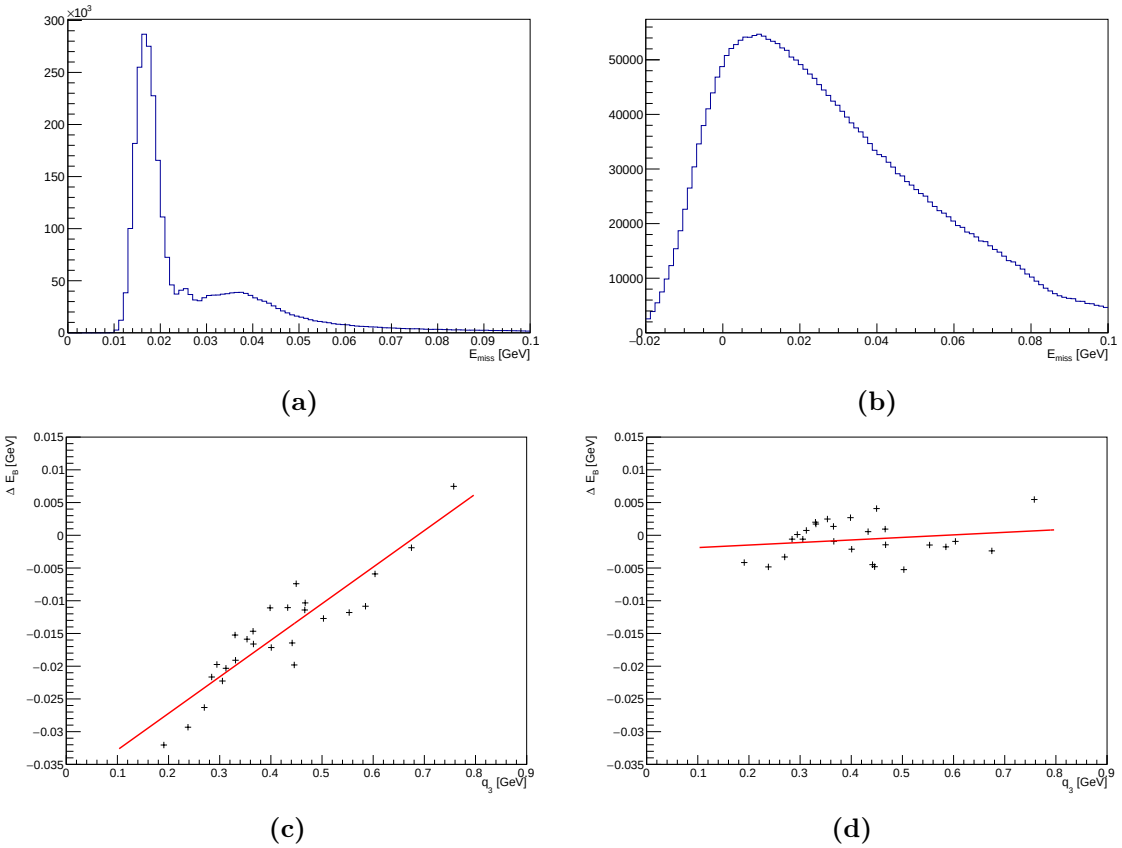

Fig. 5.12: Missing energy distributions with their associated $\mathbf{q_3}$-E_B fit. **(a)** and **(c)** is the standard missing energy and kinematic correction correction to the removal energy (as above). **(b)** and **(d)** is the missing energy distribution after the kinematic removal energy has been applied, with the residual kinematic correction. It shows the non-negligible portion of events having a negative removal energy. Fit parameters shown previously.

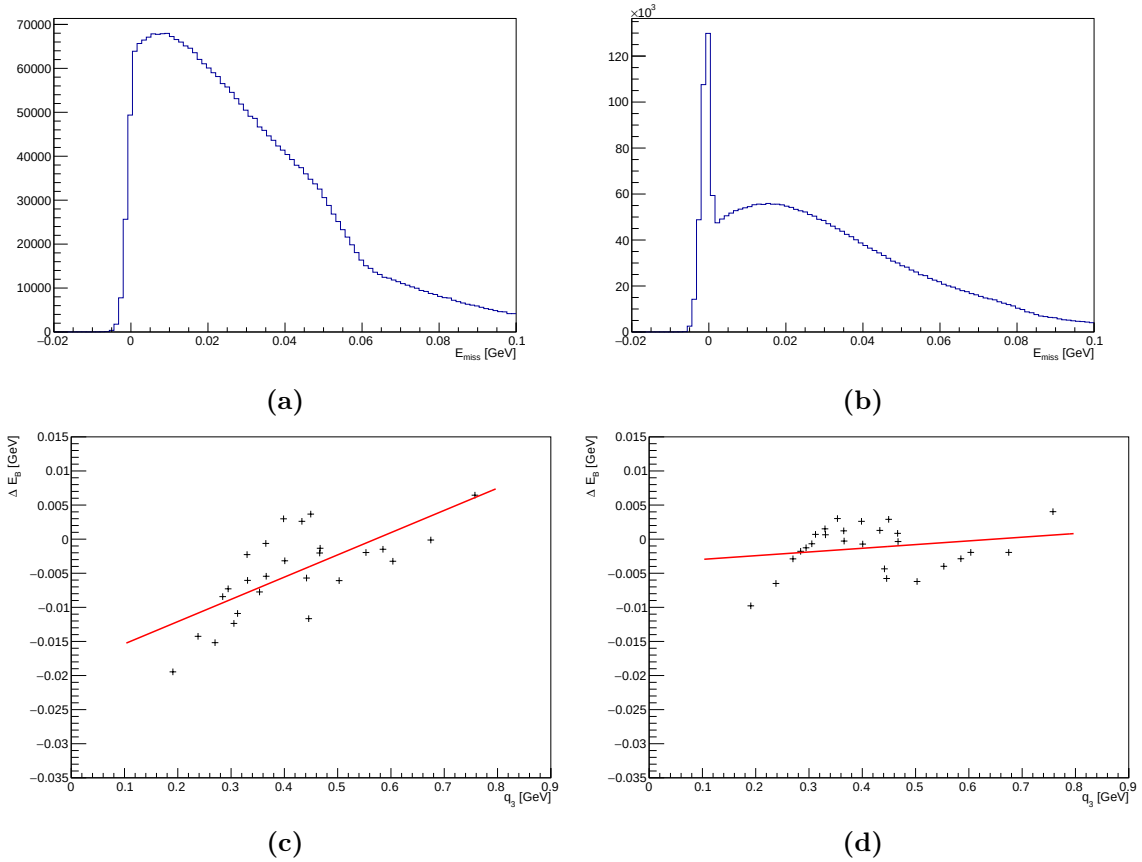

Fig. 5.13: Different methods of forcing a physical removal energy after the kinematic correction has been applied. **(a)** shows the missing energy re-drawing from the spectral function if $E_B < 0$, with **(c)** showing the residual kinematics correlation of the removal energy. **(b)** shows the distribution truncating E_B to 0. There is a much smaller residual on $\mathbf{q_3}$-E_B than redrawing. Fit parameters are summarised in Table 5.2.

For the oscillation analyses, it is decided it would be better to keep all events physical, rather than including the negative removal energy events in the oscillation probability determination. Methods 2 and 3 are effectively two ways of implementing a similar effect, but the former removes the events and is not recommended. However, redrawing events can cause issues if a large global removal energy shift is applied, as most events will have an unphysical removal energy. This would mean only a small sample of the events would be used, and drastically increases generation time. The effect of globally shifting the events is shown in Fig. 5.14 *without* the kinematic removal energy correction applied. For the oscillation analysis, it was recommended to truncate events to 0, as it does not suffer the limitations mentioned previously, but also has the least effect on the kinematic correction, as shown in Fig. 5.13 and summarised in Table 5.2. Though this does have a slight impact on worsening the residual kinematic dependence of the removal energy, it is still within the fitting errors and is a small price for ensuring all events are physical. These truncated events are thus almost treated as scattering off a free nucleon, rather than bound in the nucleus.

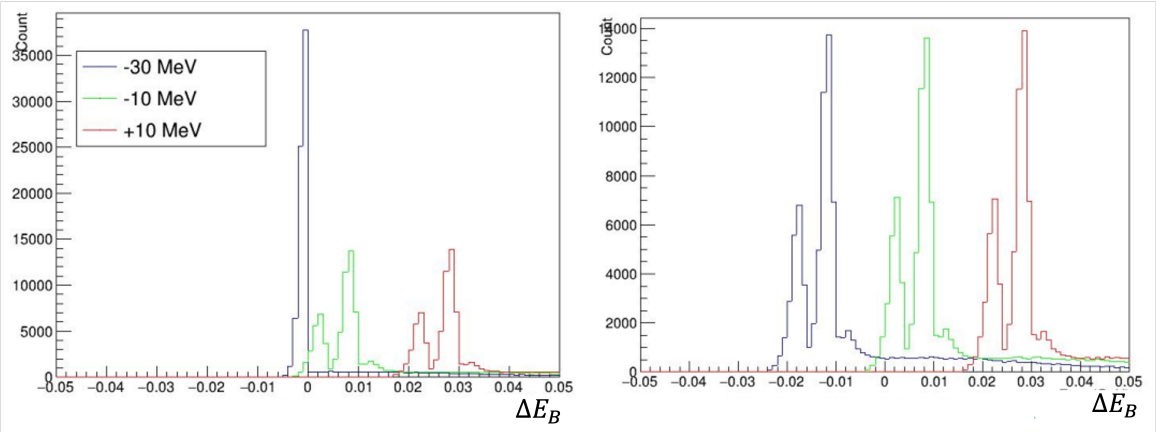

Fig. 5.14: *Left.* Effect of truncating the removal energy distribution at 0 when applying a universal shift to said energy. Even though events are truncated to zero, there is some residual events below it. *Right.* Globally shifting the removal energy without truncating to zero.

It is worth noting that a small portion of events still have a removal energy of less than 0, even after forcing the events to be physical. This is due to a difference in the definitions of the removal energy. In this case, the removal energy is estimated with the observed missing energy, defined by:

$$E_B = E_\nu - E_\ell + m_N - E'_N - T_R \,, \tag{5.8}$$

where the definitions are as before, N is the nucleon and T_R is the kinetic energy of the remnant nucleus,

$$T_R = \sqrt{p_{miss}^2 + M_R^2} - M_R \,, \tag{5.9}$$

where M_R is the mass of the remnant, and p_{miss} is the missing momentum (*i.e.* the Fermi momentum). This is defined as

$$p_{miss} = |\vec{p_\nu} - \vec{p_\ell} - \vec{p_N}| \,. \tag{5.10}$$

This is different to the removal energy as defined in the SF (given in chapter 4) as

$$E_B = E_\nu - E_\ell + m_N - E_N \,, \tag{5.11}$$

which does not include the kinetic energy of the remnant. This extra term forces some of the events to still retain a negative removal energy, therefore this is purely a case of semantics. The difference is shown in Fig. 5.15. Though most of the events are now as expected, one bin is still being filled just below zero, even when the distribution tapers off. It is unclear exactly what these are, however it seems more likely this is an underflow memory effect as opposed to anything more sinister.

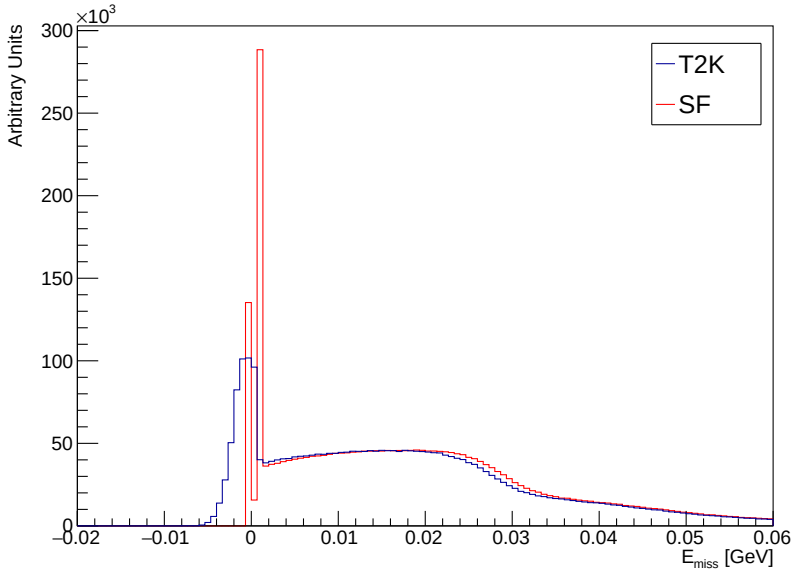

Fig. 5.15: Distributions for the different definitions of the removal energy. One is for the T2K definition (blue), which includes the kinetic energy of the remnant, whilst the other is using the spectral function definition (red). These are the corrected distributions. There are still some residual events below zero, but most are mitigated.

When the kinematic correction is applied, the resulting removal energy distribution does not show any sign of the shell structure of the nucleus: this effect is clearly seen in Figs. 5.12a and 5.12b. This is due to the correction being applied as a function of the momentum transfer, artificially shifting events between bins and changing the shell occupancy. One can regain the nuclear shell structure if these data are plotted for any particular slice in $\mathbf{q_3}$, shown in Fig. 5.16, similar to how the data was originally obtained.

As mentioned in section 4.1, neutrino experiments are only sensitive to the reconstructed energy, E^{rec}_{QE}. The inclusion of nuclear effects bias the reconstructed energy, and artificially shifting the removal energy will have a direct impact on the measurement. Fig. 5.17 shows the effect of the including the kinematic dependent removal energy with both the full correction applied, and with the truncated removal energy distribution that was decided upon. For reference, the normal reconstructed energy is shown. The correction biases the peak position by quite a substantial amount, around 60 MeV, which is not ideal. Truncating the removal energy improves the bias quite substantially, reducing it to about 30 MeV, much closer to

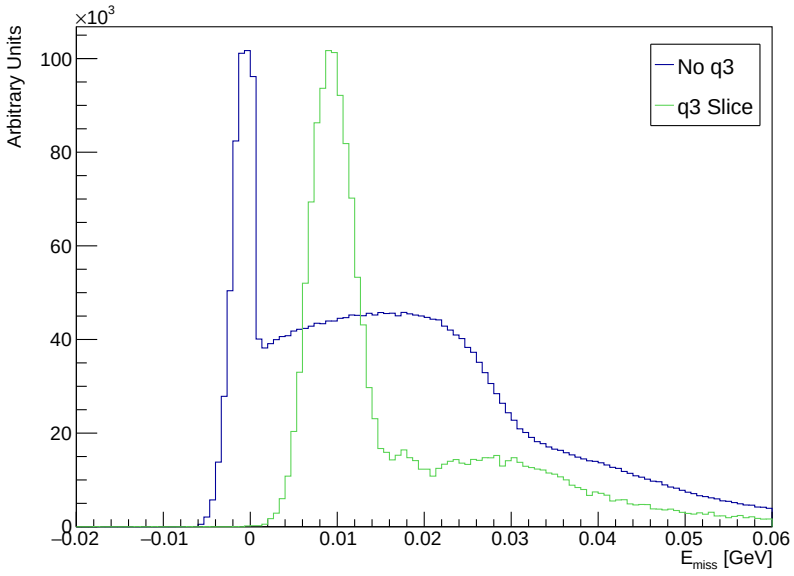

Fig. 5.16: Removal energy distributions after the correction has been applied and truncated to zero. The blue shows the distribution over all kinematics, which smooths out the shell structure. The green shows a particular slice of $\mathbf{q_3}$, recapturing the shell structure of the nucleus.

the ideal unbiased reconstruction. However, as long as the bias is understood, it can be accounted for in the oscillation analysis. This reduced bias is another reason for choosing to truncate the removal energy distribution to zero.

Another potential method is to use a $\mathbf{q_3}$ cut, in a similar fashion to electron scattering experiments, in order to remove the negative removal energy events. However, as is clear from Fig. 5.18, the cut required to force all events to be greater than 0 is very high, and cuts out most of the kinematic phase space of interest for T2K analyses. Thus, whilst an interesting method, it is not useful here.

5.2.2 Implementation for Oscillation Analyses

Whilst this derived $\mathbf{q_3}$ correction has been included into NEUT, the question remains as to how to include it in the oscillation analysis. It was decided this could be included with the current removal energy shift parameter. The details of the implementation will be described here.

The above analysis produces a shift in the removal energy in order to account for deviations from the PWIA the SF is built on. A previous analysis, also based on the comparison to electron scattering data, derives a shift in the removal energy which is different for carbon and oxygen targets, and the differences in probes between neutrinos and antineutrinos [178, 306]. These can be combined into one overall correction factor, with

$$(\Delta E_B)_{\nu,T} = \delta_{\nu,T} + \alpha(m\mathbf{q_3} + c)\,, \tag{5.12}$$

where $\delta_{\nu,T}$ is the removal energy correction for neutrinos and antineutrinos (ν), for a partic-

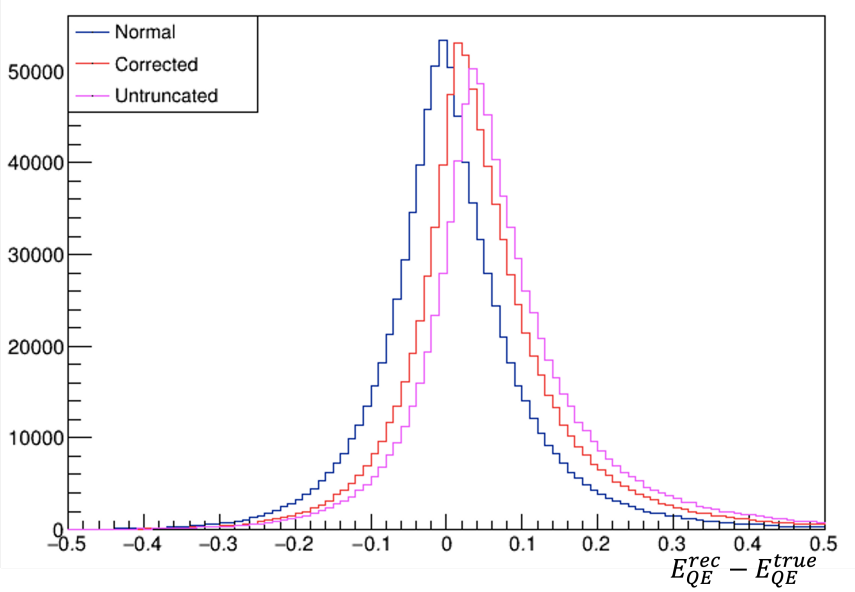

Fig. 5.17: Effect of the $\mathbf{q_3}$-E_B correction on the reconstructed neutrino energy. The red shows E_{QE}^{rec} with the removal energy truncated to zero, while the magenta is the same without the truncation. The blue histogram shows the normal distribution for reference. The correction biases the reconstruction substantially, with the truncation improving this issue.

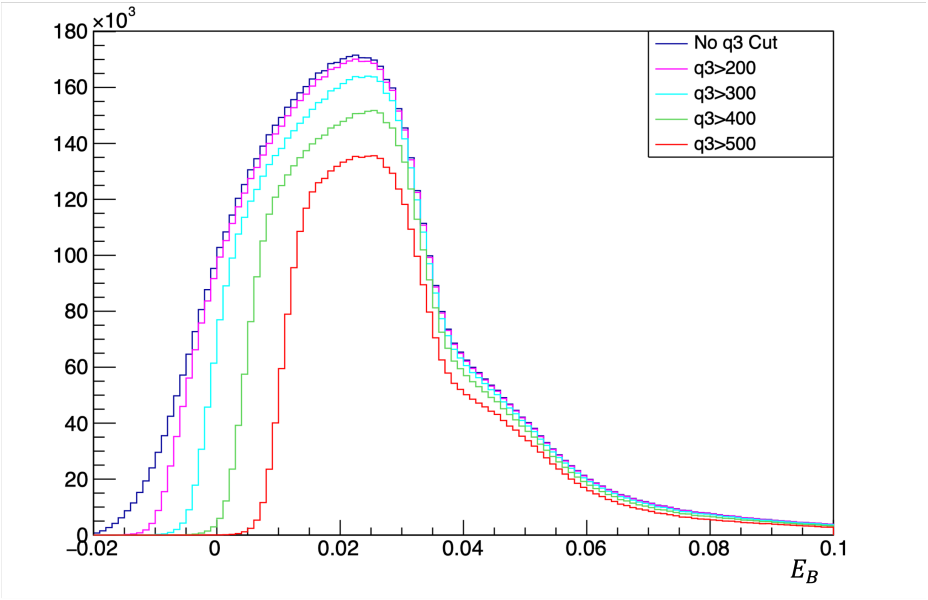

Fig. 5.18: Corrected missing energy distributions with different momentum-transfer cuts applied. These could be used in place of truncating the distribution to zero, however this removes a substantial proportion of events.

ular target (^{12}C or ^{16}O) derived from the previous analysis; m and c are derived from the analysis presented here; and α controls the strength of the $\mathbf{q_3}$-correction.

The m and c parameters should be fixed at the value derived in the analysis, however α can vary between 0 (no correction) and 1 (the full correction applied). There are small uncertainties from the fit above (full uncertainties will be described later) however these have little impact on model predictions, and these do not cover the full list of uncertainties that would need to be included for a full T2K oscillation prediction. It is only assumed that the correction is only a function of $\mathbf{q_3}$ and any other kinematics of the interaction, such as q_0, incoming lepton energy or scattering angle have been ignored. As the correction is derived for electron scattering, the fit as derived here may not be entirely applicable to neutrino scattering, as the different coupling constants (more specifically the inclusion of $1/Q^4$ for the massless propagator) means that a particular slice of $\mathbf{q_3}$ will sample different ranges of q_0 for electrons and neutrinos. Thus the uncertainties from the fit are not used as priors for the oscillation analysis, but that both the nominal SF (with no $\mathbf{q_3}$) and the SF with the full correction applied are completely covered by the prior uncertainties.

However, there comes a problem with the inclusion of this correction into oscillation fitters. These fitters take all the unknown parameters and allow them to vary until the parameters maximise the likelihood[2]. The problem with implementing the correction is the fitters need access to the individual events (and their kinematics) in order to apply it. Out of the fitters used by T2K (p-theta, VaLOR[3] and MaCh3[4]) only MaCh3 has access to this information as the only one based on Bayesian statistics. This lack of access to events is a problem as if a fitter cannot obtain the momentum transfer, then the δ and α dials (values these parameters can vary between) cannot be implemented. To work around this, the dials were tested in MaCh3 to assess their impact on the oscillation analysis and, if producing radically different results than the two others, the uncertainties on each of these dials would be inflated.

Once this was performed, it became clear the α parameter derived in this analysis was not having a large impact. Indeed, the fit value in MaCh3 settled on 0. Whilst at first glance this may appear unexpected, this is actually a rather unsurprising result once the other implemented dials are considered. Within the CCQE systematic constraints, Fig. 5.19, there are two dials controlling the impact of an optical potential (section 2.3.4). However, as will be discussed in more detail later, the inclusion of an optical potential is capturing the same features as the kinematic dependent removal energy. This means that dials controlling an optical potential and $\mathbf{q_3}$-E_B will be strongly anti-correlated, as both are working against each other to include the same features. Therefore, it is expected that with the optical potential dials there will not be any effect observed from the $\mathbf{q_3}$-E_B dial.

Though it is unlikely the effect of the dial will be seen in the oscillation analysis due to the optical potential dials, if these were not included a much greater effect from the kinematic

[2]This actually depends on whether your fitter uses frequentist or Bayesian statistics, but is a sufficient explanation for here.

[3]Valencia, Lancaster, Oxford, Rutherford Group.

[4]Which stands for MArkov CHain Monte Carlo, or MCMC.

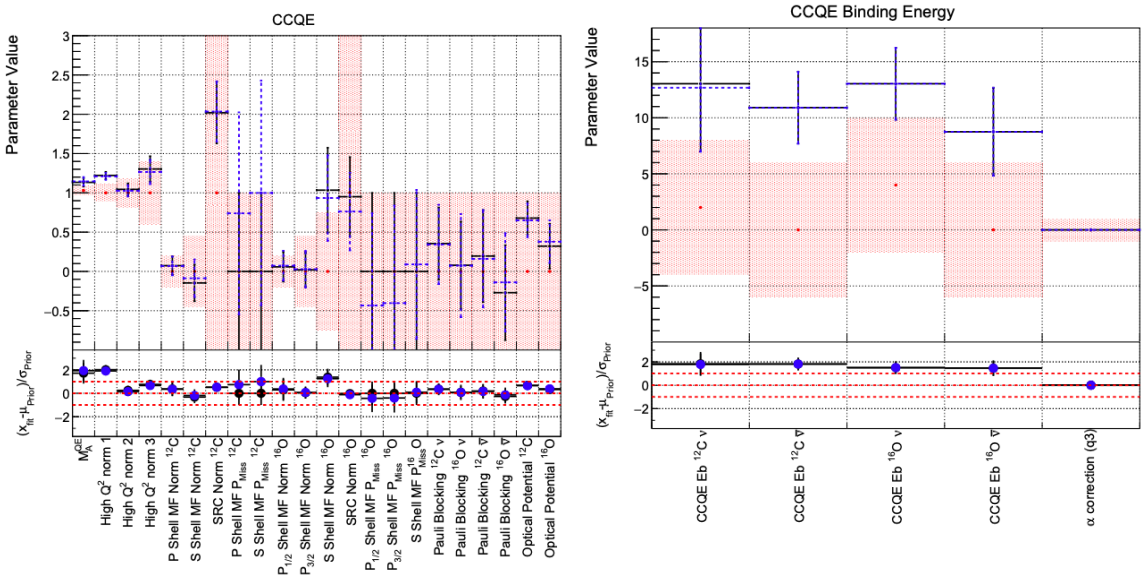

(a) (b)

Fig. 5.19: Systematic constraints for the cross section parameters for **(a)**, the CCQE interaction and **(b)**, the removal energy dials. On the plots, the red shows the prior constraints, black is the near detector only fit and blue is the near detector plus SK fits.

dial would have been observed. However, as this effect is only included at the oscillation analysis stage, it is still important to have this correction included in the NEUT generator in order for analyses to make accurate predictions of neutrino (and electron) cross-sections.

5.3 2p2h Interactions

The above analysis assumed the elastic peak in the electron scattering data consists entirely of 1p1h elastic scattering events. As is clear from Fig. 5.4, there is a large contribution from electron-induced resonant interactions, and also from 2p2h interactions. Some of these latter interactions are accounted for within the SF ground state (in the form of short-range correlated pairs), but the contribution from meson-exchange currents (MEC) has yet to be included, and will help to fill in the dip region.

However, the development of a MEC interaction event generation is much more involved, and cannot be derived simply from the neutrino interaction like the simpler CCQE/NCE interaction. The SuSAv2 model implemented in the GENIE generator has included 2p2h excitations from MEC interactions using full microscopic calculations based on an RFG model[5] [307, 308]. Using this GENIE implementation, one can estimate the contribution from the final channel in the elastic scattering regime.

An example of NEUT predictions with GENIE 2p2h contributions is shown in Fig. 5.20. The inclusion of the 2p2h channel could be completed in two ways: scale both the NEUT 1p1h and GENIE 2p2h events to a full cross-section prediction and sum their responses; use the relative strength of the GENIE 1p1h and 2p2h channels to influence the NEUT events. As the

[5] Yet another example of the Frankenmodels used in generators.

overall normalisation of the predictions is not relevant for this analysis (*i.e.* a full scaling to a cross-section), it was decided the latter would be a more correct approach. Therefore, any differences in the factors absorbed into the lepton and hadronic tensors of the two generators would not effect the calculation here. As such, the NEUT and GENIE events are scaled by the same factor before the MEC contribution is added to the predictions, ensuring the strength of their inclusion is the same.

Whilst not a large contribution to the elastic peak, the MEC contribution has a greater influence over the tail of the elastic channel, slightly shifting the position of the peak further away from the data. Once again, a 5^{th} order polynomial can be fit to the peaks in order to derive the same correction as above, shown in Fig. 5.21. The inclusion of the MEC channel shifts the peaks slightly towards increased energy transfer, thus one would expect a greater gradient than the fit without MEC. Interestingly, the gradient is shallower, 0.044 ± 0.005 as opposed to 0.056 ± 0.005. This effect is likely due to the 2p2h contributions having a greater influence at the higher values of $\mathbf{q_3}$, where the elastic peak of the predictions naturally matches more closely with the data or returns a positive value of ΔE_B. The 2p2h inclusion effects these fits greater, thus the points at high $\mathbf{q_3}$ shift further down than those at low values and cause a shallower $\mathbf{q_3}$-E_B fit.

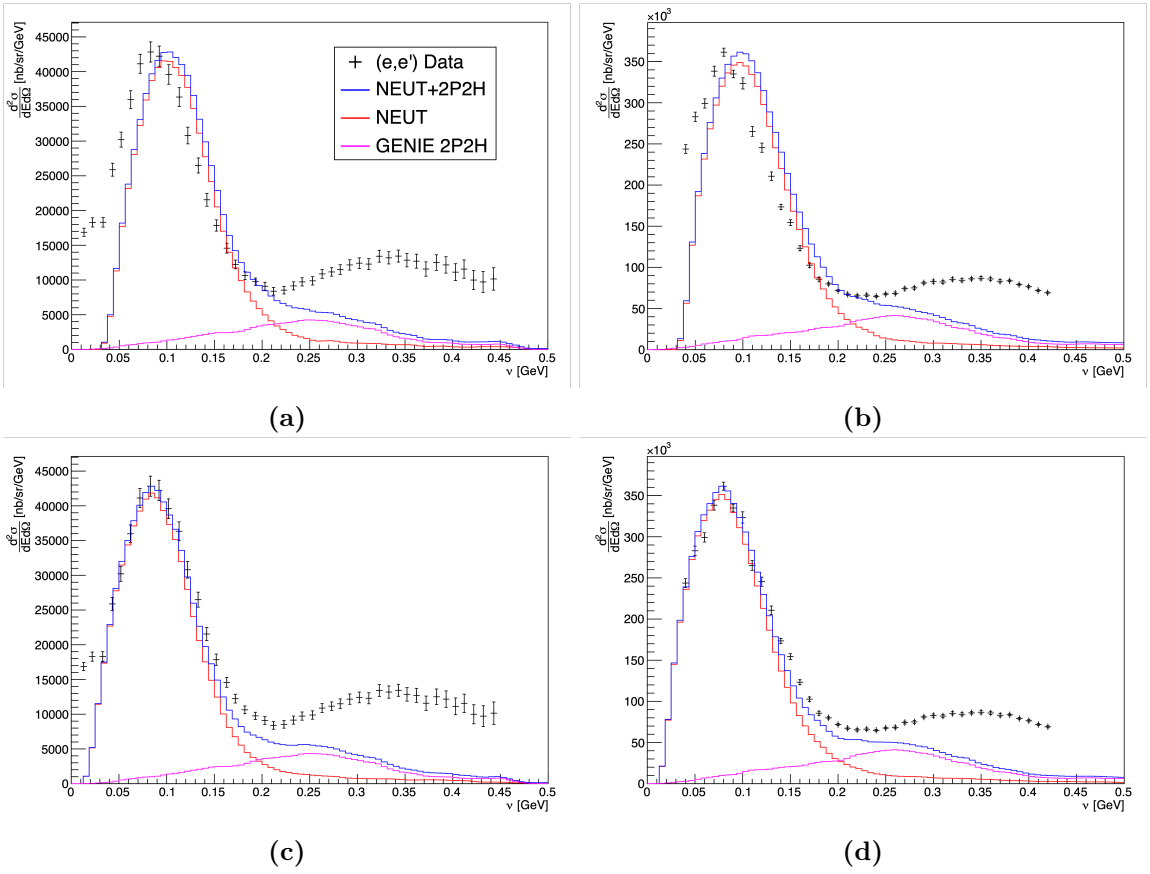

Fig. 5.20: NEUT electron scattering prediction including the GENIE 2p2h contribution. The strength of the 2p2h component is scaled to be identical to its contribution to the GENIE prediction. The beam energies and scattering angles are: **(a)** and **(c)** 620 MeV at 36°, **(b)** and **(d)** 1.5 GeV at 13.54°. *Top.* Plots pre-kinematic removal energy. *Bottom.* Post-kinematic removal energy.

Once the fit is applied, Fig. 5.21b, applying the derived fit once again fully corrects for the kinematic dependence of the removal energy. The electron scattering predictions with 2p2h included fit the shape of the (e,e′) data much closer than without its inclusion. These also, remarkably, fit better than the pure 1p1h prediction, though this is likely due to the better description of the dip region. The left hand side of the elastic peak is fit extremely well, as well as the region around the peak itself, with the only discrepancies occurring near the dip region. This is filled in slightly with the MEC interactions, however there still remains a missing contribution from resonant (RES) interactions.

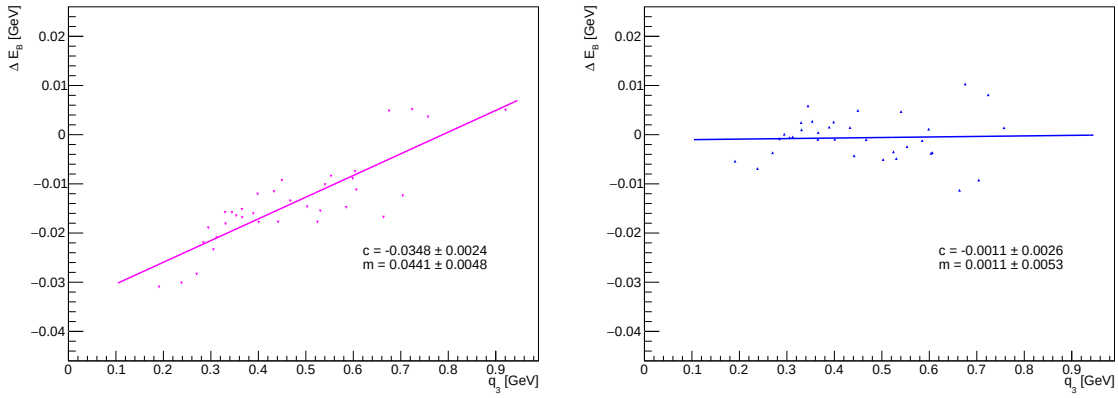

(a) **(b)**

Fig. 5.21: $\mathbf{q_3}$-E_B effect with the inclusion of 2p2h interactions. Surprisingly, this has a shallower gradient than the pure 1p1h prediction.

For a complete description of the elastic peak, the Δ-resonance would also need to be included. Recently, an updated description of this region was developed into a model known as SuSAv2-Δ, which unifies the elastic and RES interactions under the super-scaling framework [307, 309]. Once the quasi-elastic and 2p2h contributions were subtracted from the experimental inclusive electron cross-sections, the resulting cross-sections showed a similar scaling as the quasi-elastic regime. Including this model in the future, and other inelastic contributions such as deep inelastic scattering, would improve the fit to the data. However, this would not substantially change the correction to the elastic removal energy at the kinematics of interest for the T2K experiment. If this were to be expanded towards higher energy transfers, it is likely these would contribute more substantially. However, once these higher ν values are reached, the validity of the derived correction comes under question. This will be discussed further in section 5.7.

5.4 Charged Current Quasi-Elastic Framework

In chapter 4, it was described in detail how neutrinos were converted to electrons inside the NEUT generator. It was decided that neutral current elastic interactions would be used as a framework, due to differing isovector and isoscalar contributions; this is fully described in section 4.2.1. However, as T2K's main signal process, it is important to make sure there are no large differences between using NCE and charged-current quasi-elastic (CCQE)

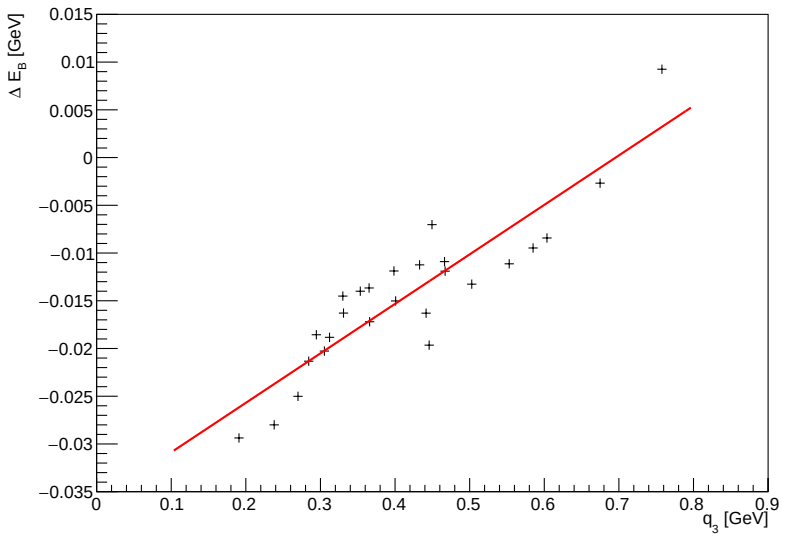

Fig. 5.22: $\mathbf{q_3}$-E_B fit using the charged-current interaction as a framework for the interaction. As the different isoscalar and isovector effects enter via the form factors, one does not expect a difference between two frameworks. The fit parameters are $m = 0.052 \pm 0.005$ and $c = -36 \pm 2$, shallower than using NC, though this is within the fitting error.

interactions as a foundation.

From a purely theory perspective, as the derived $\mathbf{q_3}$-E_B only depends on the position of the elastic peak, the overall normalisation will not effect the fit. The two interaction channels use the same Llewellyn-Smith model, only differing in the nucleon form factors, which have been altered for electron scattering. As the isovector component of neutrino charged-current interactions is built into the nucleon form factors themselves, theoretically there should not be a difference between using the different models for the framework.

However, as is shown in Fig. 5.22, the gradient of the fit is slightly shallower than when using NCE as a framework, although they agree within the uncertainty. This is still somewhat surprising, as comparing the lepton energy transfer for both models shows they are indeed very similar, seen in Fig. 5.23. Though seemingly similar, there is a systematic shift to slightly lower energy transfers when using the CCQE interactions, clear from the ratio of the two channels. This difference is small, but is enough to cause a $\sim 7\%$ shift in the fit gradient.

This variation between the models is likely due to mass effects of the final state. In the neutral current predictions, it is assumed both the initial and final state are massless, with the mass not being included in the calculations of the kinematics. This is not the case in the charged current interaction, where the final state is a massive, charged lepton. This also makes sense with the shift direction, as some of the energy transferred is being 'lost' in the creation of the massive outgoing lepton. This hypothesis is also backed up by the fact the size of this difference decreases as the energy of the incident lepton increases, as is seen in the differences of the ratio in Fig. 5.23. The higher incident particle energy of 1500 MeV shows only a small difference (a few percent) as opposed to the $\sim 10\%$ difference in the 620 MeV particle.

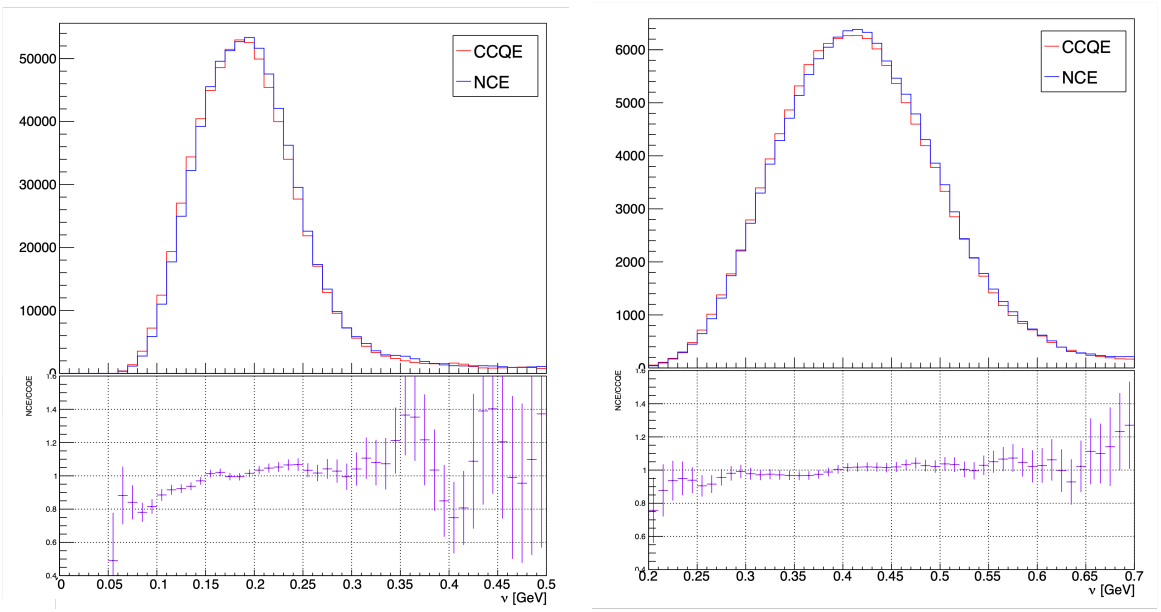

(a) **(b)**

Fig. 5.23: Difference in lepton energy transfer between using CCQE and NC as a framework. While similar, there is a small shift in the peak to smaller energy transfers for the CCQE channel. This is clearer in the bottom panels, showing the ratio of neutral to charged current. This is likely due to mass effects. **(a)** Incident energy 620 MeV, 60° scattering angle. **(b)** Incident energy 1500 MeV, 37.5° scattering angle.

Whilst this slight difference is not ideal, it does not pose a problem to the fit derived here, as the deviation comes entirely due to mass effects. This difference will be negligible once propagated to the T2K observables, and is entirely covered by the CCQE fitting uncertainty.

5.5 2D Minimization

Whilst the polynomial fit to the data gives a good description of the peak, it is sensitive to the choice of fitting region and the particular binning chosen. This is described slightly further in the following section, however it still relies on making sure the fit is good 'by-eye' to the shape in order to derive the correction. One can also minimize the χ^2 returned by the polynomial fit over different fitting and binning regions, however to some extent this relies on the analyser as often a minimised fit can describe the data poorly. This can never be negated completely, however the analysis was extended further to reduce this effect and test a new method of deriving the correction.

Moving beyond the polynomial case, one can also fit the simulation directly to the data. By artificially shifting the peak, the χ^2 between the data and prediction can be minimised until the best fit is found. Once again, the overall normalisation is not important, and thus the strength of the elastic peak can be varied simultaneously during the minimisation. In this way, a two dimensional search can be completed over the removal energy shift and total normalisation of the prediction, thus hopefully reducing the input from the analyser.

Once a NEUT prediction has been made, one has to be careful with artificially translat-

ing events, as moving them between bin boundaries can cause the resulting histograms to produce un-smooth distributions unlike the originals. This is a result of altering the final state kinematics and not the underlying removal energy, and thus the event kinematics have not been recalculated. On a small scale of shift, up to $\sim$ 10 MeV, this does not cause a problem, any higher can produce difficult to describe distributions: this is a particular problem when attempting to match the binning of the electron data. Examples of the irregular distributions are shown in Fig. 5.24, after undergoing smoothing.

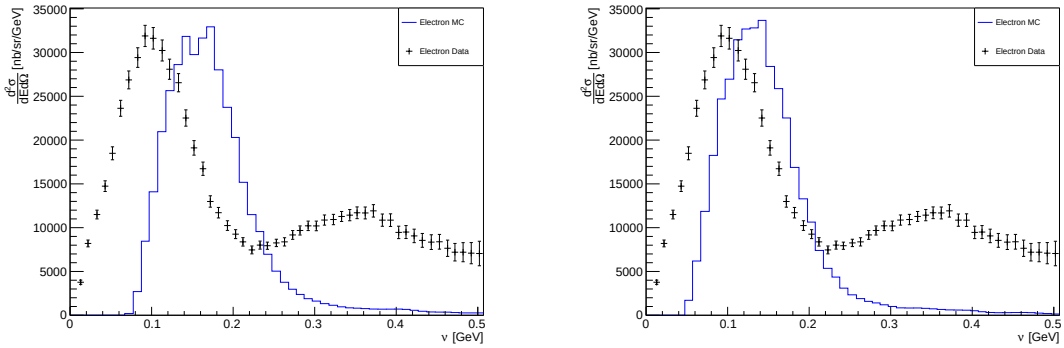

(a) **(b)**

Fig. 5.24: Effect of artificially shifting events between bins. Both show the same data (incident energy of 620 MeV and a scattering angle of 36°) with a different shift applied in each case. It is clear this causes the shape of the prediction to become distorted.

To mitigate this, the difference derived from the polynomial fit is applied to the removal energy during event generation, for each incident energy and scattering angle to ensure the elastic peak is already close to correct. Note this is not the $\mathbf{q_3}$-E_B fit, but the individual measurement. The generated peak is also scaled to match the strength of the (e,e′) elastic peak. Once this is completed, the peak is allowed to vary between ±10 MeV at 1 MeV increments, with the peak height varying between 0.9 and 1.1 times its original value, in increments of 0.01. The NEUT predictions are binned in the same way as the electron data, with the bin boundaries set as the midpoint between neighbouring data points. At each combination of removal energy shift and normalisation, the reduced chi-squared test is used to test the goodness-of-fit, *i.e.*

$$\chi^2_N = \frac{1}{N}\sum_{i=1}^{N}\frac{(B_i - D_i)^2}{D_i}\,, \tag{5.13}$$

where N is the number of data points in the particular set of electron data (*i.e.* the degrees of freedom), B is the NEUT bin and D is the specific data point. This is minimised for each energy and angle. Examples of the 2-dimensional grid search are shown in Fig. 5.25.

Once the value has been measured from the χ^2 minimisation, this is applied on top of the previously derived fit. The error was estimated by using half the size of the bin width for the energy shift, 0.5 MeV. This produces a new fit function, shown in Fig. 5.26. Although for most energies and scattering angles there is a reasonable fit to the elastic peak, in some

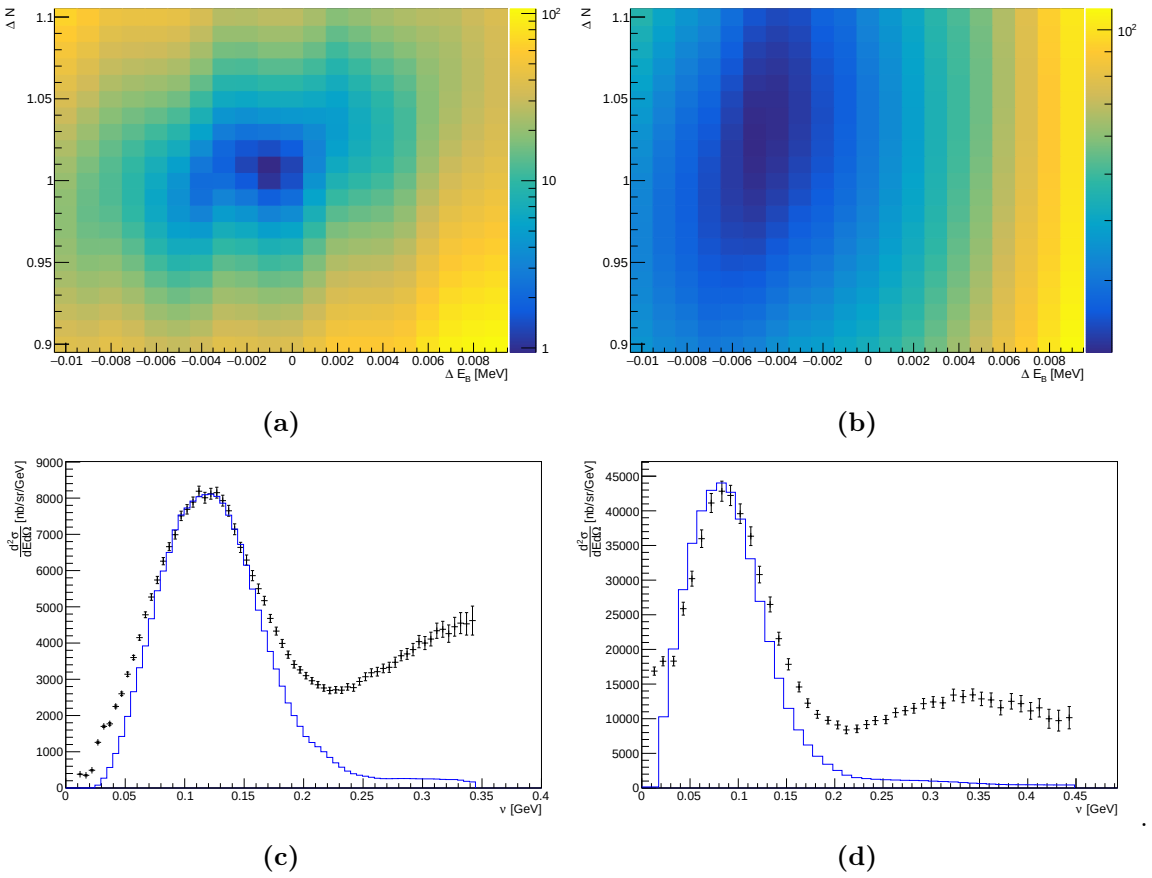

Fig. 5.25: The χ^2 surface for the 2-dimensional fit of the change in removal energy, ΔE_B, and normalisation, ΔN and their associated best fit energy transfer plots. **(a)** and **(c)** have incident energy of 480 MeV scattered at 60°, and **(b)** and **(d)** are 620 MeV at 36°.

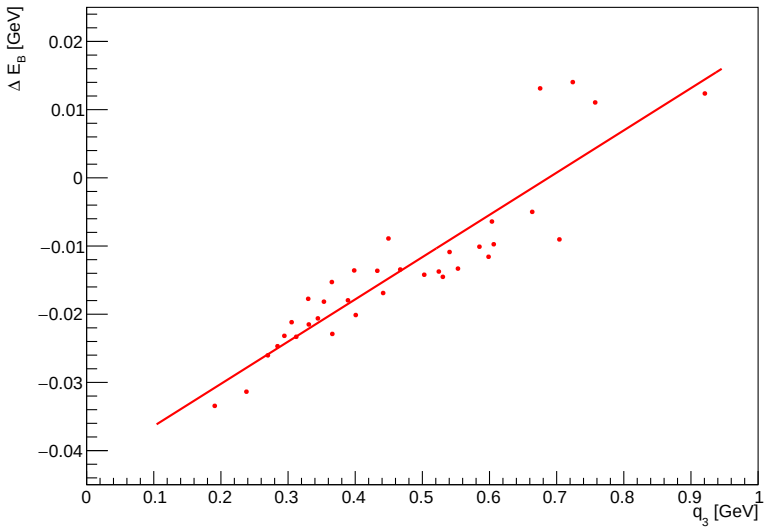

Fig. 5.26: $\mathbf{q_3}$-E_B fit including both the polynomial fit and χ^2 minimisation. These data come from fitting both the normalisation and energy shift. The fit gives parameters of $m = 0.062 \pm 0.005$ and $c = -0.043 \pm 0.002$.

cases there are clear problems. The most obvious disparities from the data come with the inclusion of 2p2h and RES interactions (*i.e.* transverse data sets), as such minimising the reduced χ^2 tends to shift the peak further to left to match with the 'rise' of the elastic peak. This is clearer in the data that does not feature the 'giant resonances', where the probe has scattered off the entire nucleus. In this situation it was chosen to keep the peak as measured with the polynomial fit, as the predictions clearly did not match the data. However, this is the case in only a small group of the sample of inclusive electron data, and the overall technique is an improvement over purely using the polynomial fit.

Fig. 5.26 shows the resultant fit after using the χ^2 minimisation to alter the elastic peak position. As this fit tends to shift the peaks toward lower energy transfers, in a way similar to including 2p2h, naïvely one would expect a similar effect: *i.e.* a shallower gradient. In fact the converse has happened, with the gradient increasing. This effect is not too large, and almost matches the polynomial fit within the errors, however there is a distinct difference. Examining the individual fits, most data are only shifted from the polynomial prediction by a few MeV roughly equally in both the positive and negative directions. However, the larger differences (between 7 and 10 MeV from the polynomial) are always in the lower energy transfer direction, and tend to be toward lower momentum transfers. This forces the fit to a slightly higher gradient. However, the validity of whether these are the true best position of the elastic peak can be questioned and will be discussed later.

Examining both the shift and normalisation phase space is a useful result, however an interesting test of robustness is holding the normalisation fixed and varying the removal energy shift. This is completed in much the same way as above, by minimising the χ^2 over the same ΔE_B range as the 2D fit. The overall strength of the prediction peak was matched to the strength of the elastic peak (negating the inclusion of any other interactions). Fig. 5.27 shows the minimisation curves for the same energies and angles as above for an example.

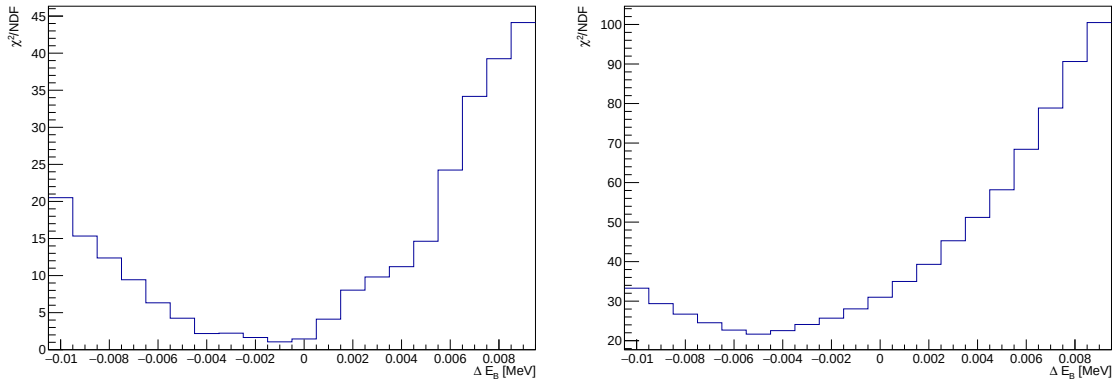

(a) **(b)**

Fig. 5.27: χ^2 minimisation of ΔE_B. These are the same energies and angles as Fig.5.25.

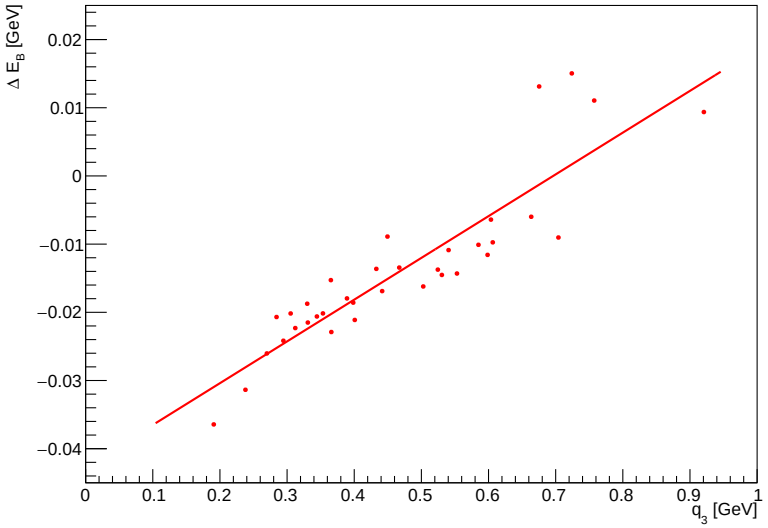

Fig. 5.28: $\mathbf{q_3}$-E_B fit including both the polynomial fit and χ^2 minimisation. As opposed to the above, this is 1D, only varying over the removal energy shift. The fit gives parameters of $m = 0.061 \pm 0.005$ and $c = -0.043 \pm 0.002$.

Again, in a similar way to the above, the gradient of the $\mathbf{q_3}$-E_B relation is larger than the polynomial only fit and similar to the 2D minimisation. Overall the individual fits are similar, however once again their validity can be called into question. It is much more apparent here that the minimisation is not necessarily fitting to the peak, rather the data points surrounding the peak. This is because the low energy transfer region, with its giant resonances, is not modelled well, with the elastic peak rising much quicker than the predictions. This causes problems with the minimisation. While this can be partially accounted for with a careful selection of the data points used in the fit, it continues to prove problematic.

There could be various definitions of the elastic peak that could be used for the χ^2 scans, however in this case it was decided that data likely related to coherent nuclear scattering and giant resonances (in most cases the first 3 data points) would be ignored. Data after the peak maximum were considered up until 2 data points before the data begin to rise again, thus removing any contribution from resonant (and possibly deep inelastic) events.

This could be tuned for each of the data sets and selecting each peak manually, however this negates the reason behind using the χ^2 fit, which was to reduce the intervention needed in producing the fit.

It is interesting to note, although expected, that longitudinal electron data tends to perform better under the minimisation technique than does transverse electron scattering data. The reason behind this is fairly logical, as transverse data includes a stronger contribution from the resonant interactions, which necessarily alter the elastic peak. Future analyses could examine the differences between the longitudinal and transverse data to see if there are any differences between them. One would expect this to be the case, as Fig. 5.1 shows a slightly different kinematic removal energy depending on the channel used, this is more obvious in the RPWIA based model. This would rely on access to a greater selection of electron data, which was not possible in this thesis. Perhaps with new data from the CLAS12 detector, this could become possible in the future.

Due to the reasons above, it was decided that only the polynomial fit would be used for the inclusion into NEUT and the oscillation analysis. This was mainly due to the tendency of to produce too large of a shift and fitting the rise of the peak as opposed to the peak itself. For a more complete fit, the analysis discussed here could be tuned to a higher degree, with a more careful selection of the data that describe the elastic peak. The differences between the χ^2 minimised fit and polynomial fit do not, however, produce an appreciable difference when extrapolated to the effect on the T2K observables, and the fits themselves match each other within their errors.

It is possible this method could be used to expand the search to a greater variety of data, particularly at the higher energy transfers. At higher transfers, it is often the case the data do not show an elastic peak as the measurements do not continue far enough to include the peak. Using this technique, it could be possible to minimise the lepton transfer just on the rise of the elastic peak as opposed to the peak itself. This option is not explored here however.

5.6 Systematic Uncertainty

In section 5.2, the kinematics dependent removal energy was introduced in order to correct for an observed disparity between the elastic peaks from predictions and observed data. This was derived using a polynomial fit to the peaks of both distributions. The error of the overall $\mathbf{q_3}$-E_B fit was taken and considered for the oscillation analysis, with it being observed that a change in the values had a minimal effect on the observables p_μ and $\cos\theta_\mu$. It was decided for a first pass on the analysis, the inclusion of the correction was more crucial than their error, as this should be covered by the prior uncertainty in the oscillation analysis. Here will discuss applying an appropriate systematic to the fit.

The value of the shift calculated from the peak positions relies on two things: the chosen fitting region and the histogram binning. In order to estimate the uncertainty on each of these points, both of these were varied around their nominal values (*i.e.* those giving the

best fit by eye) and their average result is used for the fit. The standard deviation can then be used as their associated error. Figs. 5.29 and 5.30 shows the variation of the histogram binning and fitting region respectively.

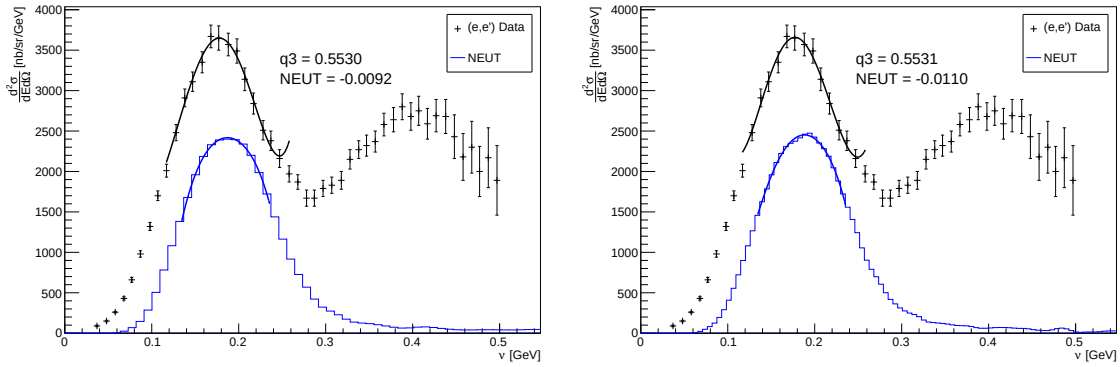

(a) **(b)**

Fig. 5.29: Two extremes of the number of bins (or bin width) for the polynomial fit, with **(a)** having 60 and **(b)** having 100. This is for an incident energy and scattering angle of 620 MeV and 60° respectively. In this case, the changing bin width changes the shift fit by 2 MeV.

The binning is calculated from 0 to the end of the electron data, and was varied between 60 and 100 bins in 10 bin increments. Due to the differences in electron scattering data, this means that each data set will have a slightly different number of bins in the elastic peak. This is not necessarily a problem, as long as the number of bins vary the exact number of bins in the peak should not effect the result. The two extremes of the number of bins are shown in Fig. 5.29. In the case of the examples above, the varying bin width alters the shift calculation by ~ 2 MeV, which is common across all data. The lower bound of 60 bins was chosen as any lower began to cause problems with a sparse sample of bins over the elastic peak, causing obvious deviations of the fit from the peak itself.

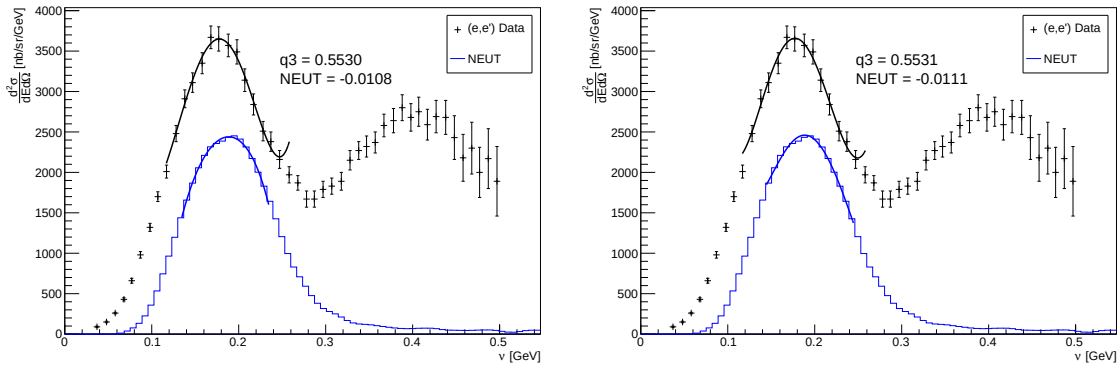

(a) **(b)**

Fig. 5.30: The two extremes of the fitting values for the polynomial fit. The nominal values were varied by ±5 MeV. In this case, with the same energy and angle as Fig. 5.29, this does not cause much of a change in the value of the shift.

For the fitting region, the nominal value of the fitting regions was chosen as the one

that described the peak best by eye. This was allowed to vary by ±5 MeV in 2.5 MeV increments. Varying the region any larger, in a similar fashion to a larger bin width, produced clear disparities from the prediction. In general, this caused up to ∼2 MeV changes in the differences in the peaks.

Thus far, the variation has only been applied in the simulated data, as these are much simpler to manipulate. In the case of the electron data, it is constrained by the format in which the data is provided. This makes it difficult to vary fitting regions (and impossible to alter the binning) as in most cases there are few data points in the elastic peak, thus each peak has been specifically tuned in order to give a good description with the polynomial. Changing these tunes can give wildly different fits which are clearly incorrect. Due to this, it has been chosen to keep the data fits fixed and only vary the fitting of the simulation, assuming the error calculated will encompass any errors that would be calculated varying the data fit.

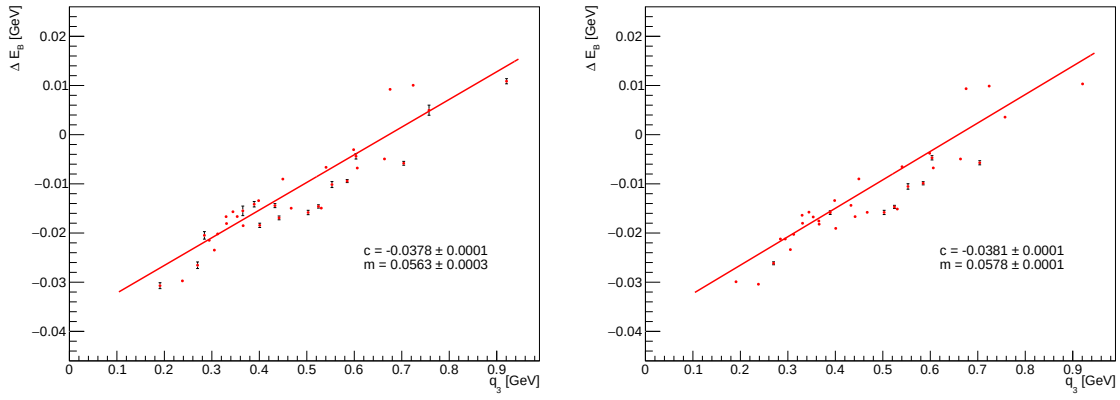

(a) **(b)**

Fig. 5.31: Standard $\mathbf{q_3}$-E_B relation for the SF, calculated with varying the **(a)** bin width and **(b)** fitting region.

Fig. 5.31 shows the resultant fits varying the different fitting parameters on the NEUT predictions. These give similar values to the data without varying the parameters, as is expected. Combining these, the gradient and intercept are $m = 0.0571 \pm 0.0003$ and $c = 38.0 \pm 0.1$ MeV, matching nicely to the fit from before. As these match closely, it adds some validity and robustness to the fits produced without the inclusion of the systematic. As mentioned before, this error is very small compared to the overall systematic on the removal energy, and the prior uncertainty entirely covers them, thus do not need to be considered in the oscillation analysis. Again, as stated at the end of the previous section, either extreme of this error does not effect T2K observables, thus is ultimately irrelevant as applied within the event generation.

5.7 Validation

This chapter has focused on deriving a correction to the removal energy, motivated by its indication from more sophisticated microscopic calculations used in the RMF model. In this

way, the simple IA NEUT is built upon can begin to be broken, by including some form of kinematical dependence on the nuclear ground state model. The method applied here is not based on any theoretical calculations, but derived empirically comparing predictions to data. However, while there are many methods of moving beyond the IA, the overall result for any particular ground state model should remain the same, thus each model can be directly compared to each other.

The different ways of moving beyond factorising the ground state and the interaction vertex were mentioned in section 2.2, however these will be summarised again quickly here. SuSAv2 utilizes superscaling behaviour exhibited by electron scattering that suggests all nuclear effects can be extrapolated by applying an appropriate scaling function, $f(\psi')$ - where ψ' is the scaling variable, derived from the ratio between the experimental quasi-elastic cross-section and the corresponding single nucleon one. This works extremely well in the QE region and below ($\psi' < 0$), but begins to break down where other interactions start to dominate (above the QE peak), this is shown in Fig. 5.32. SuSAv2 also automatically builds nucleon final state interactions into the model using relativistic mean field calculations, treating the nucleon kinematics in the same potential for the initial and final state. The crux of this means the model reproduces the asymmetric scaling function (as opposed to the symmetric RFG), along with predicting a shift in the QE peak as a direct consequence of the incident lepton kinematics.

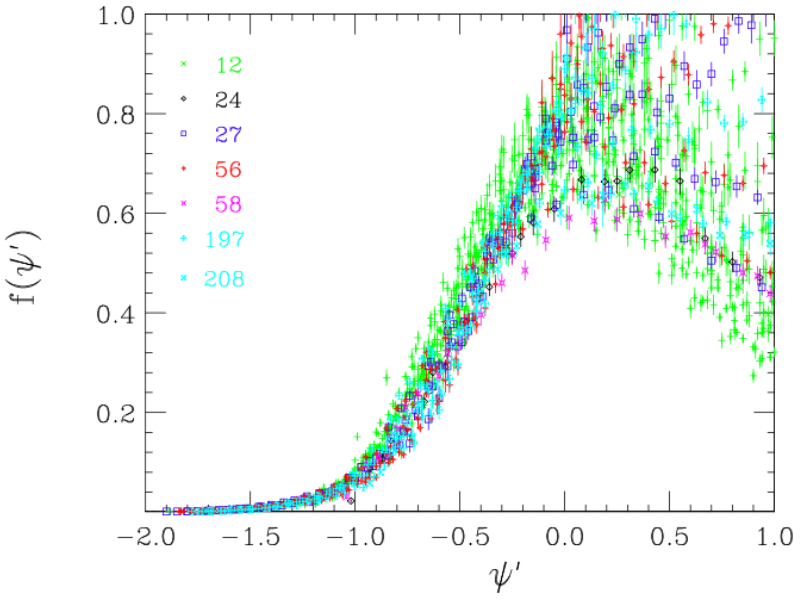

Fig. 5.32: A comparison of scaling functions ($f(\psi')$) for complex nuclei (with $A > 12$) as a function of the scaling variable, ψ' over a large range of kinematics. These begin to diverge at $\psi' > 0$, where inelastic contributions become important. Taken from [187].

Similar to the RMF, by reducing a many body problem to a single mean field, one can calculate the absorption effect from the resultant nucleus using a complex potential, known as an optical potential model. Within this, the absorption (inelastic channels) and scattering parameters are automatically applied to the outgoing lepton. These models also consider surface and volume terms, which describe the difference between 'surface bound' nucleons

and those more highly bound, or 'volume' nucleons, that are accessed at higher energies. This once again builds the lepton kinematics into the interaction, thus not being limited by the IA approach.

The linear fit derived in this chapter can be compared to these different approaches of moving beyond the limits of the IA which, although simplifying the calculations, breaks down at low energy transfers. Fig. 5.33 compares three event generators, each of which use one of the methods described. GENIE has been generated using the SuSAv2 model and thus uses superscaling; the linear fit has been taken from the derived fit to the shift of the superscaling function peak, and implemented as a change in the removal energy during generation. NUWRO implements the optical potential model on top of the Benhar-Fantoni SF, offering a direct comparison to this correction. Under normal parameters, the model predicts the elastic peak of electron data well, however turning off the optical potential calculation removes its contribution to the final state lepton. This acts as an impulse approximation model and, although this is changing the lepton kinematics, effectively maps to a change of the nuclear state and more specifically the removal energy. Fitting these in the same way as the $\mathbf{q_3}$-E_B correction was derived in the above sections can lead to a comparison in the two techniques. Finally, NEUT uses the fit derived in this thesis. The difference with and without the optical potential is shown in Fig. 5.34. Table. 5.3 contains a summary of the fits, including the RFG model and the inclusion of 2p2h interactions.

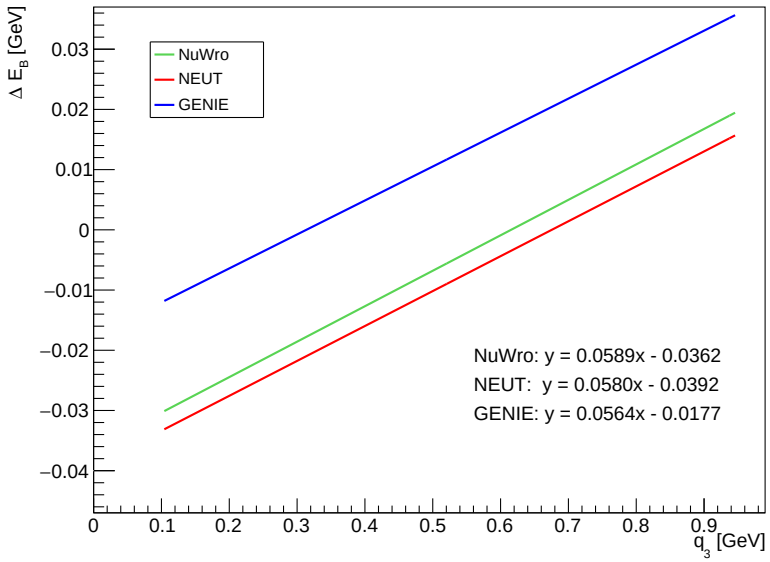

Fig. 5.33: Comparison of the techniques moving beyond the impulse approximation, with each generator utilising a different method. NEUT uses the fit derived in this chapter, NUWRO uses an optical potential and GENIE is based on SuSAv2. Each model produces a very similar fit.

At first glance, it is only the optical potential and $\mathbf{q_3}$-E_B that agree with each other. However, in this case it is only the gradient of the fit that matters, as the intercept is governed by the initial value chosen for the removal energy. As is clear from both Fig. 5.33 and Table 5.3, the independent methods of including a kinematic dependent removal energy match each other extremely well. Whilst their validity could be measured by the ability to

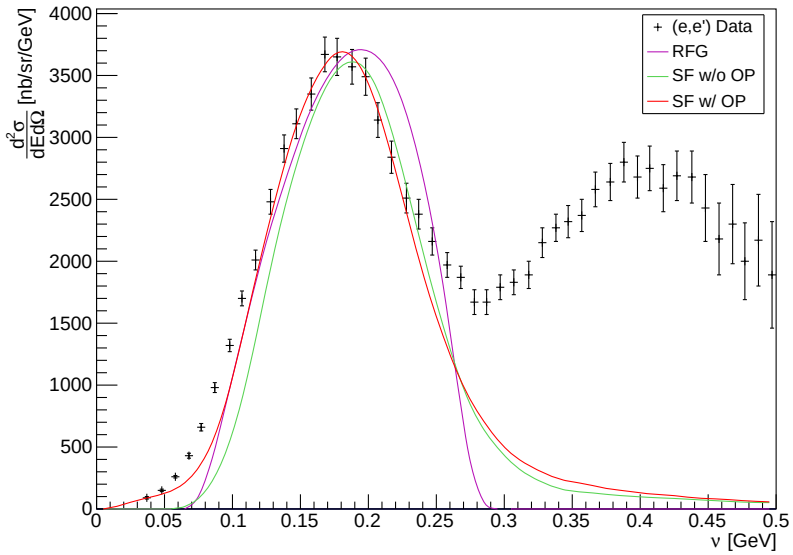

Fig. 5.34: NuWro predictions for various models compared to inclusive electron scattering data with incident energy of 620 MeV and scattered at 60°. The shift between using the optical potential and not is clear, and can be attributed to the removal energy. Shown also is the relativistic Fermi gas without the optical potential for reference.

	Gradient (m)	Intercept (c) [MeV]
Neut	0.057 ± 0.0003	-38.0 ± 0.1
NuWro	0.057 ± 0.005	-38 ± 2
Genie	0.0564	-17.7
Neut RFG	0.043 ± 0.006	-27 ± 3
NuWro RFG	0.046 ± 0.005	-36 ± 3
Neut + 2p2h	0.044 ± 0.005	-35 ± 2

Table 5.3: Results from the individual $\mathbf{q_3}$-E_B fits. Neut and NuWro are assumed to use a spectral function unless specified. Genie uses the SuSAv2 model. The 2p2h inclusion comes from genie.

predict the available electron data, the fact that each predicts a similar dependence of the removal energy on the momentum transferred is an important result. The extremely similar results of the gradient and intercept of the optical potential and $\mathbf{q_3} - E_B$ fit is interesting, as these models both use the Benhar-Fantoni SF as the ground state model and therefore use the same removal energy as a reference.

Interestingly, although one expects similar models to produce similar fits, it is important to note the SuSAv2 model implements a very different ground state to the other models derived here, using superscaling and RMF theory, yet produces a consistent result with those using the SF. Replacing the ground state in these latter models with a relativistic Fermi gas produces a very different result. Fig 5.35 shows the RFG results for the NuWro optical potential. Whilst this matches the neut RFG prediction (Fig. 5.7) in their gradients, their intercept is very different, indicating the different generators use a different starting point for their Fermi removal energy but the kinematic dependence of this energy is the same (which, of course, it should be).

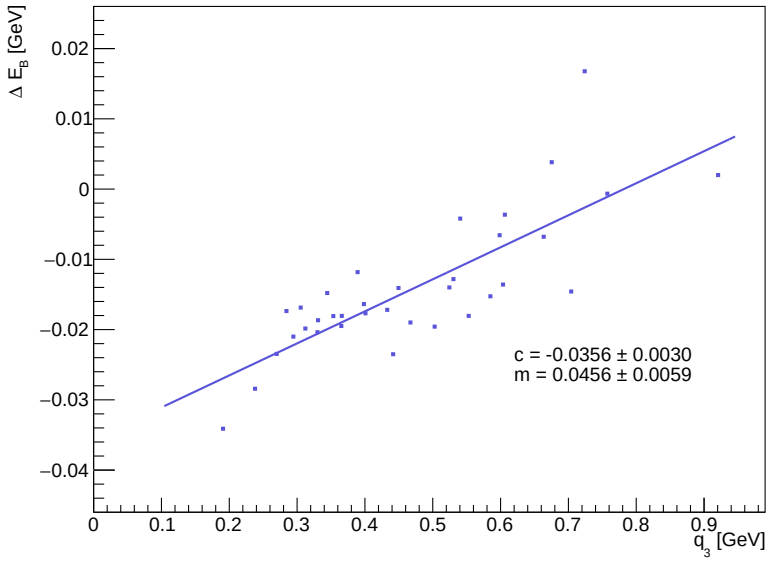

Fig. 5.35: $\mathbf{q_3}$-E_B fit for the RFG model using NuWro with the optical potential switched off. As expected, this model produces a similar gradient to the neut RFG, however the intercepts are much different due to the different reference removal energies.

The differences between two separate ground state models (and similarities between the methods of moving beyond the IA) adds a layer of confusion as to why two separate ground states models (SuSA and the SF) are so consistent. This could lie on the side of coincidence, however is likely a consequence of the two models being based on electron scattering data: the SF a shell model built from the missing energy in the data, and SuSA derived from the electron scattering cross-sections. These are designed to be able to reproduce electron scattering data and the corresponding nuclear system and thus both produce the same kinematic dependence of the ground state. This again adds some validity to both of the models.

As all models produce similar results, the usefulness of deriving a new method of moving

beyond the IA could be brought into question: there is no point in reinventing the wheel. However, the more theoretically based models (superscaling and the optical potential) are based on detailed and complicated calculations that are extremely computationally expensive. The method developed here, however, is built upon the IA framework that simplifies all the calculations. Applying the simple $\mathbf{q_3}$-E_B fit at generation includes only a few extra calculations, whilst able to predict the data to a similar degree as other, more complex models, reducing the computational expense without forfeiting prediction power. Though this is, of course, at the expense of a having a theoretically rigorous model.

The final thing to mention is in what $\mathbf{q_3}$ phase space the correction is applied. It should be noted that at high $\mathbf{q_3}$, where the energy imparted on the struck nucleon is high, the outgoing nucleon has a high kinetic energy such that any FSI effects should be suppressed. This also applies to the removal energy shift, where at high energies this $\mathbf{q_3}$-dependence should begin to drop off. Within the SuSAv2 model, the q-dependences of the RMF and RPWIA models are blended as the momentum transfer increases. Energy-dependent optical potential models also take this into account. Within our parameterisation, it is unclear whether this change into a more flat momentum dependence will be seen as this high $\mathbf{q_3}$ data was not available (or the elastic peak could not be observed). However, as this is derived directly from electron scattering data, one would expect this to present itself if the data were available. For the moment, it is suggested the shift is applied over all energy transfers, but if any further analysis is completed this should be the first investigation. This could be combined with a more thorough χ^2 analysis, which could be used to measure the energy shift without an elastic peak, but only from its rise.

Chapter 6

Super-Kamiokande Detector Monitoring

Good luck, son. I'm moving to Solihull.

Pepe (S2E7 18:01)

The work completed in previous chapters has involved neutrino interaction simulations as inputs for oscillation analyses. This would not be possible without a far detector to measure the oscillated beam, which in turn would not be functional without a full and detailed calibration campaign. This chapter will describe the general process behind the Super-Kamiokande (SK) calibration system, particularly focusing on the laser analysis. This will be followed by a description of the recently installed UK Light Injection (UKLI) system and the efforts by the author to use this system for monitoring the detector's water quality. During the time working on the system, the author acted as a system expert, giving regular updates on its functioning and producing the first analysis using the data.

6.1 Super-Kamiokande Calibration

A general description of the SK detector has been outlined in section 3.5. There, however, the details of its calibration were omitted. A full calibration programme for SK is composed of two broad areas: detector properties, such as the PMT response and water quality; and physics properties, those related to vertex reconstruction and energy resolution. Both of these steps are important to improve the quality of the raw data collected, and it would be all but useless without them. This chapter will focus on the former, with further details on the calibration of the physics properties to be found in Ref. [310]. This section also provides a description of SK-Gd: whilst not entirely a calibration topic, the impact of gadolinium on the water properties will be described later.

6.1.1 PMT Response

Arguably the most important part of any detector are its signal detectors, in the case of SK these are the PMTs. Their charge response must be calibrated for two things: the gain and the quantum efficiency (QE). The gain is a conversion factor between the amount of charge a particular PMT outputs (in pico-Coulombs, pC) and the number of photoelectrons (p.e) from the photocathode. Here, the QE is defined as a product of the *real* QE, the photon-to-electron conversion factor of the photocathode, and the electron collection efficiency, the ratio of p.e to collected electrons on the first dynode.

To effectively reconstruct the energy of an event it is important for each PMT to output the same charge per p.e. The gain calibration must be completed on a PMT-by-PMT basis, as no two installations of PMTs are identical. To this end, a number of PMTs were pre-calibrated to establish the required high-voltage to return the same charge for the same number of p.e. These calibrated PMTs were installed around the tank, and act as a reference for the high-voltage settings of the PMTs in a similar geometrical position upon being illuminated by an isotropic diffuser ball installed at the centre of the tank.

Any remaining differences in the gain can be attributed to the QE. The relative difference in gain between each PMT is obtained using a dye-laser that can be filtered in order to change its intensity, and its light delivered to the diffuser ball via an optical fibre. Comparing a high to low intensity light sample, one can obtain both the gain of each PMT and also the average gain over all PMTs: normalisation to the latter quantity leads to a calculation of the relative gain. A nickel source can then be used for an absolute gain measurement; after absorbing a thermal neutron from a californium source, the nickel isotropically emits ~ 9 MeV gamma rays at a 1 p.e level. The resulting charge distribution, corrected for dark hits, is averaged to achieve a single conversion from charge to p.e; this is applied on a run-by-run basis to the detector. Interestingly, as has been observed in multiple experiments, the absolute value of this gain has been increasing over time: the cause of this is yet unknown.

As a final step in the charge calibration, the single p.e data from the nickel source can be normalised with SKDETSIM, SK's Monte Carlo simulator, to remove the effects of scattering and absorption parameters (section 6.1.2). Interestingly, it was discovered the new PMTs installed after the implosion event have a much higher QE. This is due to the improvements in the glass transparency made by Hamamatsu over the years of production.

Each readout channel for the PMTs has to be calibrated for the reconstruction of the event vertex and track direction. The timing of each PMT response can vary due to different lengths of signal cables and electronics processing and also the 'time walk': a high PMT pulse height will have a faster rise time than a smaller one. These can be calibrated by injecting a fast light pulse, using a nitrogen laser with a variable intensity, into the diffuser in the centre of the tank. This is monitored with a fast-response PMT in order to define the light injection time. Using this one can create a 'TQ-map' (time-charge map) for each readout channel; this is a polynomial fit to the TQ distribution, which contains the calibration constants for the process time and time-walk effect.

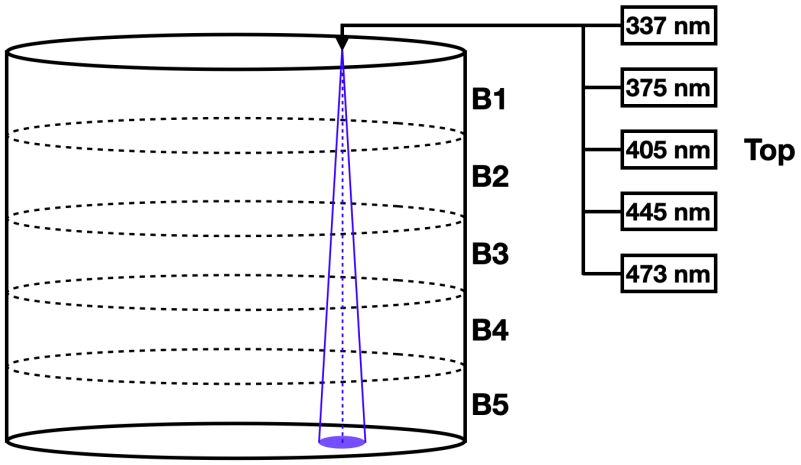

Fig. 6.1: Schematic of the optical calibration system installed at Super-Kamiokande. The horizontal injectors B1 to B5 are the positions of the UKLI system, but also denote the sections of the detector the anaysis is split into. The top laser can have five wavelengths, and is injected via an optical fibre. Figure reproduced from [310].

6.1.2 Water Quality

The particle identification (PID) in a water Cherenkov detector is dependent on the photon propagation, which in turn depends on the water properties. It is therefore important to understand these effects in order to make detailed measurements of neutrino parameters. Any changes in the water properties can be a sign of contamination in the detector, thus making measurements of the scattering and absorption coefficients one can establish the potential causes and therefore potentially mitigate the problem: or at the minimum, correct for it.

Two types of elastic scattering are important for measuring the water coefficients: Rayleigh and Mie scattering. In both cases the scattered light is polarised, and is the same wavelength as the incident light. Rayleigh scattering occurs on particles whose diameters are small compared to the wavelength, λ, of light; this scattering consists of symmetric forward and backwards scattering in relation to the direction of the incoming light. Mie scattering is primarily off particles that are similar (or greater) in size than the wavelength of light and is asymmetric, *i.e.* the light is more forward scattered. The larger the particle, the more forward scattered the light becomes. In the SK analysis, these effects are combined to form the symmetric, α_{sym}, and asymmetric, α_{asy}, scattering coefficients. The symmetric factor contains both Rayleigh and Mie scattering, whilst the asymmetric coefficient only consists of forward Mie scattering.

The scattering, and the absorption, parameters are measured with a vertical collimated laser injected into the tank, which can be varied over five different wavelengths. Fig. 6.1 displays the schematic of the calibration system and the injection points: the 'Top', 'Bottom' and 'B1-5' (barrel positions 1 to 5). The bottom injector is no longer used, and so has not been included in the diagram. The B1-5 positions denote the five regions the detector is divided into and are not injectors used in the official analysis. The same notation indicates

the positions of the UK light injectors, also unused in the official analysis, and will be described fully in section 6.2.

The spatial and timing distributions of the injected light are compared to output from SKDETSIM, where the scattering and absorption parameters are varied and the χ^2 between data and MC is minimised. The number of photons decreases exponentially in the water, at a rate given by the total attenuation length

$$L(\lambda) = \frac{1}{\alpha_{abs}(\lambda) + \alpha_{sym}(\lambda) + \alpha_{asy}(\lambda)}\,, \tag{6.1}$$

where $\alpha_{abs}(\lambda)$ is the absorption coefficient. $L(\lambda)$ is also known as the water transparency, which varies dependent on the wavelength of light traversing the water. The water scattering parameters are not physically driven and are empirical functions tuned to the SK data. These functions are given by

$$\alpha_{abs}(\lambda) = P_0 \times \frac{P_1}{\lambda^4} + C\,, \tag{6.2}$$

$$\alpha_{sym}(\lambda) = \frac{P_4}{\lambda^4} \times \left(1.0 + \frac{P_5}{\lambda^2}\right)\,, \tag{6.3}$$

$$\alpha_{asy}(\lambda) = P_6 \times \left(1.0 + \frac{P_7}{\lambda^4} \times (\lambda - P_8)^2\right)\,, \tag{6.4}$$

where $P_0 - P_8$ are fitting parameters. C is an amplitude based on experimental data, and is only valid for $\lambda \geq 464$ nm. If $\lambda \leq 464$ nm, it is replaced with the formula

$$C = P_0 \times P_2 \times \left(\frac{\lambda}{500}\right)^{P_3}\,, \tag{6.5}$$

where once again the P parameters are obtained from a data fit. The symmetric light follows an angular distribution described by $1 + \cos^2\theta$, whereas the asymmetric light scattering probability increases linearly from $\cos\theta = 0$ to 1 (and no scattering occurs for $\cos\theta < 0$). A summary of a general set of fit parameters is given in Table 6.1. For a wavelength of 400 nm, the water transparency in SK is approximately 120 m.

P_0	P_1	P_2	P_3	P_4	P_5	P_6	P_7	P_8
0.624	2.96×10^7	3.24×10^{-2}	10.9	8.51×10^7	1.14×10^5	1.00×10^{-4}	4.62×10^6	392

Table 6.1: Summary of the typical water quality parameter fits from the April 2009 SK data. These enter via equations 6.2-6.5 to give a measurement of the water transparency. Values taken from [310].

6.1.3 Gadolinium Loading

The SK detector upgrade has now led to the period denoted SK-Gd, which has an end goal of introducing a 0.2% concentration of soluble gadolinium sulphate ($Gd_2(SO_4)_3$) into the SK pure water. The inclusion of gadolinium opens the opportunity for measurements of the

diffuse supernova neutrino background (DSNB), this would be the first observation to date. Typical DSNB events are critically limited by backgrounds from reactor (low energies) and atmospheric neutrinos (high energies), thus leaving a small window for their measurements. These are detected via inverse beta decay, with a prompt positron signal followed by a thermal neutron capture on hydrogen. This latter process releases a 2.2 MeV photon, which is extremely difficult to detect. Gadolinium, on the other hand, has a much higher thermal neutron capture cross-section, and the neutron itself will be absorbed 10 times faster than in pure water: this occurs about 4 cm from the interaction vertex, a small separation in SK. This capture also releases a gamma cascade of 8 MeV, much easier to detect than a capture on hydrogen. 90% of the neutron captures should occur on gadolinium, thus extending SK's ability to observe the DSNB and allow for neutrino-antineutrino discrimination in other physics searches. The first step towards the final goal started on the 14^{th} July 2020, with 13 tons added over a 1 month period. Recently, the second loading period was completed (starting on the 1^{st} June 2022), where another $\sim$27 tons of gadolinium sulphate was added, finishing with a total concentration of 0.03%.

6.2 UK Light Injection System

With the new generation of neutrino experiments, a new calibration system was proposed that was able to calibrate several detector properties using the same system. This could measure both the scattering and absorption parameters, and also the PMT properties described in section 6.1. To do this, several light sources are required, each with different beam profiles of different opening angles. This UKLI system was installed at the 5 injector positions, B1-B5, each with 3 distinct optical sources. This adds 15 new calibration channels to the SK detector. The 3 beam profiles are a diffuser, a collimator and a bare fibre; these will be described in the following sections, with a summary of their uses in Table 6.2. Whilst providing calibration for SK, these are also a prototype for the future system that will be installed into the Hyper-Kamiokande (HK) detector. The wavelength of the barrel injectors is set to 435 nm. A UK diffuser ball was also installed into the top of the SK tank. This was originally supplied with a 473 nm diode, however this was changed on 14^{th} April to 368 nm for a greater sensitivity to the water parameters.

6.2.1 Bare Fibre

The installed UKLI system contains a bare fibre injector that was never planned for use in calibration measurements as other beam profiles are more suitable. The current official analysis is built using a bare fibre, thus the UK bare fibres can be used to verify the new system produces results consistent with current system. These long fibres are the same as the ones which deliver the light from the pulser board to the collimator and diffuser, which are 200 μm core Thor Labs step index fibres. For consistency a 20 cm short fibre is connected to the long one for the bare fibre, in a similar fashion to the collimator and diffuser, before being screwed into the optical plate.

Property	Pulse Intensity	Beam Angle
Water Scattering	High	Narrow
Water Attenuation	Medium	Narrow
Water Attenuation	Single p.e	Wide
PMT Charge Uniformity	Single p.e	Wide
PMT Timing Uniformity	Single p.e	Wide
PMT Incident Angle Dependence	Single p.e	Wide

Table 6.2: Summary of the water quality properties that can be measured using different beam types. Table from [311].

6.2.2 Diffuser

The diffuser is a wide-angled, uniform beam that can be used for measurements of the PMT characteristics and water coefficients. The attenuation can be measured by supplying PMTs with single p.e intensity light and studying the hit rate against the distance from the source. This beam profile can also measure the PMT charge uniformity, timing uniformity and incident angle dependence. This is made simple as the diffuser can illuminate many PMTs at once, providing light of a known origin and time, thus by also studying the changes in the timing profile water properties could potentially be measured.

The diffuser is a hemisphere of acrylic resin with Poly(methyl methacrylate) (PMMA) particles suspended. The path length of the injected photons is small compared to the size of the diffuser, such that they are scattered randomly and isotropically over the 45° opening angle. The diffuser is mounted in a sealed housing so as not to leech PMMA into the pure water of the detector, and to maintain the operation of the diffuser ball itself. A 20 cm short fibre supplies light to the diffuser, which connects to a long fibre as described in the previous section.

6.2.3 Collimator

The collimator is a narrow angled beam with an opening half-angle of 2°, which covers a 5×5 area of PMTs on the opposite tank wall. It consists of a gradient index (GRIN) lens coupled to the same optical fibre setup as with the diffuser and bare fibres, focusing the beam to the required opening angle. This is contained within a stainless steel sleeve which is sealed with epoxy to ensure the system is waterproof.

A collimated beam has many advantages over the current bare fibre method employed by SK. The collimator provides a precise target on the detector wall, thus scattering lengths can be measured by analysing the charge collected by PMTs outside of the beam spot. Conversely, by analysing the light collected inside the beam spot one can measure the water attenuation, and utilising the 5 injector positions the depth dependence can be extracted.

This is only possible as there is no overlap in the beam spots. Due to the focused nature of the injector, it allows a high statistics measurement of the water parameters.

6.2.4 Monitor PMT

An important constituent of the system is the monitor PMT, used to independently monitor the light output of the LEDs providing light to the optics[1]. The PMT itself is a 2 inch Hamamatsu photosensor with a peak response at 400 nm, staged outside of the SK tank. Each optic channel is threaded to the monitor PMT, which measures the total charge output from LED pulser board. This information can be used to normalise the data when deriving the water coefficients. Fig. 6.2 compares normalisation using the total charge measured in the tank against normalising with the injected photons measured with the monitor. It is clear that the monitor returns a more distinct measurement of the absorption parameter.

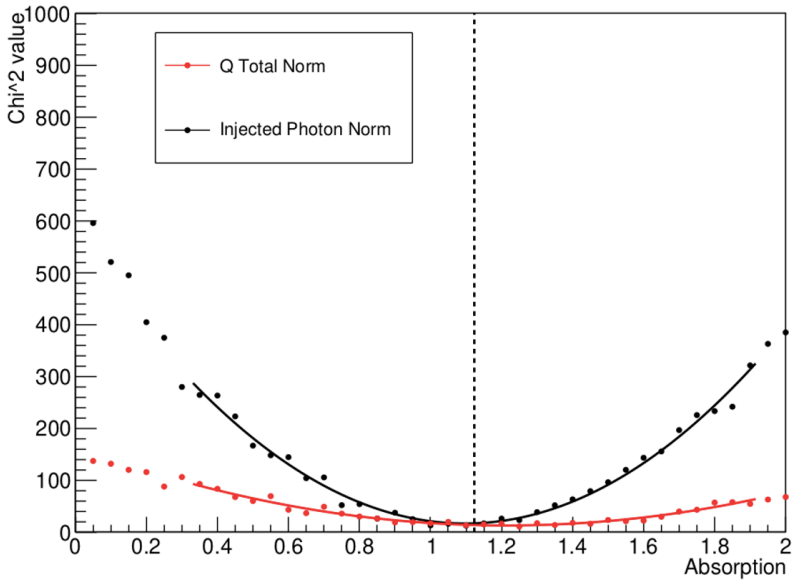

Fig. 6.2: χ^2 comparison of fake data between two methods of normalisation. The black line is normalised using injected photons calculated with the monitor PMT, the red using the total charge as measured in SK. The vertical, black, dotted line shows the set absorption value of 1.123. The monitor returns a well defined measurement of the parameter. Figure reproduced from an analysis written by A. Pritchard.

The monitor PMT is coupled to an optical power meter (OPM) for calibration, and the gain can be controlled via a potentiometer. It is housed in a dark box in the dome over the SK tank to reduce its light exposure. More details related to the monitor PMT will be given in section 6.3.5.

[1]For the rest of the chapter, the word 'optic' collectively refers to the diffuser, collimator and bare fibres in all injection positions.

6.2.5 Beam Profiles

Using the system described above, some information about the water quality could be obtained from the raw PMT information that SK collects (an example shown later in section 6.4). However, to complete a full calibration campaign with up-to-date measurements of the water transparency parameters, comparison with detailed detector simulations is required. For these to be accurate, it is important to have specific simulations of the light injection systems used for calibration. To this end, it was necessary for the beam profiles of the various optics to be included into SKDETSIM for future analyses. Using these, it becomes possible to make detailed comparisons between data and MC for combined measurements of the scattering and attenuation properties of the detection medium.

The beam profiles for each of the collimators and diffuser were supplied by the Warwick group, who designed and built each of the injectors. To measure the light intensity, the diffusers were mounted on a rotation stage that allowed it to revolve around its full opening angle, *i.e.* between $-40°$ to $+40°$. The light intensity was measured using a fixed PMT that scanned the surface as the diffuser was rotated. An example of a profile measured is shown in Fig. 6.3a, this is the average integrated area under multiple laser diode light pulses. In the case of the collimator, the injector itself was held fixed and the horizontal profile scanned linearly by a PMT (with the position measured using a rotary encoder). These were both 'in air' measurements.

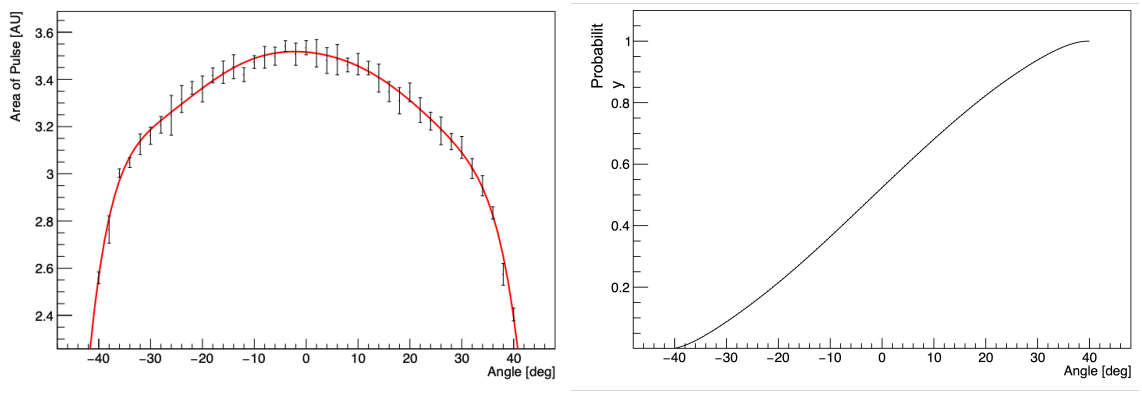

(a) **(b)**

Fig. 6.3: **(a)** Beam profile for the B1 diffuser, measured in air using a PMT and the diffuser mounted on a rotation stage. **(b)** Cumulative distribution function for the beam profile. This can be sampled from in order to simulate the beam for each injection event.

Using these profiles, one can create a cumulative distribution function (CDF) for each individual injector, an example is shown in Fig. 6.3b. A random event can be generated by linearly sampling the CDF across the full opening angle of the injector, populating the simulation to match the supplied profile. These CDFs were generated for every injector type and position, and can now be used to sample from during generation in SKDETSIM. The collimator beam profiles have to be corrected with a factor of $\sin\theta$, as their measurement was made using linear scan. Example occupancy plots comparing data and MC for a single injection event is shown in Fig. 6.4. These simulations can now be utilised in future analyses.

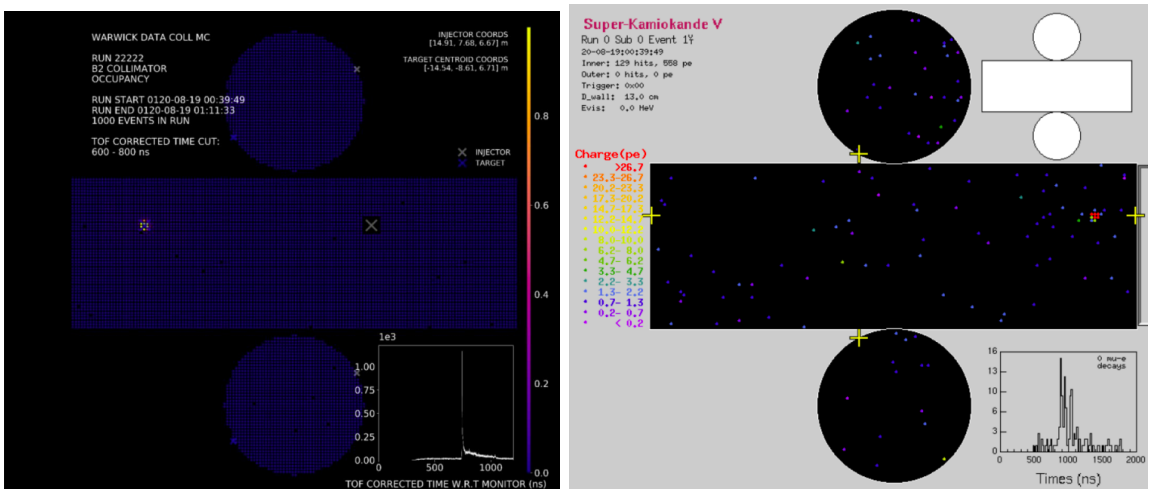

(a) **(b)**

Fig. 6.4: Occupancy plots for the B2 collimator injector for a single event. **(a)** shows the profile as measured from the light intensity measurements. **(b)** shows a single injection event from the test injections.

The current implementation, although useful, can be improved with future measurements. Currently the profiles implemented only cover a single dimension, thus to make the simulations as accurate as possible, full 3-dimensional measurements of the injector light intensity are required. These are complex measurements, and the current method of sampling the beam profiles would need to be adapted to handle a 3D map. However, similar structures are already in place for other calibration light sources employed in SK. The new measurements should also take place in water as, although likely similar, the profiles will differ from those taken in air. These measurements are currently being planned.

6.3 Online Monitoring

A large body of work completed during the PhD was on building an automated monitoring system using the UK light injectors for the purpose of real time data on the water quality. During a normal SK run, data is collected using all of the calibration sources. This is controlled using the auto-calibration process, or AUTOCALIB, which cycles through the current SK laser system and also the UK light injectors. The SELCALIB program reads the raw data files, and separates the calibration events from the raw data. This data is then used for UKLI monitoring. The full system will be described in detail in the following sections, however as a summary the process proceeds as follows (UKLI monitoring begins from step 2):

1. Raw data is taken from the DAQ and converted to the ZEBRA bank system (ZBS) format. This is transferred out of the mine by means of an optical fibre. Data is saved as permanent ROOT files for each subrun.

2. The subrun ROOT file is converted to ZBS format and SELCALIB is applied. This

separates the UKLI system data into each optic (*i.e.* B1 diffuser, B1 collimator *etc.*).

3. The separated ZBS files are converted back to ROOT for the rest of the analysis.
4. The charge and timing information is extracted for each injector type/position and saved as a generic data file (DAT).
5. Check if the current subrun is the final in a particular run. If not, return to step 2.
6. Merge all DAT and ROOT subrun files for this run and move to permanent storage.
7. Every 30 mins, plot the data using the information contained in the DAT files. Copy these plots to the monitoring web page.

Step 7 occurs concurrently with the data extraction in the previous steps.

Beginning at step 2, this process will now be described in detail. The author created, developed and maintained the monitoring for the UK system, along with being in charge of the team to present and develop it further. Any other's contributions are discussed in the declaration at the beginning of the thesis.

6.3.1 AUTOCALIB and SELCALIB

The AUTOCALIB process is an automated system that loops through all the calibration sources during a normal physics data taking run (there are also dedicated calibration runs and during these AUTOCALIB is often disabled). The duration of an SK run is 16 hours, recently reduced from 24 hours. The time between each UKLI injection (so the total cycle time for AUTOCALIB) is 3.6 seconds, with Fig. 6.5 showing the order of the injectors with the inclusion of the UKLI system. Each source pulse lasts only a few nanoseconds, so does not contribute largely to reducing the detector live-time. For each cycle, the UK injectors are also cycled, *e.g.* B1 collimator on the first cycle, B2 collimator on the second *etc.*

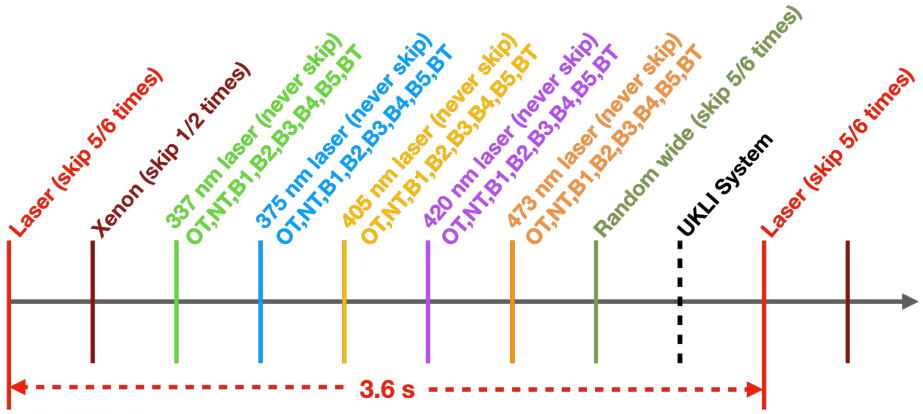

Fig. 6.5: The AUTOCALIB light injection cycle. The cycle takes 3.6 secs between the same injectors. The UK system cycles through each of the injectors on its trigger.

Whilst the AUTOCALIB process controls the hardware and the injectors, SELCALIB is the corresponding software process flattening the data. The program reads the raw run data

and returns calibration data for study. All of the bad channels are masked, and the data are reformatted. The calibration events are tagged by triggers sent to dedicated calibration electronics, and as such are separated from physics events. Each optic has its own 4 bit number tagged via a NIM trigger, which is used to separate individual optics into data files so each can be accessed easily. This is completed in real time for each subrun[2], producing subrun files for each optical channel. Once a run is complete, the subruns are combined and saved for future analyses.

The above occurs automatically for calibration analyses. However, for UK calibration purposes, a local version of SELCALIB was written. Originally completed in order for the UK system to be included into the software, this has been adapted for UKLI monitoring applications. As only the UKLI and top diffuser ball events are required, the remaining calibration data is no longer extracted from the raw data files, saving on both disk space and computing time.

The UKLI system only covers the collimator, diffuser and bare fibre structure, however as mentioned previously a UK diffuser has also been installed in the top of the tank. This has now been included into the UK monitoring system. Whilst it was successfully included in the data extraction, this involved bypassing the SELCALIB step as the information required to extract the data from the raw files could not be found (*i.e.* the specific calibration tag). However, work to include this in the local version of SELCALIB is underway.

6.3.2 Prompt Charge and Timing

In the official calibration process, all data are permanently stored in the ZBS format. From purely practical motivations, it is more useful for the UKLI data to be stored in ROOT files, as most users are only familiar with this format. It is not, however, feasible to store both copies of the data as disk space is limited. It was therefore decided that only the preceding 6 months (or 200 GB) of data would be stored in the ROOT format, allowing those completing analyses with the system quick access to the data. If data from a period before this is required, this can always be converted from the permanent ZBS officially stored.

It is clear, however, that for the monitoring system the charge and timing information prior to the 6 month cutoff would still be required. Therefore, the prompt charge and timing information for each event is extracted and stored elsewhere in the DAT format. This reduced data significantly saved on disk space, and allows us to keep all of the monitoring information since the system was installed.

The simplest method of monitoring the real-time water quality is to measure both the total and prompt charge and the time for every event for each injector. The total charge is simply defined as the sum of all charges across all PMTs in the tagged injection event. It is worth noting that the timing information is only the time the injection took place, not the hit time of each PMT. Whilst the total charge is useful for normalisation purposes and provides information on the diode supplying the light, the prompt, or spot, charge is a more

[2]Each subrun is a few minutes long within a normal data taking run.

direct indicator of water quality information. For example, if the collimator suddenly sees a decrease in the spot charge, it could be due a change in attenuation of the water as a result of temperature change, or possibly the introduction of contaminants increasing the prominence of scattering with the beam. Thus it is important to have a stringent definition of the prompt charge to ensure only the direct light is being measured.

The prompt charge is defined by two things: a spatial and a temporal cut. The time cuts selects around the peak of the timing distribution, and defines light that *directly* hits the opposite wall of the tank, an example cut is shown in Fig 6.6a. The rise above background seen around the prompt signal is due to scattered and reflected light, with the rise before prompt likely due to light being scattered toward the top end cap, or immediately reflected back to PMTs around the injector position, hence a shorter path length. This cut reduces the charge collected by a significant amount, as demonstrated in Fig 6.6b. This cut is tuned for each injector position and beam profile, their values are summarised in Table 6.3.

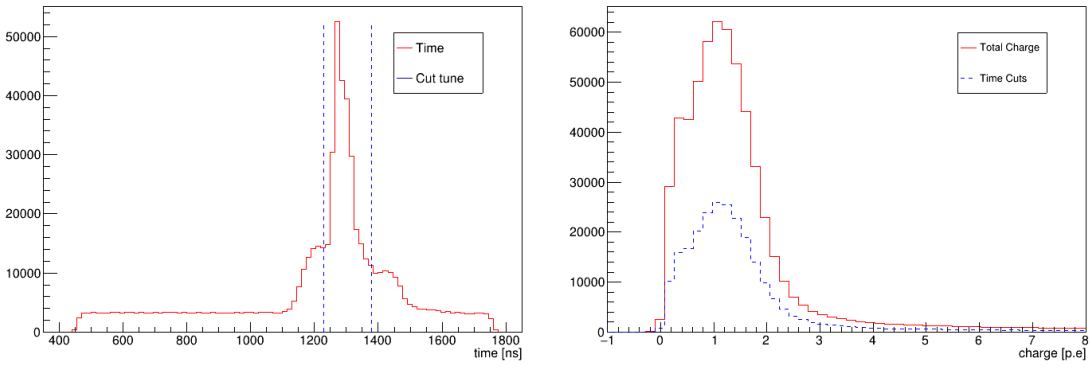

(a) **(b)**

Fig. 6.6: **(a)** Timing profile of the B1 injector. Shown in dotted lines are the cuts making up part of the definition of the prompt charge. **(b)** The effect of the time cut on the charge profile of the B1 collimator. Red shows the initial distribution, while the blue dotted line shows the cut charge.

Position	Collimator			Diffuser		
	Lower	Upper	TOF	Lower	Upper	TOF
1	1230	1380	1190	1150	1450	1400
2	1240	1400	1240	1210	1410	1400
3	1240	1410	1250	1200	1360	1400
4	1230	1380	1225	1190	1370	1400
5	1240	1400	1250	1140	1410	1400

Table 6.3: Summary of the UKLI time and time-of-flight (TOF) tunes for each injector position and beam profile. Each value is given in nanoseconds. The bare fibre is not included due to problems with the installation.

Although a time cut is usually sufficient and quick, perhaps a more interesting variable

is the time-of-flight (TOF) corrected timing distributions. This is defined by

$$t_{TOF} = t - \frac{\overrightarrow{pmt} - \overrightarrow{inj}}{c/n}\,, \tag{6.6}$$

where $\overrightarrow{pmt}$ and $\overrightarrow{inj}$ are the position vectors of the hit PMT and injector respectively, c is the speed of light and n is the refractive index of the medium. The TOF corrected distributions both before and after the time cut are shown in Figs. 6.7a and 6.7b. The time tune removes most of the indirect light, however there is still a 'wing' of scattered and reflected light included in the distribution, seen to the right of the blue dotted line in Fig. 6.7b. Another cut is included here to tune the prompt charge still further. Again, these are summarised in Table 6.3. The TOF corrected distributions for the B2 collimator are shown in Figs. 6.7c and 6.7d. These both have the time and TOF cuts applied, however in the latter the TOF cut is reversed. It is clear the TOF 'wing' mostly contains light reflected back toward the injector, along with a small amount from scattered light - this can be seen around the beam direction. It is possible this scattered light could be used as a monitor for reflectivity measurements and supporting the current analysis, but this is not explored any further.

Whilst the time cuts are likely enough to perform water quality monitoring, the inclusion of a spatial cut removes any coincidence of light hitting PMTs in the defined time window that is not direct. The definition of this cut should be a simple case of searching the tank wall opposite to the injector position, within the injectors opening angle. However, due to the practical difficulties of installation, the injectors are not perfectly perpendicular with the tank wall. This is particularly a problem with the collimators, where the initial spatial cut did not contain the prompt charge. In order to find the injector target, Gaussian fits to the x, y and z charge profiles were used to define the beam centre, and therefore the centre of the cut. This could be used to find the misalignment angle for each of the collimators, these are summarised in Table 6.4. For the collimators, the prompt charge is defined within 5° of the beam target. Examples of the collimator beam spot and spatial cut is shown in Fig 6.8b.

Position	1	2	3	4	5
Angle	4.1	3.5	3.4	6.3	*

Table 6.4: Misalignment angles of the UKLI collimators, each measured in degrees. The beam spot position was measured using Gaussian fits to the charge distributions in the x-, y- and z-planes. The B5 beam spot was too faint, thus its position could not be measured.

The diffusers follow the same definitions as the collimators, with obvious adjustments for the difference in beam profile. Example event displays for 2 diffuser profiles are shown in Fig 6.9. It is likely the diffuser are aligned slightly differently than the collimators, again due to the practical limitations in installation. Due to their faint (∼1 p.e) illumination and diffuse beam, however, it was not possible to measure the centre of the beam spot; therefore the same alignment was used as for the collimators. But, due to their wide opening angle, a slight misdirection on the spatial cut should not have an adverse effect on the charge

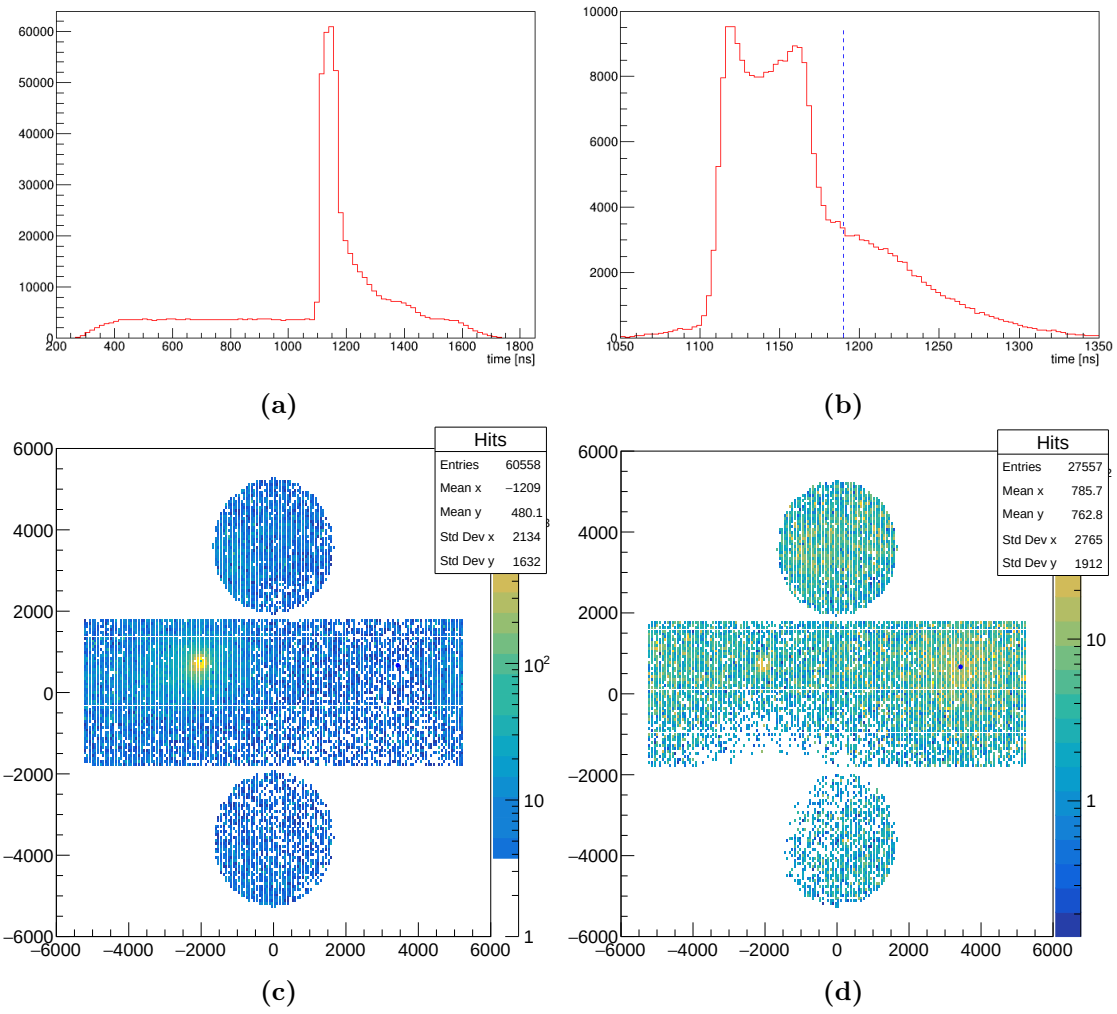

Fig. 6.7: Example time-of-flight (TOF) corrected timing distributions and event displays for the collimators. **(a)** Regular TOF corrected timing distribution. **(b)** TOF time distributions with the time cut applied. The dashed blue line shows the TOF cut. **(c)** TOF corrected event display for the B2 collimator, with the time and TOF cut applied. **(d)** The same as (c), but with the TOF cut reversed. It is clear the cut removes lots of scattered and reflected light. The blue dot indicates the injector position.

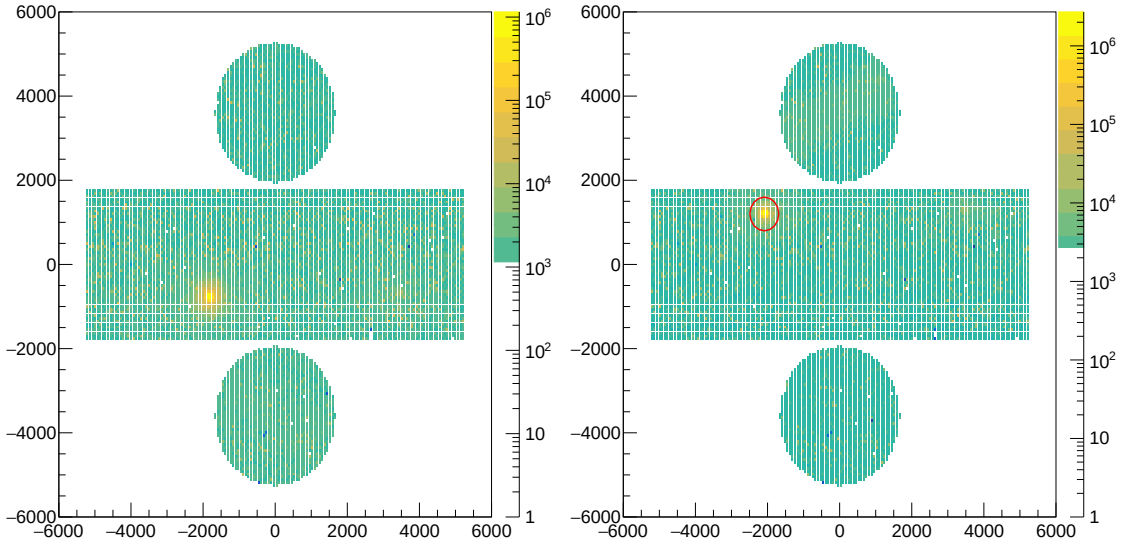

(a) **(b)**

Fig. 6.8: Examples of the collimator beam spot for the B4, **(a)**, and B1, **(b)**, injector positions. The red circle shows the 5° opening angle spatial cut used for the prompt charge definition.

collected within its definition. The opening angle in this case is 50°. The effect of tuning both the spatial and temporal cuts on the prompt charge is shown in Fig. 6.10.

The top diffuser follows the same definition as for the barrel injectors, with a spatial cut (and a temporal cut included later[3]). Once again this is defined within a 50° opening angle. Due to its unique position, the top diffuser samples a large range of photon travel lengths, making it ideally placed to make attenuation measurements. In this case, rather than use the prompt charge, the charge measured from the bottom end cap PMTs and PMTs installed on the barrel were extracted separately. The bottom PMTs are defined by cutting on PMTs with $z < -1805$ cm. Fig. 6.11 shows the definition of the cuts placed on the top diffuser.

6.3.3 Automation

For the period of March 2020 to December 2020, all data was being processed and analysed to provide real time automated monitoring of the detector, with all information being available on an internal SK webpage. Due to some issues with computing, this was interrupted, and was reduced to a weekly report at the SK steering meetings. Once it was understood how to prevent the automation issue from arising again, this was turned back online and is currently running smoothly.

The system itself runs on the Kamioka computing cluster, SUKAP. Every 10 minutes, the raw data from the DAQ is examined to confirm if a new run has started. If so, a new job

[3]This was a slight oversight. It was believed a time cut had been included for this top injector, however this was not the case. Once it was included, the charge measurement did not alter the data by a huge amount.

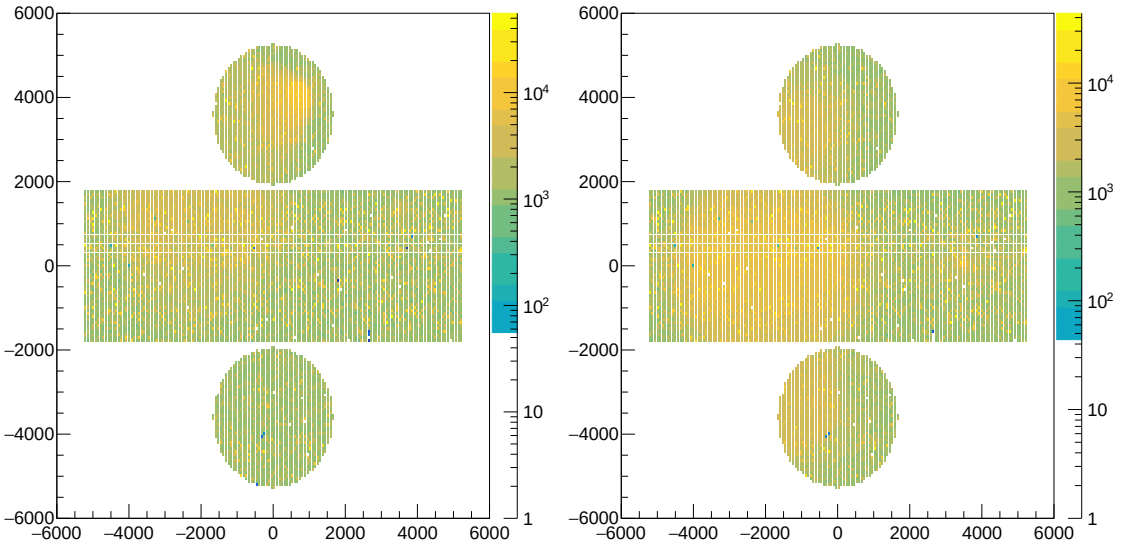

(a) **(b)**

Fig. 6.9: Examples of the diffuser beam spot for the B1, **(a)**, and B3, **(b)**, diffusers. This is summed over all subruns for a single run, as a single injection event would have too few hits to be seen.

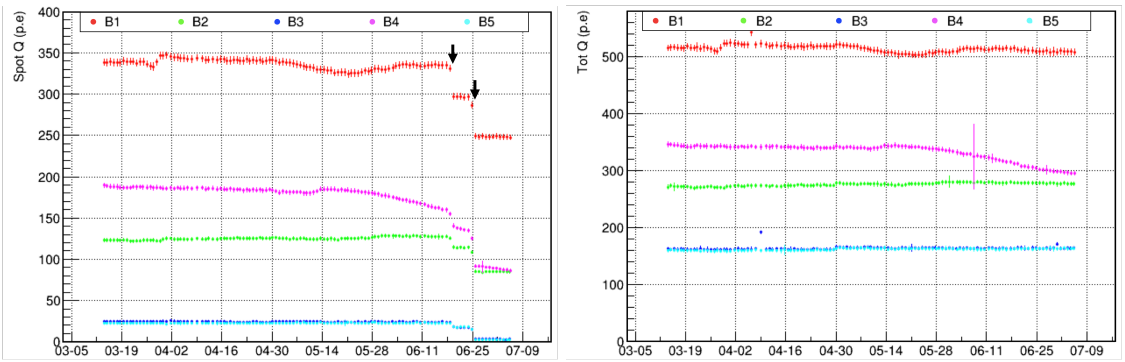

(a) **(b)**

Fig. 6.10: **(a)** Effect of the temporal and spatial cut on the prompt charge measurements. This example is for the collimator. The first step (arrow) is the time cut while the second is the spatial cut. The effect is clearest at the B1 injector position (red). **(b)** Total charge measured for the collimator, compared to the prompt charge.

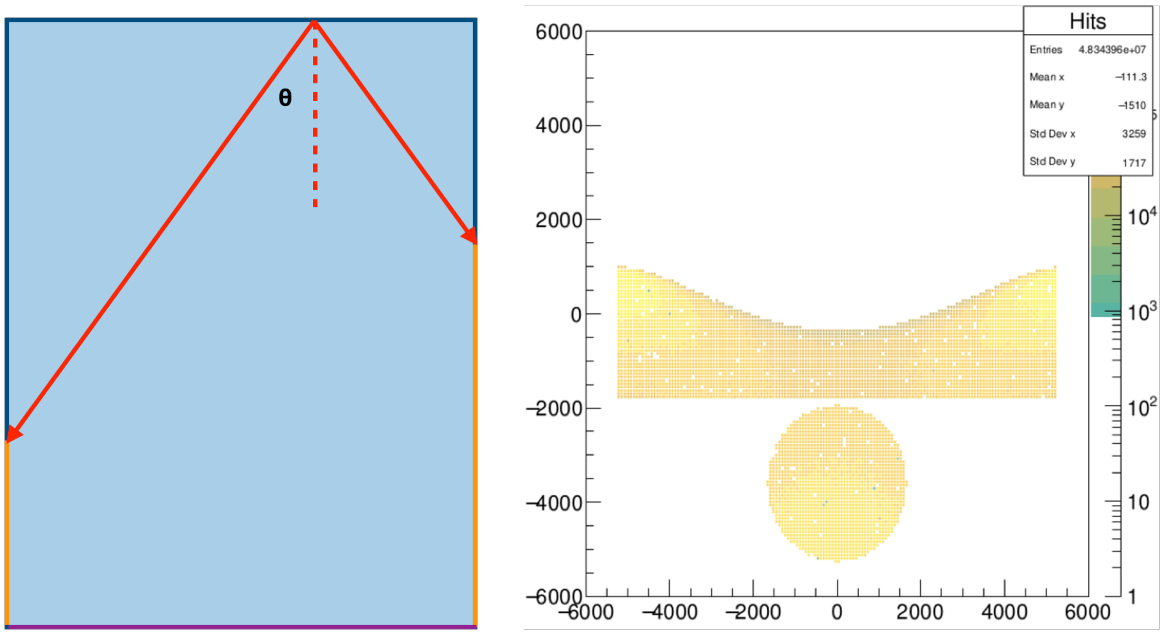

(a) (b)

Fig. 6.11: **(a)** Definition of the top diffuser spatial cut. The orange lines on the tank walls denote the barrel PMTs, whilst the purple line denotes the bottom cap PMTs. θ is the opening angle of the diffuser. **(b)** Event display of the top diffuser with the spatial cut applied. It is clear it illuminates most of the bottom region of the tank.

is created and tagged with the new run number, and subsequently submitted to the batch processor for analysis. The number of concurrent jobs is limited to 60 so as not to overrun the batch system, however when the system is running this value should never be reached[4].

Once data processing has begun for a particular run, it will only terminate once the SK run has ended and all data contained is analysed. Once a subrun has been analysed, the program waits for new subrun data in the current run. The number of subruns analysed per run is currently limited to 2000 in order to prevent the analysis of one run taking longer than one day on the batch system. This number should not be reached however, as SK defines a maximum number of subruns per run lower than this value.

Each subrun is stored individually as ROOT files while the run is being analysed, before being merged and kept for permanent storage. The charge and time information is extracted with each subrun and stored in a single DAT file for the run. Once the run is complete, the information in this data file is collated into a single data file containing all the extracted information for a particular injector position and beam type. To ensure the process does not quit prematurely, the system waits 2.5 mins for a new subrun before merging all subrun files and quitting their analysis.

As mentioned previously, a limit of $\sim$ 200 GB was agreed for storing UKLI monitoring data. This equates to approximately 6 months of data stored as ROOT files. A subprogram checks the total data usage of the storage directory and also the start time of the earliest

[4]This turned out to be necessary. After the computer handling the monitoring was switched off for a weekend, upon its restart all the backlogged jobs were submitted at once. This would have resulted in thousands of the same process attempting to run simultaneously, if the number of jobs were not limited.

run stored. If either the data limit is exceeded or the earliest run is not within 6 months, runs are removed until the condition is met. This process occurs once per day. The DAT files are exempt from this elimination as they require little memory usage.

The plotting is controlled separately. The extracted data is used for the monitoring plots, which are then copied to the webpage. During gadolinium loading, it was important to see the initial impact of the new salt water, and also the long term impact on the water quality. Therefore the monitoring plots covered a variety of time ranges: 6 hours, 24 hours, 1 week, 6 months and since the instigation of the system. These were originally updated every 3 minutes, however as all data was contained inside a single DAT file, it would soon become inefficient to sample data from all time with such frequency. This inefficiency was noted before the system came online, and will be discussed more in section 6.3.6.

The plotting stage also acts a final veto for any erroneous events. As is often the case with hardware, occasionally events are recorded incorrectly, and a null value will get passed into the data. This causes either a very low (basically zero) or very high (an overflow number) value to be saved into the data. This effects a small number of events, but can skew data points with low statistics (*i.e.* in the short term plots). Cuts place upper and lower bounds on the total and prompt charge in order to remove these events, an example of such a point is shown in Fig. 6.12b. Examples of the monitoring plots created by the automated system are shown in Fig. 6.12. These were generated early in the lifetime of the system. The last 24 hour plot generated each day is saved permanently for posterity.

As is clear from Figs. 6.10 and 6.12, any change in the total charge injected into the detector can effect the prompt charge. This can swamp any changes to the prompt charge caused by the water quality, removing any distinguishing ability the system may have. This is the reason for the inclusion of the monitor PMT, however due to issues described later in section 6.3.5, this was not possible. Thus, until the problem with the monitor is fixed, the total charge injected has been used to normalise, a similar method to that used in the Korean system. Whilst not as sensitive as using the monitor PMT for normalisation, it is sufficient to ensure any changes are due to the varying water quality parameters.

Due to the number of events per run, each data point is an average of many injected events. The number of events contained in each data point differs depending on the time range of the plot, and removes most of the random fluctuation due to detector inefficiencies and allows us to focus on the overall structure of the changing water qualities. The error on each of the points is the standard error on the mean,

$$\sigma_{\mathrm{SEM}} = \frac{\sqrt{\sum (x_i - \mu)^2}}{N}\,, \tag{6.7}$$

where μ is the mean and N is the number of events in a data point.

6.3.4 Steering Committee

The above was all completed for day-to-day monitoring of the detector, with a particular focus on gadolinium loading. However, a weekly report was also completed for a summary at

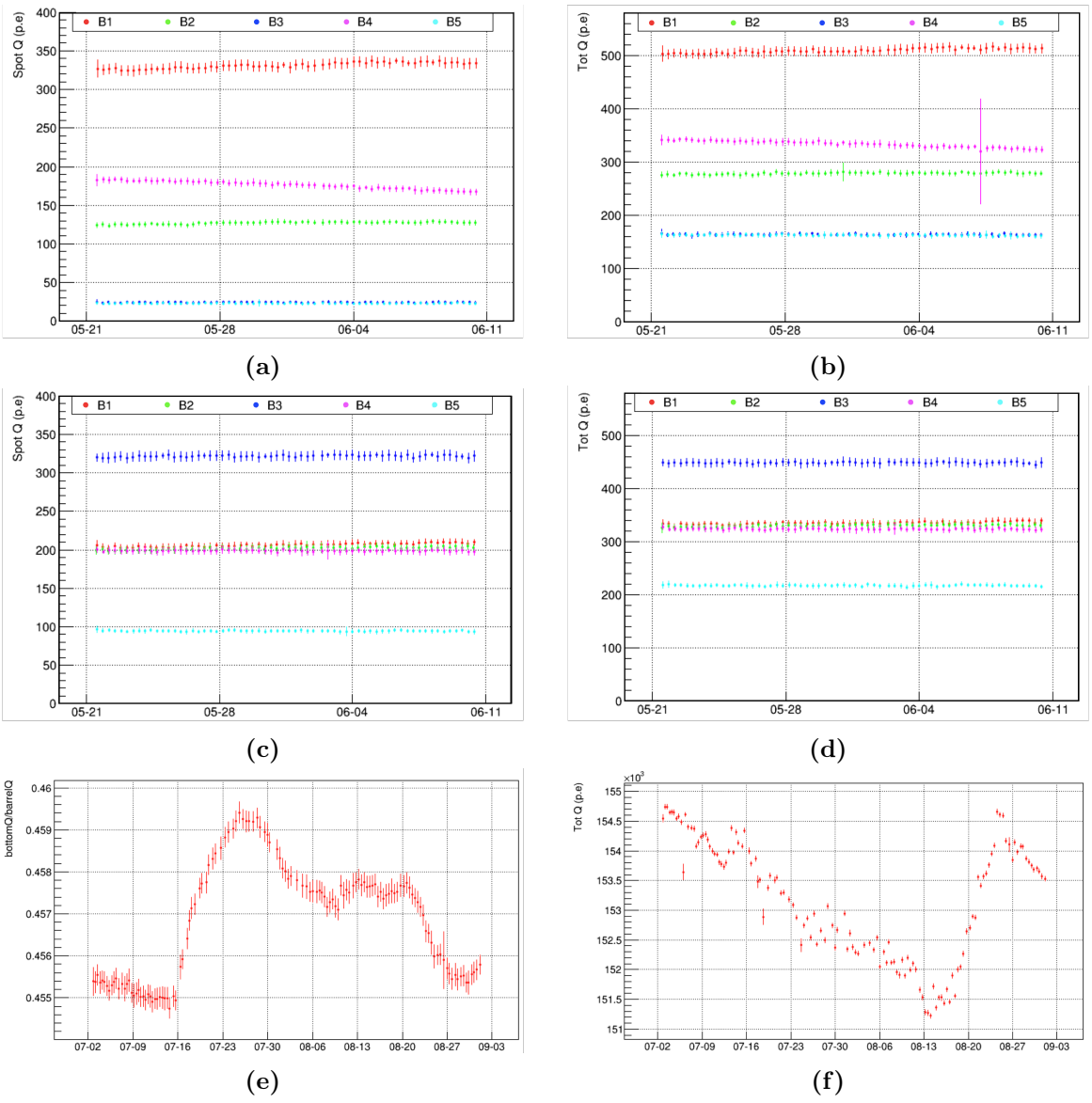

Fig. 6.12: Examples of the plots generated by the automated system used for monitoring water quality in the detector. The top diffuser plots clearly show the importance of normalising the prompt charge to the total charge injected: any variation in the injector is now removed. **(a)** Collimator prompt charge. **(b)** Collimator total charge. The B4 data point with large errors contains an incorrect charge value saved by the hardware. **(c)** Diffuser prompt charge. **(d)** Diffuser total charge. **(e)** Top diffuser bottom/barrel charge. **(f)** Top diffuser total charge.

the SK steering meetings, comparing the UKLI system to the other analyses. The pertinent plots were determined from the automated analysis and included in the steering meeting plots. These slides are once again generated automatically and sent to the UK group for inspection before the meeting.

Outside of the normal UK injector plots, the collimators have also been employed for a bacteria analysis. Since the beginning of SK-Gd, there has been an increase in the dark noise measurements which seem correlated with a systematic increase in the input water particle (and bacterial) count. The size of these particles is similar to the wavelength used in the UK injectors (435 nm). This, and the small opening angle and focused beam of the collimator, opens up the potential to investigate the forward scattering due to the water particle count.

In a similar calculation of the position of the beam spot centre, a charge weighted histogram along the z-plane is fit with a Gaussian, *i.e.*

$$f_n(x) = A_n + \frac{B_n}{\sigma_n} \exp\left(\frac{-(x-\mu_n)^2}{2\sigma_n^2}\right) , \tag{6.8}$$

where B_n is the intensity of the light injection (the total charge injected), σ_n is the variation with respect to the reference period due to scattering and μ_n is the position of target measured before. The reference period is the beginning of gadolinium loading, between 9$^{\text{th}}$ to 14$^{\text{th}}$ July 2020. A_n varies and is related to the dark rate in the detector, however this parameter is obtained by fitting the area outside of the prompt charge time window over a large range of PMTs. The overall fit is only completed for the B1 collimator, due to issues discussed in section 6.3.5. Fig 6.13 shows the Gaussian fit to the charged weighted histogram and the comparison between the collimator width and particulate count in the water supply.

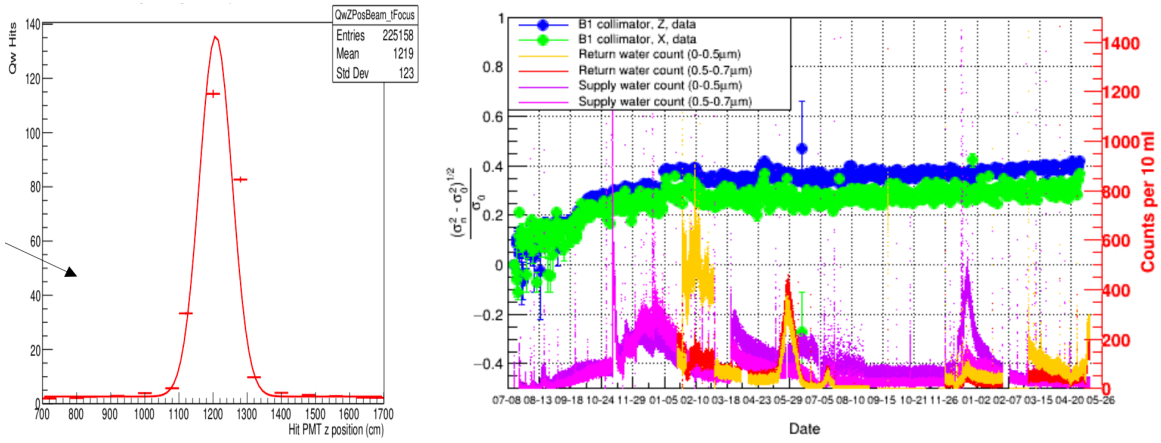

(a) **(b)**

Fig. 6.13: **(a)** Charged weighted number of hits as a function of hit PMT position. **(b)** B1 collimator width in the x- and z-planes, compared to the number of particles in the return and supply water, separated into different particulate sizes.

Fig. 6.13b shows the particulate count since the beginning of gadolinium loading. There is a quick rise in the width of the beam spot over the gadolinium loading period, followed by a slow drift in width. The particulate count during the same period seems to follow the same trend, however the later rapid changes in said count do not map onto the collimator data.

Though the collimator fit is useful to monitor the width and profile of the beam spot, it is not clear whether this is following the particulate count. As the particulate count is directly related to the amount of asymmetric (forward) scattering, this is perhaps a little surprising. However this does rely on the wavelength being similar to the particle size, which is not necessarily the case for the 435 nm barrel injectors. It is likely more work is needed here, with the collimator data combined with Monte Carlo in order to perform a measurement of the scattering. This plot (Fig. 6.13b) is updated each week for the steering meeting.

The final part of steering meeting is the comparison to the muon attenuation measurements. A more complete attenuation analysis will be described in section 6.4, however a simple comparison is made for the steering slides. Through-going cosmic muons are an almost constant source in the SK detector, and deposit a near constant amount of energy per unit path length regardless of the particle energy. This makes them a useful tool in the measurement of the attenuation length. The total charge, Q, reaching the PMTs is given by

$$Q = Q_0 \frac{f(\theta)}{l} \exp\left(\frac{-l}{L}\right) , \tag{6.9}$$

where l is the light path length, L is the effective attenuation length, $f(\theta)$ is the relative sensitivity of the PMT depending on the angle struck by the photon and Q_0 is a constant. The advantage of using muons is the near constant supply of cosmogenic samples during regular data taking, thus no down time is required in order to continuously monitor the attenuation length as a function of time.

An example of the muon monitoring plot is shown in Fig 6.14b, describing the change in the p.e ratio outside the Cherenkov angle (43°) against the total charge as a function of time. The all time plot is reported separately, however for the UK group's purposes all plots begin at gadolinium loading. Most of the hit PMTs in this analysis are in the barrel region, thus this is compared to the barrel charge from the top diffuser. Over the first gadolinium loading period, there seems to be some agreement between the two methods, however after that the data do not seem to match. This is not surprising as scattering is a strong function of wavelength, and with two different wavelengths of 420 nm and 473 nm (for the muon Cherenkov light and the top diffuser respectively) one should not expect to see a correlation. This is one of the driving factors behind changing the wavelength of the top diffuser laser.

6.3.5 Problems with the UKLI Hardware

As is often the case with new hardware designs, there have inevitably been issues that were only noticed since the data has been examined. This section will describe the problems noticed when implementing and examining the monitoring system, and have thus effected the data analyses that have taken place.

Before monitoring started, each injector was tested with a dedicated run. As part of this, it was noticed the bare fibre looked more diffuse than was expected. Shown in Fig. 6.15, the fibres should appear almost similar to the collimator, however it is clear the opening angle is much wider. Unfortunately, this is nothing to do with the installation or the injection

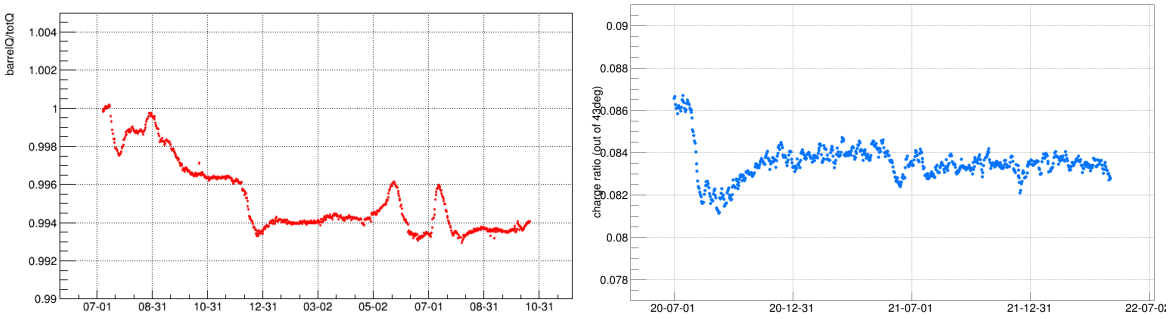

(a) **(b)**

Fig. 6.14: **(a)** The ratio of the barrel to the total charge of the top diffuser. This is normalised to the first data point. **(b)** Relative attenuation measurements made by cosmogenic through-going muons. This is the ratio of the charge outside the Cherenkov angle to the total charge. These sources have different wavelengths, thus they are not expected to share the same features.

system; it seems this is a problem with the fibre itself. It was assumed the ends of the fibres were squared and polished upon production, however this is obviously not the case. Without the sanding and polishing, the rough surface of the fibre behaves as an uneven diffuser, which will not be usable for analysis. Some of the profiles appear as would be expected, however it is uncertain whether this is by chance or the fibres being correctly polished. Due to this, the bare fibres are being ignored for any future analyses. Another unexpected complication became apparent by simply analysing the event displays by eye. A shadow is being cast across the beam profiles of the more diffuse bare fibres. This is clearly seen in the B3 injector (Fig. 6.15b), where a circular shadow is cutting out part of the light of the detector. This is a problem with the installation of the collimator, as the sealing epoxy blocked the collimator from being pushed completely into the housing, making it protrude and block part of the bare fibre. This would not be a problem if the fibres were not acting as a pseudo-diffuser. Although the bare fibres being unusable is not ideal, it does not affect analyses with this system, only that it is not possible to directly compare to the Korean results using a similar injector. However, the problem with the collimator housing is a lesson to be carried forward to the injectors for HK.

One of the issues noticed early after monitoring began was the monitor PMT. The main idea is that by finding a linear fit between the charge measured on the monitor PMT and the charge injected, one can associate any changes in the beam parameters with changes in the water quality in a more sensitive way than with total charge normalisation. This will only work while the PMT response is linear; if the PMT is near saturation however, the PMT response becomes non-linear and cannot be used for normalisation purposes. Although the monitor PMT seemed to be functioning during the injector test runs, once the injectors were included into AUTOCALIB and monitoring began, it seems to be sitting at the saturation limit. This limit is around 2900 p.e, and is shown in Fig. 6.16. The potentiometer controlling the voltage on the PMT had been turned 90° in the wrong direction, increasing the gain and setting the PMT at its limit. This could have been fixed much sooner, however because of the coronavirus pandemic, it was uncertain whether the potentiometer itself had drifted upwards

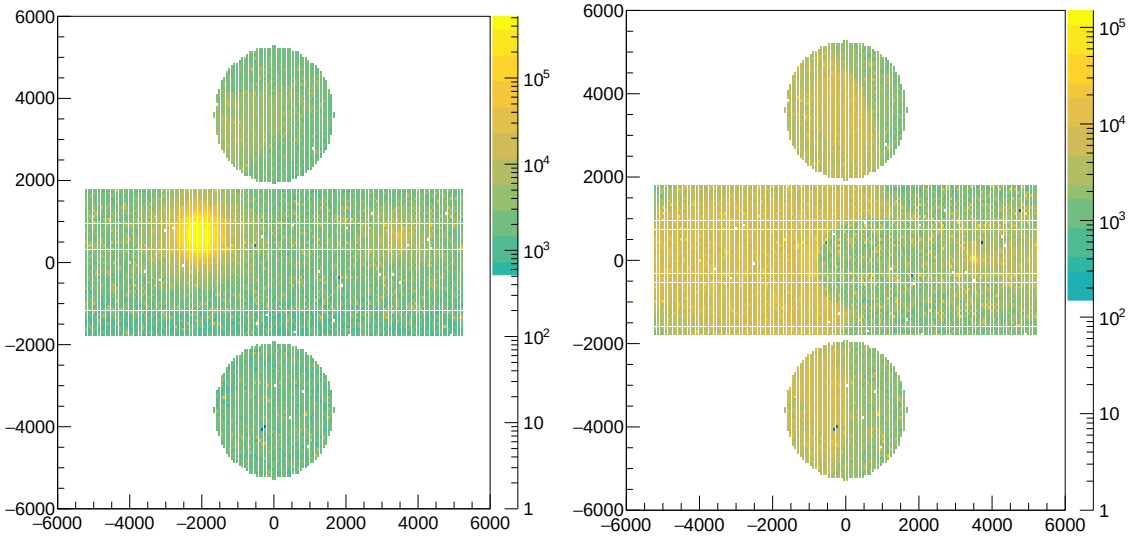

(a) **(b)**

Fig. 6.15: Examples of the bare fibre injectors for barrel positions B2 and B3, **(a)** and **(b)** respectively. Although B2 looks mostly as expected, the B3 injector seems to look more similar to a diffuser. There is also a shadow cast over the beam spot from the collimator protruding from the injector housing.

as no-one was able to enter the mine in order for testing to take place. The potentiometer has now been corrected, with its setting similar to before, however crucially no injectors are at their saturation limit (Fig. 6.17). Though the problem has now been fixed, the current setup is still not ideal. The potentiometer and power supply unit both have long wires that can easily pick up noise, and the former's wires are unshielded. The potentiometer itself depends on a physical resistor, whose resistance can drift with temperature and humidity and also has no feedback on the voltage. These can also fail mechanically. The proposal is to replace the entire system, with the PMT being sealed inside the darkbox and all electronics mounted outside. An Arduino Due will replace the potentiometer, which has built in voltage regulator, and an encoder will be used for fine control of the voltage. The encoder does not depend on temperature, thus is superior to the current approach. The PMT gain response to temperature and humidity will be corrected for, with sensors supplying real time measurements for both. With this new system for the monitor PMT, future analyses can use this for charge normalisation.

One major problem encountered during the monitoring was due to the collimators. As is shown in Fig. 6.18, the charge in most of the collimators has been slowly decreasing. This is particularly prevalent in the spot charge, shown in Fig 6.18a, in which all of the injectors (aside from B1) can be seen to quickly drop off in the prompt charge to less than 30% of its original value. The cause of this is not fully understood, however it seems likely this is due to water ingress into, specifically, the collimator injectors. As the collimators are attached to the same pulser boards as the diffusers, it would be expected the same drop in intensity would be seen in the diffusers if it were due to the boards themselves[5]. Examples for all the

[5]One might say there is a drop in the B2 diffuser too. Whilst this might be the case, one would expect to see more degradation in the other injectors too.

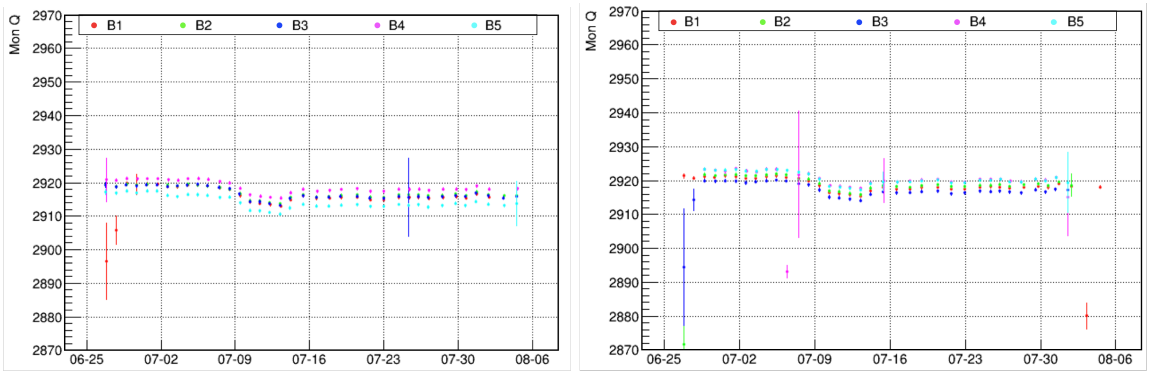

(a) **(b)**

Fig. 6.16: Monitor PMT charge early after the UKLI inclusion into the AUTOCALIB process. Sitting around 2900 p.e., it is sitting around its saturation limit. **(a)** and **(b)** are the collimator and diffuser injectors respectively.

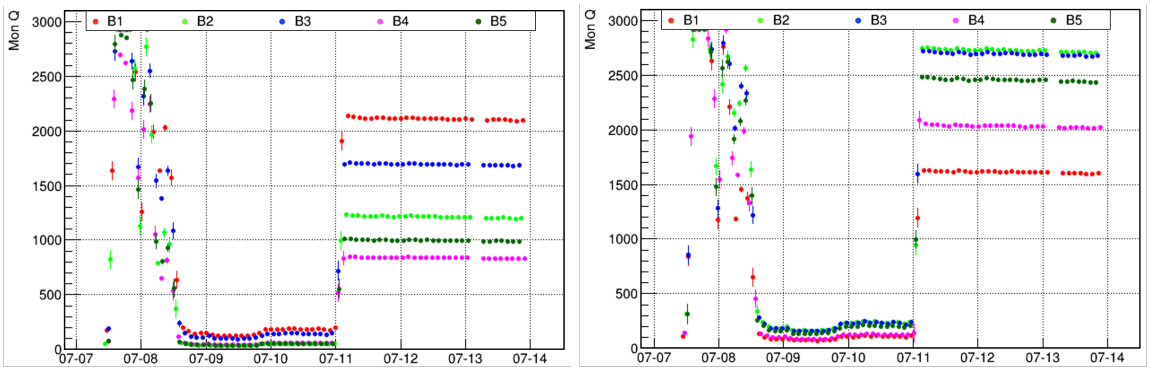

(a) **(b)**

Fig. 6.17: Monitor PMT charge for the collimator and diffuser, **(a)** and **(b)** respectively, after the potentiometer has been changed. These are sitting at a similar level to before, but are no longer reaching saturation limit for any injectors. The instability at the beginning is after the potentiometer was turned in the opposite direction, before stabilising to the low value. This was then turned back to the final values.

diffusers and collimators are in Fig. 6.18, with it being clear the problem is mostly limited to the collimators. As the collimators had previously been tested for water-tightness, this is somewhat unexpected; the likely culprit comes from the installation. The collimators themselves are pushed into the housing, specifically designed to be flush with the collimator size, and then sealed with epoxy. It is possible that as the collimators were pushed into their slot, this loosened some of the sealing epoxy on the collimator housing itself, stopping it from being watertight. This would cause a much greater drop in the prompt charge than the total charge, as the light would be more diffuse coming out of the collimator and thus be outside of the spot definition. The degradation may also explain the low charge seen in the B3 and B5 collimators: these both had higher injected charges when first installed in the detector. Fig. 6.19 shows the low prompt charge of these injectors. It seems likely these are advanced stages of the degradation seen most strongly in the B2 and B4 injectors. The supposed water ingress hypothesis is also supported with the survival of the B1 collimator, the only one not strongly undergoing degradation. As it is installed in the top of the tank, it feels a much lower water pressure than the lower injector positions, and so the epoxy around the feedthrough has remained mostly watertight. Due to the deterioration of the B2-B5 injectors, these are no longer applicable for analyses: the B1 collimator will continue to be be used however. This is something that must be fixed for the system installed into the HK detector.

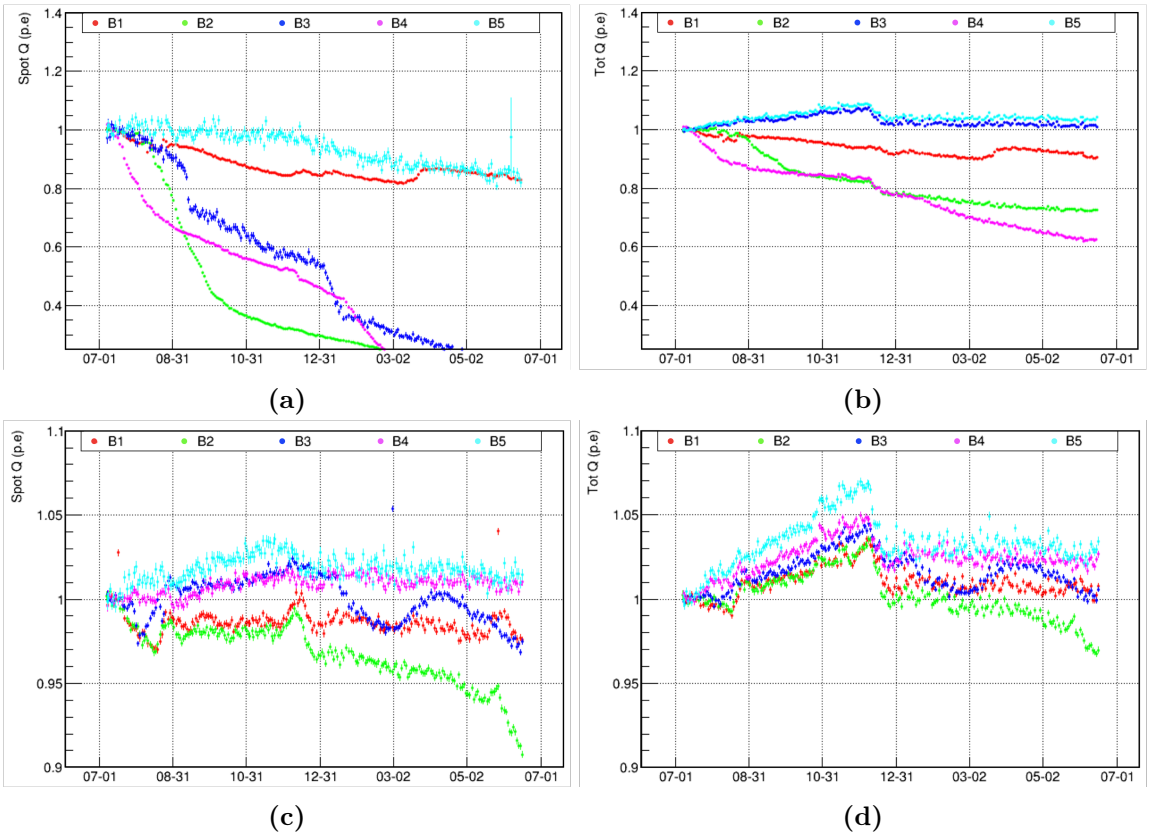

Fig. 6.18: The degradation of the collimator prompt charge, **(a)**, and its total charge, **(b)**. The diffuser prompt and total charge, **(c)** and **(d)** respectively, are shown for reference. The collimator beam spot is clearly degrading, likely due to water ingress through the epoxy seal, leaving only the B1 collimator still usable.

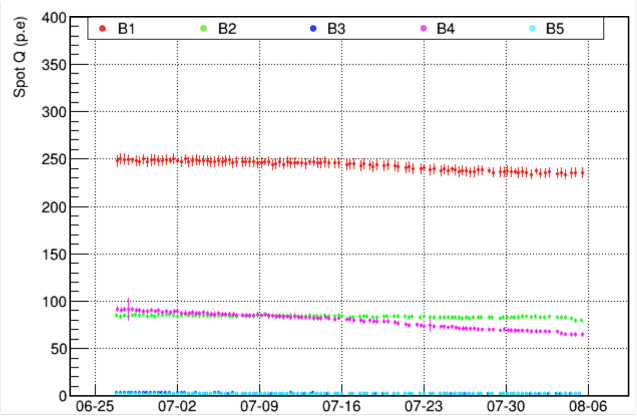

Fig. 6.19: Prompt charge of the collimators. The B3 and B5 positions are likely at an advanced stage of degradation, causing their prompt charge to sit at almost 0. The B4 position has only just begun to degrade.

6.3.6 Future Improvements to the Software

Although the above automated monitoring system is in place and working well, it is not perfect and will need to be improved as more data is collected. This section will focus on how changes in the implementation of the software can improve the efficiency of the full system for future analysers.

The main issue that must be addressed is the inclusion of the top diffuser in the local version of SELCALIB. Once this is completed, the top diffuser will be fully integrated with the automation system, and will not have issues relating to losing data due to subruns being removed. This often led to the software becoming stuck, and thus data runs to not be included in the monitoring. This is not a large problem, as the run could be reanalysed offline, however this can waste both computing and human resources in trying to fix the problem. This integration of the top diffuser is currently underway, and is now more crucial with the lowering of the injectors wavelength.

An important efficiency improvement will be in the plotting, as currently all plots are updated together, and ideally the shorter time span plots should be updated more frequently than the longer ones. This becomes a particular problem as the amount of data collected increases. This should be investigated in the near future.

The final improvements are related to the problems with the hardware. Now the monitor PMT is back online, it needs to be included for data normalisation as soon as possible. This should increase the sensitivity to water parameters, due to the independence of the amount of injected light measurement and the charge in the tank. However, before this is completed a linearity study will need to be performed to map changes in the injected light to changes observed in the tank. Also, with the degradation and subsequent low charge of the B2-B5 collimators, they are no longer useful for analyses. These will always being included in the official SELCALIB process, but it is no longer worth extracting and plotting these as part of the local measurement as they cannot be accurately used. These should be removed in order to increase the system efficiency, and only analysed if necessary.

6.3.7 Effect of Gadolinium Loading

An important milestone for the system as a whole was the monitoring of the first (and recently second) gadolinium loading period. The rate of gadolinium loading for both phases is shown in Fig. 6.20. The purpose of the water system is to ensure the transparency of the water is good enough for physics analyses, thus it is important to know whether the gadolinium loading has any effect on the transparency. Previously EGADS (Evaluating Gadolinium's Action on Detector Systems) has shown that gadolinium sulphate is transparent to Cherenkov light [312], however this has a different water flow rate and pattern than SK. Although the through-muon analysis, mentioned in section 6.3.4, is used for the official analysis of the water quality, the effect should also be observed with the UK injectors.

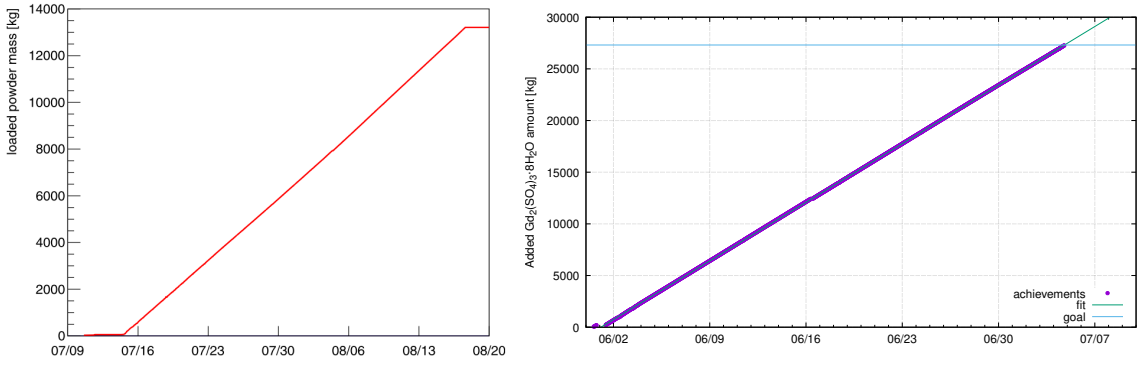

(a) **(b)**

Fig. 6.20: Gadolinium loading schedule for both phase 1 and 2. **(a)** Gadolinium loading phase 1. 13.2 tons of $Gd_2(SO_4)_3 \cdot 8\,H_2O$ powder was added over a period of 35 days. This is 5426 kg of Gd. Figure taken from [313]. **(b)** Gadolinium loading phase 2. 27.265 tons of gadolinium powder was added over 36 days following upgrades to the loading system, corresponding to 11208 kg of Gd.

The muon attenuation analysis, Fig. 6.21, has shown after the gadolinium is dissolved the water quality decreases substantially before settling back to a similar water transparency as pure water. With this in mind, Fig. 6.22 displays the effect of the gadolinium front (*i.e.*, the top layer of the gadiated water) as it passes over the barrel injector positions. In the top two collimators, there is a distinct ∼5% drop in the prompt charge as the Gd-front raises above the level of collimators. Although the muon data shows the water quality recovering (albeit on a longer timescale than Fig. 6.22), this is not seen in the collimator data. This is, however, likely to be due to the collimator degrading and thus the recovery cannot be observed, even in the mostly unaffected B1 data. Though, as the EGADS measurement suggests, there should be no change in water transparency with the inclusion of the gadolinium sulphate, the gd-front clearly reduces the quality. This is most likely due to a layer of particulates and dirt rising on the slightly denser gadiated water, causing a greater amount of scattering in the beam spot.

Whilst it was a large milestone for the barrel injectors to see the impact of gadolinium loading, the top injector has a much higher potential for sensitivity to changes in the bottom of the tank and should be a very powerful tool. Unfortunately, however, the wavelength of

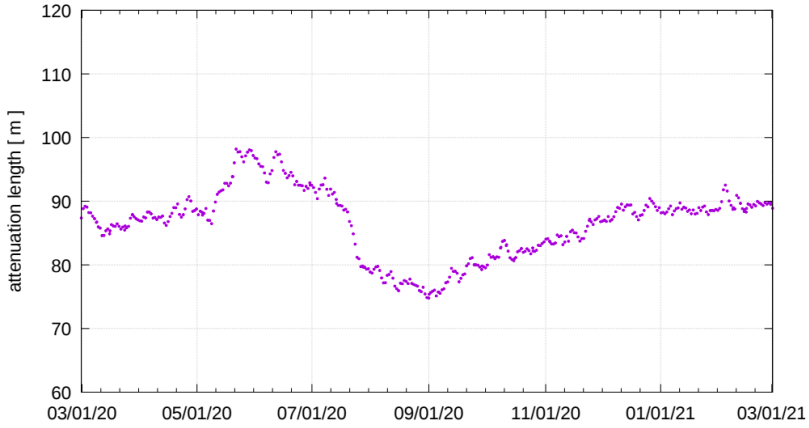

Fig. 6.21: Calculated muon attenuation length over the gadolinium loading period. On April 29$^{\text{th}}$ 2020, the water temperature was lowered which increased light transparency. This started to decrease after gadolinium began being loaded into the detector. This began to stabilize after loading was complete, becoming stable back at ∼90 m at the beginning of December 2020. Figure taken from [313].

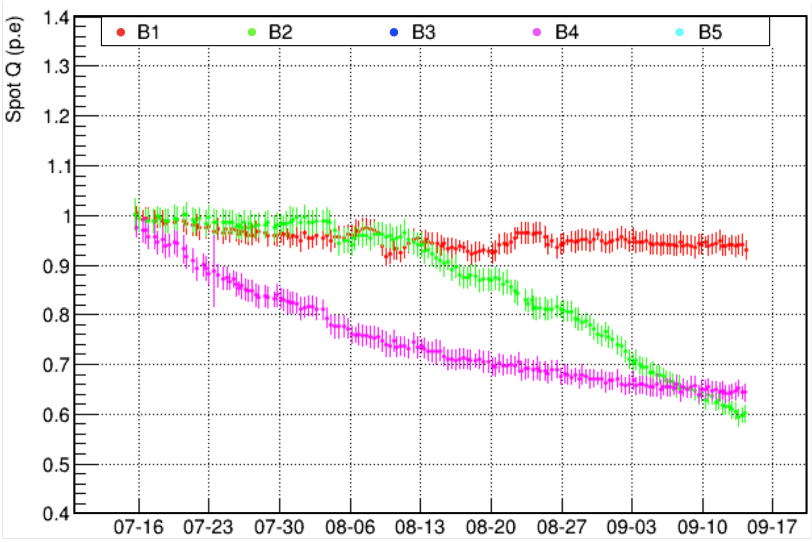

Fig. 6.22: The gadolinium front passes the injector positions, B1, B2 and B4 at 8$^{\text{th}}$ August, 4$^{\text{th}}$ August and 25$^{\text{th}}$ July respectively. The gadolinium front is not clear on the B4 injector, however a clear $\sim 5\%$ drop in the prompt charge can be seen in the top two collimators as the gd-front passes over the position.

the injector of the top diffuser is 473 nm, which is largely resistant to changes in the water quality: certainly compared to the smaller wavelengths associated with Cherenkov light. Nevertheless, it is still interesting to monitor the changing quality of this light.

Fig. 6.23 shows the variation of the top diffuser over ∼6 months from the beginning of gadolinium loading. During the loading itself there is some variation in the water quality, mostly translating to a decrease in the attenuation length inside the tank (as the bottom PMTs are, on average, further from the injector position than the barrel). Whilst this change looks substantial, it is important to note this is only a variation on the order of 1%. This shows the sensitivity the top diffuser has for the attenuation, however it is currently limited by the wavelength of the injector. Comparing this to the Korean injectors in Fig. 6.24, there is a notable drop in the attenuation for the lower wavelengths, up to 17% after the first gadolinium loading, whereas the longer wavelengths there is very little change. Of course, the fine changes cannot be seen due to the binning, however extrapolating the Korean data to longer wavelengths, the top diffuser data would seem to match. The wavelength of the top diffuser was lowered to 368 nm on the 14^{th} April 2022, in order to gain a greater sensitivity to the changing parameters and a more direct comparison with the other injectors.

The plots shown above were for the first gadolinium loading period, where it was uncertain how the water quality would vary in the detector. With the second loading, there was more expectation for the behaviour of the water quality, and with the lower wavelength there is more sensitivity to the changing parameters. To utilise this new sensitivity, a two bin relative attenuation measurement was used to monitor the changes. This uses a ratio of PMTs with z and y less than 0, to those with greater than 0, ignoring the bottom PMTs, within the opening angle of the diffuser. The reaction to gadolinium loading is shown in Fig. 6.25.

Even with the difference in wavelength, both measurements show a similar reaction to the gadolinium loading period. After ∼2 weeks of loading, there is a ∼1% drop in the water quality, followed by a ∼0.5% rise post loading ending. However, there is a difference in the initial 2 weeks of dissolving, and in the tank following the end of the period. This is likely only from differences in wavelength, and different water temperatures and circulation structure; however, it will be interesting to continue monitoring the relative change as data continues to be collected. Importantly, there is a direct comparison with the Korean system which, for the lower wavelengths in Fig. 6.24, match up well with the structure seen in the top diffuser.

The impact of the first gadolinium loading on the collimators was very apparent, and it would be expected to see a similar effect for the second loading. Due to the issues discussed in section 6.3.5, the impact can only be measured in the B1 injector. Fig. 6.26 shows the B1 collimator over the gadolinium period. The front passes over the injector position on the 28^{th} June, however there does not seem to be any effect as the more gadiated water passes over the injector position, a complete contrast to the first loading. The theory of the first drop in the collimators was due to a layer of particulates rising on the denser water: it may be possible this debris from the bottom of the tank has already been circulated and passed

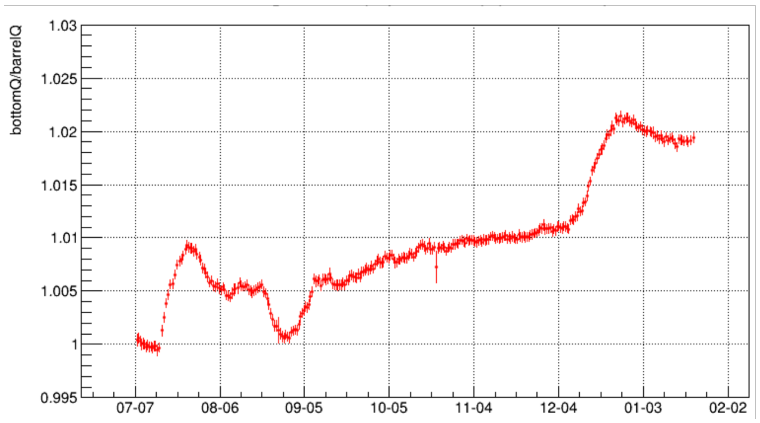

(a)

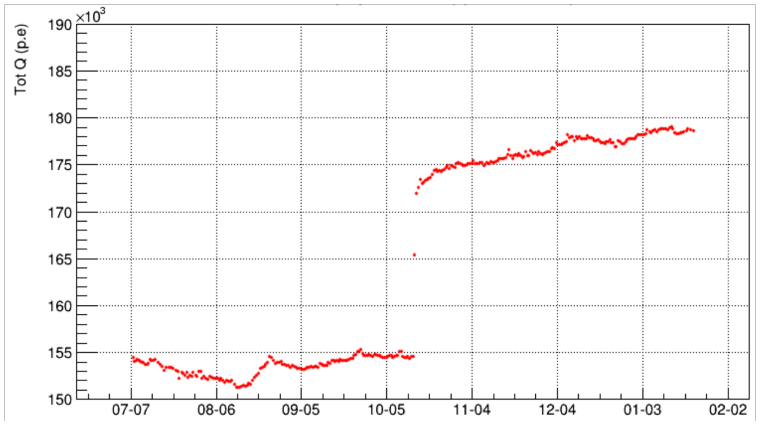

(b)

Fig. 6.23: Top diffuser plots during gadolinium loading. **(a)** The ratio between the bottom and barrel PMT charge. This is normalised to the first data point, which is just before gadolinium loading. **(b)** The top diffuser total charge over the same period. The power was increased, but it is clear this does not effect the measurement. There is a lot of variation in the ratio after the gadolinium period, which stabilises after this period is up.

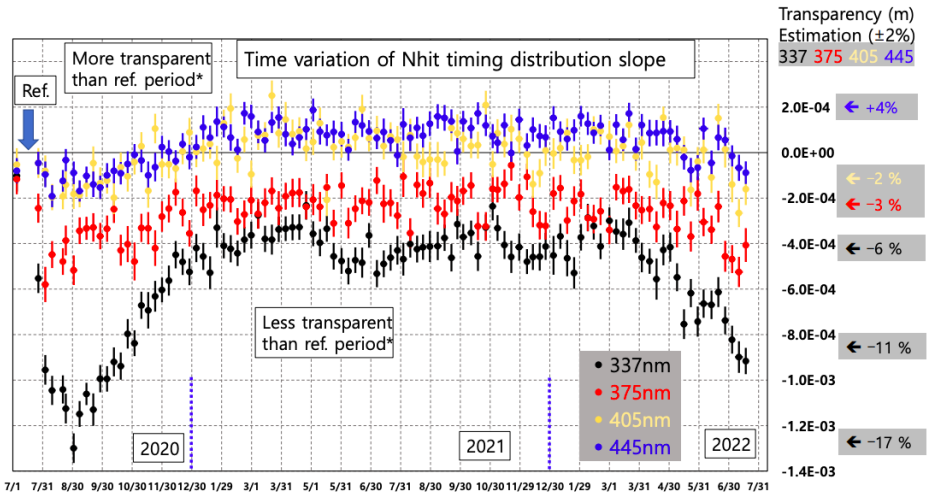

Fig. 6.24: Time variation of the Korean laser injectors for various wavelengths. It is clear the shorter wavelengths exhibit more sensitivity to the changing water quality. The reference period begins on the week commencing 2nd July 2020.

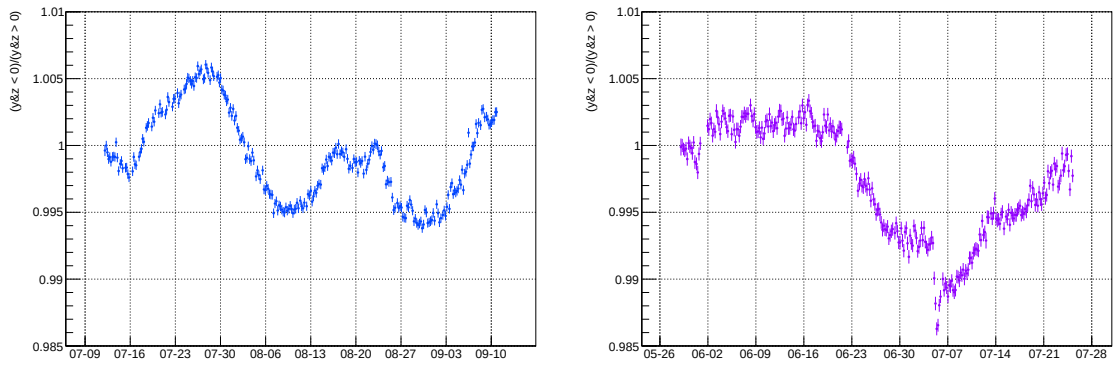

(a) **(b)**

Fig. 6.25: Two bin relative attenuation measurements for the first and second, **(a)** and **(b)**, gadolinium loading periods. Between these, the wavelength of the injector was changed from 473 nm to 368 nm. Both drop by 1% during loading before rising again after the loading was complete.

through the filter and hence no effect on the collimator. There is substantial variation on the collimator over this period, though the trend downwards could to be indicative of the same degradation seen in the other collimators.

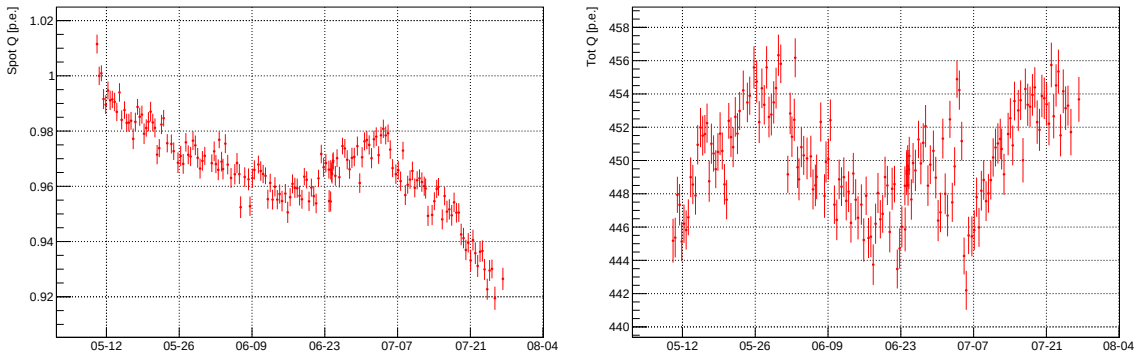

(a) **(b)**

Fig. 6.26: Effect of the second gadolinium loading on the B1 collimator prompt charge. The gadolinium front passed the injector position on the 28$^{\text{th}}$ June. There does not seem to be any effect as it passes.

Again, due to the change in wavelength of the top diffuser, it is now possible to more closely compare to the muon measurements. Comparing Figs. 6.26b and 6.27, it can be seen the tail of the latter matches well with the former. After the loading began, there is little fluctuation in the water quality, then dropping until the end of loading. This is followed by a rise, matching perfectly in each case. Although there is no new information contained in the top diffuser, it lends credence to the sensitivity of the system and the future analyses completed with it. Measurements with the top diffuser also have no reliance on the randomness of muon interactions inside the tank, providing a constant and measurable light injection.

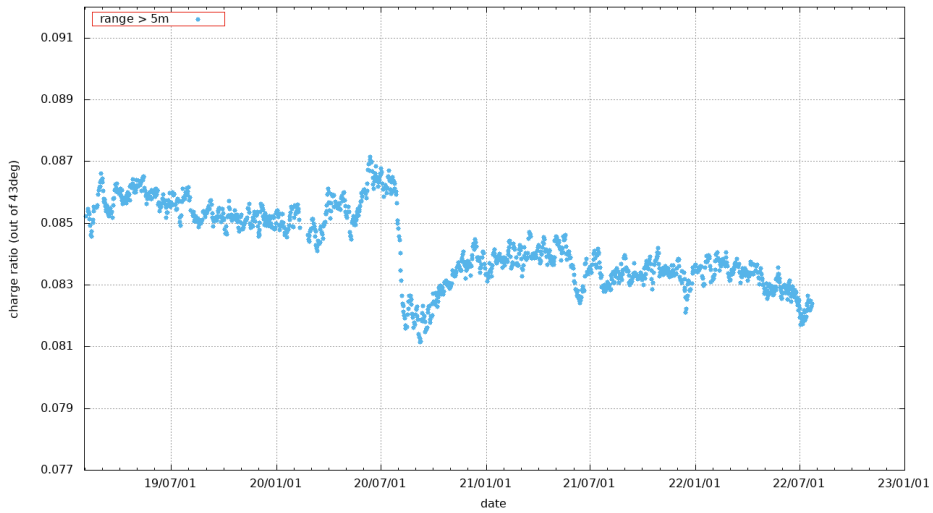

Fig. 6.27: Muon charge ratio measurement of the water quality. This is the ratio of the charge outside the Cherenkov cone, to the charge within the cone.

6.4 Attenuation Measurement

A key point of the new system is a greater sensitivity to the water quality parameters. Although the full fit to the water absorption and scattering parameters can be completed by comparing simulated data from SKDETSIM to real data, an attenuation measurement can be made using the diffusers (using both the top and barrel injectors). The attenuation length in pure water is roughly 100 m, which is comparable to the SK tank size (the diagonal of the tank being ∼50 m), so it is important to monitor any changes in the total attenuation.

A typical attenuation plot from the cosmic ray muon analysis is shown in Fig. 6.28, with the fit for the attenuation length using equation 6.9. With the top and barrel diffusers, the same measurement can be performed. The measured charge first needs to be corrected for the relative sensitivity of the PMT. This is calculated using a simple fit to the data with a polynomial, given by

$$f(\theta) = 0.205349 + 0.523981x + 0.389951x^2 - 0.131959x^3\,, \tag{6.10}$$

where $x = \cos\theta$: the function and its definition is shown in Fig. 6.29. The effective charge is defined by $Ql/f(\theta)$, where the definitions are the same as before. The factor of l comes from the reduction in intensity of a line source (such as that from a muon Cherenkov cone). Currently, the analysis with the UK system also uses this definition: the reason will be explored later.

By plotting the effective charge against the photon travel length and fitting with an exponential, one can obtain the effective attenuation length for each run. For each run, the total charge collected is averaged over the number of hits, and only the barrel PMTs are used for the analysis. There is also a cut for PMTs with $Y > 0$, to remove any geometrical effects. Within this analysis, it must be assumed that all the light reaching the PMTs is direct light: this is helped with the temporal and spatial cut, but some will still be contained

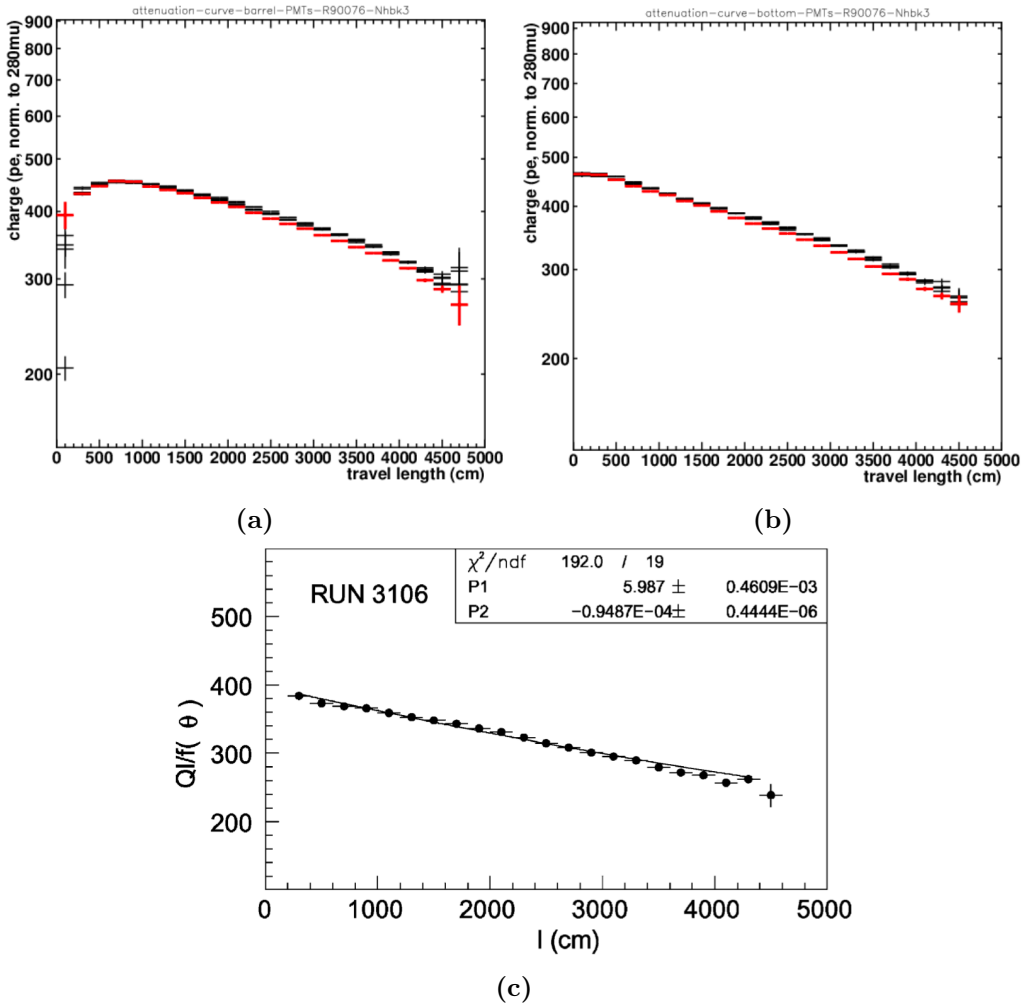

Fig. 6.28: **(a)** and **(b)** show the muon curves created for the barrel and bottom PMTs. **(c)** is the effective observed charge as a function of the path length, with the fit applied. This gives an attenuation length of 105.4 m. (a) and (b) are taken from [314], (c) is taken from [233].

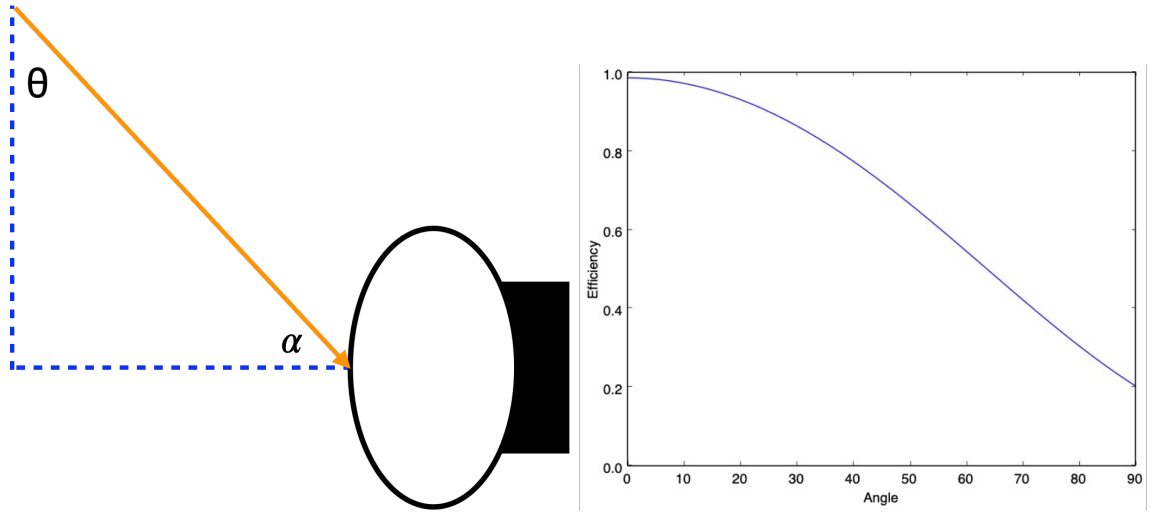

(a) **(b)**

Fig. 6.29: PMT sensitivity as a function of angle. The measurements were fit with a third degree polynomial, shown in **(b)**. **(a)** shows the definition, with α the angle the sensitivity is measured from.

within the prompt charge definition.

Fig. 6.30 shows example attenuation curves for the top diffuser. The exponential fit returns the constant, Q_0, and the effective attenuation length, L. For the examples in Fig. 6.30, the attenuation lengths are 87±2 m and 99±2 m for runs 82914 and 86418 respectively. These are in the right proximity with the value for the attenuation length of pure water, and also closely matches the attenuation length calculated from the bottom PMTs in the muon analysis. Each run has its own individual attenuation measurement.

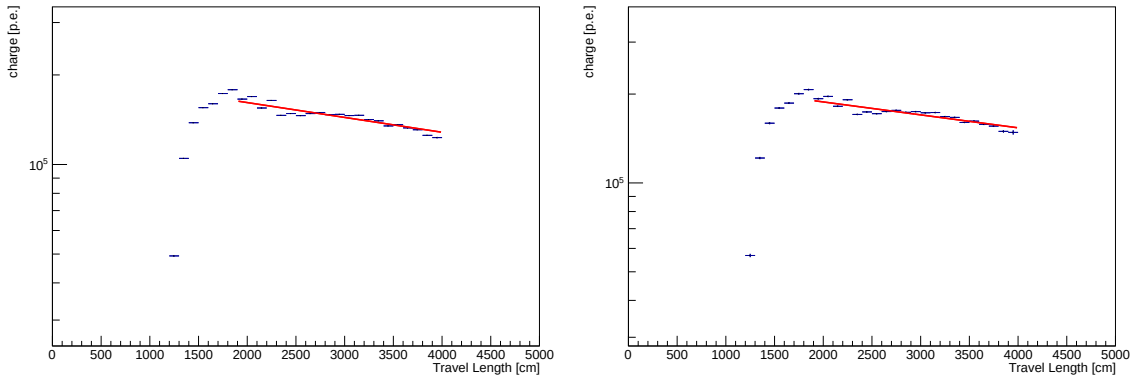

(a) **(b)**

Fig. 6.30: Attenuation curves from the top diffuser for runs 82914, **(a)**, and 86418, **(b)**. The lines show an exponential fit, which gives the value for the attenuation length. The values of $1/L$ are $(1.15 \pm 0.03) \times 10^{-4}$ and $(1.01 \pm 0.02) \times 10^{-4}$ cm^{-1}, giving attenuation lengths of 87 ± 2 and 99 ± 2 m.

The accuracy of the independent attenuation length measurements is difficult to verify, as measurements using the same system (*i.e.* barrel vs bottom PMTs from cosmic through-going muons) can give wildly different results. Fig. 6.31 shows same analysis for the muon

measurements and their variation over time. Whilst the general trends of data match well, the absolute value of the attenuation changes dependent on the PMTs used. Therefore although the absolute measurement from the top diffuser is interesting, perhaps more useful is the relative change with each run which, in combination with the muon analysis, can be used to correct for the water quality in physics analyses.

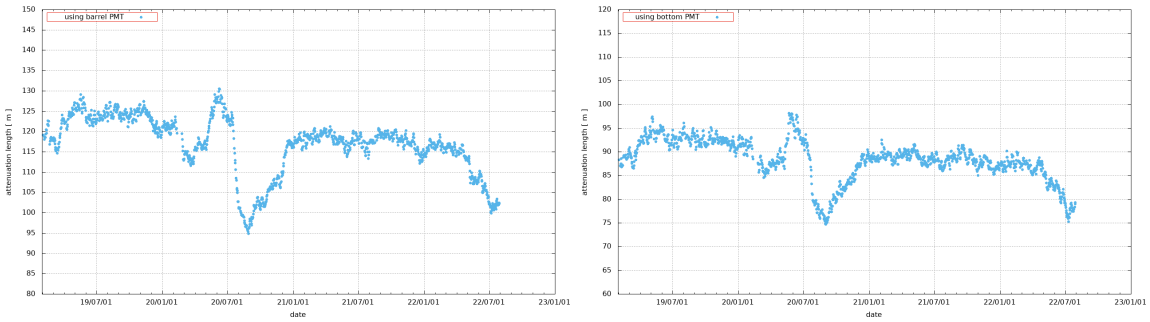

(a) **(b)**

Fig. 6.31: Muon attenuation length measurements for the barrel, (a), and bottom, (b), PMTs respectively. The same shape is seen in both, but the absolute value is very different. Figure taken from [315].

The absolute value of the attenuation length as a function of time measured using the top diffuser is shown in Fig. 6.32. Each data point corresponds to a single run, and only runs with greater than 1000 events were considered. It is clear the general form is different to the muon analysis due to the different wavelengths of each source, however it is most interesting comparing to the charge ratio in Fig. 6.23a. Whilst the latter has a more restricted time frame, it is clear the overall form is similar, however the time-variation measured using absolute attenuation measurements is clearly more sensitive, showing much greater variation in small periods of time. It is somewhat surprising so much variation is seen with a wavelength of 473 nm, as longer wavelengths are less sensitive to water quality changes than their shorter counterparts. However, this is likely due to the unique position of the top injector, which is highly sensitive to changes in the bottom of the tank.

As mentioned, it is difficult to verify the absolute measurements of the attenuation lengths, as each analysis gives a different result. Some of this is due to the differences in wavelength, however this cannot explain the differences between the two muon analyses. In the top diffuser analysis shown here, the reduction in intensity due to solid angle is corrected for using the same method as the muon analysis, *i.e.* using l. The top diffuser, however, can be viewed as a point source in the detector, thus one would expect to correct for the solid angle with a factor of l^2. Using this latter method, the attenuation curves gained energy with distance, an obvious violation of what is expected[6]. This is an obvious issue, however as the more important information is the *relative* change in the attenuation length, it was decided that this is not necessarily a problem. For future and more complex analyses, this is something that should be investigated further.

A similar process could be completed with the barrel diffusers, however because of their

[6]Though it would solve the world's energy crisis, and stop the current cost of living being so high.

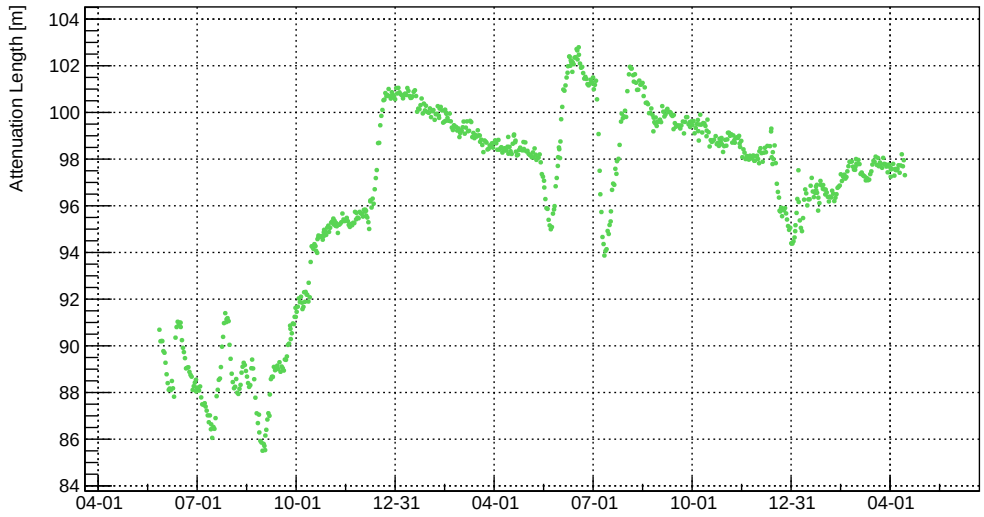

Fig. 6.32: Time variation of the attenuation length as measured from the top diffuser. Each data point represents a single run, and only runs with greater than 1000 events are used. Much more variation is observed than using other methods.

location and lower event rate, these are much more effected by statistics and problems with geometry. A full attenuation measurement has not been made, and a relative measurement is still subject to these complications. It is likely that in order to use the barrel diffusers for this purpose, a more complex analysis is needed, likely involving combinations of multiple diffuser positions to access a full range of hit distances. Once this is completed, it will be an interesting and important development for the UK system as a whole.

6.5 Summary

For any physics analysis, it is clear a detector must be fully and carefully calibrated in order for any measurement to be meaningful. The work in this chapter, whilst not the most glamorous, is the first stepping stone to make raw data into a discovery. Monitoring of the water quality, particularly during gadolinium loading, translates directly into detector performance, which leads to the light yield and therefore the energy scale of the detector. A major achievement of the new UK light injection system was the direct observation of the effect of gadolinium loading on the water quality at different levels within the SK tank, and making an independent measurement of the attenuation length. This latter quantity can continue to be measured during normal SK data runs, and thus used to correct for the water quality within the detector. As the analyses are developed and improved, the system itself will feed directly into the sensitivity of the future detector HK, and thus into potential future discoveries about the properties of neutrinos.

Chapter 7

Concluding Remarks

I regret nothing. The end.

Ron Swanson (S5E17)

With the new generation of neutrino experiments (Hyper-Kamiokande, DUNE, JUNO, PINGU *etc.*) being designed and planning the most sensitive measurements of neutrino oscillation parameters, it is becoming vital for the systematics to be reduced to a level where these are possible. It is clear that at the systematic error current experiments are working with, this will not be achievable. A large part of these systematics come from the underlying interaction model, and whilst new models are being produced that allow a more thorough description of nature, these often take some time before appearing in generators. Experiments then have to rely on ad-hoc tunings to available data. It is evident that electron scattering is an important tool in this endeavour, and this thesis mainly focuses on using said data to derive inputs for the T2K oscillation analyses. In essence, all work completed here has been to reduce the systematic errors associated with neutrino experiments, be it in deriving new corrections to apply to neutrino interaction simulations, or calibration work to ensure the correct energy scale is achieved in the all important physics analyses.

Chapter 4 describes an electron extension implemented into NEUT, T2K's primary interaction generator. Due to its well defined kinematics and the link between electron and neutrino interactions, electron scattering can provide key information to improve models that neutrino predictions are based on. Indeed, some in the community believe that one cannot trust the results of a generator that cannot reproduce the available electron scattering data. The prescription for the implementation allows electrons to be generated in multiple ways, one which uses ad-hoc methods to create 'pseudo-electrons' and one that builds them directly into the generator. The full electron scattering description has only been implemented using the spectral function ground state, however producing 'pseudo-electrons' can be achieved relatively simply with any model implemented in generators, such as the (still widely used) relastivistic Fermi gas model. This can also be completed with other generators which do not yet have an electron scattering implementation. Comparisons of these electron scattering models were made to other generators with electron capabilities, which show considerable

agreement in the position of the elastic peak, however due to the tools available in the neutrino scattering community, there was some disparity in the differential cross-section scaling. Unfortunately, there remain some issues with fully integrating an electron scattering mode into NEUT, which is extraordinarily resistant to new implementations. This relies on generating new cross-section tables for electron scattering predictions, set with a particular Q^2 threshold in a similar fashion to that employed in the GENIE generator. However, despite the problems encountered (both within the software and in the world at large), this is the first time NEUT has been used to generate electron scattering events.

The T2K interaction models are all based on the impulse approximation, which assumes that an interaction occurs on a single nucleon and the lepton does not undergo final state interactions. This allows the ground state and the fundamental interaction to be factorised. However, this is not a true description of nature, where one expects the lepton kinematics to have a impact on the sampling of the nuclear state, and also to undergo interactions with the nucleus as a whole. In chapter 5, a correction to the charged-current quasi-elastic interaction was derived, allowing the model to move beyond the impulse approximation to a more 'natural' model. Here, it was shown that in order for electron scattering predictions to match (e,e$'$) data, a kinematic dependent shift applied to the nucleon removal energy was required. This is reminiscent of features that appear in more sophisticated relativistic mean field calculations, and also reproduced with optical potential models. Applying this kinematic removal energy necessarily allows the NEUT electron predictions to match with data, but also produces similar results to the more theoretically rigorous models. One issue with this approach is that it artificially shifts the spectral function removal energy distribution, causing a non-negligible portion of events to become unphysical and having a negative removal energy. This has been rectified by truncating the removal energy distributions to keep nucleons bound within the nucleus, however this does slightly reduce the effect the kinematic removal energy has on the outgoing lepton kinematics. Nevertheless, moving NEUT beyond the simple factorisation model is an important step, and the close agreement of the different models adds a level of certainty to each of them. This method is computationally inexpensive, and allows a simplified model to match the results produced by in-depth calculations and is relatively easy to include on top of a pre-existing model.

Finally, in chapter 6, the efforts to introduce the UK light injection system into the every day Super-Kamiokande monitoring has been described. This has described the newly installed system, and the definitions of each injector used in the monitoring have been outlined. A significant milestone with the system was measuring the effect of both gadolinium loading periods, allowing a real-time measurement of the gadolinium's effect on water quality. This is all completely automated, and can continue to be used and developed for future analyses, continuing into the next generation of Japanese neutrino experiments. Aside from the numerous hardware issues that plague any experiment, these efforts have allowed continuous monitoring since 2020. Also described is the first analysis completed with the system, deriving attenuation measurements for each SK run. These can be compared to the currently used muon attenuation measurements, which can be taken into account when physics analyses take place. Whilst this still needs some work and analysis, this is the first stepping stone

to a fully integrated system that can make measurements of all water quality constants.

As neutrino physics moves into the era of precision measurements dominated by systematic errors over statistical, the large uncertainties on the neutrino cross-sections and the underlying ground state will need to be overcome. Although future efforts will always be required to build on the work presented here, this thesis hopefully contributes a tiny portion to the large body of work that will be needed to overcome this task.

References

[1] W. Pauli, *Letter of 4th Dec 1930*, 1930.

[2] J. Chadwick, "Intensitätsverteilung im magnetischen Spectrum der β-Strahlen von radium B + C", Verhandl. Dtsc. Phys. Ges. **16**, 383 (1914).

[3] J. J. Thompson, "XL. Cathode Rays", The London, Edinburgh, and Dublin Philosophical Magazine and Journal of Science **44**, 293–316 (1897).

[4] E. Rutherford, "LIV. Collision of α particles with light atoms. IV. An anomalous effect in nitrogen", The London, Edinburgh, and Dublin Philosophical Magazine and Journal of Science **37**, 581–587 (1919).

[5] E. Fermi, "Versuch einer Theorie der β-Strahlen. I", Zeitschrift für Physik **88**, 161–177 (1934).

[6] W. J. Henderson, "The Upper Limits of the Continuous β-Ray Spectra of Thorium C and C″", Proceedings of the Royal Society A **147**, 10.1098/rspa.1934.0237 (1934).

[7] J. Chadwick, "The existence of a neutron", Proceedings of the Royal Society A **136**, 10.1098/rspa.1932.0112 (1932).

[8] "The "Neutrino"", Nature **133**, 532 (1934).

[9] B. Pontecorvo, "Inverse β Process", Chalk River Laboratories Report (1946).

[10] R. Davis, "Attempt to Detect the Antineutrinos from a Nuclear Reactor by the $Cl^{37}(\overline{\nu}, e^-)Ar^{37}$ Reaction", Phys. Rev. **97**, 766–769 (1955).

[11] Los Alamos Science, "Detecting the Poltergeist", Los Alamos Science **25** (1997).

[12] C. L. Cowan, F. Reines, et al., "Detection of the Free Neutrino: a Confirmation", Science **124**, 103–104 (1956).

[13] F. Reines and C. L. Cowan, "Free Antineutrino Absorption Cross Section. I. Measurement of the Free Antineutrino Absorption Cross Section by Protons", Phys. Rev. **113**, 273–279 (1959).

[14] J. C. Street and E. C. Stevenson, "New Evidence for the Existence of a Particle of Mass Intermediate Between the Proton and Electron", Phys. Rev. **52**, 1003–1004 (1937).

[15] E. P. Hincks and B. Pontecorvo, "Search for Gamma-Radiation in the 2.2-Microsecond Meson Decay Process", Phys. Rev. **73**, 257–258 (1948).

[16] G. Danby et al., "Observation of High-Energy Neutrino Reactions and the Existence of Two Kinds of Neutrinos", Phys. Rev. Lett. **9**, 36–44 (1962).

[17] M. L. Perl et al., "Evidence for Anomalous Lepton Production in $e^+ - e^-$ Annihilation", Phys. Rev. Lett. **35**, 1489–1492 (1975).

[18] D. DeCamp et al., "Determination of the number of light neutrino species", Phys. Lett. B **231**, 519–529 (1989).

[19] B. Adeva et al., "A determination of the properties of the neutral intermediate vector boson Z0", Phys. Lett. B **231**, 509–518 (1989).

[20] M. Z. Akrawy et al. (OPAL Collaboration), "Measurement of the Z0 mass and width with the OPAL detector at LEP", Phys. Lett. B **231**, 530–538 (1989).

[21] P. A. Aarnio et al. (DELPHI Collaboration), "Measurement of the mass and width of the Z0 particle from multihadronic final states produced in e^+e^- annihilations", Phys. Lett. B **231**, 539–547 (1989).

[22] G. S. Abrams et al., "Measurements of Z-boson resonance parameters in e^+e^- annihilation", Phys. Rev. Lett. **63**, 2173–2176 (1989).

[23] S. Schael et al., "Precision Electroweak Measurements on the Z Resonance", Physics Reports **427**, 257–454 (2006).

[24] K. Kodama et al., "Observation of tau neutrino interactions", Phys. Lett. B **504**, 218–224 (2001), arXiv:`0012035[hep-ex]`.

[25] H. A. Bethe, "Energy Production in Stars", Phys. Rev. **55**, 434–456 (1939).

[26] J. N. Bahcall, M. H. Pinsonneault, and S. Basu, "Solar Models: Current Epoch and Time Dependences, Neutrinos, and Helioseismological Properties", The Astrophysical Journal **555**, 990–1012 (2001).

[27] J. N. Bahcall, "Solar Neutrinos", Phys. Rev. Lett. **17**, 398–401 (1966).

[28] J. N. Bahcall, A. M. Serenelli, and S. Basu, "New Solar Opacities, Abundances, Helioseismology, and Neutrino Fluxes", The Astrophysical Journal **621**, L85–L88 (2005).

[29] R. Davis, "Solar Neutrinos. II. Experimental", Phys. Rev. Lett. **12**, 303–305 (1964).

[30] B. T. Cleveland et al., "Measurement of the Solar Electron Neutrino Flux with the Homestake Chlorine Detector", The Astrophysical Journal **496**, 505–526 (1998).

[31] J. N. Bahcall, M. H. Pinsonneault, and G. J. Wasserburg, "Solar models with helium and heavy-element diffusion", Rev. Mod. Phys. **67**, 781–808 (1995).

[32] K. S. Hirata et al. (Kamiokande-II), "Observation of B-8 Solar Neutrinos in the Kamiokande-II Detector", Phys. Rev. Lett. **63**, 16 (1989).

[33] V. A. Kuzmin, "Detection of solar neutrinos by means of the 71Ga(nu, e-)71Ge reaction", Zh. Eksp. Teor. Fiz. **49**, 1532–1534 (1965).

[34] J. N. Bahcall et al., "Proposed Solar-Neutrino Experiment Using ^{71}Ga", Phys. Rev. Lett. **40**, 1351–1354 (1978).

[35] M. Cribier et al., "Results of the whole GALLEX experiment", Nuc. Phys. B **70**, 284–291 (1999).

[36] M. Altmann et al., "Complete results for five years of GNO solar neutrino observations", Physics Letters B **616**, 174–190 (2005).

[37] J. N. Abdurashitov et al. (SAGE Collaboration), "Solar neutrino flux measurements by the soviet-american gallium experiment (sage) for half the 22-year solar cycle", Journal of Experimental and Theoretical Physics **95**, 181–193 (2002).

[38] B. Pontecorvo, "Mesonium and anti-mesonium", Sov. Phys. JETP **6**, 429 (1957).

[39] B. Pontecorvo, "Neutrino Experiments and the Problem of Conservation of Leptonic Charge", Zh. Eksp. Teor. Fiz. **53**, 1717–1725 (1967).

[40] V. Gribov and B. Pontecorvo, "Neutrino astronomy and lepton charge", Physics Letters B **28**, 493–496 (1969).

[41] D. Casper et al., "Measurement of atmospheric neutrino composition with the IMB-3 detector", Phys. Rev. Lett. **66**, 2561–2564 (1991).

[42] K. S. Hirata et al. (Kamiokande-II), "Observation of a small atmospheric muon-neutrino / electron-neutrino ratio in Kamiokande", Phys. Lett. B **280**, 146–152 (1992).

[43] Y. Fukuda et al. (Kamiokande), "Atmospheric ν_μ/ν_e ratio in the multi-GeV energy range", Phys. Lett. B **335**, 237–245 (1994).

[44] Y. Fukuda et al., "Evidence for Oscillation of Atmospheric Neutrinos", Phys. Rev. Lett. **81**, 1562–1567 (1998), arXiv:`9807003[hep-ex]`.

[45] P. A. Zyla et al. (Particle Data Group), "Review of Particle Physics", PTEP **2020**, 083C01 (2020).

[46] J. Boger et al., "The Sudbury Neutrino Observatory", Nuclear Instruments and Methods in Physics Research Section A: Accelerators, Spectrometers, Detectors and Associated Equipment **449**, 172–207 (2000).

[47] Q. R. Ahmad et al., "Measurement of the Rate ofν_e+d→p+p+e-Interactions Produced by B^8 Solar Neutrinos at the Sudbury Neutrino Observatory", Physical Review Letters **87**, `10.1103/physrevlett.87.071301` (2001).

[48] Q. R. Ahmad et al., "Direct Evidence for Neutrino Flavor Transformation from Neutral-Current Interactions in the Sudbury Neutrino Observatory", Physical Review Letters **89**, `10.1103/physrevlett.89.011301` (2002).

[49] S. Fukuda et al. (Super-Kamiokande Collaboration), "Solar B8 and hep Neutrino Measurements from 1258 Days of Super-Kamiokande Data", Phys. Rev. Lett. **86**, 5651–5655 (2001).

[50] B. Aharmim et al., "Electron energy spectra, fluxes, and day-night asymmetries of ^{8}B solar neutrinos from measurements with NaCl dissolved in the heavy-water detector at the Sudbury Neutrino Observatory", Physical Review C **72**, `10.1103/physrevc.72.055502` (2005).

[51] Z. Maki, M. Nakagawa, and S. Sakata, "Remarks on the unified model of elementary particles", Prog. Theor. Phys. **28**, 870–880 (1962).

[52] M. Kobayashi and T. Maskawa, "CP Violation in the Renormalizable Theory of Weak Interaction", Prog. Theor. Phys. **49**, 652–657 (1973).

[53] L. Maiani, "CP Violation in Purely Lefthanded Weak Interactions", Physics Letters B **62**, 183–186 (1975).

[54] R. N. Mohapatra et al., "Theory of neutrinos: a white paper", Reports on Progress in Physics **70**, 1757–1867 (200), arXiv:0510213[hep-ph].

[55] J. Schechter and J. W. F. Valle, "Neutrino masses in SU(2) $\bigotimes$ U(1) theories", Phys. Rev. D **22**, 2227–2235 (1980).

[56] E. K. Akhmedov and A. Y. Smirnov, "Paradoxes of neutrino oscillations", Physics of Atomic Nuclei **72**, 1363–1381 (2009).

[57] L. Wolfenstein, "Neutrino oscillations in matter", Phys. Rev. D **17**, 2369–2374 (1978).

[58] S. P. Mikheyev and A. Y. Smirnov, "Resonance Amplification of Oscillations in Matter and Spectroscopy of Solar Neutrinos", Sov. J. Nucl. Phys. **42**, 913–917 (1985).

[59] X. Qian and P. Vogel, "Neutrino mass hierarchy", Progress in Particle and Nuclear Physics **83**, 1–30 (2015).

[60] R. Patterson, "Prospects for Measurement of the Neutrino Mass Hierarchy", Annual Review of Nuclear and Particle Science **65**, 177–192 (2015).

[61] K. Abe et al. (Super-Kamiokande Collaboration), "Atmospheric neutrino oscillation analysis with external constraints in Super-Kamiokande I-IV", Phys. Rev. D **97**, 072001 (2018).

[62] S.-K. Collaboration, *Atmospheric Neutrino Oscillation Analysis with External Constraints in Super-Kamiokande I–IV*.

[63] I. Esteban, M. Gonzalez-Garcia, M. Maltoni, T. Schwetz, and A. Zhou, "The fate of hints: updated global analysis of three-flavor neutrino oscillations", Journal of High Energy Physics **2020**, 10.1007/jhep09(2020)178 (2020).

[64] A. Piepke (KamLAND), "KamLAND: A reactor neutrino experiment testing the solar neutrino anomaly", Nucl. Phys. B Proc. Suppl. **91**, edited by J. Law, R. W. Ollerhead, and J. J. Simpson, 99–104 (2001).

[65] P. F. de Salas et al., "2020 global reassessment of the neutrino oscillation picture", Journal of High Energy Physics **2021**, 10.1007/jhep02(2021)071 (2021).

[66] S. Abe et al., "Precision Measurement of Neutrino Oscillation Parameters with KamLAND", Physical Review Letters **100**, 10.1103/physrevlett.100.221803 (2008).

[67] F. Kaether, W. Hampel, G. Heusser, J. Kiko, and T. Kirsten, "Reanalysis of the Gallex solar neutrino flux and source experiments", Physics Letters B **685**, 47–54 (2010).

[68] J. N. Abdurashitov et al., "Measurement of the solar neutrino capture rate with gallium metal. III. Results for the 2002–2007 data-taking period", Physical Review C **80**, 10.1103/physrevc.80.015807 (2009).

[69] G. Bellini et al., "Precision Measurement of the Be^7 Solar Neutrino Interaction Rate in Borexino", Physical Review Letters **107**, 10.1103/physrevlett.107.141302 (2011).

[70] J. Hosaka et al., "Solar neutrino measurements in Super-Kamiokande-I", Physical Review D **73**, 10.1103/physrevd.73.112001 (2006).

[71] J. P. Cravens et al., "Solar neutrino measurements in Super-Kamiokande-II", Physical Review D **78**, 10.1103/physrevd.78.032002 (2008).

[72] K. Abe et al., "Solar neutrino results in Super-Kamiokande-III", Physical Review D **83**, 10.1103/physrevd.83.052010 (2011).

[73] B. Aharmim et al., "Combined analysis of all three phases of solar neutrino data from the Sudbury Neutrino Observatory", Physical Review C **88**, 10.1103/physrevc.88.025501 (2013).

[74] Y. Nakajima, *Recent results and future prospects from Super-Kamiokande*, June 2020.

[75] A. Gando et al., "Constraints on θ_{13} from a three-flavor oscillation analysis of reactor antineutrinos at KamLAND", Physical Review D **83**, 10.1103/physrevd.83.052002 (2011).

[76] G. Bak et al., "Measurement of Reactor Antineutrino Oscillation Amplitude and Frequency at RENO", Physical Review Letters **121**, 10.1103/physrevlett.121.201801 (2018).

[77] D. Adey et al., "Measurement of the electron antineutrino oscillation with 1958 days of operation at daya bay", Physical Review Letters **121**, 10.1103/physrevlett.121.241805 (2018).

[78] P. Harrison, D. Perkins, and W. Scott, "Tri-bimaximal mixing and the neutrino oscillation data", Physics Letters B **530**, 167–173 (2002).

[79] Y. Abe et al. (Double Chooz Collaboration), "Indication of Reactor $\overline{\nu}_e$ Disappearance in the Double Chooz Experiment", Phys. Rev. Lett. **108**, 131801 (2012).

[80] F. P. An et al., "Observation of Electron-Antineutrino Disappearance at Daya Bay", Phys. Rev. Lett. **108**, 171803 (2012).

[81] H. Nunokawa, S. Parke, and R. Z. Funchal, "Another possible way to determine the neutrino mass hierarchy", Physical Review D **72**, 10.1103/physrevd.72.013009 (2005).

[82] K. Daum et al. (Frejus), "Determination of the atmospheric neutrino spectra with the Frejus detector", Z. Phys. C **66**, 417–428 (1995).

[83] M. Aglietta et al., "Experimental Study of Atmospheric Neutrino Flux in the NUSEX Experiment", EPL **8**, 611–614 (1989).

[84] M. Aartsen et al., "The IceCube Neutrino Observatory: instrumentation and online systems", Journal of Instrumentation **12**, P03012–P03012 (2017).

[85] M. Ageron et al., "ANTARES: The first undersea neutrino telescope", Nucl. Instr. Meth. **A656**, 11–38 (2011).

[86] A. Albert et al. (ANTARES), "Measuring the atmospheric neutrino oscillation parameters and constraining the 3+1 neutrino model with ten years of ANTARES data", JHEP **06**, 113 (2019), arXiv:1812.08650 [hep-ex].

[87] M. G. Aartsen et al., "Measurement of Atmospheric Neutrino Oscillations at 6-56 GeV with IceCube DeepCore", Physical Review Letters **120**, 10.1103/physrevlett.120.071801 (2018).

[88] Z. Li et al., "Measurement of the tau neutrino cross section in atmospheric neutrino oscillations with Super-Kamiokande", Physical Review D **98**, 10.1103/physrevd.98.052006 (2018).

[89] M. G. Aartsen et al., "Measurement of atmospheric tau neutrino appearance with IceCube DeepCore", Physical Review D **99**, 10.1103/physrevd.99.032007 (2019).

[90] N. Agafonova et al., "Final Results of the OPERA Experiment on ν_τ Appearance in the CNGS Neutrino Beam", Physical Review Letters **120**, 10.1103/physrevlett.120.211801 (2018).

[91] R. Bailey et al., *The CERN Neutrino beam to Gran Sasso (NGS)*, tech. rep. (June 1999).

[92] P. Dunne, *Latest neutrino oscillation results from t2k*, July 2020.

[93] A. Himmel, *New Oscillation Results from the NOνA Experiment*, July 2020.

[94] M. H. Ahn et al., "Measurement of neutrino oscillation by the K2K experiment", Physical Review D **74**, 10.1103/physrevd.74.072003 (2006).

[95] P. Adamson et al., "Combined Analysis of ν_μ Disappearance and $\nu_\mu \to \nu_e$ Appearance in MINOS Using Accelerator and Atmospheric Neutrinos", Physical Review Letters **112**, 10.1103/physrevlett.112.191801 (2014).

[96] K. Abe et al. (T2K), "Constraint on the matter–antimatter symmetry-violating phase in neutrino oscillations", Nature **580**, 339–344 (2020).

[97] M. Aker et al., "Improved Upper Limit on the Neutrino Mass from a Direct Kinematic Method by KATRIN", Physical Review Letters **123**, 10.1103/physrevlett.123.221802 (2019).

[98] C. Kraus et al., "Final results from phase II of the Mainz neutrino mass search in tritium β decay", The European Physical Journal C **40**, 447–468 (2005).

[99] V. N. Aseev et al., "Measurement of the electron antineutrino mass in tritium beta decay in the Troitsk nu-mass experiment", Physics of Atomic Nuclei **75**, 10.1134/S1063778812030027 (2012).

[100] A. L. Turkevich, T. E. Economou, and G. A. Cowan, "Double beta decay of U-238", Phys. Rev. Lett. **67**, 3211–3214 (1991).

[101] S. Dell'Oro, S. Marcocci, M. Viel, and F. Vissani, "Neutrinoless Double Beta Decay: 2015 Review", Advances in High Energy Physics **2016**, 1–37 (2016).

[102] M. Agostini et al., "Probing Majorana neutrinos with double-β decay", Science **365**, 1445–1448 (2019).

[103] D. Q. Adams et al., "Improved Limit on Neutrinoless Double-Beta Decay in Te^{130} with CUORE", Physical Review Letters **124**, 10.1103/physrevlett.124.122501 (2020).

[104] A. Gando et al., "Search for Majorana Neutrinos Near the Inverted Mass Hierarchy Region with KamLAND-Zen", Physical Review Letters **117**, 10.1103/physrevlett.117.082503 (2016).

[105] S. Al Kharusi et al., "Search for Majoron-emitting modes of Xe^{136} double beta decay with the complete EXO-200 dataset", Physical Review D **104**, 10.1103/physrevd.104.112002 (2021).

[106] M. Betti et al., "Neutrino physics with the PTOLEMY project: active neutrino properties and the light sterile case", Journal of Cosmology and Astroparticle Physics **2019**, 047–047 (2019).

[107] J. Lesgourgues and S. Pastor, "Massive neutrinos and cosmology", Physics Reports **429**, 307–379 (2006).

[108] S. Riemer-Sørensen, D. Parkinson, and T. M. Davis, "What Is Half a Neutrino? Reviewing Cosmological Constraints on Neutrinos and Dark Radiation", Publications of the Astronomical Society of Australia **30**, 10.1017/pas.2013.005 (2013).

[109] N. Aghanim et al., "Planck 2018 results", Astronomy & Astrophysics **641**, A6 (2020).

[110] S. Alam et al., "The clustering of galaxies in the completed SDSS-III Baryon Oscillation Spectroscopic Survey: cosmological analysis of the DR12 galaxy sample", MNRAS **470**, 2617–2652 (2017).

[111] P. Minkowski, "$\mu \to e\gamma$ at a Rate of One Out of 10^9 Muon Decays?", Phys. Lett. B **67**, 421–428 (1977).

[112] K. N. Abazajian et al., *Light Sterile Neutrinos: A White Paper*, 2012, arXiv:1204.5379 [hep-ph].

[113] A. Aguilar et al., "Evidence for neutrino oscillations from the observation of $\bar{\nu}_e$ appearance in a $\bar{\nu}_\mu$ beam", Physical Review D **64**, 10.1103/physrevd.64.112007 (2001).

[114] A. A. Aguilar-Arevalo et al., "Significant Excess of Electron-like Events in the MiniBooNE Short-Baseline Neutrino Experiment", Physical Review Letters **121**, 10.1103/physrevlett.121.221801 (2018).

[115] B. Armbruster et al., "Upper limits for neutrino oscillations $\bar{\nu}_\mu \to \bar{\nu}_e$ from muon decay at rest", Physical Review D **65**, 10.1103/physrevd.65.112001 (2002).

[116] M. G. Aartsen et al., "PINGU: a vision for neutrino and particle physics at the South Pole", Journal of Physics G: Nuclear and Particle Physics **44**, 054006 (2017).

[117] S. Aiello et al., "Determining the neutrino mass ordering and oscillation parameters with KM3NeT/ORCA", The European Physical Journal C **82**, 10.1140/epjc/s10052-021-09893-0 (2022).

[118] A. Kumar et al., "Invited review: Physics potential of the ICAL detector at the India-based Neutrino Observatory (INO)", Pramana **88**, 10.1007/s12043-017-1373-4 (2017).

[119] K. Abe et al. (Hyper-Kamiokande Proto-Collaboration), *Hyper-Kamiokande Design Report*, 2018, arXiv:1805.04163 [physics.ins-det].

[120] B. Abi et al. (DUNE Collaboration), *The DUNE Far Detector Interim Design Report Volume 1: Physics, Technology and Strategies*, 2018, arXiv:1807.10334 [physics.ins-det].

[121] R. Patterson, "Prospects for Measurement of the Neutrino Mass Hierarchy", Annual Review of Nuclear and Particle Science **65**, 177–192 (2015).

[122] S. Ajimura et al., "The JSNS^2 detector", Nuclear Instruments and Methods in Physics Research Section A: Accelerators, Spectrometers, Detectors and Associated Equipment **1014**, 165742 (2021).

[123] J. F. Beacom et al., "Physics prospects of the Jinping neutrino experiment", Chinese Physics C **41**, 023002 (2017).

[124] F. An et al., "Neutrino physics with JUNO", Journal of Physics G: Nuclear and Particle Physics **43**, 030401 (2016).

[125] A. Abusleme et al. (JUNO Collaboration), *Juno physics and detector*, 2021, arXiv:2104.02565 [hep-ex].

[126] S. Kim, *New results from RENO and prospects with RENO-50*, 2014, arXiv:1412.2199 [hep-ex].

[127] Y. J. Ko et al., "Sterile Neutrino Search at the NEOS Experiment", Physical Review Letters **118**, 10.1103/physrevlett.118.121802 (2017).

[128] I. Alekseev et al., "Search for sterile neutrinos at the DANSS experiment", Physics Letters B **787**, 56–63 (2018).

[129] H. Almazán et al., "Sterile Neutrino Constraints from the STEREO Experiment with 66 Days of Reactor-On Data", Physical Review Letters **121**, 10.1103/physrevlett.121.161801 (2018).

[130] A. P. Serebrov et al., "First Observation of the Oscillation Effect in the Neutrino-4 Experiment on the Search for the Sterile Neutrino", JETP Letters **109**, 213–221 (2019).

[131] Y. Abreu et al., "A novel segmented-scintillator antineutrino detector", Journal of Instrumentation **12**, P04024–P04024 (2017).

[132] J. Ashenfelter et al., "First Search for Short-Baseline Neutrino Oscillations at HFIR with PROSPECT", Physical Review Letters **121**, 10.1103/physrevlett.121.251802 (2018).

[133] F. Feruglio, A. Strumia, and F. Vissani, "Neutrino oscillations and signals in β and $0\nu2\beta$ experiments", Nuclear Physics B **637**, 345–377 (2002).

[134] C. S. Fong, E. Nardi, and A. Riotto, "Leptogenesis in the Universe", Advances in High Energy Physics **2012**, 1–59 (2012).

[135] L. Gastaldo et al., "The Electron Capture ^{163}Ho Experiment ECHo", Journal of Low Temperature Physics **176**, 876–884 (2014).

[136] B. Alpert et al., "HOLMES", The European Physical Journal C **75**, 10.1140/epjc/s10052-015-3329-5 (2015).

[137] M. P. Croce et al., "Development of Holmium-163 Electron-Capture Spectroscopy with Transition-Edge Sensors", Journal of Low Temperature Physics **184**, 958–968 (2016).

[138] B. Monreal, "The Project 8 Radiofrequency Tritium Neutrino Experiment", Physics Procedia **61**, 274–277 (2015).

[139] J. A. Formaggio and G. P. Zeller, "From eV to EeV: Neutrino cross sections across energy scales", Reviews of Modern Physics **84**, 1307–1341 (2012).

[140] Y. Hayato, "A neutrino interaction simulation program library NEUT", Acta Phys. Polon. B **40**, 2477–2489 (2009).

[141] V. Lyubushkin et al., "A study of quasi-elastic muon neutrino and antineutrino scattering in the NOMAD experiment", The European Physical Journal C **63**, 355–381 (2009).

[142] S. L. Adler, "Tests of the Conserved Vector Current and Partially Conserved Axial-Vector Current Hypotheses in High-Energy Neutrino Reactions", Phys. Rev. **P135**, B963–B966 (1964).

[143] R. Bradford, A. Bodek, and J. Budd H. andArrington, "A New Parameterization of the Nucleon Elastic Form Factors", Nuclear Physics B - Proceedings Supplements **159**, 127–132 (2006).

[144] J. J. Kelly, "Simple parameterization of nucleon form factors", Phys. Rev. C **70**, 068202 (2004).

[145] A. Bodek, S. Avvakumov, R. Bradford, and H. Budd, "Vector and axial nucleon form factors: A duality constrained parameterization", The European Physical Journal C **53**, 349–354 (2007).

[146] E. B. Hughes, T. A. Griffy, M. R. Yearian, and R. Hofstadter, "Neutron Form Factors from Inelastic Electron-Deuteron Scattering", Phys. Rev. **139**, B458–B471 (1965).

[147] J. R. Dunning et al., "Quasi-Elastic Electron-Deuteron Scattering and Neutron Form Factors", Phys. Rev. **141**, 1286–1297 (1966).

[148] J. Arrington and I. Sick, "Precise determination of low-Q nucleon electromagnetic form factors and their impact on parity-violating e-p elastic scattering", Physical Review C **76**, 10.1103/physrevc.76.035201 (2007).

[149] N. K. et al., "Review of Particle Physics", J. Phys. G: Nucl. Part. Phys. **37**, 075021 (2010).

[150] B. Märkisch et al., "Measurement of the Weak Axial-Vector Coupling Constant in the Decay of Free Neutrons Using a Pulsed Cold Neutron Beam", Physical Review Letters **122**, 10.1103/physrevlett.122.242501 (2019).

[151] A. Liesenfeld et al. (A1 Collaboration), "A measurement of the axial form factor of the nucleon by the p(e,e'π+)n reaction at W=1125 MeV", Physics Letters B **468**, 20–27 (1999).

[152] V. Bernard, L. Elouadrhiri, and U. Meißner, "Axial structure of the nucleon", J. Phys. G: Nucl. Part. Phys. **28**, R1–R35 (2001).

[153] T. Leitner, L. Alvarez-Ruso, and U. Mosel, "Charged current neutrino-nucleus interactions at intermediate energies", Physical Review C **73**, 10.1103/physrevc.73.065502 (2006).

[154] K. Kuzmin, V. Lyubushkin, and V. Naumov, "Quasielastic axial-vector mass from experiments on neutrino–nucleus scattering", The European Physical Journal C **54**, 517–538 (2008).

[155] B. Bhattacharya, R. J. Hill, and G. Paz, "Model-independent determination of the axial mass parameter in quasielastic neutrino-nucleon scattering", Phys. Rev. D **84**, 073006 (2011).

[156] M. L. Goldberger and S. B. Treiman, "Form Factors in β Decay and μ Capture", Phys. Rev. **111**, 354–361 (1958).

[157] C. Wilkinson, "Constraining neutrino interaction uncertainties for oscillation experiments", PhD thesis (University of Sheffield, 2016).

[158] R. D. and S. L. M., "Neutrino Excitation of Baryon Resonances and Single Pion Production", Annals of Physics **133**, 79–153 (1981).

[159] C. Berger and L. M. Sehgal, "Lepton mass effects in single pion production by neutrinos", Phys. Rev. D **76**, 113004 (2007).

[160] Y. Hayato and L. Pickering, "The NEUT neutrino interaction simulation program library", The European Physical Journal Special Topics, 10.1140/epjs/s11734-021-00287-7 (2021).

[161] K. M. Graczyk, J. Żmuda, and J. T. Sobczyk, "Electroweak form factors of the Δ(1232)resonance", Physical Review D **90**, 10.1103/physrevd.90.093001 (2014).

[162] M. Kabirnezhad, "Single pion production in neutrino-nucleon interactions", Phys. Rev. D **97**, 013002 (2018).

[163] M. Kabirnezhad, "Single pion production in electron-nucleon interactions", Phys. Rev. D **102**, 053009 (2020).

[164] M. Kabirnezhad, "Single pion production in electron-proton interactions", (2022), arXiv:2203.15594 [hep-ph].

[165] C. Berger and L. M. Sehgal, "Partially conserved axial vector current and coherent pion production by low energy neutrinos", Phys. Rev. D **79**, 053003 (2009).

[166] D. Rein and L. M. Sehgal, "Coherent π^0 Production in Neutrino Reactions", Nucl. Phys. B **223**, 29–44 (1983).

[167] M. Gaździcki and M. I. Gorenstein, "Hagedorn's Hadron Mass Spectrum and the Onset of Deconfinement", Melting Hadrons, Boiling Quarks - From Hagedorn Temperature to Ultra-Relativistic Heavy-Ion Collisions at CERN, 87–92 (2016).

[168] A. Bodek and U. Yang, "A Unified Model for inelastic e-N and ν-N cross sections at all $Q^2$2", AIP Conference Proceedings, 10.1063/1.2122031 (2005).

[169] O. Benhar, D. Day, and I. Sick, "Inclusive quasielastic electron-nucleus scattering", Rev. Mod. Phys. **80**, 189–224 (2008).

[170] J. Nieves, I. R. Simo, and M. J. V. Vacas, "Inclusive charged-current neutrino-nucleus reactions", Physical Review C **83**, 10.1103/physrevc.83.045501 (2011).

[171] O. Benhar et al., "Electron- and neutrino-nucleus scattering in the impulse approximation regime", Physical Review D **72**, 10.1103/physrevd.72.053005 (2005).

[172] A. Bodek, M. E. Christy, and B. Coopersmith, "Effective spectral function for quasielastic scattering on nuclei from ${}^{2}_{1}$H to ${}^{208}_{82}$Pb", AIP Conf. Proc. **1680**, 20003 (2015), arXiv:1409.8545 [nucl-th].

[173] R. A. Smith and E. J. Moniz, "Neutrino reactions on nuclear targets", Nucl. Phys. B **43**, 605–622 (1972).

[174] E. J. Moniz et al., "Nuclear Fermi Momenta from Quasielastic Electron Scattering", Phys. Rev. Lett. **26**, 445–448 (1971).

[175] L. Alvarez-Ruso, Y. Hayato, and J. Nieves, "Progress and open questions in the physics of neutrino cross sections at intermediate energies", New Journal of Physics **16**, 075015 (2014).

[176] O. Benhar, A. Fabrocini, S. Fantoni, and I. Sick, "Spectral function of finite nuclei and scattering of GeV electrons", Nucl. Phys. A **579**, 493–517 (1994).

[177] M. Patsyuk, O. Hen, and E. Piasetzky, "Exclusive studies on short range correlations in nuclei", EPJ Web Conf. **204**, edited by S. Bondarenko, V. Burov, and A. Malakhov, 01016 (2019).

[178] J. Chakrani et al., *NIWG Model Recommendations for OA 2021*, tech. rep. T2K-TN-414 (Apr. 2022).

[179] A. M. Ankowski, O. Benhar, and M. Sakuda, "Improving the accuracy of neutrino energy reconstruction in charged-current quasielastic scattering off nuclear targets", Physical Review D **91**, 10.1103/physrevd.91.033005 (2015).

[180] K. Abe et al., "Characterization of nuclear effects in muon-neutrino scattering on hydrocarbon with a measurement of final-state kinematics and correlations in charged-current pionless interactions at T2K", Physical Review D **98**, 10.1103/physrevd.98.032003 (2018).

[181] X.-G. Lu et al., "Measurement of Final-State Correlations in Neutrino Muon-Proton Mesonless Production on Hydrocarbon at $\langle E_\nu \rangle = 3$ GeV", Physical Review Letters **121**, 10.1103/physrevlett.121.022504 (2018).

[182] A. Furmanski, *Implementing the spectral function nuclear model in NEUT, and parametrizing systematic uncertainties*, tech. rep. T2K-TN-184 (Oct. 2013).

[183] J. D. Bjorken, "Asymptotic Sum Rules at Infinite Momentum", Phys. Rev. **179**, 1547–1553 (1969).

[184] W. M. Alberico et al., "Scaling in electron scattering from a relativistic Fermi gas", Phys. Rev. C **38**, 1801–1810 (1988).

[185] M. B. Barbaro et al., "Relativistic γ-scaling and the Coulomb sum rule in nuclei", Nucl. Phys. A **643**, 137–160 (1998).

[186] R. Altemus et al., "Longitudinal and Transverse Inelastic Electron Scattering from ^{56}Fe", Phys. Rev. Lett. **44**, 965–968 (1980).

[187] G. D. Megias, "Charged-current neutrino interactions with nucleons and nuclei at intermediate energies", PhD thesis (UNIVERSIDAD DE SEVILLA, May 2017).

[188] J. E. Amaro et al., "Neutrino-nucleus scattering in the SuSA model", Eur. Phys. J. ST **230**, 4321–4338 (2021), arXiv:2106.02857 [hep-ph].

[189] R. González-Jiménez et al., "Extensions of superscaling from relativistic mean field theory: The SuSAv2 model", Phys. Rev. C **90**, 035501 (2014).

[190] G. D. Megias et al., "Inclusive electron scattering within the SuSAv2 meson-exchange current approach", Phys. Rev. D **94**, 013012 (2016).

[191] T. W. Donnelly and I. Sick, "Superscaling of inclusive electron scattering from nuclei", Physical Review C **60**, 10.1103/physrevc.60.065502 (1999).

[192] A. Bodek, M. E. Christy, and B. Coopersmith, "Effective spectral function for quasielastic scattering on nuclei", The European Physical Journal C **74**, 10.1140/epjc/s10052-014-3091-0 (2014).

[193] Nieves, J. and others, "Neutrino-nucleus CCQE-like scattering", Nucl. Part. Phys. Proc. **273-275**, 1830–1835 (2016), arXiv:1411.7821 [hep-ph].

[194] G. A. Fiorentini et al., "Measurement of Muon Neutrino Quasielastic Scattering on a Hydrocarbon Target at E$\nu \sim 3.5$ GeV", Physical Review Letters **111**, 10.1103/physrevlett.111.022502 (2013).

[195] A. Bodek, H. S. Budd, and M. E. Christy, "Neutrino quasielastic scattering on nuclear targets", The European Physical Journal C **71**, 10.1140/epjc/s10052-011-1726-y (2011).

[196] J. Carlson, J. Jourdan, R. Schiavilla, and I. Sick, "Longitudinal and transverse quasielastic response functions of light nuclei", Phys. Rev. C **65**, 024002 (2002).

[197] J. Nieves, J. E. Amaro, and M. Valverde, "Inclusive quasielastic charged-current neutrino-nucleus reactions", Phys. Rev. C **70**, 055503 (2004).

[198] R. Gran, *Model uncertainties for Valencia RPA effect for MINERvA*, 2017, arXiv:1705.02932 [hep-ex].

[199] R. Gran, J. Nieves, F. Sanchez, and M. J. V. Vacas, "Neutrino-nucleus quasi-elastic and 2p2h interactions up to 10 GeV", Physical Review D **88**, 10.1103/physrevd.88.113007 (2013).

[200] M. Martini, M. Ericson, G. Chanfray, and J. Marteau, "Unified approach for nucleon knock-out and coherent and incoherent pion production in neutrino interactions with nuclei", Physical Review C **80**, 10.1103/physrevc.80.065501 (2009).

[201] R. E. Cutkosky, "Singularities and discontinuities of Feynman amplitudes", J. Math. Phys. **1**, 429–433 (1960).

[202] A. Redij et al., *Implementation of a multi-nucleon interaction model into NEUT*, tech. rep. T2K-TN-170 (2014).

[203] J. Nieves, I. Ruiz Simo, and M. Vicente Vacas, "The nucleon axial mass and the MiniBooNE quasielastic neutrino–nucleus scattering problem", Physics Letters B **707**, 72–75 (2012).

[204] M. Martini, M. Ericson, and G. Chanfray, "Neutrino quasielastic interaction and nuclear dynamics", Physical Review C **84**, 10.1103/physrevc.84.055502 (2011).

[205] J. Nieves, I. Ruiz Simo, and M. Vicente Vacas, "Two particle–hole excitations in charged current quasielastic antineutrino-nucleus scattering", Physics Letters B **721**, 90–93 (2013).

[206] M. Martini and M. Ericson, "Quasielastic and multinucleon excitations in antineutrino-nucleus interactions", Physical Review C **87**, 10.1103/physrevc.87.065501 (2013).

[207] T. Golan, *What is inside MC generators... and why it is wrong*, 2017.

[208] O. Buss et al., "Transport-theoretical description of nuclear reactions", Physics Reports **512**, 1–124 (2012).

[209] L. L. Salcedo, E. Oset, M. J. Vicente-Vacas, and C. Garcia-Recio, "Computer Simulation of Inclusive Pion Nuclear Reactions", Nucl. Phys. A **484**, 557–592 (1988).

[210] T. Golan, C. Juszczak, and J. T. Sobczyk, "Effects of final-state interactions in neutrino-nucleus interactions", Physical Review C **86**, 10.1103/physrevc.86.015505 (2012).

[211] R. D. Woods and D. S. Saxon, "Diffuse Surface Optical Model for Nucleon-Nuclei Scattering", Phys. Rev. **95**, 577–578 (1954).

[212] L. D. Landau and I. Pomeranchuk, "Limits of applicability of the theory of bremsstrahlung electrons and pair production at high-energies", Dokl. Akad. Nauk Ser. Fiz. **92**, 535–536 (1953).

[213] X.-G. Lu et al., "Measurement of nuclear effects in neutrino interactions with minimal dependence on neutrino energy", Phys. Rev. C **94**, 015503 (2016).

[214] K. Abe et al. (The T2K Collaboration), "Characterization of nuclear effects in muon-neutrino scattering on hydrocarbon with a measurement of final-state kinematics and correlations in charged-current pionless interactions at T2K", Phys. Rev. D **98**, 032003 (2018).

[215] X.-G. Lu et al. (MINERvA Collaboration), "Measurement of Final-State Correlations in Neutrino Muon-Proton Mesonless Production on Hydrocarbon at $< E_\nu >= 3$GeV", Phys. Rev. Lett. **121**, 022504 (2018).

[216] P. E. Hodgson, *The nuclear optical model introductory overview*, tech. rep. (Oxford Univ. Nucl. Phys., Oxford, Dec. 1996).

[217] J. W. Holt and T. R. Whitehead, "Modern approaches to optical potentials", (2022), arXiv:2201.13404 [nucl-th].

[218] S. Boffi, C. Giusti, and F. D. Pacati, *Nuclear response in electromagnetic interactions with complex nuclei*, Apr. 1993.

[219] H. P. Kelly, "Use of the Optical Potential for Elastic Scattering of Electrons by Atoms", Phys. Rev. **160**, 44–52 (1967).

[220] E. D. Cooper, S. Hama, B. C. Clark, and R. L. Mercer, "Global Dirac phenomenology for proton nucleus elastic scattering", Phys. Rev. C **47**, 297–311 (1993).

[221] J. T. Sobczyk, "Multinucleon-ejection model for two-body-current neutrino interactions", Physical Review C **86**, 10.1103/physrevc.86.015504 (2012).

[222] K. Abe et al., "The T2K experiment", Nuclear Instruments and Methods in Physics Research Section A: Accelerators, Spectrometers, Detectors and Associated Equipment **659**, 106–135 (2011).

[223] *Accelerator technical design report for high-intensity proton accelerator facility project, J-PARC* (2003).

[224] K. Abe, N. Abgrall, H. Aihara, T. Akiri, J. B. Albert, C. Andreopoulos, S. Aoki, A. Ariga, T. Ariga, S. Assylbekov, et al., "T2K neutrino flux prediction", Physical Review D **87**, 10.1103/physrevd.87.012001 (2013).

[225] D. Beavis, A. Carroll, and I. Chiang (E889 Collaboration), "Long baseline neutrino oscillation experiment at the AGS. Physics Design Report", 10.2172/52878 (1995).

[226] K. Abe et al., "Measurements of the T2K neutrino beam properties using the INGRID on-axis near detector", Nuclear Instruments and Methods in Physics Research Section A: Accelerators, Spectrometers, Detectors and Associated Equipment **694**, 211–223 (2012).

[227] Y. Oyama, *Current status of the T2K experiment*, 2015, arXiv:1510.07200 [hep-ex].

[228] S. Assylbekov et al., "The T2K ND280 off-axis pi–zero detector", Nuclear Instruments and Methods in Physics Research Section A: Accelerators, Spectrometers, Detectors and Associated Equipment **686**, 48–63 (2012).

[229] P.-A. Amaudruz et al., "The T2K fine-grained detectors", Nuclear Instruments and Methods in Physics Research Section A: Accelerators, Spectrometers, Detectors and Associated Equipment **696**, 1–31 (2012).

[230] T. N. T. collaboration, *Time Projection Chambers for the T2K Near Detectors*, 2010, arXiv:1012.0865 [physics.ins-det].

[231] D. Allan et al., "The electromagnetic calorimeter for the T2K near detector ND280", Journal of Instrumentation **8**, P10019–P10019 (2013).

[232] S. Aoki et al., "The T2K Side Muon Range Detector (SMRD)", Nuclear Instruments and Methods in Physics Research Section A: Accelerators, Spectrometers, Detectors and Associated Equipment **698**, 135–146 (2013).

[233] S. Fukuda et al., "The Super-Kamiokande Detector", Nucl. Inst. Meth. A **501**, 418–462 (2003).

[234] Y. Suzuki, "The Super-Kamiokande experiment", Eur. Phys. J. C **79**, 298 (2019).

[235] A. Suzuki et al., "Improvement of 20-inch diameter photomultiplier tubes", Nucl. Instrum. Meth. A **329**, 299–313 (1993).

[236] Y. Ashie et al., "Measurement of atmospheric neutrino oscillation parameters by Super-Kamiokande I", Physical Review D **71**, 10.1103/physrevd.71.112005 (2005).

[237] J. Hosaka et al., "Solar neutrino measurements in Super-Kamiokande-I", Physical Review D **73**, 10.1103/physrevd.73.112001 (2006).

[238] R. W. Kadel et al., "Report on the Depth Requirements for a Massive Detector at Homestake", 10.2172/946806 (2008).

[239] N. Fomin, "Inclusive electron scattering from nuclei in the quasielastic region at large momentum transfer", PhD thesis (University of Virginia, Charlottesville, VA, Jan. 2008), arXiv:0812.2144 [nucl-ex].

[240] B. R. Martin, "Experimental methods", in *Nuclear and particle physics: an introduction* (John Wiley & Sons Ltd, 2009), pp. 112–114.

[241] E. L. Ginzton, W. W. Hansen, and W. R. Kennedy, "A LINEAR ELECTRON ACCELERATOR", Rev. Sci. Instrum. **19**, 89–108 (1948).

[242] R. P. Borghi, A. L. Eldredge, G. A. Loew, and R. B. Neal, "Design and Fabrication of the Accelerating Structure for the Stanford 2-Mile Accelerator", (1965).

[243] J. Seeman et al., "Design and Principles of Linear Accelerators and Colliders", in *Particle Physics Reference Library : Volume 3: Accelerators and Colliders*, edited by S. Myers and H. Schopper (Springer International Publishing, 2020) Chap. 7.8, pp. 295–336.

[244] L. Merminga, D. R. Douglas, and G. A. Krafft, "High-current energy-recovering electron linacs", Ann. Rev. Nucl. Part. Sci. **53**, 387–429 (2003).

[245] C. W. Leemann, D. R. Douglas, and G. A. Krafft, "The Continuous Electron Beam Accelerator Facility: CEBAF at the Jefferson Laboratory", Ann. Rev. Nuc. and Part. Sci. **51**, 413–450 (2001).

[246] N. Fomin et al., "Scaling of the F_2 Structure Function in Nuclei and Quark Distributions at $x > 1$", Phys. Rev. Lett. **105**, 212502 (2010).

[247] H. R. Crannell and L. R. Suelzle, "Determination of relative efficiencies for a multidetector system", Nucl. Inst. Meth. **44**, 133–136 (1966).

[248] E. J. Moniz et al., "Nuclear Fermi momenta from quasielastic electron scattering", Phys. Rev. Lett. **26**, 445–448 (1971).

[249] I. Sick and J. S. McCarthy, "Elastic Electron Scattering From *sup*12C and *sup*16O.", Nucl. Phys. A150: 631-54(1970). **150**, 10.1016/0375-9474(70)90423-9 (1970).

[250] R. R. Whitney et al., "Quasielastic electron scattering", Phys. Rev. C **9**, 2230–2235 (1974).

[251] I. Sick and J. S. McCarthy, "Elastic electron scattering from 12C and 16O", Nucl. Phys. A **150**, 631–654 (1970).

[252] D. L. Wilson, "THE REFRACTIVE INDEX OF FC-75. Technical Report No. 419", (1964).

[253] D. Zeller, "INVESTIGATION OF THE STRUCTURE OF THE C-12 NUCLEUS BY HIGH-ENERGY ELECTRON SCATTERING", Other thesis (Sept. 1973).

[254] S. Hartwig et al., "Comparison of inelastic electron and positron scattering cross sections on ^{12}C and ^{27}Al", Phys. Lett., B **82**, 297–300 (1979).

[255] J. A. Niederer, "INDEX OF REFRACTION AND DISPERSION OF SEVERAL GASES IN CERENKOV COUNTER USE", (1961).

[256] W. Albrecht et al., "Elastic Electron-Proton Scattering at Momentum Transfers up to 245 F^{-2}", Phys. Rev. Lett. **17**, 1192–1195 (1966).

[257] P. Barreau et al., "Deep-inelastic electron scattering from carbon", Nucl. Phys. A **402**, 515–540 (1983).

[258] P. Leconte et al., "The electron scattering facility at the Saclay 600 MeV linear accelerator", Nucl. Inst. Meth. **169**, 401–412 (1980).

[259] J. S. O'Connell et al., "Electromagnetic excitation of the delta resonance in nuclei", Phys. Rev. C **35**, 1063–1071 (1987).

[260] J. Haimson, "Initial Operation of the MIT Electron Linear Accelerator", IEEE Transactions on Nuclear Science **20**, 914–918 (1973).

[261] D. B. Day et al., "y scaling in electron-nucleus scattering", Phys. Rev. Lett. **59**, 427–430 (1987).

[262] D. B. Day et al., "Inclusive electron-nucleus scattering at high momentum transfer", Phys. Rev. C **48**, 1849–1863 (1993).

[263] D. S. Bagdasaryan et al., *Measurement of spectra of (e,e') scattering on ^{9}Be and ^{12}C nuclei in inelastic region at $Q^2 \leq\sim 0.4$ GeV^2/c^2*, tech. rep. DEMO-PREPRINT-2016-739. FileName: EFI10774088. RN:21092324.0. TRN: SU9007148. (Jan. 1988).

[264] V. G. Ambartsumian et al., *A SETUP FOR THE INVESTIGATION OF ELECTRON - NUCLEUS INTERACTIONS IN ENERGY RANGE UP TO 5-GeV*, tech. rep. DEMO-PREPRINT-2016-1517. Report No:EFI-648-38-83-YEREVAN.. Accession No: 200034382. (Jan. 1983).

[265] D. T. Baran et al., "Δ Electroproduction and Inelastic Charge Scattering from Carbon and Iron", Phys. Rev. Lett. **61**, 400–403 (1988).

[266] R. M. Sealock et al., "Electroexcitation of the $\Delta(1232)$ in nuclei", Phys. Rev. Lett. **62**, 1350–1353 (1989).

[267] R. Anderson, D. Gustavson, R. Prepost, and D. Ritson, "1.6 GeV/c charged particle spectrometer facility at the Stanford linear accelerator center", Nucl. Inst. Meth. **66**, 328–335 (1968).

[268] J. Arrington et al., "Inclusive electron scattering from nuclei at $x \simeq 1$", Phys. Rev. C **53**, 2248–2251 (1996).

[269] J. Arrington et al., "Inclusive Electron-Nucleus Scattering at Large Momentum Transfer", Phys. Rev. Lett. **82**, 2056–2059 (1999).

[270] V. D. Burkert et al., "The CLAS12 Spectrometer at Jefferson Laboratory", Nucl. Instrum. Meth. A **959**, 163419 (2020).

[271] M. D. Mestayer et al., "The CLAS12 drift chamber system", Nucl. Instrum. Meth. A **959**, 163518 (2020).

[272] Y. G. Sharabian et al., "The CLAS12 high threshold Cherenkov counter", Nucl. Instrum. Meth. A **968**, 163824 (2020).

[273] M. Ungaro et al., "The CLAS12 Low Threshold Cherenkov detector", Nuclear Instruments and Methods in Physics Research A **957**, 163420 (2020).

[274] M. Contalbrigo et al., "The CLAS12 Ring Imaging Cherenkov detector", Nucl. Instrum. Meth. A **964**, 163791 (2020).

[275] D. S. Carman et al., "The CLAS12 Central Time-of-Flight system", Nucl. Instrum. Meth. A **960**, 163626 (2020).

[276] G. Asryan et al., "The CLAS12 forward electromagnetic calorimeter", Nucl. Inst. Meth. A **959**, 163425 (2020).

[277] A. Acker et al., "The CLAS12 Forward Tagger", Nucl. Instrum. Meth. A **959**, 163475 (2020).

[278] M. A. Antonioli et al., "The CLAS12 Silicon Vertex Tracker", Nucl. Instrum. Meth. A **962**, 163701 (2020).

[279] A. Acker et al., "The CLAS12 Micromegas Vertex Tracker", Nucl. Instrum. Meth. A **957**, 163423 (2020).

[280] D. S. Carman et al., "The CLAS12 Forward Time-of-Flight system", Nucl. Instrum. Meth. A **960**, 163629 (2020).

[281] P. Chatagnon et al., "The CLAS12 Central Neutron Detector", Nucl. Instrum. Meth. A **959**, 163441 (2020).

[282] E. P. Segarra et al., "The CLAS12 Backward Angle Neutron Detector (BAND)", Nucl. Instrum. Meth. A **978**, 164356 (2020).

[283] C. Andreopoulos et al., "The GENIE Neutrino Monte Carlo Generator", Nucl. Instrum. Meth. A **614**, 87–104 (2010), arXiv:0905.2517 [hep-ph].

[284] J. Zmuda, K. Graczyk, C. Juszczak, and J. Sobczyk, "NuWro Monte Carlo Generator of Neutrino Interactions - First Electron Scattering Results", Acta Physica Polonica B **46**, 2329 (2015), arXiv:1510.03268 [physics.hep-ph].

[285] C. Juszczak, J. Nowak, and J. Sobczyka, "Simulations from a new neutrino event generator", Nucl. Phys. B **159**, 211–216 (2006).

[286] R. Acciarri et al. (DUNE), "Long-Baseline Neutrino Facility (LBNF) and Deep Underground Neutrino Experiment (DUNE): Conceptual Design Report, Volume 2: The Physics Program for DUNE at LBNF", (2015), arXiv:1512.06148 [physics.ins-det].

[287] A. M. Ankowski et al., "Missing energy and the measurement of the CP-violating phase in neutrino oscillations", Phys. Rev. D **92**, 091301 (2015).

[288] A. M. Ankowski, O. Benhar, C. Mariani, and E. Vagnoni, "Effect of the $2p2h$ cross-section uncertainties on an analysis of neutrino oscillations", Phys. Rev. D **93**, 113004 (2016).

[289] P. Coloma and P. Huber, "Impact of Nuclear Effects on the Extraction of Neutrino Oscillation Parameters", Phys. Rev. Lett. **111**, 221802 (2013).

[290] S. Bienstock, *Studying the impact of neutrino cross-section mismodelling on the T2K oscillation analysis*, June 2018.

[291] M. Martini, M. Ericson, and G. Chanfray, "Neutrino energy reconstruction problems and neutrino oscillations", Phys. Rev. D **85**, 093012 (2012).

[292] J. Nieves, F. Sanchez, I. Ruiz Simo, and M. J. Vicente Vacas, "Neutrino Energy Reconstruction and the Shape of the CCQE-like Total Cross Section", Phys. Rev. D **85**, 113008 (2012), arXiv:1204.5404 [hep-ph].

[293] M. Khachatryan et al., "Electron-beam energy reconstruction for neutrino oscillation measurements", Nature (London) **599**, 10.1038/s41586-021-04046-5 (2021).

[294] S. Dolan, "Neutrino-Nucleus Interactions at T2K", Neutrino 2020, 2020.

[295] A. M. Ankowski et al., "Comparison of the calorimetric and kinematic methods of neutrino energy reconstruction in disappearance experiments", Phys. Rev. D **92**, 10.1103/physrevd.92.073014 (2015).

[296] A. M. Ankowski et al., *Electron Scattering and Neutrino Physics*, Mar. 2022.

[297] D. S. Armstrong and R. D. McKeown, "Parity-Violating Electron Scattering and the Electric and Magnetic Strange Form Factors of the Nucleon", Ann. Rev. Nucl. Part. Sci. **62**, 337–359 (2012), arXiv:1207.5238 [nucl-ex].

[298] L. Alvarez-Ruso et al., "NuSTEC White Paper: Status and challenges of neutrino–nucleus scattering", Progress in Particle and Nuclear Physics **100**, 1–68 (2017), arXiv:1706.03621 [hep-ph].

[299] P. Guèye et al., "Coulomb distortion measurements by comparing electron and positron quasielastic scattering off ^{12}C and ^{208}Pb", Phys. Rev. C **60**, 044308 (1999).

[300] A. Bodek and T. Cai, "Removal energies and final state interaction in lepton nucleus scattering", EPJ C **79**, 10.1140/epjc/s10052-019-6750-3 (2019).

[301] O. Benhar, D. Day, and I. Sick, *An archive for quasi-elastic electron-nucleus scattering data*, 2006, arXiv:quant-ph/0401062.

[302] P. Stowell et al., "NUISANCE: a neutrino cross-section generator tuning and comparison framework", Jour. Inst. **12**, P01016–P01016 (2017), arXiv:1612.07393 [hep-ex].

[303] J. E. Amaro, M. B. Barbaro, J. A. Caballero, T. W. Donnelly, and J. M. Udias, "Final-state interactions and superscaling in the semi-relativistic approach to quasielastic electron and neutrino scattering", Phys. Rev. C **75**, 034613 (2007), arXiv:nucl-th/0612056.

[304] K. Yasutome et al., *P-theta 2021 Run 1-10 Joint-fit Analysis with multi-ring sample*, tech. rep. T2K-TN-430 (2022).

[305] K. Niewczas, Personal Communication, Feb. 2020.

[306] E. Atkin et al., *Updated recommendation of the 2018 NIWG parameters*, tech. rep. T2K-TN-344 (2018).

[307] J. Gonzalez-Rosa, G. D. Megias, J. A. Caballero, and M. B. Barbaro, "SuSAv2 model for inelastic neutrino-nucleus scattering", Phys. Rev. D **105**, 093009 (2022), arXiv:2203.12308 [physics.nucl-th].

[308] I. Ruiz Simo, C. Albertus, J. E. Amaro, M. B. Barbaro, J. A. Caballero, and T. W. Donnelly, "Relativistic effects in two-particle emission for electron and neutrino reactions", Phys. Rev. D **90**, 033012 (2014).

[309] M. V. Ivanov et al., "Charged-current inclusive neutrino cross sections in the SuperScaling model including quasielastic, pion production and meson-exchange contributions", J. Phys. G **43**, 045101 (2016), arXiv:1506.00801 [nucl-th].

[310] K. Abe et al., "Calibration of the Super-Kamiokande Detector", Nucl. Instrum. Meth. A **737**, 253–272 (2014), arXiv:1307.0162 [physics.ins-det].

[311] L. Anthony, "Design and Installation of an Optical Calibration System for Next-Generation Water Cherenkov Detectors", 2022.

[312] L. Marti et al., "Evaluation of gadolinium's action on water Cherenkov detector systems with EGADS", Nucl. Inst. Meth. A **959**, 163549 (2020).

[313] K. Abe et al., "First gadolinium loading to super-kamiokande", Nucl. Inst. Meth. A **1027**, 166248 (2022), arXiv:2109.00360 [physics.ins-det].

[314] *Run-by-Run Attenuation Curve*.

[315] *Water Job: Time variation of the attenuation length.*

Appendix A

Simulation Theory

A.1 Rejection Sampling

NEUT, and indeed most event generators, are based on rejection sampling - also called the acceptance-rejection method. This is a Monte Carlo algorithm used to sample from a sophisticated (*i.e.* difficult to sample from) distribution. If you have a function from which you cannot (or is difficult to) create a cumulative distribution function and find its inverse, then by comparing your distribution to a *proposal* function you can accept and reject events based on their likelihood of occurring. Thus regions of high probability in your *target* function accept more events and regions of low probability accept less.

Suppose we have some 1-dimensional target function $f(x)$ that we cannot sample from. Now take a distribution that covers the entire range of x-values of our target, called $g(x)$. This proposal distribution can be scaled by some constant, M, such that it encompasses all of our target distribution, $Mg(x)$, following the condition

$$M \geq \frac{f(x)}{g(x)}\,.$$

Choosing a value we would like to sample along the x-axis, say point X, we can find the intercept with both the target and proposal functions, $f(x = X)$ and $g(x = X)$. If we uniformly sample between 0 and $Mg(x = X)$, any value that falls below $f(x = X)$ can be accepted, and any above can be rejected. This reflects the likelihood of occurrence at any particular x value. Mathematically, this can be described by

$$\begin{aligned} u &\sim \mathcal{U}(0,1)\,, \\ u &\leq \frac{f(x)}{Mg(x)}\,. \end{aligned} \tag{A.1}$$

Therefore, a full Monte Carlo generation would proceed by:

1. Choose a sample from the proposal function.

2. Generate a random number (u) uniformly between 0 and 1.

3. Check if the condition in equation A.1 is satisfied; if true accept the event, if false reject it.

4. Repeat until the desired number of samples are taken.

This is of course a simple example, but fully describes the process. To speed up the generation and reduce computational intensity, clever choices can be made about the proposal distribution in order to reduce the number of events rejected.

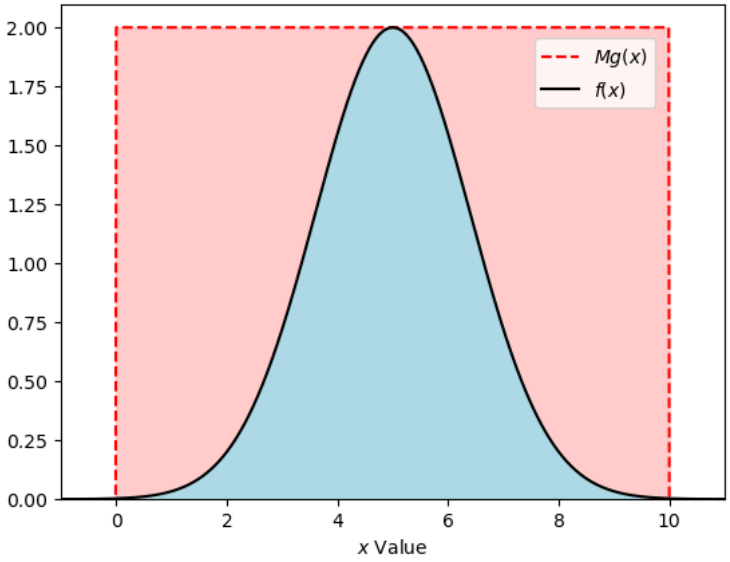

Fig. A.1: Example of rejection sampling. Any random event found under the target distribution ($f(x)$), the blue region, will be accepted. Any event found under the proposed distribution ($Mg(x)$), but above the target, will be rejected (*i.e.* the red region).

A.2 Electromagnetic Tensor Contraction

The leptonic and hadronic tensors are defined by

$$L_{\mu\nu} = 2(k_\mu k'_\nu + k'_\mu k_\nu + \vec{k}\cdot\vec{k'}g_{\mu\nu} - i\epsilon_{\mu\nu\rho\sigma}k^\rho k'^\sigma) \tag{A.2}$$

$$\begin{aligned} H^{\mu\nu} = &-g^{\mu\nu}M_N^2 H_1 + p^\mu p^\nu H_2 + \frac{i}{2}\epsilon^{\mu\nu\kappa\lambda}p_\kappa q_\lambda H_3 \\ &- q^\mu q^\nu H_4 + \frac{1}{2}(p^\mu q^\nu + q^\mu p^\nu)H_5 \end{aligned} \tag{A.3}$$

where M_N is the mass of the struck nucleon, k, k', p and q are the four-vectors of the incoming lepton, outgoing lepton, initial state nucleon and momentum transfer respectively. ϵ is the antisymmetric tensor, and $\epsilon_{\nu\mu\rho\sigma}\epsilon^{\nu\mu\kappa\lambda} = \delta^\kappa_\rho\delta^\lambda_\sigma - \delta^\lambda_\rho\delta^\kappa_\sigma$. The components, H, in the

hadronic tensor are given by

$$
\begin{aligned}
H_1 &= F_A^2(1+\tau) + \tau(F_1+F_2)^2\,, \\
H_2 &= F_A^2 + F_1^2 + \tau F_2^2\,, \\
H_3 &= 2F_A(F_1+F_2)\,, \\
H_4 &= \frac{1}{4}F_2^2(1-\tau) + \frac{1}{2}F_1F_2 + F_AF_P - \tau F_P^2\,, \\
H_5 &= H_2\,,
\end{aligned}
$$

where $\tau = \frac{Q^2}{4M_N^2}$ and the form factors are defined in section 2.1.1.

The Benhar spectral function follows the de Forest method, that treats nucleon which are originally off-shell by replacing $q^\mu(\omega,\vec{q}) \to \tilde{q}^\mu(\tilde{\omega},\vec{q})$ in the hadronic tensor, where $\tilde{\omega} = E_{\mathrm{p}'} - E_{\mathrm{p}} = \omega - E_B$ is the reduced energy transfer.

The contraction $L_{\mu\nu}H^{\mu\nu}$ is expressed as

$$
\begin{aligned}
L_{\mu\nu}H^{\mu\nu} = &-2k\cdot k' M_N^2 H_1 \\
&+ [2(k\cdot p)(k'\cdot p) - (k\cdot k')(p\cdot p)]H_2 \\
&\pm [(k\cdot q)(k'\cdot p) - (k\cdot p)(k'\cdot q)]H_3 \\
&+ [(k\cdot k')(q\cdot q) - (k\cdot q)(k'\cdot q)]H_4 \\
&+ [(k\cdot p)(k'\cdot q) - (k'\cdot p)(k\cdot q) - (k\cdot k')(p\cdot q)]H_5
\end{aligned}
\tag{A.4}
$$

where $+(-)$ refers to (anti)neutrinos.

For electrons, the components H of the hadronic tensor can be altered to remove the axial and pseudo-axial form factors, *i.e.*

$$
\begin{aligned}
H_1 &= \tau(F_1+F_2)^2\,, \\
H_2 &= F_1^2 + \tau F_2^2\,, \\
H_3 &= 0\,, \\
H_4 &= \frac{1}{4}F_2^2(1-\tau) + \frac{1}{2}F_1F_2\,, \\
H_5 &= H_2\,.
\end{aligned}
$$

Of course, because of the Goldberger-Treiman relation, setting the axial form factor to zero automatically removes the influence of the pseudo-axial form factor.